The feasibility of ultrasound elastography in monitoring high-intensity focused ultrasound therapy

Visa Suomi

St Hilda's College

University of Oxford

A thesis submitted for the degree of

Doctor of Philosophy

Trinity 2016

This thesis is dedicated to my grandmother Brita Virtanen and my grandfather Pentti Suomi who passed away before my graduation

Acknowledgements

First of all, I would like to acknowledge and thank my supervisor Prof. Robin Cleveland for his excellent guidance throughout my whole DPhil research. Without his extensive knowledge, expertise and insightful opinions, it would not have been possible for me to come to this point.

I would also like to thank my co-supervisor Prof. David Edwards, who guided me during the first year. His guidance in the beginning of my research helped me to better understand and refine the research problems.

I am grateful to Prof. Elisa Konofagou, who let me to spend a summer at her research group at Columbia University. I would also like to thank all her students and postdocs, especially Matthew McGarry, Ronny Li and Yang Han, who were very kind and helpful during the whole time.

My thanks also go to Prof. Mark Hamilton, who let me to visit his research group at University of Texas at Austin, and to his student Benjamin Treweek, who I have had pleasure to work with.

I am also very grateful to Dr. Bradley Treeby from University College London and Dr. Jiri Jaros from Brno University of Technology, who I had a great privilege to collaborate with.

I would also like to thank all my past and current labmates, who made spending countless hours in the office a lot more pleasurable. Big thanks also to our workshop technicians Jim Fisk and David Salisbury, who have helped me with my research and have been great company.

Furthermore, I would like to thank my friends from the CDT, especially Sandra, Dongli, Vikranth and George, with whom I have had great time together both in and outside the office. I also like to acknowledge our CDT administrator Jo Armitage, who has always been very helpful.

My acknowledgements also go to all my funding bodies: Engineering and Physical Sciences Research Council (EPSRC), Jenny and Antti Wihuri

Foundation, Instrumentarium Science Foundation, Otto A. Malm Foundation, Finnish Cultural Foundation and Finnish Foundation for Technology Promotion. Without their support this research would not have been possible.

Last but not least, I would like to thank my parents Reima and Leena, my brothers Juho and Tomi, my aunt Tuija and her husband Fredrik, and my grandparents Brita and Pentti for their support during my whole time in Oxford.

Abstract

High-intensity focused ultrasound (HIFU) therapy is a non-invasive therapy method for the treatment of solid tumours. One of the main barriers to wider clinical adoption of HIFU is the lack of reliable and cost-efficient therapy monitoring. One promising technique is acoustic radiation force (ARF) ultrasound elastography, which relies on the temperature dependence of tissue properties to affect displacement amplitudes.

An extensive literature review of tissue acoustic, thermal and mechanical properties identified an absence of data on the temperature dependence of the viscoelastic properties. Experiments were carried out in *ex vivo* liver to determine these properties over the range of temperatures and frequencies relevant to ARF.

ARF induced displacements were quantified experimentally in a tissue-mimicking phantom. The comparison of sine and square modulated ARF excitation showed that square modulation results in higher peak amplitudes and smaller second harmonic components in the frequency domain. A simulation model was developed, which accurately reproduced the observed displacements with different modulation frequencies and power levels.

The effect of temperature on ARF displacements was measured experimentally during HIFU therapy in *ex vivo* liver. Simulations captured the same phenomena as observed in the experiments. ARF displacements during HIFU therapy were shown to initially depend on attenuation before ablation, but once the temperature exceeded the ablation threshold, viscoelastic properties dominated.

A second barrier for HIFU is the need to reliably deliver acoustic energy to the target. Nonlinear acoustic simulations were conducted using patient derived computed tomography (CT) data to evaluate the HIFU therapy in the kidney. The simulations revealed that attenuation and refraction contributed roughly equally to intensity loss. Focal splitting associated with

refraction was found to be the main effect reducing the heating efficacy, and a method to employ phase correction at the source was proposed to mitigate the effect.

Contents

List of Figures

List of Symbols

A		Coefficient of linear term in the equation of state
A_0-A_1	[dB/cm]	Asymptotic values for sigmoidal fitting
A_S	[m^2]	Surface area
a_0-a_4		Polynomial fitting parameters for attenuation
α	[Np/m] or [dB/m]	Attenuation
α_0	[dB/m/MHz]	Attenuation coefficient
α_abs	[Np/m] or [dB/m]	Absorption
α_k	[Np/m] or [dB/m]	Absorption in kidney
α_pol	[dB/cm]	Polynomial attenuation
α_sig	[dB/cm]	Sigmoidal attenuation
α_Z		Variable in fractional Zener model
B		Coefficient of quadratic term in the equation of state
b	[m^2/s]	Sound diffusivity
B/A		Nonlinearity parameter
β		Coefficient of nonlinearity
C	[1/Pa]	Compliance modulus
c	[m/s]	Sound speed
c_0-c_2		Polynomial fitting parameters for sound speed
c_k	[m/s]	Sound speed in kidney
C_g	[1/Pa]	Glassy compliance
c_pol		Normalised polynomial sound speed
c_P	[J/kg/K]	Specific heat capacity at constant pressure
$c_{P\mathrm{b}}$	[J/kg/K]	Specific heat capacity of blood
$c_{P\mathrm{k}}$	[J/kg/K]	Specific heat capacity of kidney
$c_{P\mathrm{t}}$	[J/kg/K]	Specific heat capacity of tissue
C_r	[1/Pa]	Rubbery compliance
c_s	[m/s]	Sound speed in sample
c_T	[m/s]	Shear wave speed
c_t	[m/s]	Sound speed in tissue
c_w	[m/s]	Sound speed in water
c_V	[J/kg/K]	Specific heat capacity at constant volume
D	[m^2/s]	Thermal diffusivity
d	[m]	Distance between the transducers
d_a	[m]	Active element diameter
d_M		Variable in fractional Zener model

δ	[rad]	Phase angle in dynamic modulus
δ_{ij}		Kronecker delta
E	[Pa]	Young's modulus
ϵ		Strain
ϵ_0		Strain amplitude in dynamic modulus
ϵ_{d}		Strain in damper
ϵ_{e}		Strain in elastic arm in Zener model
ϵ_{kk}		Strain in the direction of kk
ϵ_{m}		Strain in Maxwell arm in Zener model
ϵ_{s}		Strain in spring
ϵ_{s_1}		Strain in spring 1 in Zener model
ϵ_{s_2}		Strain in spring 2 in Zener model
η	[Pa·s]	Viscosity
η_{B}	[Pa·s]	Bulk viscosity
f	[Hz]	Frequency
f_0	[Hz]	Sonication frequency
f_{AM}	[Hz]	Amplitude modulation frequency
F_{N}	[N]	Normal force
F_{T}	[N]	Tangential force
F_V	[N/m^3]	Force per unit volume
F_{Vi}	[N/m^3]	Force per unit volume in the direction of i
G	[Pa]	Shear modulus
H	[W/m^3]	Heating rate
h		Index of the harmonic component
I	[W/m^2]	Intensity
I_0	[W/m^2]	Initial intensity at $x = 0$
I_{R}	[W/m^2]	Received intensity
I_{SPTA}	[W/m^2]	Spatial peak temporal average intensity
I_{T}	[W/m^2]	Transmitted intensity
I_{TA}	[W/m^2]	Temporal average intensity
i		Index
K	[Pa]	Bulk modulus
k	[W/m/K]	Thermal conductivity
k_{k}	[W/m/K]	Thermal conductivity of kidney
k_{t}	[W/m/K]	Thermal conductivity of tissue
L	[m]	Thickness of the material
L	[J/m^3]	Lagrangian energy density
l	[m]	Transducer focal length
λ_{L}	[Pa]	Lamè constant
M^*	[Pa]	Dynamic modulus
M_0	[Pa]	Spring constant
M_∞	[Pa]	Storage modulus high-frequency limit
M_{L}	[Pa]	Loss modulus
M_{S}	[Pa]	Storage modulus
m	[kg]	Mass

n		Attenuation power law
ν		Poisson's ratio
ω	[rad/s]	Angular frequency
ω_{n}	[rad]	Normalised angular frequency
P	[Pa]	Pressure
P_h	[Pa]	Pressure of harmonic component h
P_{PN}	[MPa]	Peak negative pressure
Q	[J]	Thermal energy
R		Constant in thermal dose equation
r_1-r_3		Constants in heat equation solution
ρ	[kg/m^3]	Density
ρ_0	[kg/m^3]	Density in equilibrium
ρ_{k}	[kg/m^3]	Density of kidney
ρ_{t}	[kg/m^3]	Density of tissue
s		Laplace variable
σ	[Pa]	Stress
σ_0	[Pa]	Stress amplitude in dynamic modulus
σ_{ij}	[Pa]	Stress tensor
σ_{d}	[Pa]	Stress in damper
σ_{e}	[Pa]	Stress in elastic arm in Zener model
σ_{m}	[Pa]	Stress in Maxwell arm in Zener model
σ_{s}	[Pa]	Stress in spring
$\sigma_{\mathrm{s_1}}$	[Pa]	Stress in spring 1 in Zener model
$\sigma_{\mathrm{s_2}}$	[Pa]	Stress in spring 2 in Zener model
T	[°C] or [K]	Temperature
T_{b}	[°C] or [K]	Temperature of blood
T_{k}	[°C] or [K]	Temperature of kidney
T_{t}	[°C] or [K]	Temperature of tissue
T^{new}	[°C] or [K]	New temperature value
T^*	[°C] or [K]	Intermediate temperature value
T^{**}	[°C] or [K]	Intermediate temperature value
ΔT	[K]	Change in temperature
T_0	[°C]	Temperature value of minimum attenuation
T_{C}	[°C]	Temperature centre point of sigmoidal fit
T_{TP}	[°C]	Temperature value of maximum sound speed
T_{W}	[°C]	Width of the central area of sigmoidal fit
t	[s]	Time
Δt	[s]	Change in time
t_i	[s]	Discrete time value at step i
t_{pc}	[s]	Duration of a pressure cycle
t_{end}	[s]	Integration time window
t_{s}	[s]	Time of flight in sample
t_{w}	[s]	Time of flight in water
τ	[s]	Relaxation time
τ_{c}	[s]	Retardation time

τ_{r}	[s]	Retarded time
u	[m]	Displacement
u_i	[m]	Displacement in the direction of i
V_{sine}	[V]	Sinusoidal voltage
V_{square}	[V]	Square voltage
$\mathbf{v}$	[m/s]	Particle velocity
w	[kg/m^3/s]	Perfusion rate
w_{k}	[kg/m^3/s]	Perfusion rate of kidney
w_{t}	[kg/m^3/s]	Perfusion rate of tissue
x	[m]	Spatial coordinate
Δx	[m]	Spatial resolution
x_j	[m]	One-dimensional coordinate
ΔX	[m]	Deformation in the shear direction
Y	[m]	Original length in the tensile direction
y	[m]	Spatial coordinate
Δy	[m]	Spatial resolution
ΔY	[m]	Deformation in the tensile direction
z	[m]	Spatial coordinate
Δz	[m]	Spatial resolution

List of Abbreviations

ADI	Alternating Direction Implicit
AM	Amplitude Modulation
ARF	Acoustic Radiation Force
ARFI	Acoustic Radiation Force Impulse
BD	Beam Diameter
BHT	Bioheat Transfer
BPH	Benign Prostate Hyperplasia
CEM	Cumulative Equivalent Minute
CN	Crank-Nicolson
CT	Computed Tomography
DFT	Discrete Fourier Transform
DMA	Dynamic Mechanical Analysis
EMA	Electromagnetic Acoustic
FDA	Food and Drug Administration
FEM	Finite Element Method
FFT	Fast Fourier Transform
FOV	Field-of-View
FWHM	Full Width at Half Maximum
HIFU	High-Intensity Focused Ultrasound
HMI	Harmonic Motion Imaging
KZK	Khokhlov-Zabolotskaya-Kuznetsov
MI	Mechanical Index
MPI	Message Passing Interface
MR-ARFI	Magnetic Resonance Acoustic Radiation Force Imaging
MR-HIFU	Magnetic Resonance guided High-Intensity Focused Ultrasound
MRI	Magnetic Resonance Imaging
PDE	Partial Differential Equation
PML	Perfectly Matched Layer
PP	Peak-to-Peak
RCC	Renal Cell Carcinoma
ROI	Region-of-Interest
SD	Standard Deviation
SSE	Sum of Squared Errors
SSI	Supersonic Shear Imaging
SWEI	Shear Wave Elasticity Imaging
USAE	Ultrasound Stimulated Acoustic Emission

List of Publications

Suomi, V., Edwards, D., and Cleveland, R. Optical quantification of harmonic acoustic radiation force excitation in a tissue-mimicking phantom. *Ultrasound in medicine & biology*, 41(12):3216–3232, 2015

Suomi, V., Han, Y., Konofagou, E., and Cleveland, R. O. The effect of temperature dependent tissue parameters on acoustic radiation force induced displacements. *Physics in Medicine and Biology*, 61(20):7427–7447, 2016a

Suomi, V., Jaros, J., Treeby, B., and Cleveland, R. Nonlinear 3-d simulation of high-intensity focused ultrasound therapy in the kidney. In *Engineering in Medicine and Biology Society (EMBC), 2016 IEEE 38th Annual International Conference of the*, pages 5648–5651. IEEE, 2016b

Suomi, V., Jaros, J., Treeby, B., and Cleveland, R. Full modelling of high-intensity focused ultrasound and thermal heating in the kidney of realistic patient models. 2017. (submitted)

Suomi, V. and Cleveland, R. Acoustic, thermal and mechanical properties of tissue. In Khokhlova, V., Crum, L., Aubry, J.-F., and ter Haar, G., editors, *Introduction to high-intensity focused ultrasound therapy*. Springer, 2017. (in press)

Chapter 1

Introduction

1.1 High-intensity focused ultrasound therapy

The clinical application of ultrasound has traditionally been diagnostic imaging whereby ultrasound beams are used to construct an image of the object using the reflections from tissue interfaces. However, ultrasound can also be used therapeutically by tightly focusing these beams into a single or multiple focal points using high power levels. High-intensity focused ultrasound (HIFU) therapy is a non-invasive thermal ablation method, which can be used for treating solid primary tumours located deep within the body (Kennedy, 2005; Dubinsky et al., 2008). By its definition, HIFU therapy uses high-energy focused ultrasound beams in order to produce a rapid local temperature rise in the focal point(s). Given that the heating duration is long enough, this results in irreversible tissue damage due to coagulative thermal necrosis (Wall et al., 1999; Wright and Humphrey, 2002), i.e. a well-defined lesion to the focal spot, while leaving the surrounding healthy tissue intact. The size of this lesion is relative to the size of the ultrasound focal point, which is typically on the order of 1-3 mm in the transverse and 8-15 mm in the axial direction. Therefore, to ablate large tumour volumes, multiple lesions have to be created systematically side-by-side in order to destroy the target volumes reliably.

There are several advantages in HIFU treatment when compared to other cancer therapy methods such as open surgery, chemotherapy and radiotherapy: (i) non-invasive therapies do not have infection risk, which improves the outcome of such procedures with fewer complications; (ii) the recovery from the therapy takes less time leading to shorter hospital stays, and in most cases, the patient can leave straight after the treatment; (iii) there are no known side effects apart from slight heating of the skin in the ultrasound pathway; (iv) the treatment can be repeated as many times as needed because there is no cumulative dose limit for ultrasound. Furthermore,

unlike chemotherapy, HIFU can be used to treat any tumour cell types that are susceptible to high temperatures, which makes it an effective therapy method for multiple cancer types. Although HIFU has several advantages over the alternative cancer therapy modalities, it has also its limitations. The main disadvantage of HIFU is that it cannot effectively penetrate through air gaps or bone, which makes it more difficult to treat tumours located in lungs, bowel, brain or other organs behind the rib cage. Another disadvantage is the duration of the treatment due to the ablation of large volumes and skin cooling periods. A typical HIFU therapy treatment time of few hours is comparable to surgical operations, but is generally longer than a radio- or chemotherapy session. Furthermore, HIFU is efficient in treating solid primary tumours, but treating a large number of metastases becomes rather inefficient.

1.1.1 A brief history of focused ultrasound

The physical effects of high-intensity ultrasound on biological tissue were first studied in the 1920s by Wood and Loomis (1927), but at the time HIFU was not used as a tissue thermal ablation therapy method. The concept of using HIFU therapy for tissue ablation was first introduced in the early 1940s by Lynn et al. (1942) who demonstrated its use in creating lesions in tissue. They used *ex vivo* animal liver and ablated lesions of different sizes by varying the acoustic parameters of HIFU. Lynn and Putnam (1944) were the first to conduct a pioneering study to treat the animal brain, but these experiments were not successful: the ultrasound beams were not able to penetrate through the intact skull bone into the brain to create lesions, while severe injuries to the skin and soft tissue overlying the skull were observed. In the following decade Fry et al. (1954, 1955) were the first to successfully use HIFU to treat the animal brain through an opening in the skull bone. They demonstrated this technique by ablating several lesions in the grey and white matter of the brain without affecting the intervening tissue.

In the end of 1950s HIFU was introduced to the field of oncology by Burov and Andreevskaya (1956). Later, in the 1970s, Lele (1975) and Marmor et al. (1978, 1979) combined hyperthermia with radiotherapy for cancer treatment and Fry and Johnson (1978) treated solid tumours using thermal ablation. Marmor et al. (1979) treated a number of patients with recurrent or metastatic tumours and found the heating to be successful in the superficial tumour locations. Fry and Johnson (1978) reported the use of HIFU in ablating implanted tumours in the hamster flank, which resulted in direct tumour tissue destruction. In the late 1980s and early 1990s, HIFU was directly applied to treat solid tumours in liver by thermal ablation (Ter Haar

et al., 1989, 1991b). Ter Haar et al. (1991b) successfully demonstrated the use of HIFU therapy to treat discrete tumours in rat livers: the treatment either delayed the tumour growth, or in some cases, the tumour completely vanished. With the development of real-time imaging modalities and modern transducer designs HIFU has since become a widely studied therapeutic modality, which has a large and growing number of clinical applications especially in the field of oncology. Furthermore, several companies in the industry have brought their HIFU systems to the market, which have been accepted to treat certain types of cancer by the regulatory bodies in different countries.

1.1.2 Clinical applications and current state of technology

HIFU therapy is a rapidly growing medical field which has an increasing number of research and treatment sites worldwide. In 2015, there were 274 research sites and 471 commercial treatment sites in the world with the majority being in Europe, Asia and North America (Foley, 2016). Furthermore, the number of companies in the field of focused ultrasound has grown steadily and is now standing at 32 (Foley, 2016). These numbers indicate that HIFU is undergoing transformation from an early-stage therapeutic technology towards an established medical field, which has several clinical applications. This evolution has been further accelerated by the Food and Drug Administration (FDA) approval of HIFU treatment for bone metastases, prostate cancer, uterine fibroids, benign prostate hyperplasia (BPH) and essential tremor. In addition to the FDA, the European regulatory approval of medical devices (CE marking) has been granted to several manufactures to treat solid tumours with HIFU therapy. The current state of research and regulatory approval of focused ultrasound applications is presented in Figure 1.1(a). It can be seen that the applications which are at the most advanced stage are for the treatment of either benign or malignant tumours, but also other conditions such as the essential tremor has recently shown promising results (Elias et al., 2016).

To date, over 116,000 patients have been treated with focused ultrasound for different conditions (Foley, 2016). The majority of the treatments have been conducted for prostate cancer (47%), uterine fibroids (31%) and liver cancer (14%), while the remaining 8% were for glaucoma, bone metastases, breast cancer, BPH and other conditions such as kidney cancer and brain tumours. Apart from uterine fibroids, glaucoma and BPH, oncology applications currently dominate as the main field for HIFU therapy. The feasibility to treat certain type of cancer with HIFU is dependent on two factors: first of all, is it technically possible to treat the condition, and

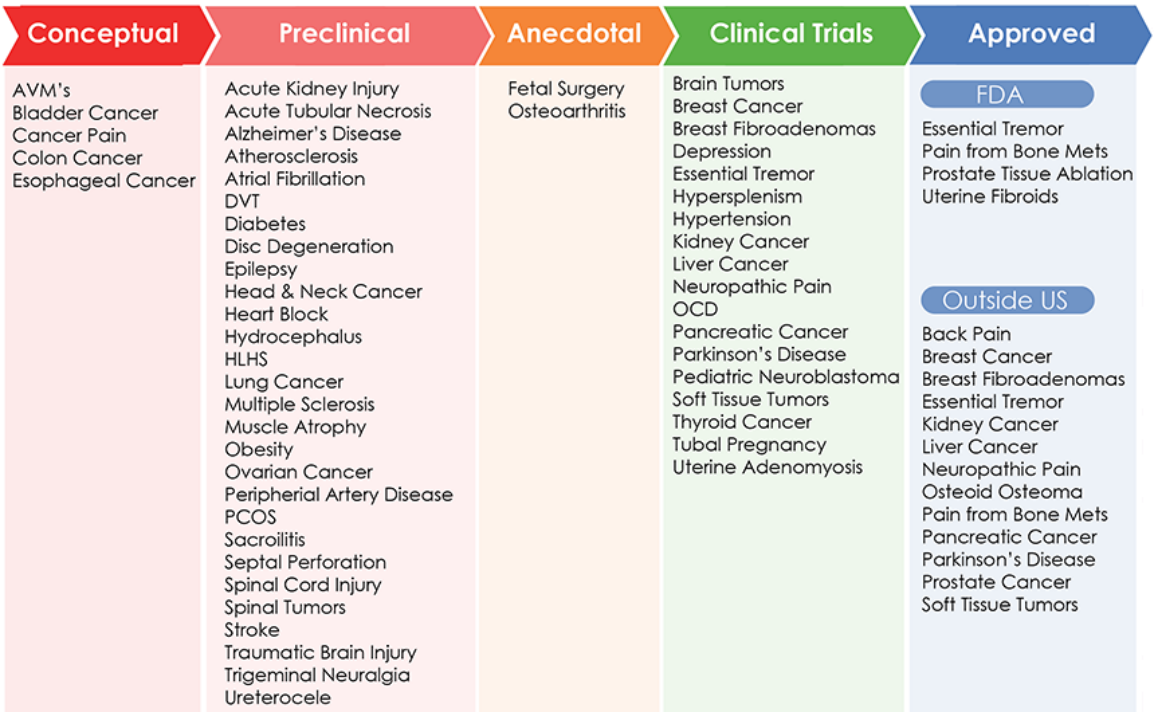

(a)

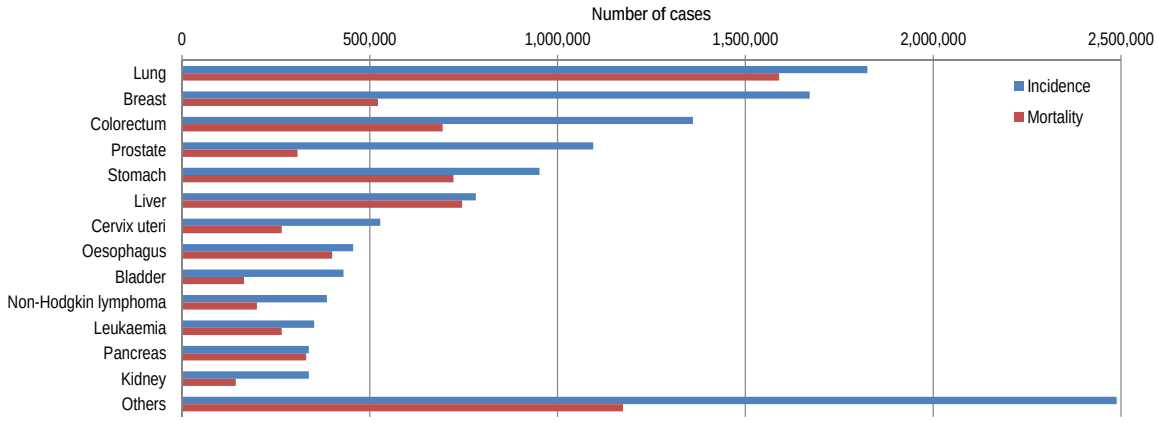

(b)

Figure 1.1: (a) State of research and regulatory approval of focused ultrasound applications by development stage in 2016 (Foley, 2016). (b) Global incidence and mortality rates of most common types of cancers for both sexes in 2012 (Ferlay et al., 2012b).

secondly, does it have enough commercial potential to be profitable. When looking at the global incidence rates of different cancer types in Figure 1.1(b), it can be seen that there is indeed big commercial potential for HIFU therapy in this field with over 14 million registered incidents in 2012. However, due to the limitations in ultrasound propagation and the lack of suitable monitoring methods, only some of these conditions are currently treatable with HIFU.

Lung cancer had the highest incidence rate with over 1.82 million cases in 2012, but the location of lungs behind rib cage and the air filled structure of the organ limit the efficiency of HIFU therapy (Dunn and Fry, 1961). One potential solution to this problem is to substitute the air in the lungs with a liquid (Sekins et al., 2004), but this technique is still at an early stage, and thus, lung cancer remains a challenging application for HIFU. Breast cancer is the second most common type cancer with an estimated 1.67 million cases globally in 2012 and is a target which provides excellent acoustic access. Despite of large commercial potential and technical feasibility, breast cancer has relatively small portion of clinically conducted HIFU treatments with less than 1% share. The HIFU treatment of breast cancer has been shown to be effective in small scale randomised clinical trials (Wu et al., 2003a), but tumours with undefined margins and those with close proximity to the nipple should be excluded as potential targets. These limitations together with the high effectiveness of other therapy methods, such as surgery and irradiation (Fisher et al., 2002), downplay the potential of HIFU therapy. Colorectal cancer had the third highest incidence rate with approximately 1.36 million cases in 2012. However, the structure of the organ with rectal-wall being situated next to the gas filled cavity can lead to an injury and complications due to undesired heating at the wall boundary (Kennedy, 2005). The same problem applies to stomach cancer, which had the fifth highest incidence rate. It is possible that these problems will be solved in the future, but for now gas-filled organs are rarely treated with HIFU.

The first both technically and commercially feasible organ for HIFU is prostate which had the fourth highest incidence rate of cancer with 1.09 million cases in 2012. Therefore, it is not a surprise that prostate cancer is also the most treated condition with HIFU accounting for almost half of all the treatments in patients to date. The prostate is typically difficult to operate surgically due to its location, which makes its transrectal treatment with HIFU an alternatively therapy (Blana et al., 2008; Crouzet et al., 2014). There are currently multiple commercial HIFU systems approved by the FDA to treat prostate cancer, and therefore, its use is expected to grow even further in the future. Another commonly treated cancer type with HIFU is liver cancer which

had 0.78 million incidents in 2012. Over the past two decades, incidence rates particularly in younger age groups have increased in the US, Japan and parts of Europe (Boyle and Levin, 2008). At the moment, there are no FDA approved commercial systems available to treat liver tumours with HIFU in the US, but in China and the UK HIFU therapy has already been used in clinical setting (Wu et al., 2004; Illing et al., 2005). Similarly, the treatment of kidney has also been approved outside the US and is currently in use in several countries (Wu et al., 2003b; Illing et al., 2005), but reliable ablation of the target locations has been shown to be challenging (Ritchie et al., 2010, 2013).

Brain tumours are seen as one possible target for HIFU in the future, but the presence of skull bone in the ultrasound pathway prevents non-invasive transmittance of acoustic power to the tumour in order to create sufficient heating. However, recently some progress has been made in the transcranial therapy by using phase-correction methods (Larrat et al., 2010), which might allow the treatment of brain tumours in the near future.

1.1.3 Therapy monitoring

One of the main barriers to the wide spread use of HIFU has been the lack of robust, reliable and cost-efficient imaging methods. Monitoring HIFU therapy requires real-time imaging modalities which can provide indicators for the therapy status either in the form of temperature data or by determining changes in the physical properties of tissue. In current practice, this is achieved by using one of the two techniques: magnetic resonance imaging (MRI) or ultrasound. To date, the gold-standard for monitoring HIFU therapy has been MRI, which offers real-time monitoring with temperature data. With MRI guidance, the lesion volume is calculated based on the thermal dose obtained from volumetric thermometry as an indicator of induced tissue damage and necrosis (Köhler et al., 2009). MRI has high sensitivity, which provides good separation of different anatomic areas, and thus, allows accurate therapy planning of the target region. The disadvantages of MRI imaging are that the temperature data is spatially averaged over the voxel volume leading to underestimation of temperature in some cases (Khokhlova et al., 2009); and that it has relatively poor temporal resolution at around one second as heating can occur more quickly (Ter Haar et al., 1991a). MRI has also higher cost and bigger size of the equipment compared to ultrasound imaging modalities, and cannot be used with some patients, such as those with metallic implants, pacemakers or other life-supporting devices.

Ultrasound-based techniques are fast, low-cost, portable and safe to use with all patient groups, which makes them promising alternatives for HIFU monitoring. The spatial and temporal resolutions of ultrasound imaging are higher than those of MRI, but the spatial definition of different anatomic regions is usually worse. Another disadvantage of ultrasound imaging is that it cannot provide reliable temperature information at high therapeutic temperatures (Lewis et al., 2015). However, the feedback from the therapy can also be obtained from the lesion formation. Standard B-mode ultrasound imaging would provide fast real-time monitoring of lesion formation, but without cavitation the echogenity of ablated lesion does not change enough in order to be detected (Bush et al., 1993; Rabkin et al., 2005). This makes conventional ultrasound imaging unreliable in determining lesions since hyperechoic regions are not always present after HIFU exposure and they dissolve away quickly (Vaezy et al., 2001).

One tissue property that has been shown to change significantly and irreversibly in thermal ablation is tissue stiffness (Wu et al., 2001; Sapin-de Brosses et al., 2010), which can be used as an indicator of complete thermal necrosis of cancerous tissue (Varghese et al., 2002, 2003). The increase in stiffness has been shown to be reversible at temperatures below 60 °C (Wu et al., 2001), and the irreversible increase occurs at temperatures above 60 °C due to collagen denaturation (Wu et al., 2001; Lepetit et al., 2000). These fundamental changes in tissue structure result in good contrast differences between necrotic and healthy tissue, which can be detected using different ultrasound elastography techniques. Therefore, accurate quantification of tissue stiffness before, during and after thermal ablation would provide a reliable indicator for lesion formation.

1.2 Ultrasound elastography imaging

Ultrasound elastography imaging is a non-invasive method for measuring the mechanical properties of tissue (Palmeri and Nightingale, 2011; Gennisson et al., 2013). It is a widely used medical imaging technique, which has several clinical applications (Cosgrove et al., 2013). Some ultrasound elastography techniques including acoustic radiation force impulse (ARFI) imaging (Lizzi et al., 2003), shear wave elasticity imaging (SWEI) (Bercoff et al., 2004a) and harmonic motion imaging (HMI) (Konofagou and Hynynen, 2003) have also been used in monitoring HIFU therapy. The use of ultrasound elastography to monitor HIFU therapy is based on the changes in tissue

stiffness during thermal ablation as discussed in the previous section. Typically ultrasound elastography techniques measure the stiffness of tissue either by measuring the strain in the tissue under stress, or by imaging shear waves which can be generated in different ways. There are also quasi-static ultrasound elastography methods available (Ophir et al., 1991), but they are beyond the scope of this chapter, which focuses only on ultrasound elastography methods employing acoustic radiation force (ARF).

1.2.1 Acoustic radiation force

Several ultrasound elastography methods rely on ARF by monitoring the dynamic response of tissue to the ultrasound excitation pulse. ARF is a phenomenon where propagating ultrasound waves transfer their momentum to the surrounding medium by the processes of absorption and scattering (Torr, 1984). In a viscous fluid (i.e., no scattering) the absorption of ultrasound waves creates a force in the direction of wave propagation, which results in a displacement of the medium in the same direction.

ARF for a plane-travelling wave can be derived by using the series expansions of the pressure, density and particle velocity as used by Nyborg (1965). In these approximations, the time-average change in the momentum in a unit volume is non-zero (Sarvazyan et al., 2010), which creates a force in the wave propagation direction. The magnitude of this force is proportional to the local intensity of the wave, which can be expressed per unit volume F_V [N/m^3] by the equation (Nyborg, 1965; Torr, 1984; Starritt et al., 1991):

$$F_V = \frac{2\alpha_{\text{abs}} I_{\text{TA}}}{c} \tag{1.1}$$

where α_{abs} [Np/m] is the absorption of the medium, I_{TA} [W/m^2] is the temporal average intensity of the ultrasound field at a given location and c [m/s] is the sound speed in the medium. According to the equation (1.1), the magnitude of ARF is directly dependent on absorption of tissue. However, absorption is the main factor contributing to attenuation in soft tissue (Lyons and Parker, 1988), and hence, it can be considered as attenuation in this case.

By assuming the medium to be (i) linear (i.e., the strain and stress follow a linear relationship); (ii) elastic (i.e., the medium returns back to its original state after an applied stress is removed); and (iii) isotropic (i.e., the mechanical properties of the medium are not orientation dependent); the resulting dynamic deformation caused by ARF is described by (Callé et al., 2005):

$$\rho \frac{\partial^2 u_i}{\partial t^2} = \frac{\partial \sigma_{ij}}{\partial x_j} + F_{Vi} \tag{1.2}$$

where u_i [m] is the displacement in the direction of i, t [s] is time, ρ [kg/m^3] is the density, σ_{ij} [Pa] is the stress tensor, x_j [m] is the spatial coordinate in the direction of j and F_{Vi} [N/m^3] is the radiation force in the direction of i. The magnitude of the deformation is therefore dependent on both the force and the elastic properties of tissue. In ARF-based ultrasound elastography applications, focused ultrasound fields are typically used to create local tissue displacements, in which case the greatest force is in the region of the transducer focal point. Furthermore, the attenuation properties of tissue together with the selection of the centre frequency also affect the spatial distribution and magnitude of the ARF field (Palmeri and Nightingale, 2011).

1.2.2 Acoustic radiation force impulse imaging

ARFI imaging is a diagnostic ultrasound method which provides information about the mechanical properties of tissue by measuring the strain (i.e., the displacement) induced by ARF in the axial direction. In ARFI imaging, short-duration (≤ 0.5 ms), high-intensity focused pulses are used to cause localised tissue displacements in the focal area of the ultrasound field. This dynamic deformation is then quantified both spatially and temporally using speckle-tracking (Dickinson and Hill, 1982), which results in axial displacement curves in time in the focal area. In order to create larger, two-dimensional image the focal point has to be moved either manually or electronically in the area of interest to form a relative strain map. In addition to ultrasound imaging, MRI can also be used to measure ARF induced displacements using a technique called MR-ARFI (McDannold and Maier, 2008).

Sugimoto et al. (1990) first introduced the concept of quantifying the tissue mechanical properties by its response to ARFI, while Lizzi et al. (2003) were the first to apply ARFI imaging to monitor HIFU lesion creation. They demonstrated the feasibility of ARFI imaging to detect HIFU ablated lesions with computational simulations and *in vitro* experimental studies in bovine liver. Since then, several papers have studied its feasibility to visualise lesions due to HIFU thermal ablation (Nightingale et al., 2004, 2007; Bing et al., 2009, 2011). Nightingale et al. (2004, 2007) compared B-mode, ARFI and pathology images of an *ex vivo* bovine liver sample after exposure to HIFU ablation, and found good correlation of the lesion structure between the images. Bing et al. (2009, 2011) demonstrated the feasibility of using simultaneous ARFI imaging to monitor HIFU therapy with *ex vivo* liver samples, and found good contrast difference between the areas of ablated and healthy tissue.

By assuming the material to be isotropic, homogeneous and linear elastic, the measured strain can be related to the applied stress by the first order approximation

(Doherty et al., 2013):

$$\sigma_{ij} = \lambda_{\mathrm{L}} \epsilon_{kk} \delta_{ij} + 2G\epsilon_{ij} \tag{1.3}$$

where ϵ_{kk} is the strain in the direction of kk, δ_{ij} is the Kronecker delta, and λ_{L} [Pa] and G [Pa] are known as the Lamè constants (or the latter also as the shear modulus). For a homogeneous, isotropic and linear elastic material, the Young's modulus E [Pa] can then be defined as:

$$E = \frac{G(3\lambda_{\mathrm{L}} + 2G)}{\lambda_{\mathrm{L}} + G} \tag{1.4}$$

However, in practice the applied stress is usually unknown due to its dependency on the geometry of the ultrasound field and the acoustic properties of tissue, which makes the quantitative assessment of elastic modulus challenging. Furthermore, soft tissues tend to be viscoelastic, inhomogeneous and anisotropic (Fung, 1993). In this case a relative map of displacements in the area of interest is generally shown.

1.2.3 Shear wave elasticity imaging

In SWEI, propagating shear waves are used to derive the elastic modulus of the material. Shear waves are secondary elastic waves which are generated in the direction perpendicular to the propagating ultrasound wave. The propagating shear waves in tissue can be generated in multiple ways. In the method implemented by Sandrin et al. (2002), a mechanical vibrator is attached on top of the transducer to generate low frequency (around 50 Hz) shear waves travelling in the axial direction. After a number of shear waves have been generated, the transducer switches into a fast imaging mode which allows to follow the shear wave as it propagates trough the tissue. Imaging of shear wave propagation is possible because their speed is lower than that of compression waves. Shear waves can also be generated in the radial direction using a series of ARF pulses (Nightingale et al., 2003; Bercoff et al., 2004b). In the Supersonic Shear Imaging (SSI) method developed by Bercoff et al. (2004b), the imaging transducer is first used to create a series of ARF induced displacements at different depths in the axial direction. These displacements then constructively create a propagating shear wave in the radial direction of the transducer. After the creation of the shear wave, the transducer switches into imaging mode to follow the shear wave propagation through the tissue. In addition to ultrasound-based imaging methods, MRI can also be used to monitor shear wave propagation (Muthupillai et al., 1995; Wu et al., 2001).

SWEI was first developed by Sarvazyan (1995); Sarvazyan et al. (1998) who demonstrated the use of ARF to generate shear waves in the medium. They used an optical laser-based system and MRI to validate the theoretical model of SWEI. Bercoff et al. (2004a) were the first to use SWEI to quantify the elastic moduli of HIFU-induced lesions in *ex vivo* tissue. They successfully demonstrated the feasibility of SWEI in detecting thermally ablated lesions and quantifying their stiffness. More recently Arnal et al. (2011) used SWEI to determine the shear modulus-temperature relation in *ex vivo* tissue. They showed that in muscle the shear modulus decreases with temperature to approximately 65 °C after which the tissue ablation causes the modulus to increase rapidly. Similar study was conducted by Sapin-de Brosses et al. (2011) who quantified the relationship between shear modulus and temperature in anaesthetised rats *in vivo*. They found the shear modulus to rapidly increase eight-fold at around 202 cumulative equivalent minutes at 43 °C ($\mathrm{CEM}_{43^\circ\mathrm{C}}$), which is close to the limit of 240 $\mathrm{CEM}_{43^\circ\mathrm{C}}$ for thermal necrosis (Sapareto and Dewey, 1984). These findings indicate that changes in tissue stiffness could possibly be used as an indicator of coagulative thermal necrosis.

SWEI is usually implemented using one of two different methods. In the first approach, shear wave speed is directly measured and converted into shear modulus of tissue using the relation (Cobbold, 2006):

$$G = \rho c_{\mathrm{T}}^2 \tag{1.5}$$

where c_{T} [m/s] is the shear wave speed. This method requires *a priori* knowledge about the shear wave propagation direction in order to calculate the wave arrival times and propagation speed based on the ultrasound images. In the second approach, an inverse problem of Helmholtz-equation is solved in order to recover the shear wave speed according to (Palmeri and Nightingale, 2011; Catheline et al., 2004):

$$G\nabla^2 u - \rho\frac{\partial^2 u}{\partial t^2} = 0 \tag{1.6}$$

This method does not need any *a priori* information, but requires a good signal-to-noise ratio in the image data in order to yield reliable results.

1.2.4 Harmonic motion imaging

HMI is an ultrasound-based elasticity imaging technique, which uses focused, amplitude-modulated waveforms to create an oscillatory ARF (Suomi et al., 2015). The oscillatory ARF makes the tissue vibrate at the modulation frequency (usually at

50 Hz), which can be recorded using a speckle-tracking technique similarly to ARFI imaging. Due to its similarities with ARFI imaging, HMI also has the same limitations in estimating the tissue elastic modulus quantitatively due to the unknown stress induced by the ARF. One possibility is to use the equation (1.2) to do least-squares fitting with the oscillatory displacement data to give an estimate of the dynamic modulus. The advantage of HMI for HIFU monitoring is that the ultrasound used to ablate tissue can be amplitude modulated to create the ARF. Simultaneous speckle-tracking is possible by using bandpass filtering and a separate imaging transducer whose centre frequency is different to that of the spherical therapeutic transducer creating the oscillations (Maleke and Konofagou, 2008). The ability to track displacements continuously during HIFU treatment makes HMI a good candidate for real-time therapy monitoring.

Fatemi and Greenleaf (1998) were the first to introduce US-stimulated acoustic emission (USAE) imaging to determine human artery calcifications. This method induces vibrations in tissue internally by using two separate focused transducers with slightly different frequencies and detects the amplitude and phase of these vibrations using raster-scanning. Later, Konofagou and Hynynen (2003) applied the same excitation method together with a diagnostic transducer, i.e., HMI, to estimate localised displacements in tissue using cross-correlation. They simulated vibrations using finite-element method (FEM) and conducted feasibility measurements in phantoms and *in vitro* porcine muscle (Konofagou and Hynynen, 2003; Konofagou et al., 2003, 2004). They found good agreement between the simulations and experimental data. Zaitsev et al. (2004) examined and confirmed the feasibility of the HMI method using phased-array transducer in gel phantoms and *ex vivo* liver. Maleke et al. (2005, 2006) further developed HMI to use a single-element transducer with amplitude modulated ultrasound pulses instead of two separate transducers to induce harmonic vibrations in tissue. They demonstrated the feasibility of this method to monitor HIFU ablation real time in *ex vivo* porcine liver and later performed more extensive demonstrations with different sonication durations and temperatures using *in vitro* bovine liver (Maleke and Konofagou, 2008).

Curiel et al. (2009) validated HMI with *in vivo* experiments in rabbit muscle and used MRI to confirm the coagulation. They found the displacement amplitudes to be 17 to 81% lower after the lesion formation using modulation frequencies from 50 to 300 Hz in 14 different locations. Curiel and Hynynen (2011) also determined the spatial resolution of HMI using phantoms with inclusions together with *in vivo* tumours implanted in rabbits. They were able to separate inclusions as small as 4 mm

diameter and tumours 10 mm in length and 4 mm in width. Maleke and Konofagou (2010) conducted a similar study where they monitored ablation of transgenic breast cancer in mice *in vivo*. They found the peak-to-peak displacement amplitudes to be approximately 17.3 ± 1.3 μm before and 11.0 ± 1.8 μm after ablation, which confirms that the decrease in amplitude can be used as an indicator of lesion formation. Recently, Hou et al. (2013, 2014) and Shahmirzadi et al. (2014) investigated how different parameters such as displacement amplitude, relative phase shift, lesion size, compressive strain, lesion contrast and dynamic modulus change after different ablation durations and power levels in *ex vivo* canine liver. They showed that changes are observed in these parameters after thermal ablation, which suggests that multi-parametric models could be considered in the future.

1.3 Objective of the thesis

Although academic research in the field of ultrasound elastography for monitoring HIFU therapy has been conducted for over a decade, there are no commercial HIFU systems utilising this technology. Even in academia only a couple of different ultrasound elastography methods for the purpose of HIFU therapy monitoring have been actively researched in recent years - those being mainly HMI and SSI. The slow (arguably non-existent) commercial adoption of ultrasound elastography for thermal ablation therapy monitoring suggests that there are still problems to overcome before ultrasound elastography can be considered robust and reliable enough for clinical use.

Monitoring thermal ablation therapy with ultrasound elastography fundamentally relies on measuring the irreversible changes in tissue elastic modulus due to coagulative thermal necrosis (Wall et al., 1999; Wright and Humphrey, 2002). However, according to the equation (1.1), ARF is also dependent on tissue attenuation and sound speed, both of which are known to change with temperature. Furthermore, the viscoelastic properties of tissue are also temperature dependent, which affects the displacements induced by periodic ARF excitation. All these tissue parameters affect the magnitude of the ARF induced tissue deformations, and therefore, also the therapy monitoring capabilities of ultrasound elastography techniques.

Another problem faced by any ultrasound-based diagnostic or therapeutic modality is the attenuation, reflection and refraction of acoustic waves as they propagate through different layers of tissue in the human body. This is especially important in the case of focused ultrasound fields which need to create a tight and well-defined ultrasound focal point in the target region. In terms of ultrasound elastography,

changes in the focal point (both spatial distribution and intensity) affect the magnitude and direction of ARF, which consequently affect the tissue deformation induced by ARF. This might lead to unreliable quantitative estimates of tissue elastic modulus, if the changes in acoustic fields are not taken into account. Furthermore, in the case of HIFU treatment the spatial changes in the focal volume shape and reduction in ultrasound intensity might significantly degrade the therapeutic heating effect.

Given the problems introduced above, the scope of this thesis is to address three major issues:

(i) *to quantify the temperature dependent tissue parameters affecting the ARF*

(ii) *to evaluate their effect on ARF induced displacements*

(iii) *to characterise therapeutic HIFU fields in the human body*

Addressing these problems would benefit the development of ARFI, SWEI, HMI and other ultrasound elastography modalities which rely on ARF.

In the second chapter of the thesis, the temperature dependent changes in tissue properties are quantified by conducting an extensive literature review of available data. In the third chapter, the covering equations for the used acoustic, thermal and viscoelastic models are defined. In the fourth chapter, harmonic ARF induced displacements are quantified both experimentally and with simulations in a tissue-mimicking phantom. In the fifth chapter, the temperature dependent viscoelastic properties of *ex vivo* liver are measured, and the effect of temperature on ARF induced displacements is quantified by using HMI for HIFU therapy monitoring and conducting numerical simulations. In the sixth chapter, computationally intensive numerical simulations are conducted to determine the changes in nonlinear acoustic and thermal fields during HIFU therapy in the kidney. In the seventh and final chapter, conclusions based on the results are drawn and future research directions are suggested.

Chapter 2

Temperature dependence of tissue properties

Therapeutic ultrasound for thermal ablation involves the propagation of nonlinear acoustic beams into tissue which results in heating of the target area. The change in temperature is high enough to result in changes to the underlying medium properties which in turn will affect the ultrasound propagation. In this chapter[1], a review of the literature looking at temperature dependent changes in the acoustic, thermal and mechanical properties of tissue is conducted. The changes in mechanical properties are also considered as they are relevant to ultrasound elastography in monitoring the thermal ablation process. It was found that there was a range in the values of these properties due to a number of reasons, including natural biological variation, measurements being done in a variety of species, and the methods of measurement. Therefore, empirical models are provided for changes in the acoustic properties with temperature and bounds on the variation that might be expected.

The acoustic properties of tissue change as ultrasound propagates through it predominantly due to two main mechanisms: thermal and mechanical. Thermal changes result from the conversion of acoustic energy into heat energy which increases the temperature of the tissue. As the temperature of the tissue rises, it induces changes in the properties of the tissue some of which are reversible and some irreversible. The exact mechanisms are not fully understood but as the tissue heats its chemical structure changes with effects varying from collagen denaturation to cell death (Wall et al., 1999; Sapareto and Dewey, 1984; Wright and Humphrey, 2002; Anema and McKenna, 1996). These changes can affect all of the underlying properties of the tissue.

[1]The contents of this chapter will be published in Suomi and Cleveland (2017).

Mechanical disruption is normally associated with the presence of cavitation. The mechanical action of the cavitation bubbles also results in a range of tissue responses from subtle opening of cell membranes to complete mechanical destruction of the tissue. From the point of view of tissue properties the main contribution of the presence of cavitation bubbles is a large increase in acoustic attenuation and backscatter, however, other acoustic properties such as sound speed and coefficient of nonlinearity can also be affected.

2.1 Acoustic properties

The medium parameters that affect the propagation of ultrasound in the body are: density, sound speed, attenuation and coefficient of nonlinearity. In addition, changes in backscatter coefficient may be used to monitor the ablation process. This section looks at the changes in acoustic properties due to both temperature and thermal ablation.

2.1.1 Sound speed

Sound speed in tissue is typically measured in a water bath by axially aligning two unfocused transducers and comparing the time of flight of an ultrasound pulse through the same distance with and without the sample in between. The sound speed in the sample can then be calculated with the equation:

$$c_{\mathrm{s}} = \frac{c_{\mathrm{w}} t_{\mathrm{w}}}{t_{\mathrm{s}}} \tag{2.1}$$

where c_{w} and c_{s} [m/s] are the sound speeds of water and sample; t_{w} and t_{s} [s] are the times of flight in water and sample, respectively. It should be noted that using this method requires the transducers to be touching the sample (i.e., no propagation in the water when the sample is in between), although a water path can be corrected for. Temperature dependence of the tissue can be measured using this setup by controlling the temperature of the water bath during the measurements. This technique is called water immersion heating and it has been widely used in the literature to study temperature dependent properties of tissue. It requires information about the sound speed temperature dependence in water which can be found from the reference (Marczak, 1997).

In Figure 2.1 are shown measurements of the sound speed in (a) liver, (b) kidney, (c) brain, (d) muscle and (e) fat as a function of temperature (Bamber and Hill, 1979; Bronez et al., 1985; Bush et al., 1993; Choi et al., 2011; Ghoshal et al., 2011;

Jackson et al., 2014; Nasoni et al., 1979; Rajagopalan et al., 1979; Sehgal et al., 1986; Techavipoo et al., 2002, 2004; Kremkau et al., 1981; Robinson and Lele, 1972; Wladimiroff et al., 1975; Cetas and Connor, 1978; Lu et al., 1996). It can be seen that as the temperature increases from below 20 °C the sound speed increases in all tissue types apart from fat in which it decreases. This behaviour is common to most fluids and soft tissues due to the temperature dependent properties of pure water (Marczak, 1997). However, in tissue it can be seen that there is a turning point in this trend somewhere from 55 to 70 °C depending on the tissue type after which sound speed decreases due to the properties of water.

The data in Figure 2.1 show variation in absolute values which could be due to differences in biological properties or experimental methods. Therefore, in Figure 2.2 the sound speed of each tissue-type has been normalised by the sound speed at 37 °C. The normalised data aligns in much more consistent way in different tissue types. Parabolic curves were fitted to the normalised data (grey lines) according to equation:

$$c_{\mathrm{pol}} = c_2 T^2 + c_1 T + c_0 \tag{2.2}$$

where c_{pol} is the polynomial sound speed, T [°C] is the temperature and c_0-c_2 are the fitting parameters. In Table 2.1 are shown the second order fitting parameters together with the turning points T_{TP} [°C] of parabolic fits. It can be seen that from the non-extrapolated turning points the lowest is for liver at 57.5 °C and the highest for kidney at 68.5 °C. In pure water the turning point is approximately 75 °C (Marczak, 1997), which suggests that the biological content of the tissue shifts the turning point towards lower temperature values.

The effect of thermal ablation on sound speed is shown in Figure 2.3. In this case the sample was measured at baseline temperature after thermal ablation by water immersion heating or HIFU ablation (Jackson et al., 2014; Choi et al., 2011; Bush et al., 1993; Techavipoo et al., 2004; Keshavarzi et al., 2001). It can be seen that in liver the sound speed went down slightly in two of the data sets, and went up slightly in three of the data. On average there was +0.35% increase in sound speed which however was not statistically significant. This suggests that thermal ablation does not result in irreversible changes in sound speed, and hence, the turning point of sound speed is dependent on the properties of water rather than changes in the protein structure.

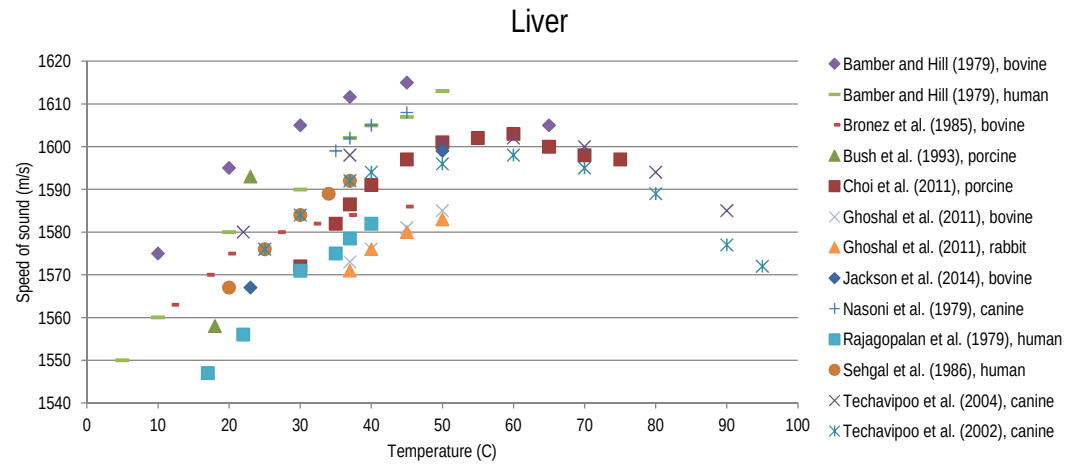

(a)

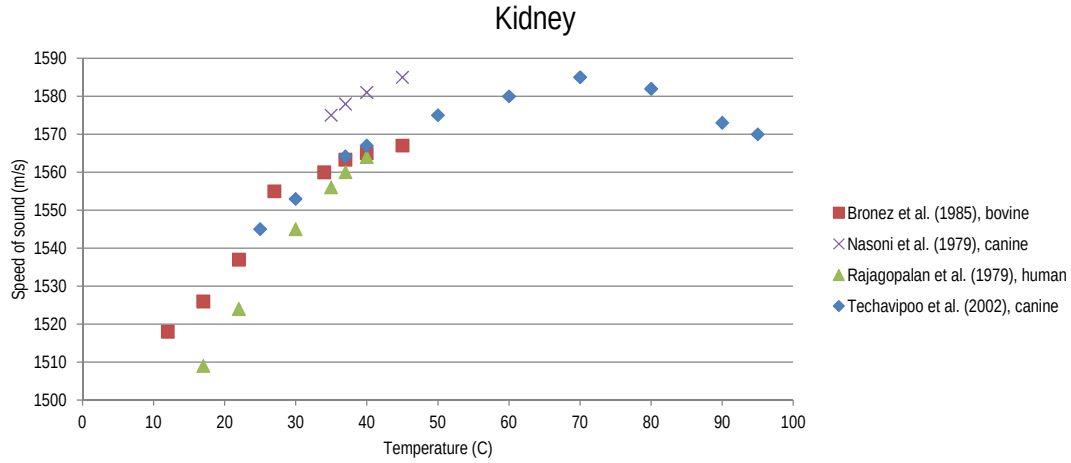

(b)

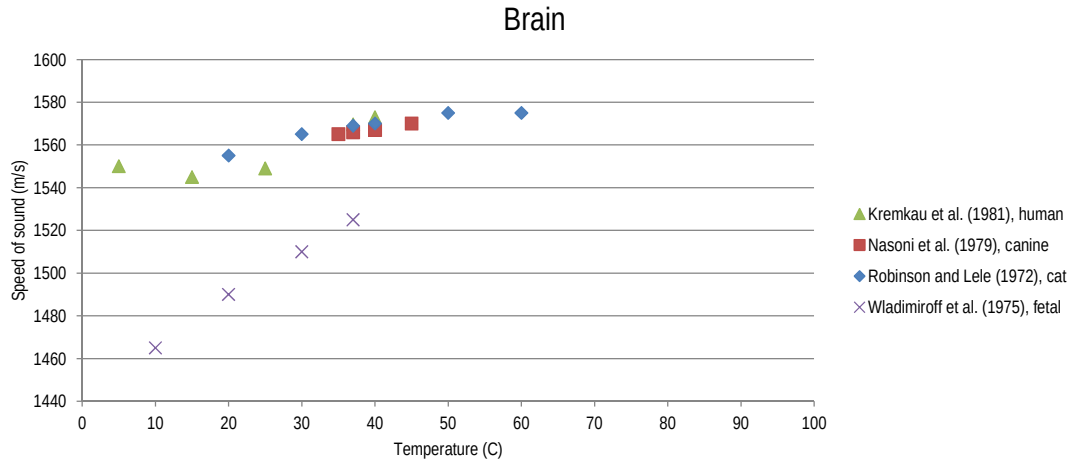

(c)

Figure 2.1: Temperature dependence of sound speed in (a) liver, (b) kidney and (c) brain.

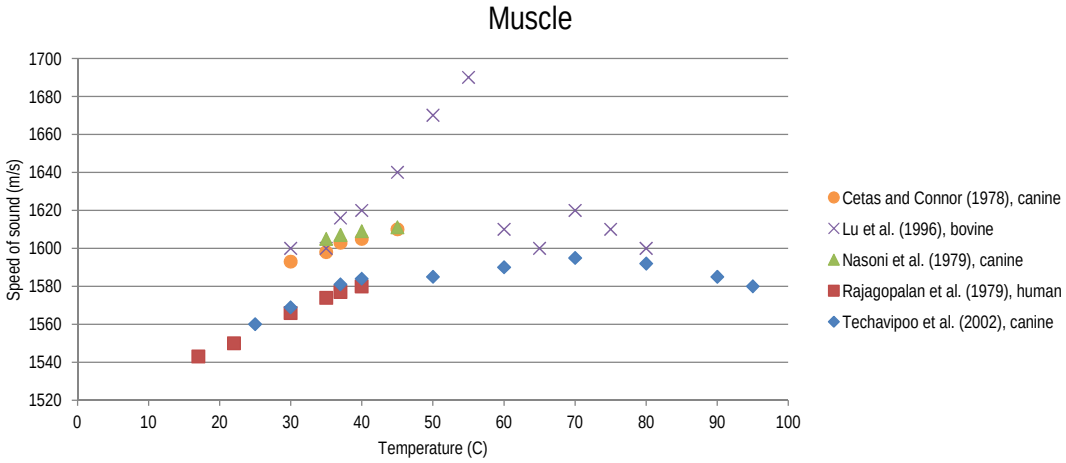

(d)

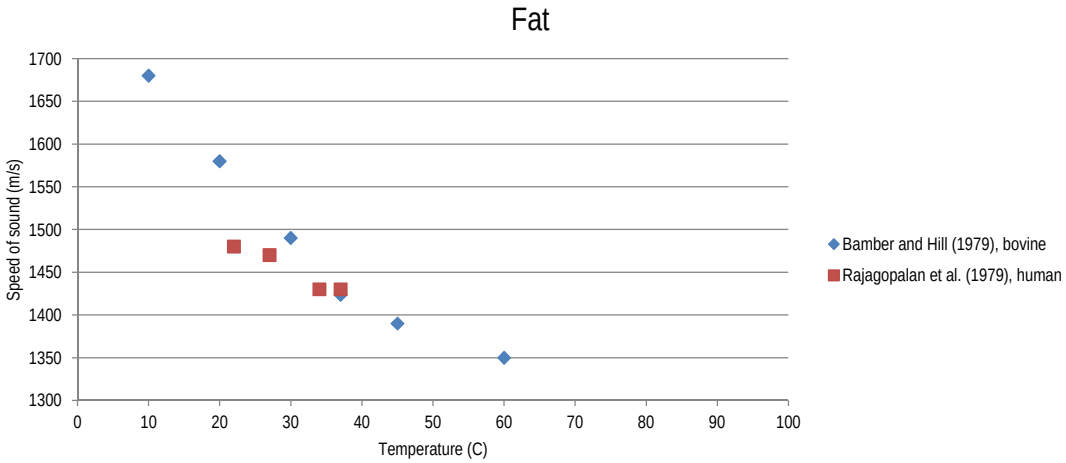

(e)

Figure 2.1: (continued) Temperature dependence of sound speed in (d) muscle and (e) fat.

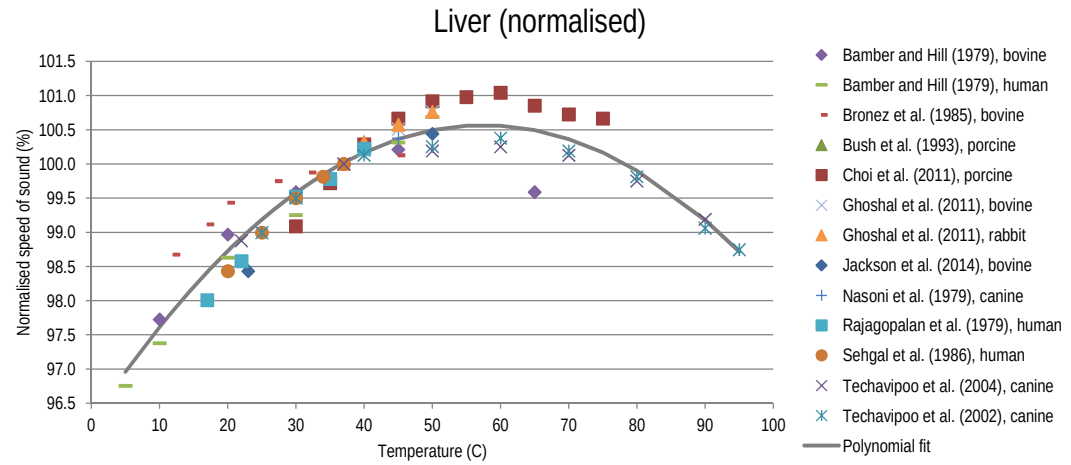

(a)

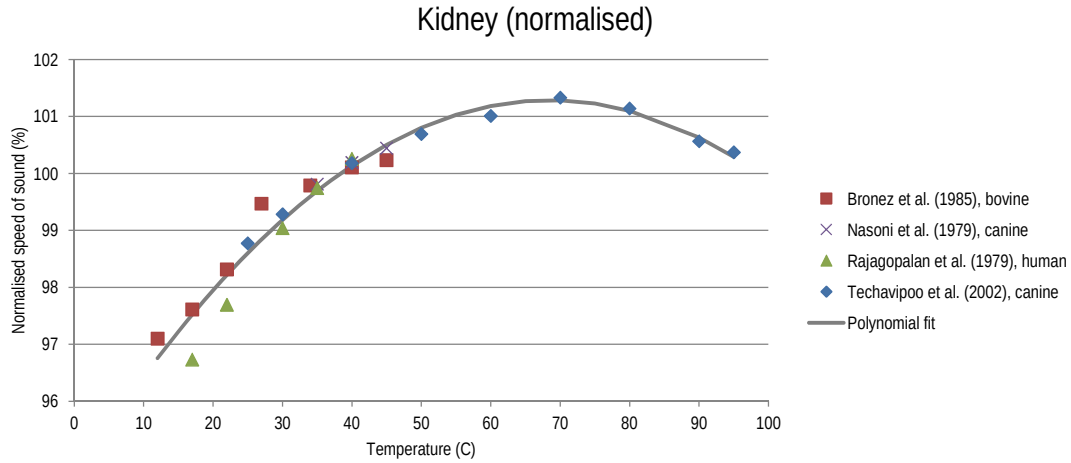

(b)

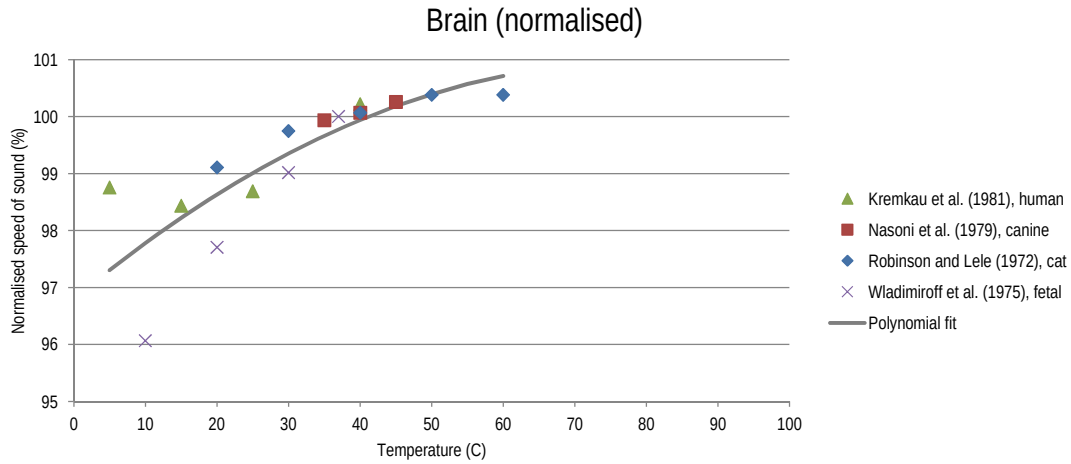

(c)

Figure 2.2: Temperature dependence of normalised sound speed in (a) liver, (b) kidney and (c) brain.

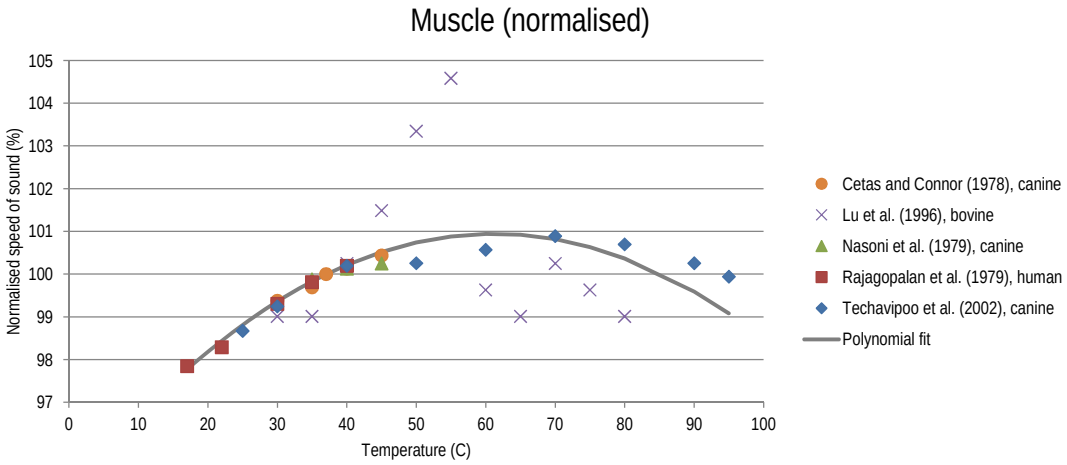

(d)

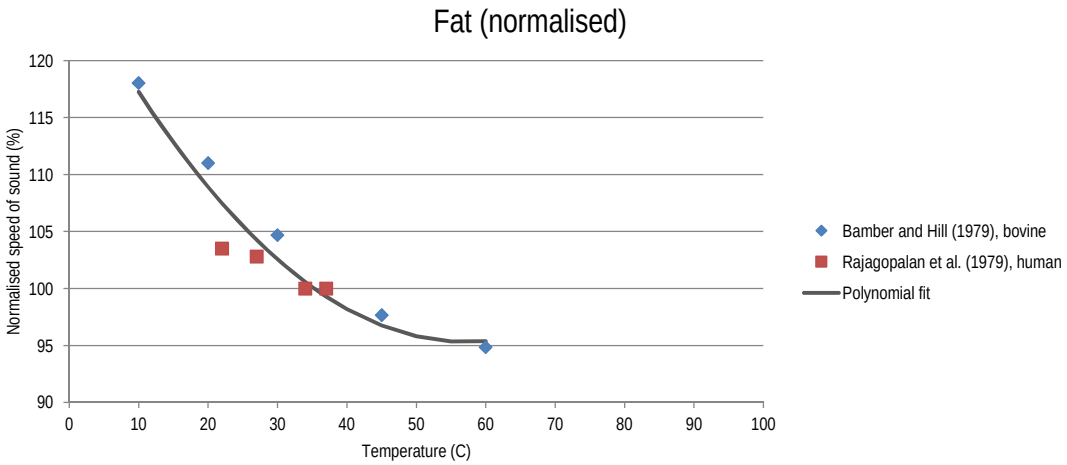

(e)

Figure 2.2: (continued) Temperature dependence of normalised sound speed in (d) muscle and (e) fat.

Table 2.1: Polynomial fitting parameters for normalised sound speed in different tissues. T_{TP} shows the temperature value where sound speed is at its maximum.

	c_2	c_1	c_0	T_{TP} [°C]
Liver	−1.31E−03	1.51E−01	9.62E+01	57.5
Kidney	−1.42E−03	1.94E−01	9.46E+01	68.5
Brain	−6.65E−04	1.05E−01	9.68E+01	79.2
Muscle	−1.63E−03	1.99E−01	9.48E+01	61.2
Fat	9.89E−03	−1.13E+00	1.28E+02	57.1

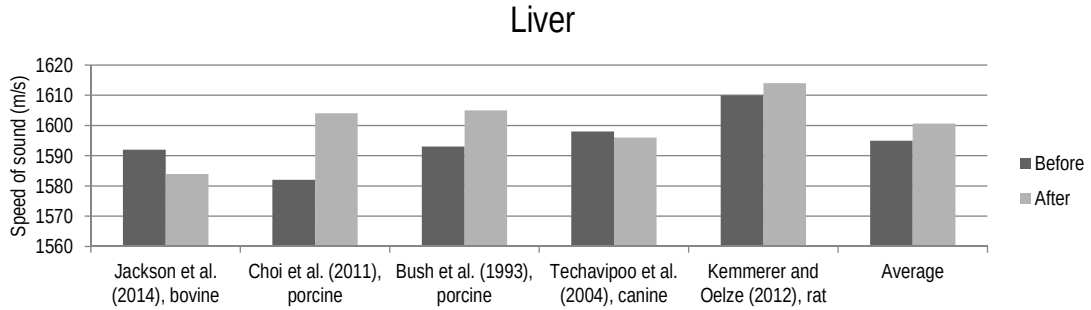

(a)

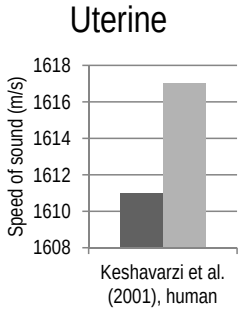

(b)

Figure 2.3: The change in (a) liver and (b) uterine sound speed before and after thermal ablation.

2.1.2 Attenuation

Attenuation measurements are typically made using the same approach as sound speed measurements, where two unfocused transducers are positioned opposite to each other and receiving the signal with and without the sample over the same distance. The attenuation of a material can then be calculated with the equation:

$$\alpha(f) = \frac{1}{d} 10 \log_{10} \left(\frac{I_{\mathrm{R}}(f)}{I_{\mathrm{T}}(f)} \right) \tag{2.3}$$

where $\alpha(f)$ [dB/m] is the frequency dependent attenuation, d [m] is the distance between the transducers and $I_{\mathrm{T}}(f)$ and $I_{\mathrm{R}}(f)$ [W/m^2] are the intensities of the transmitted and received signals, respectively. However, in order to get a more accurate

attenuation estimate the diffraction loss due to ultrasound beam variations can be taken into account (Beissner, 1981). This requires implementing a diffraction compensation technique in the measurements (Kim and Varghese, 2007; Huang, 2002). In addition, acoustic impedance mismatches between water and the sample should be taken into account in order to yield accurate values. Typically attenuation measurements are done using the centre frequency of the transducer, but because transducers have a finite frequency bandwidth, it is possible to fit attenuation power law curves to frequency domain data giving an estimate for the frequency dependence of the attenuation. In order to get broadband measurements, multiple transducers with different centre frequencies should be used. Some authors only report the attenuation at the centre frequency while others include also the estimate for the frequency dependence.

Figure 2.4 shows published measurements of the change in attenuation at 1 MHz as a function of temperature in (a) liver, (b) kidney, (c) prostate, (d) brain, (e) muscle and (f) fat (Bamber and Hill, 1979; Bush et al., 1993; Choi et al., 2011; Damianou et al., 1997; Gammell et al., 1979; Ghoshal et al., 2011; Jackson et al., 2014; Techavipoo et al., 2002, 2004; Gertner et al., 1997; Worthington and Sherar, 2001; Worthington et al., 2002; Kremkau et al., 1981; Robinson and Lele, 1972; Shore et al., 1986). In the cases where attenuation was not measured at 1 MHz it has been extrapolated to 1 MHz using the power law specified by the author or in the absence of a stated power law by assuming a linear power law. As with sound speed, there exist variations in absolute values across the various studies, and hence, in Figure 2.5 the data has been normalised to attenuation at 37 °C. It can be seen that the normalised data collapse to a common trend and that attenuation decreases as the temperature increases from 37 °C until the temperature reaches about 50 °C at which point the attenuation starts to increase until it approximately doubles.

There is not a clear functional dependence in the data, and therefore, fourth order polynomial and sigmoidal functions were fitted:

$$\alpha_{\mathrm{pol}} = a_4 T^4 + a_3 T^3 + a_2 T^2 + a_1 T + a_0 \tag{2.4}$$

$$\alpha_{\mathrm{sig}} = A_0 + \frac{A_1 - A_0}{1 + \exp\left(-\frac{T - T_{\mathrm{C}}}{T_{\mathrm{W}}}\right)} \tag{2.5}$$

where α_{pol} and α_{sig} are the polynomial and sigmoidal attenuation coefficients respectively, a_0-a_4 are the polynomial fitting parameters, A_0-A_1 [dB/cm] are two asymptotic values, T_{C} [°C] is the centre point of the sigmoidal fit and T_{W} [°C] is the width of the central area of the fit. This was done to estimate the temperature dependence of

attenuation. The fitting parameters are presented in Table 2.2 for polynomial and in Table 2.3 for sigmoidal functions.

For liver most of the data suggest a significant rise in the attenuation as temperature increases beyond 60 °C except for the data by (Techavipoo et al., 2002, 2004) where the increase is minimal. Therefore, fitting to experimental data beyond 60 °C was not done as the line of best fit would lie in between two very different data sets. It is noted that up to 60 °C the polynomial function captures the decrease in attenuation below approximately 50 °C, which is not possible with the sigmoidal function. The polynomial function was fit up to 70 °C for the three data sets which showed an increase, and it appears to extrapolate to about 75 °C based on the results by Choi et al. (2011).

For kidney, prostate and muscle the normalised data all look very similar; initially as the temperature increases, there is no change in the attenuation, however between 50 °C and 60 °C attenuation increases and by 70 °C it has plateaued at roughly double the baseline value. In these cases, the data are well fitted with a sigmoidal function. For the brain, the attenuation also increases above 200% at 70 °C for the one data set found and keeps increasing all the way to 500% at 95 °C.

Figure 2.6 shows the attenuation values at 1 MHz before and after thermal ablation in (a) liver, (b) prostate, (c) brain, (d) spleen, (e) uterine and (f) abdominal wall (Jackson et al., 2014; Choi et al., 2011; Zderic et al., 2004; Clarke et al., 2003; Pauly and Schwan, 1971; Kemmerer and Oelze, 2012; Bush et al., 1993; Diederich and Burdette, 1996; Robinson and Lele, 1972). In liver, the average increase in attenuation is +109% compared to the original value at the same temperature. For other tissue types, the increase in attenuation after ablation ranges from +51% for prostate up to +220% for uterine. Therefore, the data show that the attenuation coefficient roughly doubles after thermal ablation and that the change is irreversible.

Attenuation is also dependent on the frequency of the ultrasound wave with higher frequencies experiencing greater attenuation. In biological tissue the attenuation typically follows the relation (Cobbold, 2006):

$$\alpha = \alpha_0 f^n \tag{2.6}$$

where α_0 [dB/m/MHz] is the attenuation coefficient and n is the frequency dependence power law coefficient. It is most common to assume the exponent is unity although the literature reports values between 1.0 and 1.3 for the majority of soft tissue (Goss et al., 1979; Gammell et al., 1979). The attenuation power law is not often reported for tissue and even fewer data are available on the change in the power

law as a function of temperature (Jackson et al., 2014; Shore et al., 1986). Figure 2.7 shows the data for the power law exponent of (a) liver, (b) spleen and (c) abdominal wall before and after thermal ablation. There is negligible average change in the power law after ablation in liver (-0.26%). Large changes are reported for spleen and abdominal wall, but these results are from a single study, and given the variability in other studies, more data would be needed to confirm this. For linear simulations, the nature of the power law is likely not a critical parameter but for nonlinear simulations, where multiple harmonics are generated contributing to heating, an accurate power law is likely to be important and more measurements on the frequency dependence of the power law are needed.

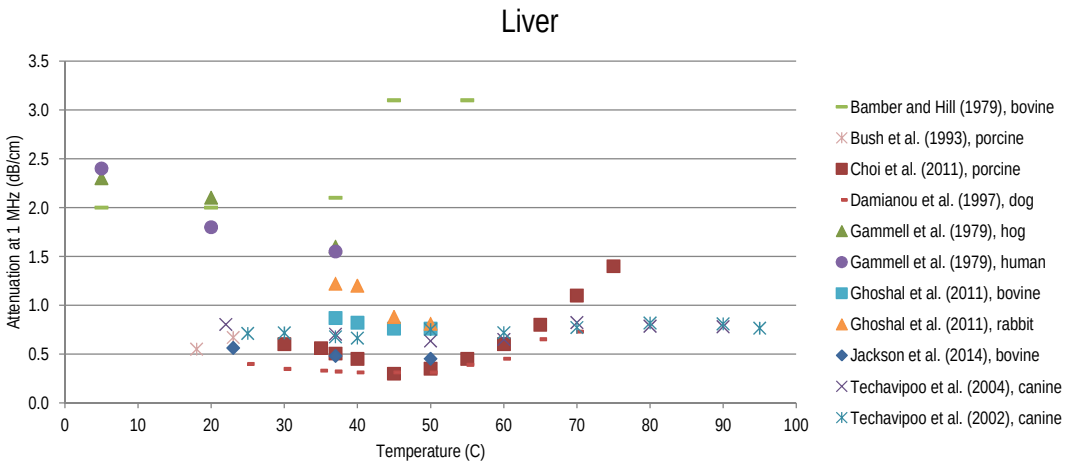

(a)

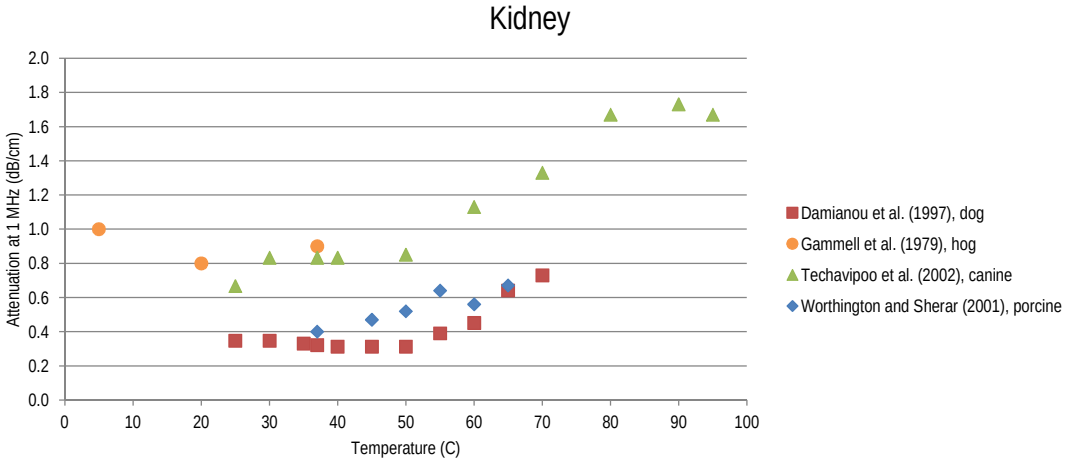

(b)

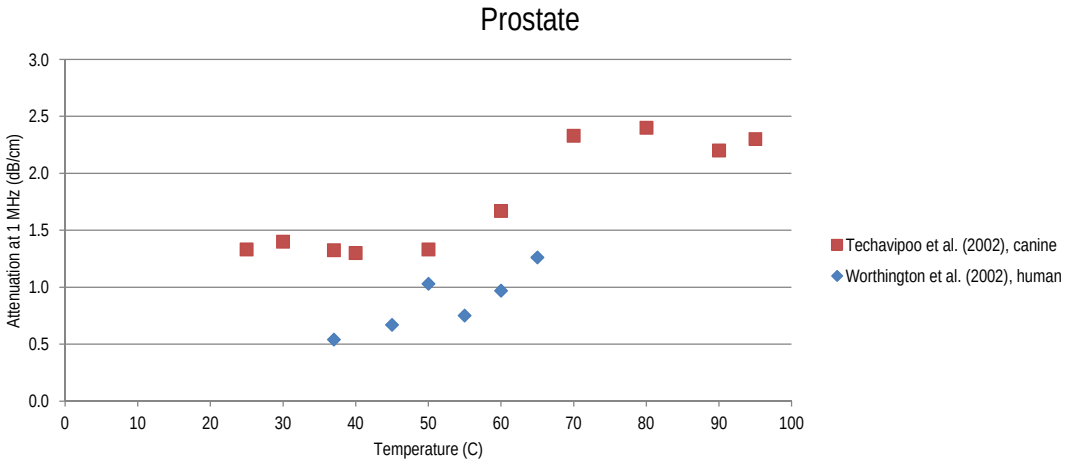

(c)

Figure 2.4: Temperature dependence of attenuation coefficient in (a) liver, (b) kidney and (c) prostate.

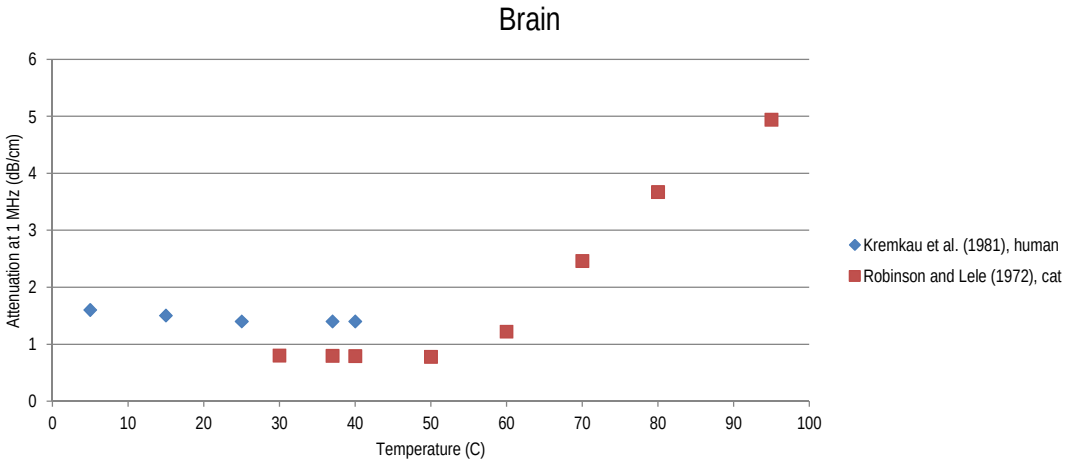

(d)

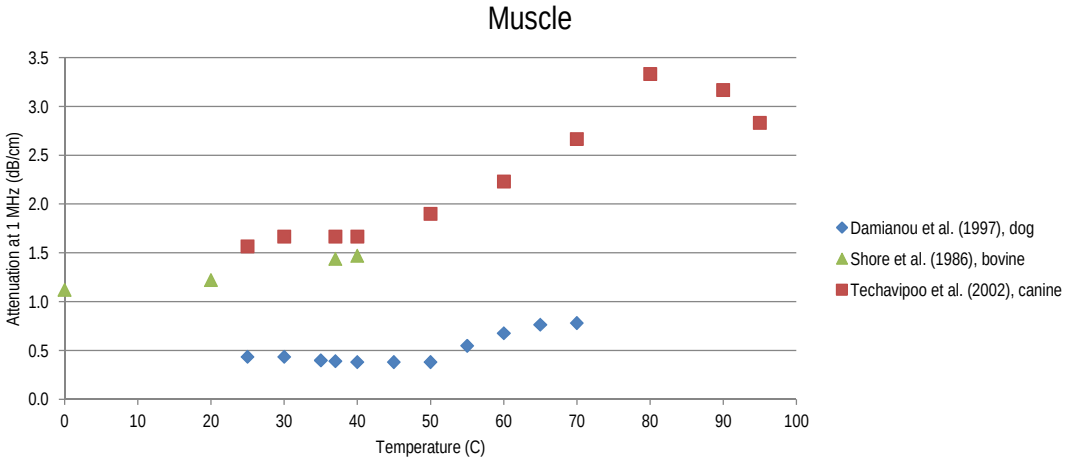

(e)

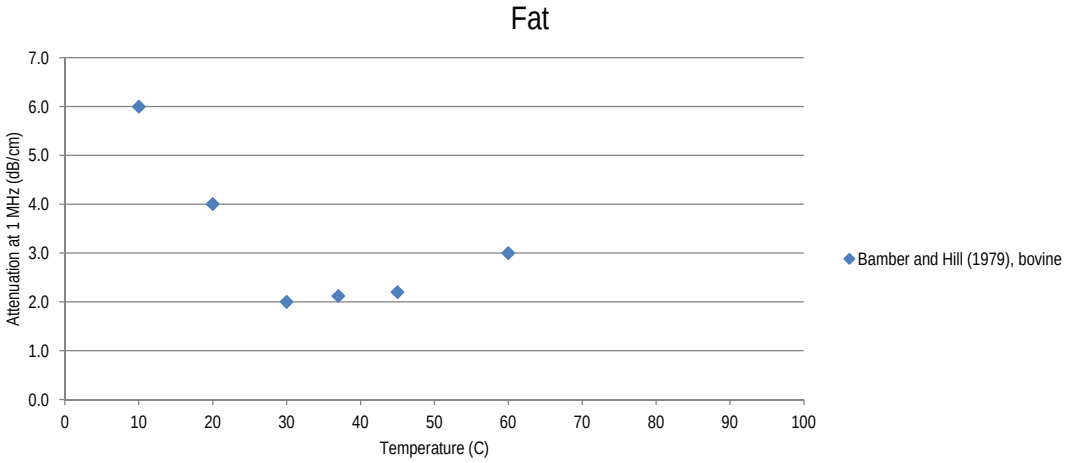

(f)

Figure 2.4: (continued) Temperature dependence of attenuation coefficient in (d) brain, (e) muscle and (f) fat.

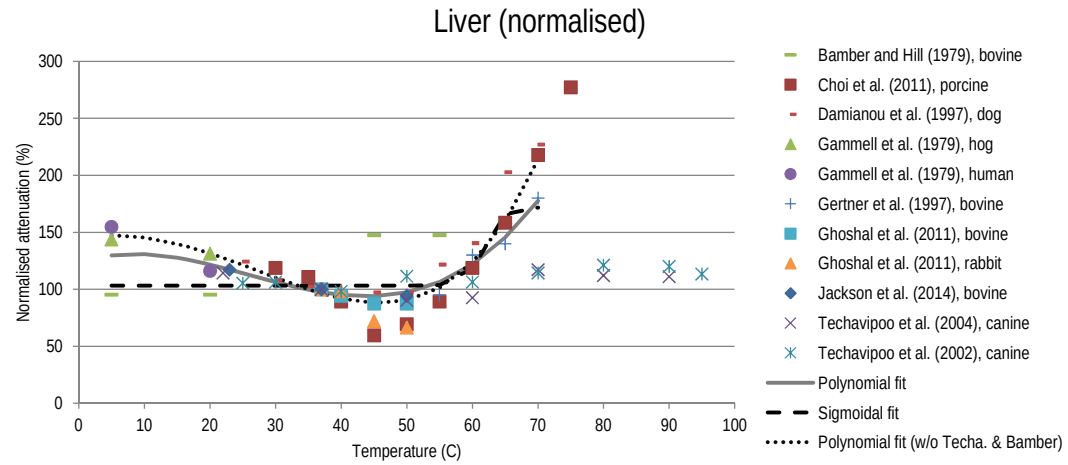

(a)

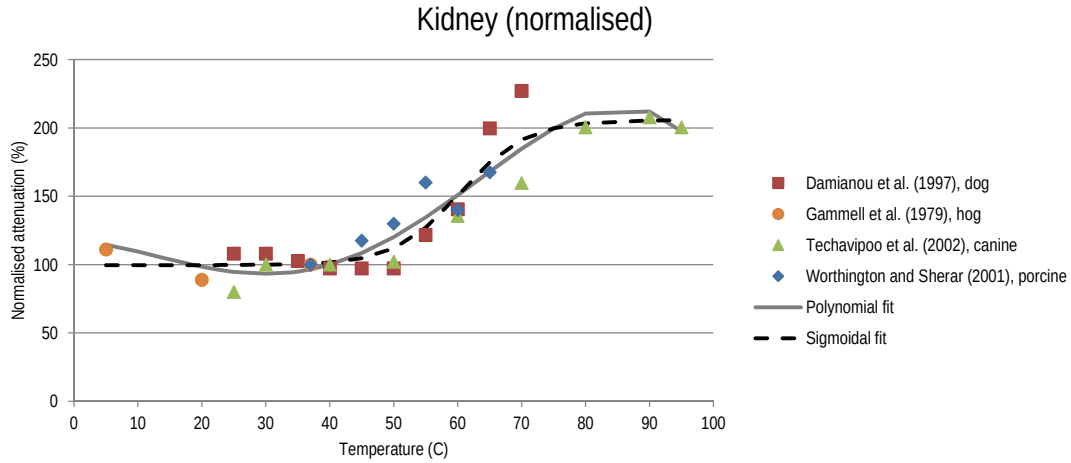

(b)

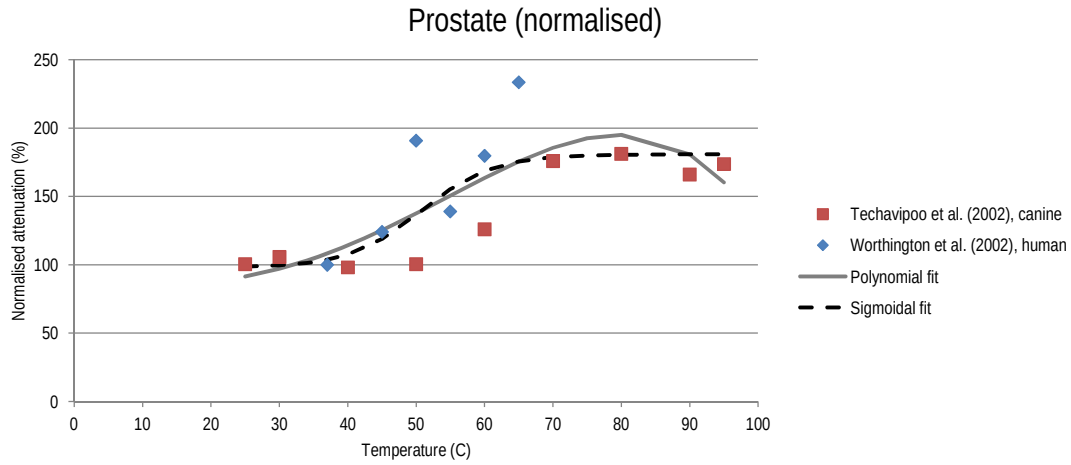

(c)

Figure 2.5: Temperature dependence of normalised attenuation coefficient in (a) liver, (b) kidney and (c) prostate.

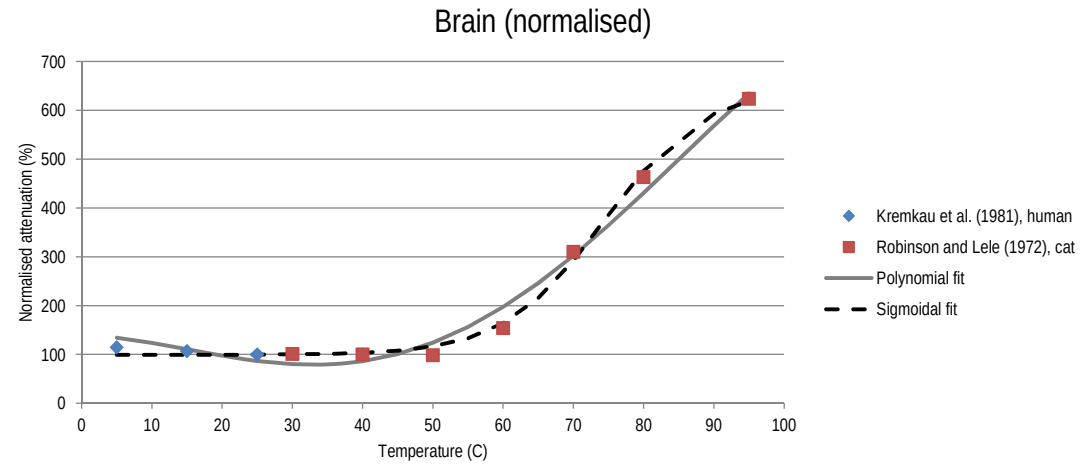

(d)

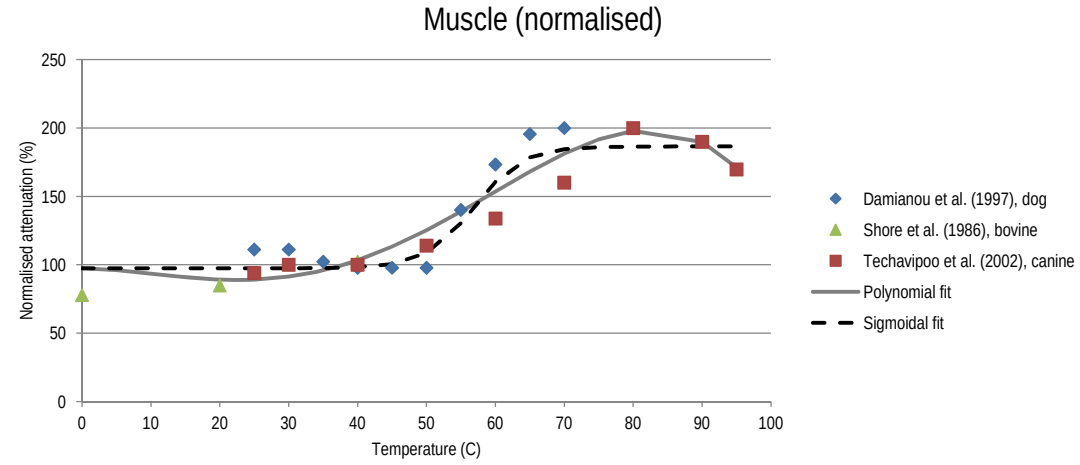

(e)

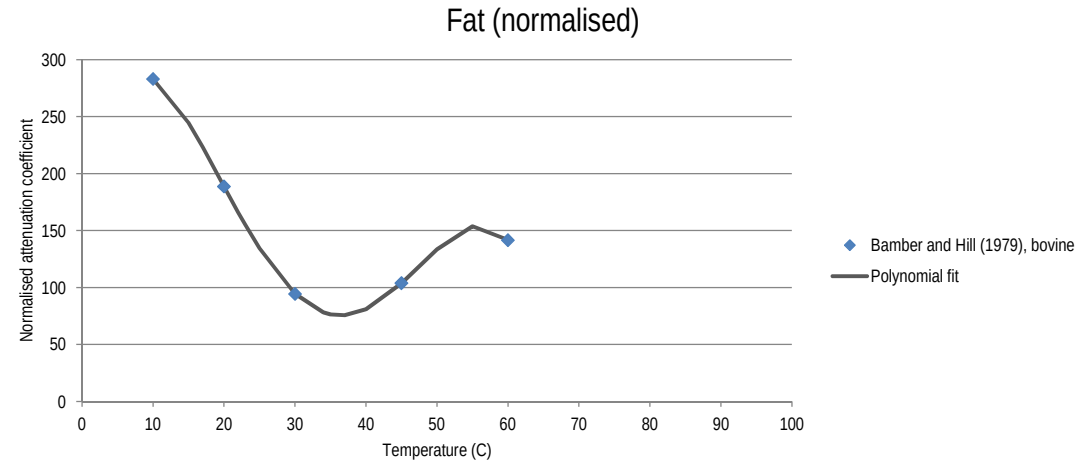

(f)

Figure 2.5: (continued) Temperature dependence of normalised attenuation coefficient in (d) brain, (e) muscle and (f) fat.

Table 2.2: Polynomial fitting parameters for normalised attenuation coefficient in different tissues. T_0 shows the temperature value where attenuation is at its minimum. (*) (Techavipoo et al., 2002, 2004) and (Bamber and Hill, 1979) excluded from the fit.

	a_4	a_3	a_2	a_1	a_0	T_0 [°C]
Liver	−2.55E−06	1.94E−03	−1.41E−01	1.99E+00	1.23E+02	44.1
Liver*	1.69E−05	−3.32E−05	−7.66E−02	6.82E−01	1.46E+02	46.0
Kidney	−1.82E−05	2.80E−03	−9.24E−02	−3.22E−02	1.17E+02	29.9
Prostate	−1.03E−05	1.21E−03	−1.34E−02	−3.20E−02	8.58E+01	9.3
Brain	−2.42E−05	4.84E−03	−1.86E−01	−6.70E−02	1.38E+02	33.0
Muscle	−1.44E−05	2.01E−03	−5.24E−02	−5.74E−02	9.75E+01	22.7
Fat	−3.99E−04	5.34E−02	−2.21E+00	2.54E+01	2.00E+02	36.6

Table 2.3: Sigmoidal fitting parameters for normalised attenuation coefficient in different tissues.

	A_0	A_1	T_W	T_C [°C]
Liver	103.08	171.94	1.38	61.7
Kidney	99.62	205.65	5.14	60.4
Prostate	97.94	180.78	5.27	50.7
Brain	98.93	647.66	7.14	74.4
Muscle	97.46	186.58	3.53	56.9

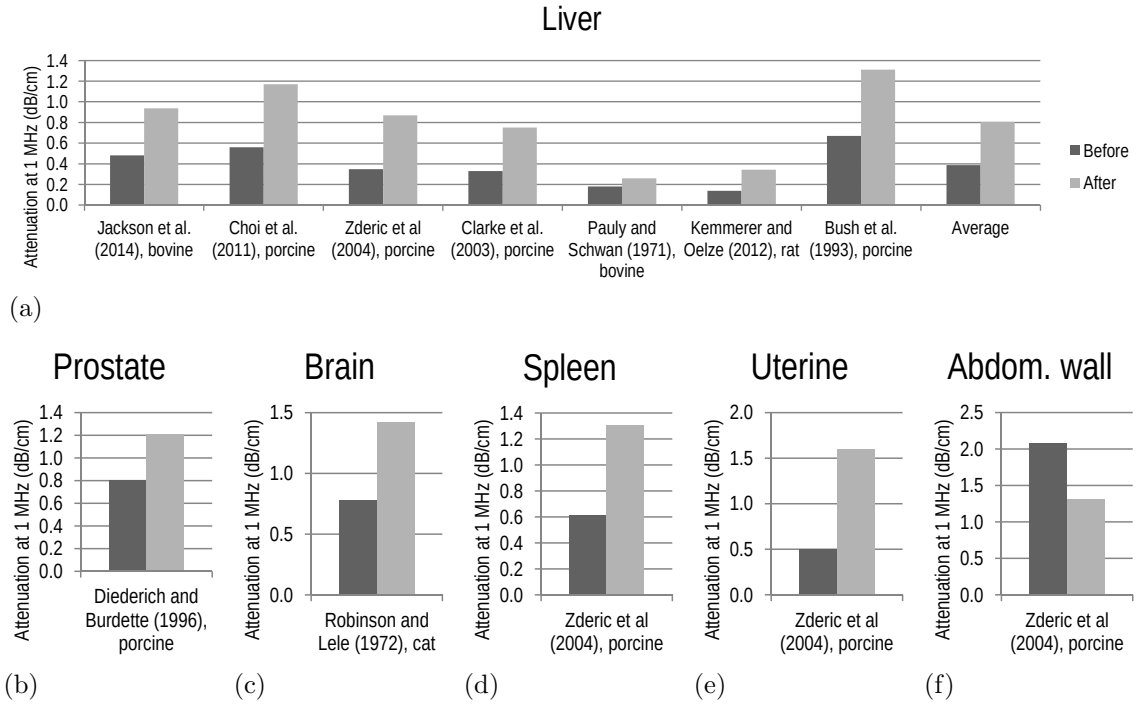

Figure 2.6: The change in (a) liver, (b) prostate, (c) brain, (d) spleen, (e) uterine and (f) abdominal wall attenuation coefficient before and after thermal ablation.

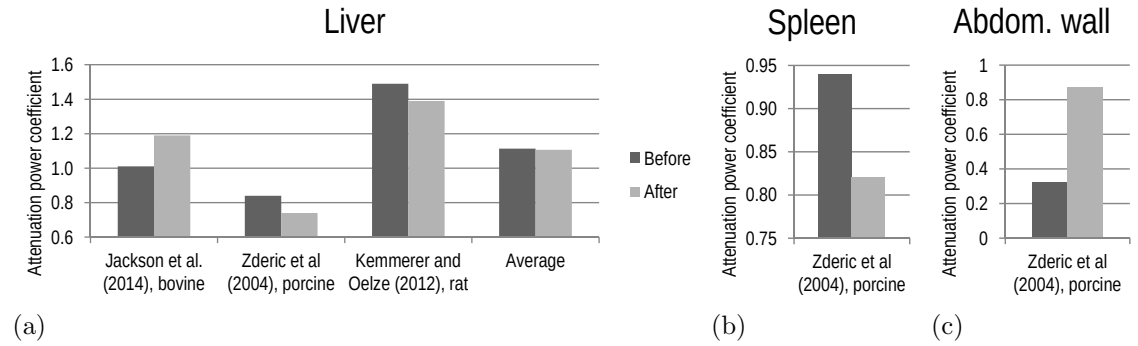

(a) (b) (c)

Figure 2.7: The change in (a) liver, (b) spleen and (c) abdominal wall attenuation power law coefficient before and after thermal ablation.

2.1.3 Backscatter coefficient

The backscatter coefficient describes the signal scattered by small, typically subwavelength, inhomogenities in tissue. These are the structures that produce the speckle seen in B-mode images. The backscatter coefficient is typically measured using a pulse-echo method where the power spectrum of the backscattered signal from a sample is compared to that of a perfect reflector (typically a flat metal plate) placed at the same position instead of the sample (Fei and Shung, 1985). Methods have been developed to account for transmission and reflection loss, absorption and diffraction (Yao et al., 1990). However, the measurement of the backscatter coefficient is strongly dependent on the measurement protocol, and hence, large variations (up to 18%) in the experimental results can be expected (Madsen et al., 1999).

Figure 2.8 shows the backscatter coefficient as a function of temperature for liver (Bush et al., 1993; Choi et al., 2011; Ghoshal et al., 2011). There is no consistent trend in this data with some showing an increase and other a decrease. Furthermore, there seems to variability even within the same author depending on the species: the values measured by Ghoshal et al. (2011) in rabbit liver are approximately five-fold higher than the ones in bovine. Therefore, no clear trend among the different studies can be concluded.

Figure 2.9 shows the backscatter coefficient before and after thermal ablation in liver (Choi et al., 2011; Bush et al., 1993; Kemmerer and Oelze, 2012). The small number of studies appeared to generally show an increase, on the order of 40 to 50%, in the backscatter coefficient after ablation. The mechanism for this could be changes in the structure of tissue due to ablation (Wall et al., 1999; Wright and Humphrey, 2002) or the presence of gas bubbles (Rabkin et al., 2005).

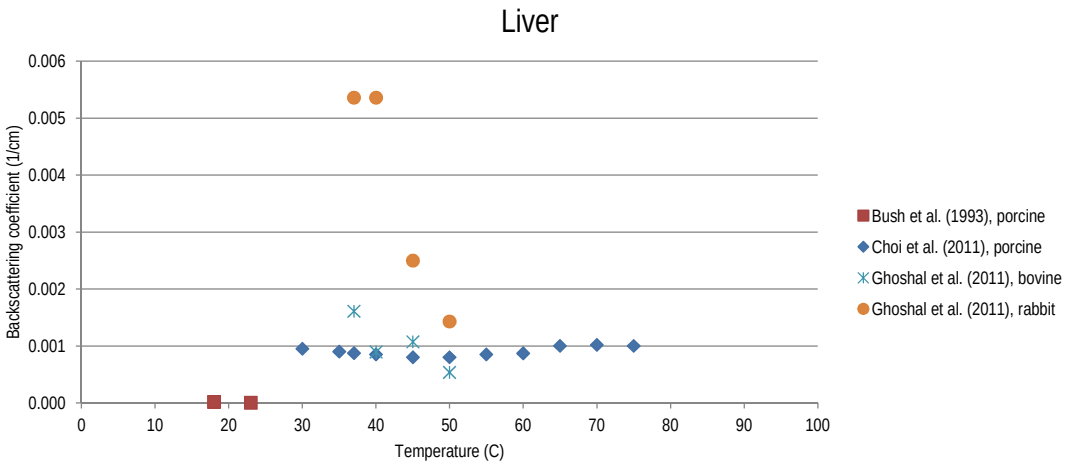

Figure 2.8: Temperature dependence of backscatter coefficient in liver.

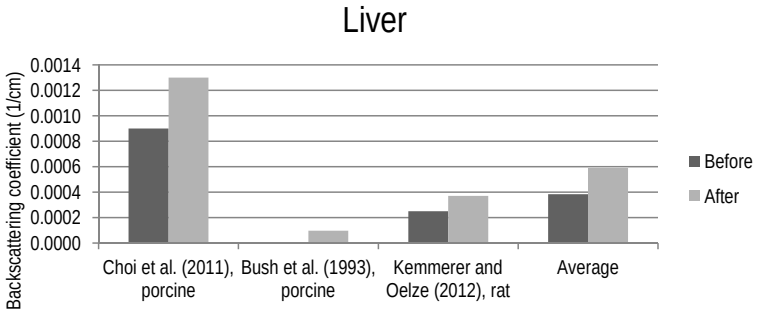

Figure 2.9: The change in liver backscatter coefficient before and after thermal ablation.

2.1.4 Nonlinearity parameter

The nonlinearity parameter B/A quantifies the nonlinearity in the pressure-density relation of the equation of state of a medium where A is the coefficient of the linear term and B the coefficient of the quadratic term. It is related to the coefficient of nonlinearity β by:

$$\beta = 1 + \frac{B}{2A} \tag{2.7}$$

which appears in the nonlinear wave equation (3.8) in Chapter 3. The nonlinearity parameter can be measured by either a thermodynamic method or a finite-amplitude method. Most tissue data measurements employ the finite-amplitude method, where the amplitude of a nonlinearly generated second harmonic is measured after a pulse has propagated trough a finite medium. The nonlinearity parameter can then be calculated typically by normalising the measurements to those in water (Dong et al., 1999).

Figure 2.10 shows the nonlinearity parameter as a function of temperature for (a) liver and (b) muscle (Choi et al., 2011; Jackson et al., 2014; Lu et al., 2004; Sehgal et al., 1986). Multiple studies in liver show a monotonic increase in the nonlinearity as a function of temperature with one study in muscle demonstrating a similar trend. These data suggest a 20% increase in B/A between 37 °C and 60 °C with one study showing an approximately 60% continuous increase at 75 °C.

Figure 2.11 shows measurements of nonlinearity parameter in liver before and after ablation from two studies (Jackson et al., 2014; Choi et al., 2011). In one study no significant change in the nonlinearity parameter was reported where as in the other study it appeared to approximately double. This suggests that more measurements are needed in order to determine if the nonlinearity changes with ablation.

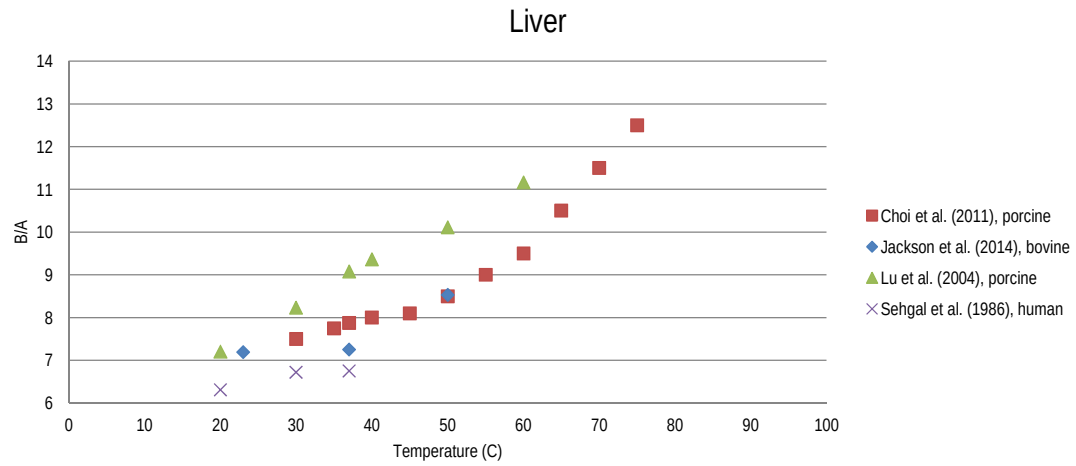

(a)

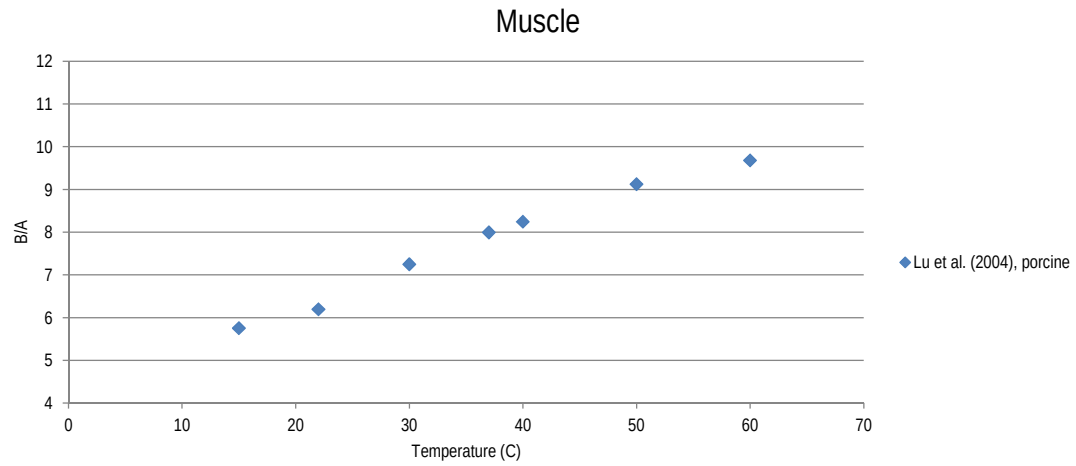

(b)

Figure 2.10: Temperature dependence of nonlinearity parameter in (a) liver and (b) muscle.

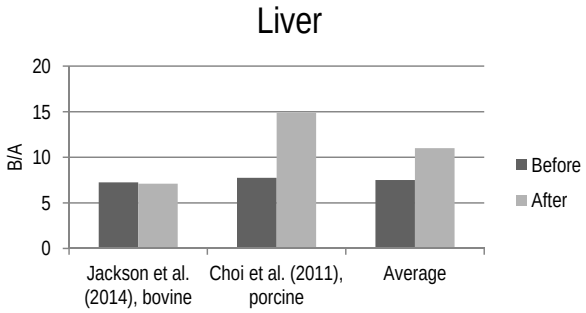

Figure 2.11: The change in liver nonlinearity parameter before and after thermal ablation.

2.2 Thermal properties

Tissue thermal properties, including specific heat capacity, thermal diffusivity and thermal conductivity, all affect the heat deposition in tissue. Consequently, the changes in these parameters affect the creation of thermal necrosis required destroy tissue in HIFU therapy (Sapareto and Dewey, 1984). This sections studies the changes in thermal properties as a function of temperature as well as before and after ablation.

2.2.1 Specific heat capacity

Specific heat capacity c_P [J/kg/K] describes the ability of a material to store thermal energy. It is defined by the amount of thermal energy required to raise the temperature of a unit mass by one degree. It can be calculated from:

$$c_P = \frac{Q}{\Delta T m} \tag{2.8}$$

where Q [J] is heat transfer, m [kg] is mass and ΔT [K] is the change in temperature. In the literature, the specific heat capacity of tissue is typically measured by either by assuming uniform temperature distribution in the sample and monitoring the power input causing the temperature rise (Haemmerich et al., 2006) or using purpose-built devices such as the transient line heat source technique (Guntur et al., 2013).

Figure 2.12 shows the experimentally measured changes in specific heat capacity in liver as a function of temperature for two authors (Guntur et al., 2013; Haemmerich et al., 2006). The specific heat capacity decreases from its initial value for both after which it starts to increase almost linearly after 40-50 °C. Figure 2.13 shows the change specific heat capacity before and after thermal ablation in liver (Guntur et al., 2013; Giering et al., 1995). Measurements by Guntur et al. (2013) suggest that the change is irreversible after certain temperature with an increase of +17% when compared to the initial value. However, similar observations were not made by Giering et al. (1995) who heated several ($N = 29$) tissue samples up to 100 °C and back to room temperature before measuring the changes in specific heat capacity. This suggests that more experiments need to be carried out before drawing conclusions.

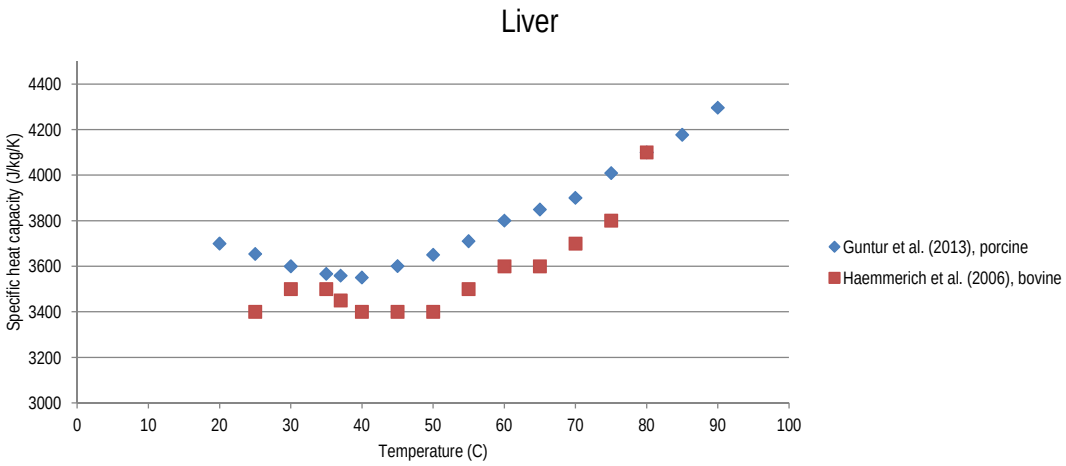

Figure 2.12: The change in liver specific heat capacity with temperature.

Figure 2.13: The change in liver specific heat capacity before and after thermal ablation.

2.2.2 Thermal conductivity and diffusivity

Thermal conductivity describes the ability of a material to conduct heat. It is defined by the power conducted per unit area and can be calculated from:

$$\frac{Q}{tA_{\mathrm{S}}} = -k\frac{\Delta T}{L} \qquad \Longleftrightarrow \qquad k = -\frac{QL}{t\Delta T A_{\mathrm{S}}} \tag{2.9}$$

where k [W/m/K] is the thermal conductivity, A_{S} [m^2] is surface area and ΔT [K] is the difference in temperature over a thickness L [m]. A related variable is the thermal diffusivity:

$$D = \frac{k}{\rho c_P} \tag{2.10}$$

where D [m^2/s] is the thermal diffusivity. Thermal conductivity and diffusivity are measured with purpose built devices which create and monitor the heat flux in the sample (Guntur et al., 2013; Valvano et al., 1985).

Figure 2.14 shows the temperature dependence of thermal conductivity in (a) liver, (b) kidney and (c) spleen (Guntur et al., 2013; Valvano et al., 1985; Bhattacharya and Mahajan, 2003). The data from (Valvano et al., 1985) has been derived from the reported linear fit values. An increasing trend in thermal conductivity with temperature is seen in all data over the range of temperature measured, up to 90 °C in liver and 45 °C in kidney and spleen. Figure 2.15(a) shows the effect of thermal ablation on thermal conductivity in liver. An average increase of +31% compared to the initial value is seen which suggest the changes due to heating to be irreversible.

Figure 2.16 shows the temperature dependence of thermal diffusivity in (a) liver, (b) kidney and (c) spleen (Guntur et al., 2013; Valvano et al., 1985). Again the data from Valvano et al. (1985) are presented using the reported linear fit values. A similar increase with temperature in all tissues is seen as in the case of thermal conductivity, which is consistent with the data showing density and specific heat capacity to have weak dependence on temperature. Figure 2.15(b) shows the thermal diffusivity values in liver before and after thermal ablation. An increase of +38% is seen compared to the original value.

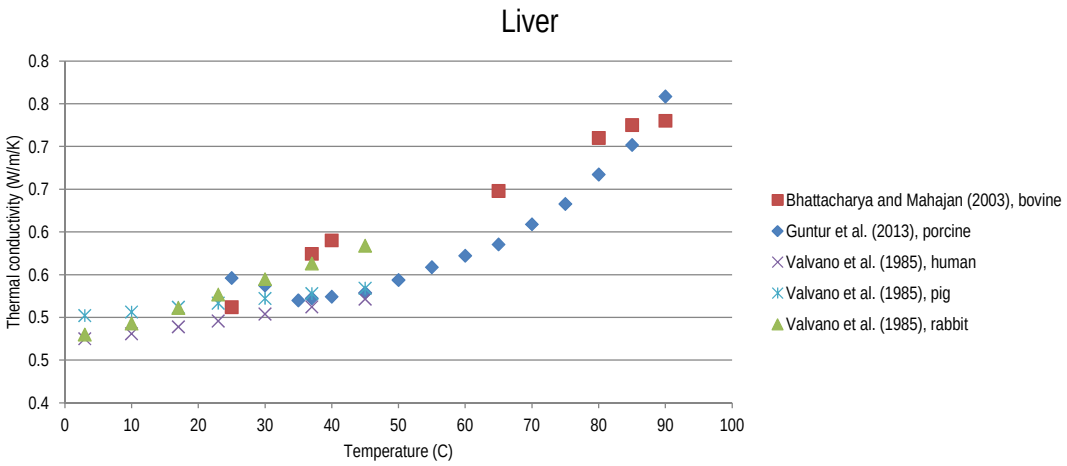

(a)

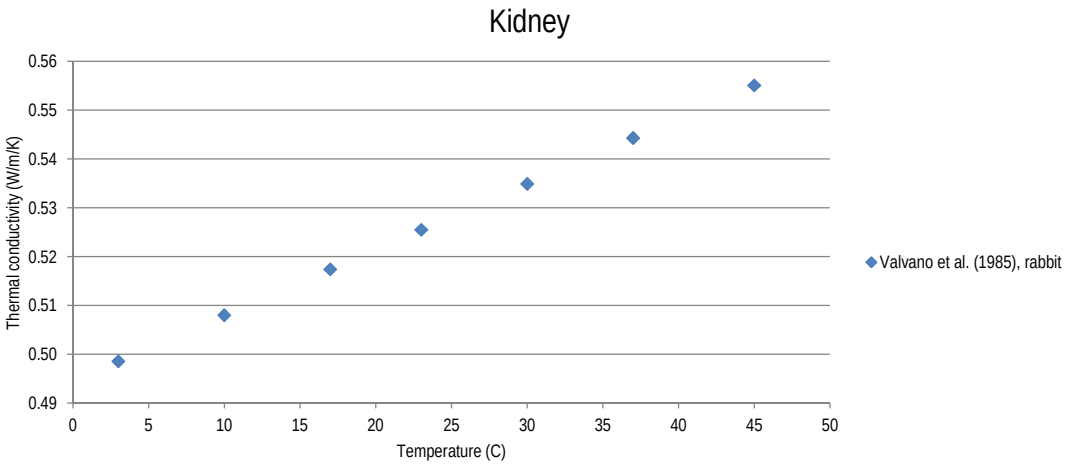

(b)

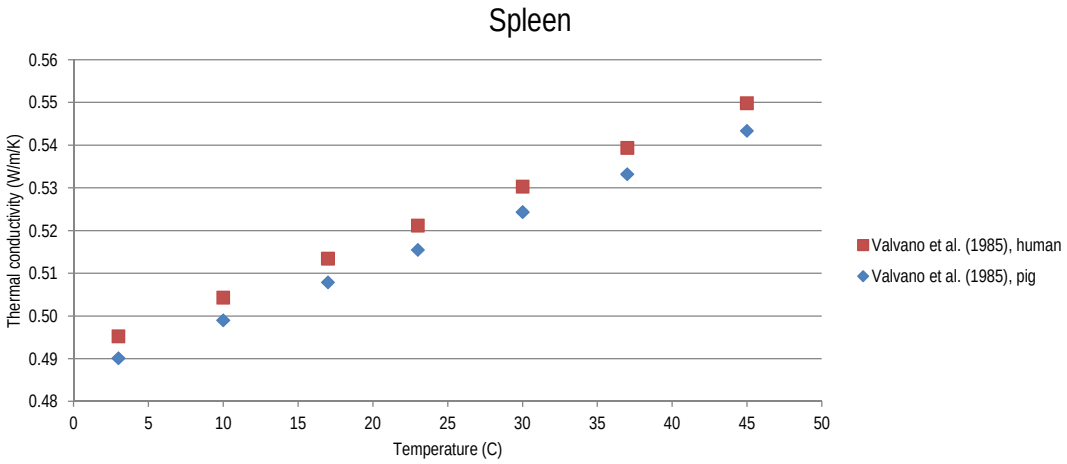

(c)

Figure 2.14: Temperature dependence of thermal conductivity in (a) liver, (b) kidney and (c) spleen.

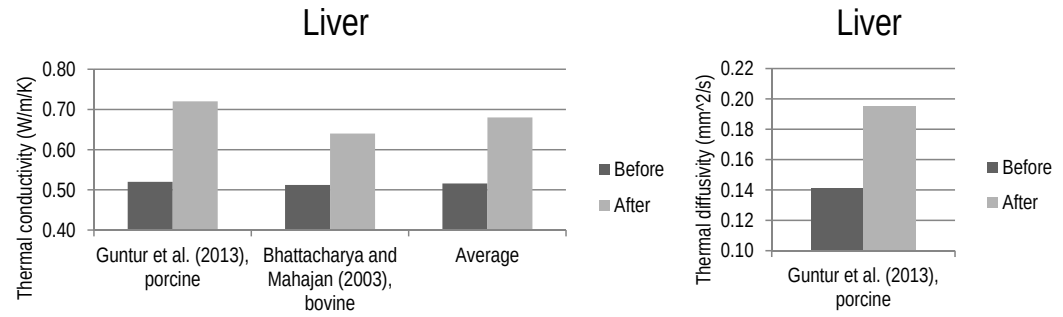

(a) (b)

Figure 2.15: The change in liver (a) thermal conductivity and (b) thermal diffusivity before and after thermal ablation.

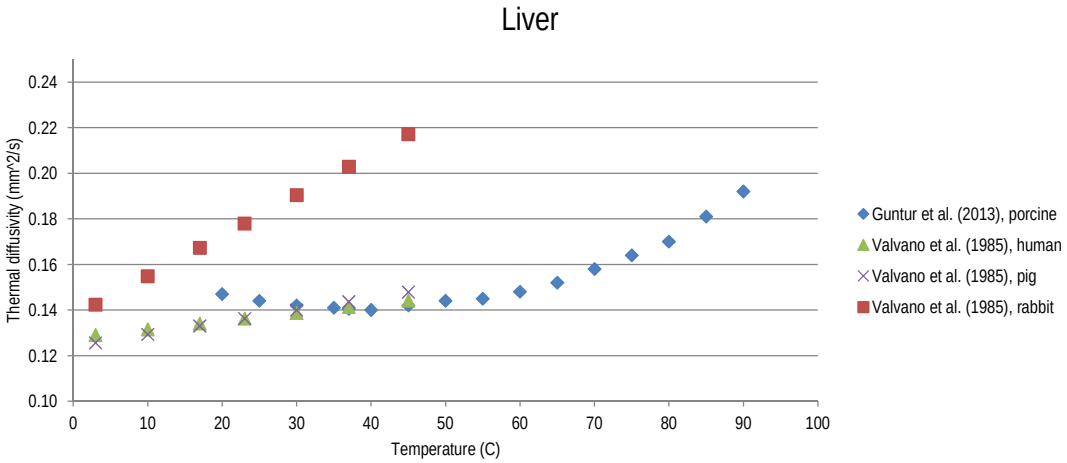

(a)

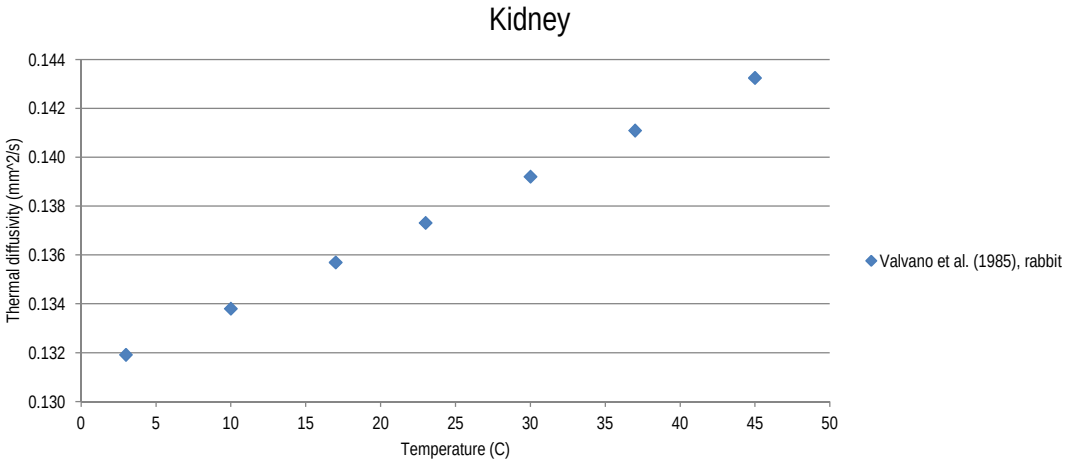

(b)

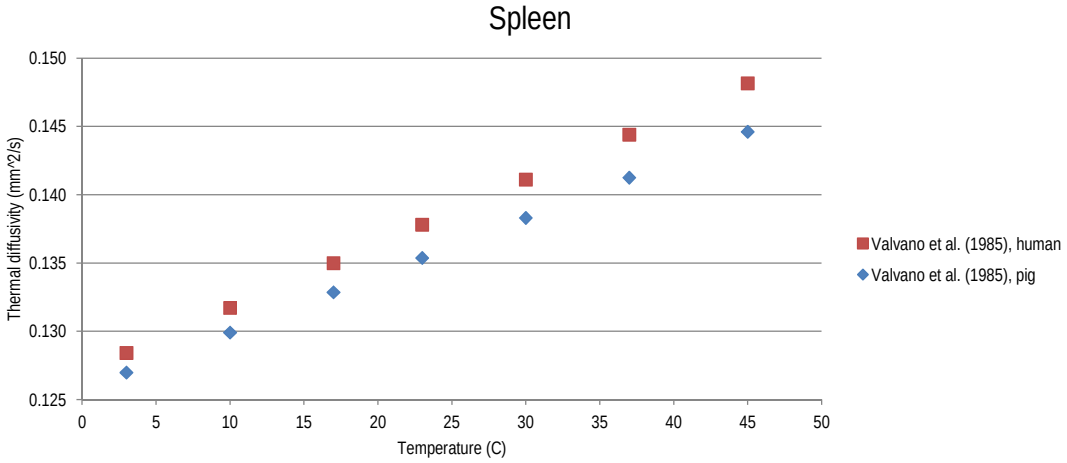

(c)

Figure 2.16: Temperature dependence of thermal diffusivity in (a) liver, (b) kidney and (c) spleen.

2.3 Mechanical properties

Changes in tissue mechanical properties, such as the density, elastic modulus and viscoelasticity, affect the displacement induced by ARF. Temperature dependence of these properties is an important factor in HIFU monitoring, where rapid temperature rises cause the tissue mechanical properties to change. These changes form the basis for detecting thermally ablated areas (i.e., lesions) using ultrasound elastography techniques. This section studies the changes in tissue mechanical properties with temperature and before and after ablation.

2.3.1 Density

The changes in tissue density with temperature have been characterised by Guntur et al. (2013) who immersed *ex vivo* tissue samples in a temperature controlled water bath. They used an indirect method where thermal diffusivity was first measured using a thermal probe after which the density was calculated using the equation (2.10) while keeping the values of c_P and k constant.

Figure 2.17 shows the experimentally measured behaviour of liver density with temperature in the range from 20 to 90 °C. The density can be seen to stay approximately constant with small variation up to 55 °C after which an almost linear decrease is seen. The decrease at 90 °C was 11.8% less than the value at 40 °C as reported by the authors. Figure 2.18 shows the changes in liver density before and after thermal ablation at 40 °C. The irreversible change due to ablation causes the density to decrease approximately 14.1% compared to the initial value.

The reason for the turning point at which the density starts to decrease and does not recover to the original value was hypothesised by Guntur et al. (2013) to be the process of protein denaturation combined with the changes in tissue water content. However, Yang et al. (2007) showed the tissue water content to decrease significantly in thermal ablation only after about 80 °C, which is higher than the onset of the density decrease in Figure 2.17. Therefore, more measurements are needed to ascertain the physical basis of the phenomenon.

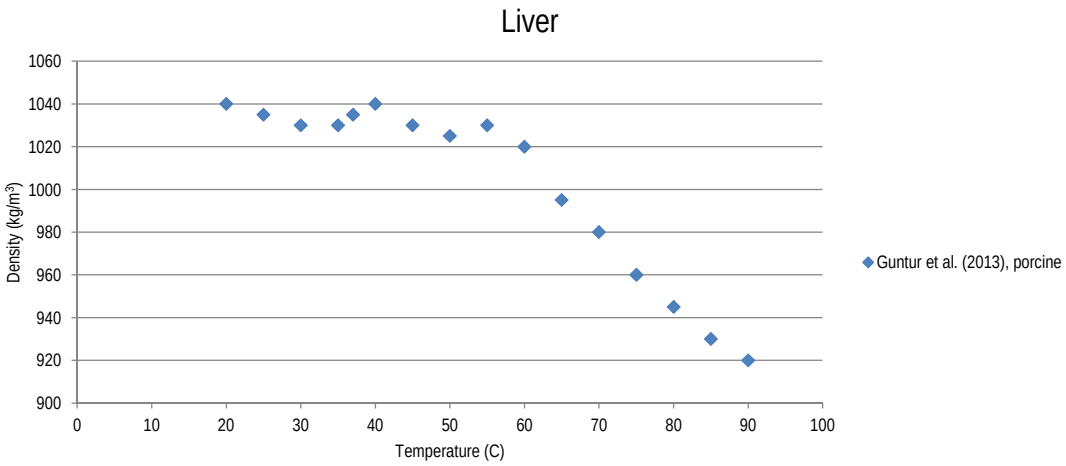

Figure 2.17: The change in liver density with temperature.

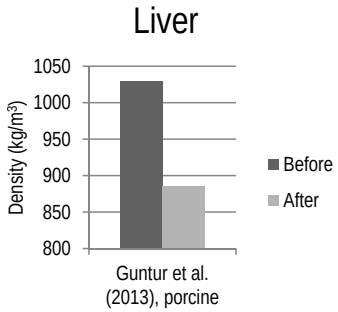

Figure 2.18: The change in liver density before and after thermal ablation.

2.3.2 Elastic moduli

Tissue elastic behaviour can be quantified by elastic moduli which relate the stress and strain relationship of the material. For linear, lossless media three common moduli are Young's modulus E [Pa], shear modulus G [Pa] and bulk modulus K [Pa]. For isotropic materials these are related by the equations:

$$E = 2G(1+\nu) = 3K(1-2\nu) \tag{2.11}$$

where ν is the Poisson's ratio. For soft tissue $\nu \approx 0.5$ in which case $E \approx 3G$, but in this case bulk modulus cannot be reliably estimated from the Young's or shear modulus. Therefore, typically tissue elastic modulus is reported from measurements of either the Young's or shear modulus.

Young's modulus describes the tendency of the medium to resist deformation along the axis of the force. It is defined by the ratio of tensile stress σ [Pa] to tensile strain ϵ in the linear region (i.e., elastic) by the equation:

$$E = \frac{\sigma}{\epsilon} = \frac{F_{\mathrm{N}}/A_{\mathrm{S}}}{\Delta Y/Y} \tag{2.12}$$

where F_{N} [N] is the normal (tensile) force, ΔY [m] is the magnitude of deformation in the direction of the force and Y [m] is the original length of the object in the same direction. When measuring tissue samples compressive force is usually easier to apply than tensile force, and therefore, the values of tissue Young's modulus are generally reported as the ratio of compressive stress to compressive strain. In practice the Young's modulus measurements are conducted using dynamic mechanical analysis (DMA) or other instruments which are designed for the purpose.

Shear modulus similarly describes the resistance of the medium to resist deformation in shear. Shear is normally induced by applying a force F_{T} [N] tangentially to a surface of the material and then measuring the displacement ΔX [m] in the same direction. The shear modulus is defined by the ratio of shear stress to shear strain by the equation:

$$G = \frac{F_{\mathrm{T}}/A_{\mathrm{S}}}{\Delta X/Y} \tag{2.13}$$

where Y [m] is the original length of the object perpendicular to the force.

The shear modulus is also related to the shear wave speed of the medium by the equation (1.5) in Chapter 1. In practice the shear wave speed is easier to measure than the ratio of shear stress to shear strain, and thus, many ultrasound elastography

modalities directly measure the shear wave speed, which is then used to quantify the shear modulus of tissue by knowing the density. Other imaging modalities, such as MRI, can also be used to estimate the shear modulus in tissue (Manduca et al., 1996).

Figure 2.19(a) shows the change in liver shear modulus with temperature measured with ultrasound elastography in a temperature controlled water bath by Sapin-de Brosses et al. (2010). The shear modulus stays approximately constant up to 45 °C after which an almost exponential increase is seen. It was noted by the authors that an irreversible change in stiffness was observed approximately after 55 °C which is in accordance with the temperature region for protein denaturation.

Figure 2.19(b) shows the change in muscle shear modulus value measured by several authors (Arnal et al., 2011; Sapin-de Brosses et al., 2010; Kruse et al., 2000; Wu et al., 2001). A decrease in the shear modulus is seen up to approximately 55-60 °C after which the modulus starts to increase again. This has been postulated to be due to reversible protein denaturation where specific proteins undergo unfolding/refolding process (Anema and McKenna, 1996; Wu et al., 2001). After 60 °C irreversible protein denaturation takes place and the muscle stiffness grows exponentially.

Figure 2.20(a) and (b) show the irreversible changes to the shear modulus before and after thermal ablation for liver and muscle, respectively (Sapin-de Brosses et al., 2010; Wu et al., 2001). Both tissues show significant changes in stiffness after ablation with +1025% increase in liver and +566% in muscle.

Figure 2.21 shows the irreversible changes in Young's modulus for (a) liver, (b) kidney and (c) muscle (Bharat et al., 2005; Shi et al., 1999; Righetti et al., 1999; Stafford et al., 1998; Konofagou et al., 2004). In liver, an average increase of +448% is observed, while kidney and muscle show +500% and +18% increase, respectively. The result by Righetti et al. (1999) show unusually high values for liver with 44 and 155 kPa before and after ablation respectively, while typically the values are a magnitude lower. The relatively small increase in the Young's modulus of liver by Konofagou et al. (2004) is probably because the lesion measured was not completely ablated above the temperature limit of thermal necrosis. The large increases in tissue elastic moduli after ablation provide the fundamental basis for determining thermally ablated regions in tissue using ultrasound elastography techniques.

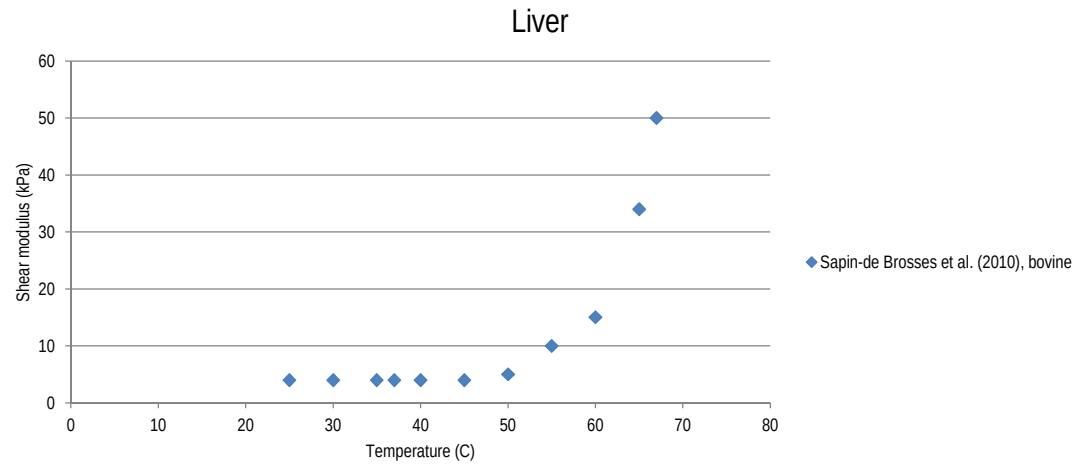

(a)

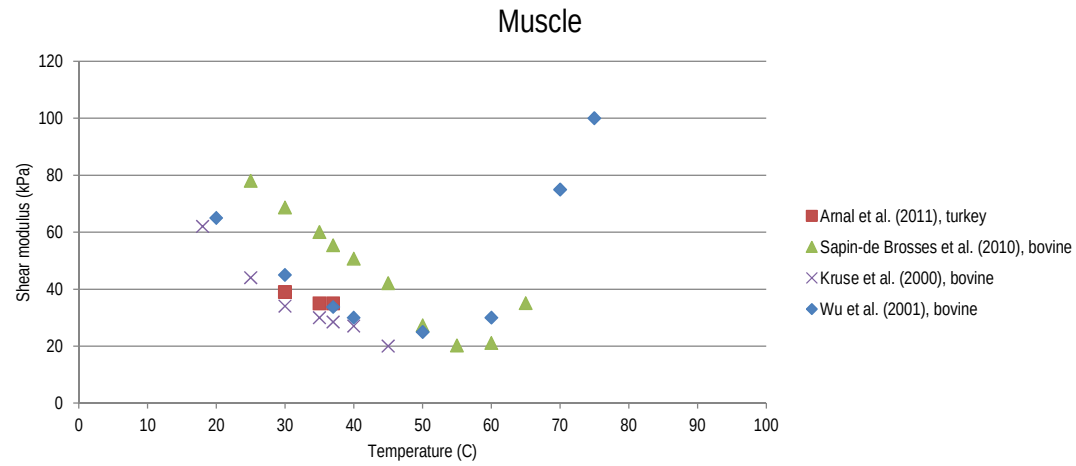

(b)

Figure 2.19: The change in (a) liver and (b) muscle shear modulus with temperature.

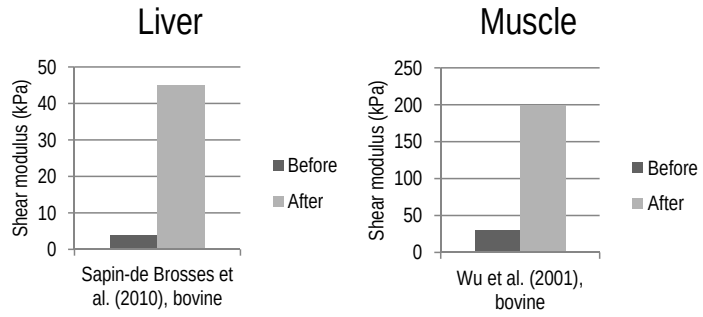

(a) (b)

Figure 2.20: The change in (a) liver and (b) muscle shear modulus before and after thermal ablation.

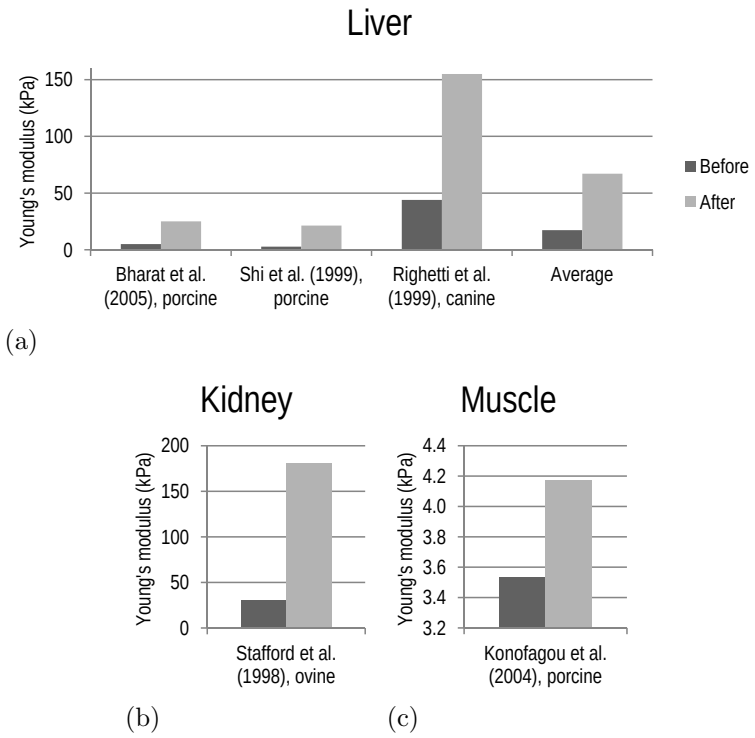

Figure 2.21: The change in the Young's modulus of (a) liver, (b) kidney and (c) muscle before and after thermal ablation.

2.3.3 Dynamic modulus

Tissue is not a simple elastic material but viscoelastic with frequency dependent properties. Therefore, although the Young's, shear and bulk moduli are useful quantities to characterise material response to stress over long duration of time (several seconds to minutes), they are less accurate to describe material properties under dynamic, short-duration stresses, which are typically used in ultrasound elastography. A more suitable parameter in this case is the dynamic modulus (aka complex modulus) which describes the ratio of stress to strain under sinusoidal (i.e., frequency dependent) conditions.

When viscoelastic materials are subjected to a sinusoidally varying stress, a steady state will eventually be reached in which the strain lags the stress by a phase angle δ [rad]. For purely elastic materials $\delta = 0$ whereas for purely viscous materials $\delta = \pi/2$. Sinusoidal stress and strain in viscoelastic materials can therefore be written as (Roylance, 2001):

$$\sigma = \sigma_0 \sin(\omega t + \delta) \tag{2.14}$$

$$\epsilon = \epsilon_0 \sin(\omega t) \tag{2.15}$$

where ω [rad/s] is the angular frequency and σ_0 [Pa] and ϵ_0 are the amplitudes of stress and strain, respectively. The elastic and viscous components are typically expressed separately as complex quantities in the dynamic modulus M^* [Pa], where the elastic component is referred as storage modulus M_S [Pa] and the viscous component as loss modulus M_L [Pa] with the relations:

$$M_\mathrm{S} = \frac{\sigma_0}{\epsilon_0}\cos(\delta) \tag{2.16}$$

$$M_\mathrm{L} = \frac{\sigma_0}{\epsilon_0}\sin(\delta) \tag{2.17}$$

$$M^* = M_\mathrm{S} + \mathrm{i}M_\mathrm{L} \tag{2.18}$$

where i is the imaginary unit. The dynamic modulus can be expressed in terms of compressive, tensile or shear stresses and strains, but with tissue samples compressive stress is usually used. In practice, storage and loss moduli can be measured using DMA which is able to characterise the viscoelastic behaviour of tissue in the frequency domain. In DMA, the storage and loss modulus are measured over a range of frequencies.

Kiss et al. (2004) used DMA to characterise the viscoelastic properties of lesions in *ex vivo* liver after thermal ablation of 80-90 °C for 5 to 10 minutes. The viscoelastic properties of the ablated tissue were measured from 0.1 Hz to 400 Hz at room temperature and fit to a fractional Kelvin-Voigt model. In a subsequent study (Kiss et al., 2009) the viscoelastic properties of lesions in liver prepared at temperatures ranging from 60 to 90 °C over a frequency range of 0.1-50 Hz were reported. It was found that the magnitude of the dynamic modulus increased with ablation temperature reaching a local maximum at around 70-75 °C in *ex vivo* porcine liver. In another case the magnitude of dynamic modulus continuously increased up to the maximum temperature of the experiment at 90 °C when *ex vivo* canine liver was used. The results suggest that the changes in the viscoelastic properties of liver will have a significant effect on the deformations in ultrasound elastography modalities which rely on short duration or frequency specific ultrasound exposures. Furthermore, the temperature dependence of dynamic modulus is yet to be studied, which will be addressed in Chapter 5 of this thesis.

2.4 Conclusions

This chapter brought together a wide variety of data that captures the temperature dependence of the key material properties that are likely relevant to therapeutic ultrasound. A large variation in reported values was found which is likely due to a combination of biological variability and experimental technique. Other useful sources for different tissue properties at body temperatures are (Chivers and Parry, 1978; Goss et al., 1979; Duck, 1990; Mast, 2000; Hasgall et al., 2015). Temperature dependent properties can be found from (Haney and OBrien, 1986; Rossmann and Haemmerich, 2014). However, this chapter is the first study to fit numerical models to the temperature dependent data. Furthermore, the summary of tissue property changes before and after thermal ablation has not been covered before.

For sound speed and attenuation, which are arguably the most important from propagation modelling, it was found by normalising measurements to values reported at 37 °C most of the data sets exhibited a common trend. Attenuation showed the strongest response to temperature and ablation whereas sound speed and nonlinearity parameter were relatively insensitive. The data for backscatter was too variable for conclusions to be drawn. Further measurements on the nonlinearity parameter and the backscatter are warranted due to limited data which is not consistent in the published literature. Measurements of the power law of attenuation would likely also be relevant particularly when nonlinear propagation is important.

The thermal properties of tissue demonstrated moderate changes in both specific heat capacity and conduction/diffusivity. These changes should be accounted for in models for tissue thermal effects.

Finally, large and irreversible changes in tissue stiffness confirm this as a parameter, which could be used as an indicator of coagulative thermal necrosis in ultrasound elastography. These changes were observed across all tissue types, which makes the technique applicable to monitor HIFU therapy in different organs.

Chapter 3

Model equations

3.1 Acoustic equations

Several acoustic phenomena affect the propagating ultrasound wave, which can be incorporated in the governing equations. First of all, the intensity of the ultrasound waveform is reduced due to attenuation, which is caused by the combination of scattering and absorption in tissue. Inhomogeneities in tissue cause scattering of the wave energy while viscous effects and particle momentum transfer (i.e., the absorption) cause the intensity to decrease with propagation distance. The magnitude of attenuation is dependent on ultrasound frequency and material properties with higher frequencies generally exhibiting greater attenuation. Another phenomenon reducing the intensity of the ultrasound field is the reflection at tissue interfaces caused by acoustic impedance mismatches. When an ultrasound wave passes through a tissue interface, for example fat and muscle, part of its energy is reflected back due to the differences in sound speed and density between the two different layers.

Due to the differences in sound speed in different tissues, the ultrasound waves are also refracted when passing through various layers in the human body. This is especially important aspect in HIFU, where tightly focused ultrasound focal point is required to create maximal heating effect. Several tissue layers in front of the transducer change the spatial pressure distribution of the ultrasound focal point, and thus, reduce the overall therapy efficacy. Furthermore, the waves are also distorted due to diffraction, dispersion and interference effects, which cause further changes in the focal point shape. Diffraction affects all waves and is defined as any deviation from the rectilinear path of propagating wave which cannot be interpreted as reflection or refraction. Dispersion is caused due to differences in sound speed depending on the frequency. Interference effects are caused due to phase differences between intersecting waves creating an amplitude superposition.

One important factor to be considered in HIFU therapy are the nonlinear effects, which cause higher harmonic frequencies to be generated in the propagating ultrasound waveform. Significant harmonic frequencies are generated if the propagation distance is long and/or the amplitude of the propagating ultrasound wave is large. These harmonics are highly attenuated, which consequently causes greater ARF and increased heating rate. Therefore, all the effects described above should be considered in the acoustic models in order to accurately predict the displacements induced by ARF and HIFU therapeutic outcome. The governing equations of linear and nonlinear acoustics are presented in this section.

3.1.1 Wave equation

In a compressible medium, a propagating ultrasound wave causes dynamic variations in the pressure, density and particle velocity. These changes can be described using a set of linearised partial differential equations (PDE) based on the conservation of mass, momentum and an appropriate equation of state (Cobbold, 2006; Treeby and Cox, 2010b):

$$\begin{aligned} \frac{\partial \rho}{\partial t} &= -\rho_0 \nabla \cdot \mathbf{v} && \text{(mass conservation)} \\ \nabla P &= -\rho_0 \frac{\partial \mathbf{v}}{\partial t} && \text{(momentum conservation)} \\ \rho &= \frac{P}{c^2} && \text{(equation of state)} \end{aligned} \tag{3.1}$$

where ρ_0 [kg/m^3] is the density of the propagation medium in the surrounding ambient pressure and $\mathbf{v}$ [m/s] is the particle velocity. When these equations are combined, they give an expression for the distribution of pressure as a function of space and time aka the wave equation (Cobbold, 2006):

$$\boxed{\nabla^2 P - \frac{1}{c^2} \frac{\partial^2 P}{\partial t^2} = 0} \tag{3.2}$$

The wave equation describes the propagation of an acoustic wave in a lossless and homogeneous medium (i.e., no absorption or scattering). This means that in an infinite domain the wave would propagate in a rectilinear path forever without reduction in amplitude. Furthermore, the propagation described by the equation is also *linear*, which means that no harmonic frequencies are generated and the wave maintains its perfectly sinusoidal shape.

The linear wave equation is an useful approximation for describing wave propagation in ultrasound applications, such as standard B-mode imaging, where the amplitudes are low and the reduction in the intensity due to absorption can be neglected. However, in the case of HIFU therapy and ARF based ultrasound elastography, these assumptions are not true anymore. Therefore, more complex models are needed to accurately predict their effect on the ultrasound field.

3.1.2 Westervelt equation

When an ultrasound wave propagates in the human body, its intensity is reduced due to attenuation in tissue. Attenuation is caused by the combined effect of absorption and scattering, although in biological tissue absorption is shown to account for 82-100% of the total attenuation (Parker, 1983; Lyons and Parker, 1988). The acoustic wave also starts to generate harmonic frequencies if the amplitude is high enough. In this case, additional nonlinear terms have to be added to the governing equations to account for this effect. When acoustic absorption due to viscosity and thermal effects, scattering due to heterogeneities (i.e., non-uniform density) and nonlinearity are included in the governing equations (3.1), they become:

$$\begin{aligned} \frac{\partial \rho}{\partial t} &= -(\rho + \rho_0)\nabla \cdot \mathbf{v} - \mathbf{v} \cdot \nabla \rho && \text{(mass conservation)} \\ \nabla P &= -\rho_0 \frac{\partial \mathbf{v}}{\partial t} - \nabla \mathrm{L} + \left(\frac{4\eta}{3} + \eta_\mathrm{B}\right)\nabla^2 \mathbf{v} && \text{(momentum conservation)} \\ \rho &= \frac{P}{c^2} - \frac{B}{2A}\frac{P^2}{\rho_0 c^4} + \frac{k}{\rho_0 c^4}\left(\frac{1}{c_V} - \frac{1}{c_P}\right)\frac{\partial P}{\partial t} && \text{(equation of state)} \end{aligned} \tag{3.3}$$

where c_V and c_P [J/kg/K] the specific heat capacities at constant volume and pressure, respectively; η and η_B [Pa·s] are the viscosity and bulk viscosity, respectively; and L [J/m^3] is the Lagrangian energy density:

$$\mathrm{L} = \frac{\rho_0 \mathbf{v}^2}{2} - \frac{P^2}{2\rho_0 c^2} \tag{3.4}$$

Compared to the linear case, the momentum conservation equation now has an additional term for viscosity. The mass conservation equation contains an additional term which accounts for a convective nonlinearity in which the particle velocity contributes to the wave velocity. The values A and B are the coefficients of the first and second order terms of the Taylor series expansion of the equation of state. The equation of state also contains a term accounting for absorption due to thermal effects.

When these equations are combined, an equation for nonlinear sound propagation accounting for viscosity and medium inhomogeneities can be derived:

$$\nabla^2 P - \frac{1}{c^2}\frac{\partial^2 P}{\partial t^2} + \frac{b}{c^4}\frac{\partial^3 P}{\partial t^3} = -\frac{\beta}{\rho_0 c^4}\frac{\partial^2 P^2}{\partial t^2} - \left(\nabla^2 + \frac{1}{c^2}\frac{\partial^2}{\partial t^2}\right)\mathrm{L} \tag{3.5}$$

where b [m^2/s] is the sound diffusivity:

$$b = \frac{1}{\rho_0}\left(\frac{4}{3}\eta + \eta_\mathrm{B}\right) + \frac{k}{\rho_0}\left(\frac{1}{c_V} - \frac{1}{c_P}\right) \tag{3.6}$$

which accounts for absorption due to viscosity and thermal conductivity in the medium. This nonlinear propagation equation can be simplified by neglecting the last term, because the effect is local and not cumulative, and for plane waves at the first order:

$$\mathrm{v} = \frac{P}{\rho_0 c} \quad \Rightarrow \quad \mathrm{L} = 0 \tag{3.7}$$

The relation then simplifies to an equation of nonlinear propagation up to second-order aka the Westervelt equation (Westervelt, 1963):

$$\boxed{\nabla^2 P - \frac{1}{c^2}\frac{\partial^2 P}{\partial t^2} + \underbrace{\frac{b}{c^4}\frac{\partial^3 P}{\partial t^3}}_{\text{absorption}} + \underbrace{\frac{\beta}{\rho_0 c^4}\frac{\partial^2 P^2}{\partial t^2}}_{\text{nonlinearity}} = 0} \tag{3.8}$$

The Westervelt equation accounts for the thermoviscous absorption and nonlinearity in the medium. A numerical solution to the generalised version of Westervelt equation using the k-space pseudospectral method can be found from (Treeby and Cox, 2010a,b; Treeby et al., 2012).

3.1.3 Khokhlov-Zabolotskaya-Kuznetsov equation

The Westervelt equation (3.8) describes the dominant effects affecting the propagating ultrasound wave, but it is computationally intensive to solve. Therefore, more efficient models are needed which not only describe the absorption, diffraction and nonlinearity but also are numerically easy to solve. In seeking a quasi-planar solution for a wave propagation in the z-direction of a Cartesian coordinate system, a parabolic approximation can be made. The parabolic approximation assumes that ultrasound field is directional and that most of its energy is contained within the ultrasound beam axis (within $\sim$20° from the transducer face). Kuznetsov (1971) extended the work of Zabolotskaya and Khokhlov (1969) by adding a viscous loss term and expressing the parabolic wave propagation in z-direction using retarded time:

$$\tau_\mathrm{r} = t - \frac{z}{c} \tag{3.9}$$

If the z-axis is the parallel to the sound propagation and xy-plane is perpendicular to that, the Khokhlov-Zabolotskaya-Kuznetsov (KZK) equation can be expressed as:

$$\boxed{\frac{\partial^2 P}{\partial z \partial \tau_\mathrm{r}} = \underbrace{\frac{c}{2}\nabla_\perp^2 P}_{\text{diffraction}} + \underbrace{\frac{b}{2c^3}\frac{\partial^3 P}{\partial \tau_\mathrm{r}^3}}_{\text{absorption}} + \underbrace{\frac{\beta}{2\rho_0 c^3}\frac{\partial^2 P^2}{\partial \tau_\mathrm{r}^2}}_{\text{nonlinearity}}} \tag{3.10}$$

where

$$\nabla_\perp^2 = \frac{\partial^2}{\partial x^2} + \frac{\partial^2}{\partial y^2} \tag{3.11}$$

is a transverse Laplacian which operates in a plane normal to the direction of propagation.

The KZK equation accounts for the combined effect of diffraction, absorption and nonlinearity of directional waves. The advantage of the KZK equation is that can be efficiently solved either in the time domain or the frequency domain. This is especially useful aspect in HIFU, where numerous nonlinear harmonics are generated. These harmonics can be easily taken into account in the frequency domain solution. Frequency domain solutions can also take into account the dispersion in sound speed and frequency dependence of absorption in tissue. The limitation of the KZK equation is that it is not accurate for solutions outside the beam axis or close to the transducer face. However, this is usually not a limitation in focused ultrasound applications which use directional beams with long focal distances. Numerical methods for solving the KZK equation can be found from (Hamilton et al., 1998).

3.2 Thermal equations

In HIFU therapy, rapid temperature rises are created in order to cause tissue damage in the therapeutic area. The magnitude of the temperature rise is dependent on the shape and intensity of the ultrasound field as well as tissue properties including thermal conductivity, specific heat capacity and perfusion. Furthermore, the response of the tissue is not only dependent on the temperature rise alone but also on the heating duration. The relationship between temperature rise and heating duration (aka the thermal dose) should also be considered in order to determine the therapeutic outcome of the treatment. Therefore, comprehensive models for temperature generation and transfer in tissue as well as quantification of thermal damage are necessary to accurately predict the result of the treatment. This section summarises the relevant thermal equations for HIFU therapy and introduces numerical methods to solve them.

3.2.1 Bioheat transfer equation

The bioheat transfer (BHT) equation is the standard model for studying temperature changes in biological systems such as the human body. In HIFU therapy, it is useful in describing the changes in temperature during thermal ablation due to heat sources and tissue properties such as conductivity, heat capacity and perfusion. The BHT equation can be written as (Pennes, 1948; Curra et al., 2000):

$$\boxed{\rho_\mathrm{t} c_{P\mathrm{t}} \frac{\partial T_\mathrm{t}}{\partial t} = \underbrace{k_\mathrm{t} \nabla^2 T_\mathrm{t}}_{\text{conduction}} - \underbrace{w_\mathrm{t} c_{P\mathrm{b}} (T_\mathrm{t} - T_\mathrm{b})}_{\text{perfusion}} + \underbrace{H}_{\text{heating}}} \tag{3.12}$$

where w [kg/m^3/s] is the perfusion rate, H [W/m^3] is the heating rate and the subscripts 't' and 'b' refer to tissue and blood, respectively. The temperature of the blood is usually defined as the body temperature ($T_\mathrm{b} = 37$ °C). A numerical solution to the heat equation can be found from Appendix A.

The intensity of the ultrasound field at a location x [m] can be expressed as:

$$I(x) = I_0 \exp(-2\alpha x) \tag{3.13}$$

where I_0 [W/m^2] is the initial intensity value at $x = 0$. The heating rate per unit volume can be obtained by differentiating this equation:

$$H = -\frac{dI(x)}{dx} = 2\alpha I(x) \tag{3.14}$$

If it is assumed that scattering can be ignored and that all the absorbed energy is converted into heat, the expression for the heat rate due to acoustic intensity can be expressed as (Cobbold, 2006):

$$\boxed{H = 2\alpha_\mathrm{abs}(f) I_\mathrm{TA}} \tag{3.15}$$

where $\alpha_\mathrm{abs}(f)$ [dB/m] is the frequency dependent absorption. Because the ultrasound fields in HIFU are typically nonlinear, the heating rate can calculated using the harmonic components of the ultrasound field according to the equation (Curra et al., 2000):

$$H = \frac{1}{c_\mathrm{t} \rho_\mathrm{t}} \sum_h \alpha_\mathrm{abs}(h f_0) |P_h|^2 \tag{3.16}$$

where h is the index of harmonic component ($h = 1$ for the fundamental), f_0 [Hz] is the sonication frequency and P_h [Pa] is the pressure amplitude of the harmonic component h.

3.2.2 Thermal dose

The thermal dose is used to quantify the relationship between therapy efficiency (i.e., the cell death) and temperature as a function of time. The concept of thermal dose was defined by Sapareto and Dewey (1984), who studied the cell death at temperatures ranging 41.5-46.5 °C. Based on the findings they derived the expression of the equivalent heating duration at 43 °C to obtain the same amount of cell death. This equivalent duration is called thermal dose, and it is defined as cumulative equivalent minutes at 43 °C (Sapareto and Dewey, 1984):

$$\boxed{\mathrm{CEM}_{43^\circ\mathrm{C}}(t) = \int_0^{t_{\mathrm{end}}} R^{43-T(t)} dt, \qquad R = \begin{cases} 0.25, & T < 43\ ^\circ\mathrm{C} \\ 0.5, & T \geq 43\ ^\circ\mathrm{C} \end{cases}} \tag{3.17}$$

where t_{end} [s] is the heating duration over which the thermal dose is calculated and R is an empirical constant depending on the temperature. The equation can be discretised as (Sapin-de Brosses et al., 2011):

$$\mathrm{CEM}_{43^\circ\mathrm{C}}(t) = \sum_i R^{43-T(i)}(t_i - t_{i-1}) \tag{3.18}$$

where i is the iteration step, $T(i) = \frac{T_i + T_{i-1}}{2}$ [°C] is the average of the temperatures between the time steps t_{i-1} and t_i [s].

Generally, the thermal dose of 240 $\mathrm{CEM}_{43^\circ\mathrm{C}}$ is accepted as the threshold value for cell death due to thermal necrosis, but this has been shown to depend on tissue type (Yarmolenko et al., 2011). Furthermore, changes in tissue elasticity due to thermal ablation has been shown to occur around 202 $\mathrm{CEM}_{43^\circ\mathrm{C}}$ (Sapin-de Brosses et al., 2011), which in ultrasound elastography can be used as an indicator of thermal necrosis (Wall et al., 1999; Wright and Humphrey, 2002).

3.3 Linear viscoelastic equations

Due to the changes in temperature during HIFU therapy, the viscoelastic properties of tissue also change. This is because the viscoleastic properties of a material are defined mainly by the molecular composition and their short-range interactions (Roylance, 2001). Therefore, the main factor driving the change in tissue viscoelastic properties are the structural modifications of collagen at temperatures above 60 °C (Wall et al., 1999; Wright and Humphrey, 2002). Ultrasound elastography can be used to quantify these changes by generating ARF in tissue and monitoring the response.

The elastic behaviour of tissue subject to small amplitude ARF can be predicted using different linear viscoelastic models, which are comprised of various combinations of purely elastic components (Hookean springs) and purely viscous components (Newtonian dampers). The behaviour of a Hookean spring can be described by:

$$\boxed{\epsilon = \frac{\sigma}{E}} \tag{3.19}$$

where the strain follows the stress with a linear dependence defined by the stiffness. The behaviour of a Newtonian damper can be modelled by:

$$\boxed{\frac{d\epsilon}{dt} = \frac{\sigma}{\eta}} \tag{3.20}$$

where the strain *rate* follows the stress with a linear dependence defined by the viscosity. Another useful parameter is the ratio of viscosity to stiffness:

$$\boxed{\tau = \frac{\eta}{E}} \tag{3.21}$$

where τ [s] is the relaxation time. The models presented in this section are linear, and although biological tissues are generally nonlinear (Fung, 1993), the small displacements induced by ARF are typically considered to be in the linear region (Zhai et al., 2008).

3.3.1 Maxwell model

The Maxwell model is a linear viscoelastic model which consists of a damper and a spring connected in series (see Figure 3.1). In the case of the Maxwell model, the total stress applied to the system is the same for both the spring and the damper due to series connection:

$$\sigma = \sigma_{\mathrm{d}} = \sigma_{\mathrm{s}} \tag{3.22}$$

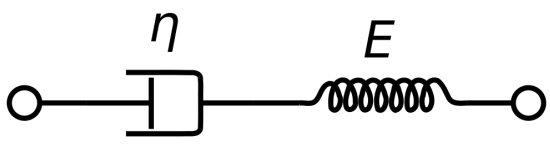

Figure 3.1: The Maxwell viscoelastic model consists of a purely viscous damper η and a purely elastic spring E connected in series. (Wikimedia Commons, 2016)

where the subscripts 'd' and 's' refer to the damper and spring, respectively. However, the total strain of the system is the sum of the strains of both components:

$$\epsilon = \epsilon_{\mathrm{d}} + \epsilon_{\mathrm{s}} \tag{3.23}$$

Now if the behaviour of the whole system is wanted to be expressed using a single equation, it is convenient to differentiate the strain equation (3.19) and write both strain rates in terms of the total stress:

$$\frac{d\epsilon}{dt} = \frac{d\epsilon_{\mathrm{d}}}{dt} + \frac{d\epsilon_{\mathrm{s}}}{dt} = \frac{\sigma}{\eta} + \frac{1}{E}\frac{d\sigma}{dt} \quad \Longleftrightarrow \quad \boxed{E\frac{d\epsilon}{dt} = \frac{1}{\tau}\sigma + \frac{d\sigma}{dt}} \tag{3.24}$$

This equation effectively describes the behaviour of a perfect 'Maxwell material' under an applied stress. When the material is put under a constant stress, the strain in the elastic component occurs immediately while the strain in the viscous component grows linearly with time as long as the stress is applied. However, this behaviour is usually the limitation of the Maxwell model since most polymers, such as proteins, exhibit decreasing rather than linear strain under a constant stress (Roylance, 2001).

3.3.2 Kelvin-Voigt model

The Kelvin-Voigt model is a linear viscoelastic model which consists of a damper and a spring connected in parallel (see Figure 3.2). Therefore, the total strain of the system is equal to that of both components:

$$\epsilon = \epsilon_{\mathrm{d}} = \epsilon_{\mathrm{s}} \tag{3.25}$$

Because the damper and spring are connected in parallel, the total stress of the system is the sum of the stresses experienced by the damper and the spring:

$$\sigma = \sigma_{\mathrm{d}} + \sigma_{\mathrm{s}} \tag{3.26}$$

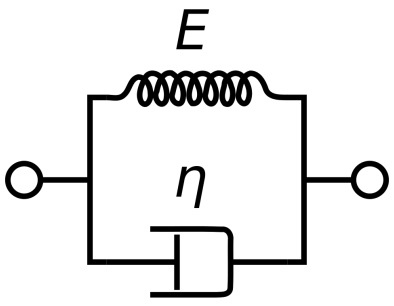

Figure 3.2: The Kelvin-Voigt viscoelastic model consists of a purely viscous damper η and a purely elastic spring E connected in parallel. (Wikimedia Commons, 2016)

which using the equations (3.19) and (3.20) can be expressed as:

$$\sigma = \eta\frac{d\epsilon}{dt} + E\epsilon \quad \Longleftrightarrow \quad \boxed{\frac{\sigma}{\eta} = \frac{d\epsilon}{dt} + \frac{1}{\tau}\epsilon} \tag{3.27}$$

This equation describes the behaviour of a perfect 'Kelvin-Voigt material'. When the material is put under a constant stress, the material deforms at a decreasing rate approaching the asymptotic value of the steady-state. When the stress is released, the material relaxes back to its original state. This behaviour is close to many organic polymers, and thus, Kelvin-Voigt model can be used to accurately predict their response under a constant stress (Kiss et al., 2004). However, the limitation of the model is that it is less accurate predicting the material behaviour under constant strain in materials such as soft tissue, where the stress decreases with time (Hoyt et al., 2008).

3.3.3 Zener model

The Zener model (aka the standard linear solid model) can be seen as a combination of Maxwell and Kelvin-Voigt model. It consists of a damper and a spring in series, both of which are also in parallel with another spring (see Figure 3.3). These two parallel components can be referred as the 'Maxwell arm' for the spring and damper combination and the 'elastic arm' for the spring alone. The total strain experienced by the systems can be written in terms of these two arms by:

$$\epsilon = \epsilon_{\mathrm{m}} = \epsilon_{\mathrm{e}}, \qquad \begin{cases} \epsilon_{\mathrm{m}} &= \epsilon_{\mathrm{d}} + \epsilon_{\mathrm{s}_2} \\ \epsilon_{\mathrm{e}} &= \epsilon_{\mathrm{s}_1} \end{cases} \tag{3.28}$$

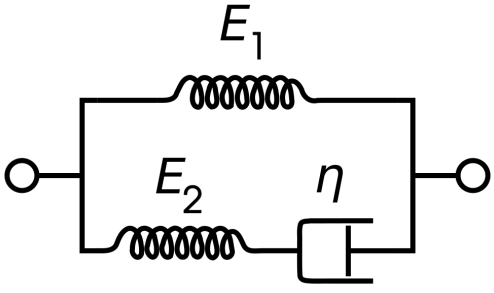

Figure 3.3: The Zener viscoelastic model consists of a purely viscous damper η and a purely elastic spring E_2 in series, both of which are in parallel with another spring E_1. (Wikimedia Commons, 2016)

where subscripts 'm' and 'e' refer to the Maxwell and elastic arms, respectively; and 's_1' and 's_2' refer to the two springs. The total stress experienced by the system is:

$$\sigma = \sigma_{\mathrm{m}} + \sigma_{\mathrm{e}}, \qquad \begin{cases} \sigma_{\mathrm{m}} & = \sigma_{\mathrm{d}} = \sigma_{\mathrm{s}_2} \\ \sigma_{\mathrm{e}} & = \sigma_{\mathrm{s}_1} \end{cases} \tag{3.29}$$

The governing equation of the whole system is difficult to solve in time domain, since equation (3.24) involves both the stress and its differential. Therefore, to solve the governing equation to predict the behaviour of the system, the Laplace transform can be used to convert the differential stress equation (3.29) to algebraic one:

$$\mathcal{L}\big(\sigma(t)\big) = \overline{\sigma}(s) = \overline{\sigma}_{\mathrm{m}}(s) + \overline{\sigma}_{\mathrm{e}}(s) \tag{3.30}$$

where s is the complex Laplace variable. The corresponding Maxwell and elastic arms in Laplace domain are as follows:

$$\mathcal{L}\big(\sigma_{\mathrm{m}}(t)\big) = \overline{\sigma}_{\mathrm{m}}(s) = E_2\left(\frac{s}{s+\frac{1}{\tau}}\right)\overline{\epsilon}(s) \tag{3.31}$$

$$\mathcal{L}\big(\sigma_{\mathrm{e}}(t)\big) = \overline{\sigma}_{\mathrm{e}}(s) = E_1\overline{\epsilon}(s) \tag{3.32}$$

Now the total stress in Laplace domain can be written in terms of the stresses in the Maxwell and elastic arms:

$$\overline{\sigma}(s) = \left[E_1 + E_2\left(\frac{s}{s+\frac{1}{\tau}}\right)\right]\overline{\epsilon}(s) \tag{3.33}$$

The presentation in frequency domain can be obtained by substituting $s{=}\mathrm{i}\omega$:

$$\overline{\sigma}(\omega) = \left[E_1 + E_2\left(\frac{\mathrm{i}\omega}{\mathrm{i}\omega+\frac{1}{\tau}}\right)\right]\overline{\epsilon}(\omega) \tag{3.34}$$

In time domain, the presentation can be derived by defining the strain with a step function:

$$\epsilon(t) = \epsilon_0 u(t), \qquad u(t) = \begin{cases} 0, & t < 0 \\ 1, & t \geq 0 \end{cases} \tag{3.35}$$

which has the Laplace transform:

$$\overline{\epsilon}(s) = \frac{\epsilon_0}{s} \tag{3.36}$$

and taking the inverse Laplace transform of equation (3.33) yields the presentation in time domain:

$$\mathcal{L}^{-1}\big(\overline{\sigma}(s)\big) = \sigma(t) = \big(E_1 + E_2\exp(-t/\tau)\big)\epsilon_0 \tag{3.37}$$

which can be presented in terms of the elastic modulus as:

$$\boxed{\frac{\sigma(t)}{\epsilon_0} = E(t) = E_1 + E_2 \exp(-t/\tau)} \tag{3.38}$$

This function presents the behaviour of a perfect 'Zener material' *under a constant strain* in time domain. The effective stiffness of the material E is now a time-dependent parameter. At $t = 0$ there is an instantaneous stress response and the stiffness of the material E is therefore the sum of the moduli E_1 and E_2. At infinite time $t = \infty$ the stress relaxes to a steady state value, and therefore, the stiffness is equal to that of the elastic band alone E_1.

Similarly, equation (3.33) can be presented in terms of constant stress loading by defining:

$$\sigma(t) = \sigma_0 u(t), \qquad u(t) = \begin{cases} 0, & t < 0 \\ 1, & t \geq 0 \end{cases} \tag{3.39}$$

which has the Laplace transform:

$$\overline{\sigma}(s) = \frac{\sigma_0}{s} \tag{3.40}$$

Substituting the Laplace transform into equation (3.33) and taking the inverse Laplace transform yields:

$$\mathcal{L}^{-1}\big(\overline{\epsilon}(s)\big) = \epsilon(t) = \left[\frac{1}{E_1 + E_2} + \left(\frac{1}{E_1} - \frac{1}{E_1 + E_2}\right)\big(1 - \exp(-t/\tau_\mathrm{c})\big)\right]\sigma_0 \tag{3.41}$$

where $C_\mathrm{g} = \frac{1}{E_1+E_2}$ [1/Pa] and $C_\mathrm{r} = \frac{1}{E_1}$ [1/Pa] are referred to the glassy and rubbery compliances, respectively, and τ_c [s] is the retardation time:

$$\tau_\mathrm{c} = \left(\frac{E_1 + E_2}{E_1}\right)\tau = \frac{C_\mathrm{r}}{C_\mathrm{g}}\tau \tag{3.42}$$

Equation (3.41) can now be presented in terms of compliance modulus C [1/Pa] as:

$$\boxed{\frac{\epsilon(t)}{\sigma_0} = C(t) = C_\mathrm{g} + (C_\mathrm{r} - C_\mathrm{g})\big(1 - \exp(-t/\tau_\mathrm{c})\big)} \tag{3.43}$$

This function presents the behaviour of a perfect 'Zener material' *under a constant stress* in time domain. Zener model is the simplest model which can be used to predict material behaviour under both a constant stress or strain. It can therefore be used for a wider set of materials than the simpler Maxwell and Kelvin-Voigt models. The three-parameter Zener model has been shown to be the most accurate model in predicting viscoelastic response in liver and brain tissues (Klatt et al., 2007).

Chapter 4

Harmonic displacements

The work reported in this chapter[1] is motivated by a desire to better quantify the ARF induced displacements in a viscoelastic material. The deformation caused by ARF can be described with equations (1.1) and (1.2) from Chapter 1:

$$F_V = \frac{2\alpha_{\text{abs}} I_{\text{TA}}}{c}$$
$$\rho \frac{\partial^2 u_i}{\partial t^2} = \frac{\partial \sigma_{ij}}{\partial x_j} + F_{Vi}$$

The magnitude of this deformation is generally tracked using ultrasound based methods, which use time-delays to estimate the dynamic response of tissue using pulse-echo data (Pinton et al., 2006). Although these ultrasound methods can track the displacement at a sub-micrometre scale in the axial direction, they have several limitations. First, the displacement estimation accuracy in the lateral direction is significantly lower compared to the axial direction. While it is possible to derive lateral displacement estimate on the basis of axial strain, it has been shown that the variance of the lateral displacement estimate is $40\times$(F-number)^2 worse than that of the axial direction (Lubinski et al., 1996). Second, real-time tracking of displacements is limited by the interference from the ARF pulse. This is because the echo signal from the excitation pulse has to be sufficiently attenuated before acquiring the pulse-echo tracking data, which prevents estimating tissue deformation during the excitation phase. Third, the depth of the region-of-interest (ROI) creates physical limitations for the temporal resolution due to the sound speed in tissue ($\sim$1540 m/s). For example, in theory a point located at a focal depth of 7.7 cm in tissue would only allow temporal resolution of 10 kHz, which is within the limit for short duration ARFI pulses. In reality, however, the temporal resolution would be even lower due to the

[1]The contents of this chapter have been published in Suomi et al. (2015).

interfering echo signals, which would have to be attenuated before starting the next pulse-echo acquisition. Furthermore, ultrasonically derived displacement estimates in solid media are also affected from the so-called shearing artefact (McAleavey et al., 2003), which is caused by the averaging of individual scatterer amplitudes in displacement calculation. This has been shown to lead to underestimation (up to 35%) of tissue peak displacement at the focal point (Czernuszewicz et al., 2013). Although ultrasound based tracking methods can be easily implemented in a clinical setting by using the same transducer for pushing and tracking the displacement, the limitations mentioned do not favour their usage in accurate characterisation of tissue dynamics.

Bouchard et al. (2009b) were the first to demonstrate the feasibility of optical tracking method utilising a high-speed camera to measure the dynamics of tissue deformation under ARF excitations. They used a phantom with embedded steel markers and tracked the displacement of these markers under both impulsive and harmonic excitations. The impulsive excitations were conducted using pulse lengths from 0.5 to 50.0 ms and the harmonic excitations using 50-300 Hz amplitude modulation. This tracking data was then compared to tracking data acquired using conventional ultrasound based tracking method. They found the mean peak displacements differ from 2.8 to 30.7% for impulsive pulses and from -4.3 to 25.3% for harmonic excitations between the two tracking methods. Bouchard et al. (2009a) also did another study, where they used the same tracking technique to characterise the deformation dynamics in a tissue-mimicking phantom. They used short duration impulsive pulses (0.1-0.4 ms) and tracked the induced displacements in both axial and lateral direction with frame rates up to 36 kHz. The displacements were tracked using several individual markers located on- and off-axis, and the results were compared to FEM models.

Later, Czernuszewicz et al. (2013) used the same optical tracking method to experimentally validate the displacement underestimation in ultrasound based techniques (McAleavey et al., 2003). For ultrasound excitation and tracking they used a clinical ultrasound scanner with linear ultrasound probe. The probe was used with F-numbers 1.5 and 3.0 to excite tissue-mimicking phantoms whose Young's moduli were 6.6, 19.8 and 30.2 kPa. They found the displacement underestimation to decrease with higher F-number due to larger cross-sectional area which the force is affecting. Similarly, stiffer phantoms exhibited smaller underestimation error due to faster shear wave spreading, which makes the scatterer movement at the focal point more uniform. Therefore, the maximum underestimation error (35%) was found using the F-number 1.5 and the softest phantom. These experimental results were in good agreement with the FEM simulations by Palmeri et al. (2006).

Several studies have characterised mechanical tissue response to impulsive ultrasound excitation using optical (Callé et al., 2005; Bouchard et al., 2009a,b; Czernuszewicz et al., 2013) and ultrasound tracking methods (Palmeri et al., 2005; Wang et al., 2014), but there has been little focus on the tissue dynamics under harmonic excitations. Konofagou and Hynynen (2003) demonstrated the feasibility of HMI with simulations and experimentally by using ultrasound tracking in tissue-mimicking phantoms. In the experimental part, they used three different transducer configurations with ultrasound modulation frequencies ranging from 200 to 800 Hz and four agar phantoms with Young's modulus between 7.1 and 94.6 kPa. The effect of stiffness on the harmonic displacement amplitude was determined and the results were compared to simulations. The experimental results showed the oscillation displacements to vary from -300 to 250 μm whilst in the simulations the estimated harmonic displacement spanned from -800 to 600 μm. An exponential decrease of the harmonic displacement amplitude with the phantom stiffness was observed both in simulations and experimentally. Later, Konofagou et al. (2012) established the correlation between ultrasonically measured harmonic displacement amplitudes and Young's moduli of tissue-mimicking gel phantoms. They also showed the harmonic displacement amplitude to decrease with increasing Young's modulus of the phantom.

Apart from the effect of tissue stiffness on harmonic displacement amplitude, some research has been done about the effect of modulation frequency on oscillation magnitude. Due to the viscoelastic properties of soft tissues, Liu and Ebbini (2007) used ultrasound amplitude modulation for viscoelastic characterisation of tissue properties. They studied the changes in harmonic displacement amplitudes using modulation frequencies from 200 to 1300 Hz in two different phantoms. It was shown that the relative displacement amplitude is dependent on the frequency response of the target material, which can be related to the corresponding stiffness. In addition to displacement amplitude, the relative phase of the displacement was also shown to vary with modulation frequency. Furthermore, some studies have also used animal tissue to study the frequency dependence of displacements. Curiel et al. (2009) used HMI to monitor HIFU ablation in rabbit muscle and measured the average normalised harmonic displacement amplitudes as a function of modulation frequency. They used modulation frequencies from 50 to 300 Hz and found the displacement amplitude to decrease with modulation frequency within this range. A similar relation was also observed in simulations performed later by Heikkila et al. (2010).

Previous studies have examined the effect of tissue stiffness and modulation frequency on displacement amplitudes, but several aspects are still to be studied: (i)

the dynamics of harmonic excitation pulses using square modulation have not been extensively compared to those of sine modulation, (ii) frequency spectrum analysis has not been conducted to characterise the harmonic frequencies and spectral components of displacement curves and (iii) the absolute harmonic displacement amplitudes and phase shifts have not been analysed in terms of both quantified ARF and modulation frequency. Furthermore, ultrasonic tracking methods have mainly been used previously, which has been shown to suffer from limitations in spatial accuracy, temporal resolution and ultrasound excitation interference. Accurate characterisation of tissue deformation under amplitude-modulated (AM) ultrasound waveforms would benefit the development of HMI, electromagnetic acoustic (EMA) imaging (Zhang et al., 2013) and other imaging modalities, which rely on ultrasound pushing the tissue periodically. The characterisation sine and square AM in the frequency domain is especially important in EMA imaging, which relies on detecting the fundamental frequency of the vibration.

This chapter focuses on characterising tissue dynamics under square and sine AM ultrasound waveforms. The axial displacement curves generated in a tissue-mimicking phantom are analysed both in the time and frequency domain. The time domain characterisation includes quantifying the absolute peak-to-peak displacements of the harmonic displacement curves by varying the intensity and modulation frequency of the ultrasound field. Furthermore, displacement curves are compared to simulated ARF waveforms to determine the phase shifts of the displacement curves. In the frequency domain, individual frequency components of the displacement curves are identified, and square and sine AM displacement curves are examined to quantify the magnitudes of first, second and third harmonic frequencies. Finally, the experimental results are compared to a FEM model using simulated nonlinear ultrasound fields.

4.1 Materials and methods

4.1.1 Tissue-mimicking phantom

Paraffin gel-wax was used to construct an optically clear tissue-mimicking phantom. Paraffin gel-waxes are transparent compounds of mineral oil and polymer resin, where the ratio of these two elements is typically 95% mineral oil and 5% polymer resin (Heilman and Morrison, 2002). Gel-waxes are commonly used in candle-making industry due to their burning properties, but their usage has also been suggested as soft tissue-mimicking materials for ultrasound-guided breast biopsy training (Vieira et al., 2013).

Table 4.1: Acoustic and mechanical properties of gel-wax phantom

Sound speed	Attenuation power law	Density	Young's modulus	Shear relaxation modulus	Relaxation time
1446 m/s	0.16 dB/cm/MHz$^{1.67}$	0.84 g/cm^3	7.8 kPa	4.8 kPa	0.35 ms

The acoustic and mechanical properties of the phantom are presented in Table 4.1. The acoustic properties were measured using standard methods (Ritchie et al., 2013). Young's modulus and the frequency response of the phantom material were experimentally measured with multiple repetitions using dynamic mechanical analysis (DMA Q800, TA Instruments, New Castle, DE, US) from 0.1 to 50 Hz and an amplitude of 15 μm. The shear relaxation modulus and relaxation time parameters (viscosity) were fitted to the frequency response using least squares method (Kohandel et al., 2005).

The tissue-mimicking phantom was constructed by melting 30 ml of gel-wax in a glass container until its temperature reached 90 °C. After this, three drops of black polystyrene microspheres (diameter 10.23 $\pm$ 0.344 μm, Polybead, Polysciences, Eppelheim, Germany) were added to act as markers for optical tracking. The water content of the drops was evaporated before adding the beads to the phantom. The liquid compound was then poured into a 100 mm (lateral) $\times$ 20 mm (axial) $\times$ 15 mm (elevation) phantom holder and was left to cool down at room temperature 21 $\pm$ 1 °C. The phantom holder was made of clear plastic for efficient light transmission and had removable sides and a top part to allow ultrasound propagation through the phantom in the axial direction.

4.1.2 Experimental setup and parameters

All the experiments were conducted using the setup shown in Figure 4.1. A spherically focused single-element transducer (H-102, Sonic Concepts Inc, Bothell, WA, US) was submersed into a water tank which was filled with degassed and distilled water. The transducer had a geometric focal length of 62.6 mm, a 64.0 mm active element diameter with a central hole of 20.0 mm resulting in F-number 0.98, and it was driven at its 3.3 MHz resonance frequency.

To align the optical and ultrasound equipment, a needle hydrophone (HMP0075, Precision Acoustics, Dorset, UK) was then attached to a three-axis micro-positioning stage (M-443, Newport Corporation, Irvine, CA, US) and was used to find the focal point of the transducer. The focal point of the ultrasound field was found by manually

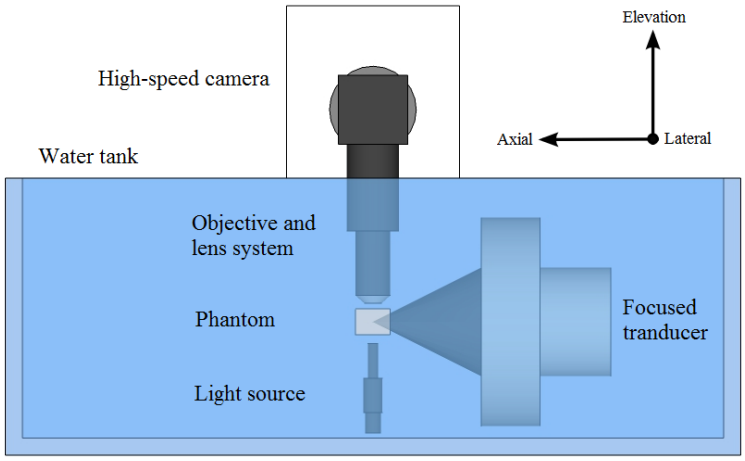

Figure 4.1: Schematic presentation of the experimental setup. The cone coming out of the transducer face illustrates the ultrasound field.

scanning the hydrophone in axial, elevation and lateral directions until the peak-positive pressure was maximal. The peak-positive pressure value of the ultrasound waveform was determined in each direction using an oscilloscope (WaveRunner 64Xi-A, Teledyne LeCroy, Spring Valley, NY, US), and the process was repeated until the maximum values of all three axes were found. The needle hydrophone had a physical tip diameter of 300 μm and an active element diameter of 75 μm, which were smaller than the approximate -6 dB beam diameter (BD) of the transducer focal point in water (Olympus, 2011):

$$\mathrm{BD}_{-6\ \mathrm{dB}} = \frac{1.02lc}{f_0 d_\mathrm{a}} = 450\ \mu\mathrm{m} \tag{4.1}$$

where l [m] is the geometrical focal length of the transducer and d_a [m] is the active element diameter.

After the location of the transducer focal point was determined, the needle hydrophone was left in its position and a mirror system consisting of a 40$\times$ objective (LUMPLFLN 40XW, Olympus Corporation, Essex, UK) was attached to another three-axis micro-positioning stage (M-443, Newport Corporation, Irvine, CA, US). The adjustment in the axial and lateral directions was done so that the tip of the hydrophone needle was in the centre of the image and in the elevation direction the visually sharpest position of the objective was determined. This was done to ensure that the acoustic focal point of the transducer and the optical focal point of the objective were coincident.

After the two focal points were aligned, the needle hydrophone was detached from the positioning stage and the phantom holder with a tissue-mimicking phantom

was attached instead. The tissue-mimicking phantom was then positioned below the lens system so that the upper surface of the phantom was flush with the end of the objective, and that the ultrasound focal point was approximately in the middle of the phantom in the lateral and axial directions. The objective had a working distance of 3.3 mm, which was the limiting factor for the ultrasound focal point depth in the elevation direction. Below the phantom, a 150-watt halogen cold light source (KL 1500 compact, Schott AG, Mainz, Germany) with an optical light guide (600 mm 1-branch gooseneck, Schott AG, Mainz, Germany) was placed so that the end of the light source was facing the objective, and a gap of approximately 10 mm was left between the phantom holder and the tip of the light source. The light guide was made waterproof by using a heat shrink and a custom made clear plastic top part.

For data acquisition, a high-speed camera (Memrecam HX-3, NAC Image Technology, Simi Valley, CA, US) was attached to the end of the optical mirror system. The ultrasound transducer was driven using two arbitrary waveform generators (33250A, Agilent Technologies, Santa Clara, CA, US) which were connected in sequence. The first generator was used to create either a 10-cycle square AM waveform with 50% duty cycle V_{square} [V] or a 10-cycle sine AM waveform as

$$V_{\text{sine}} = \frac{1}{2}\big(1 - \cos(2\pi f_{\text{AM}} t)\big)\sin(2\pi f_0 t) \tag{4.2}$$

where f_{AM} [Hz] is the modulation frequency. An example of waveforms using sine and square AM at 160 Hz are presented in Figure 4.2(a) and (b), respectively. The second function generator was used to create the carrier wave at 3.3 MHz and to trigger the

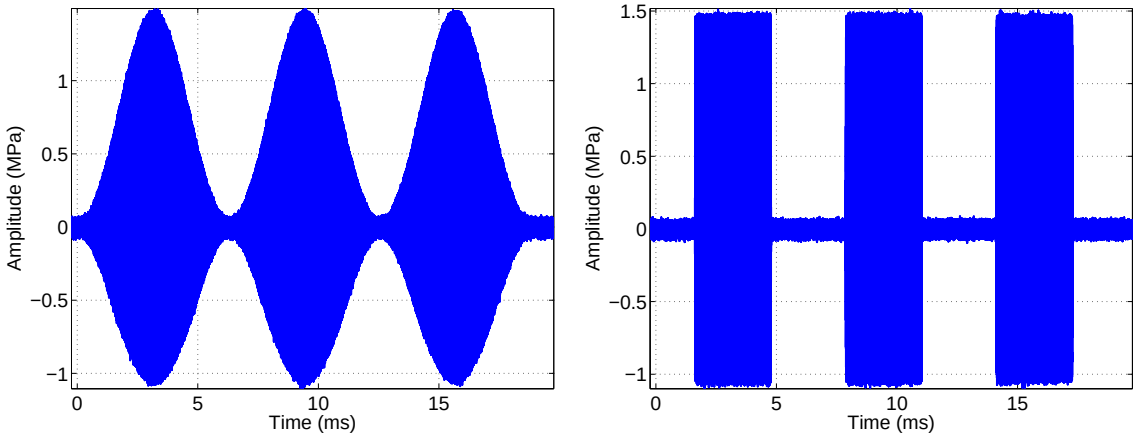

(a) (b)

Figure 4.2: Three cycles of (a) sine and (b) square amplitude modulated ultrasound signals at 160 Hz used in the experiments.

Table 4.2: Ultrasound parameters used in the experiments for square and sine modulated harmonic excitations.

Experiment no.	1	2	3	4	5	6	7	8	9	10	11
f_{AM} (Hz)	50			160				1000			
PPP (MPa)	4.62	7.39	10.73	4.62	7.39	10.73	13.32	4.62	7.39	10.73	13.32
PNP (MPa)	−3.47	−4.83	−6.25	−3.47	−4.83	−6.25	−7.09	−3.47	−4.83	−6.25	−7.09
I_{SPTA} (W/cm^2)	534	1209	2038	534	1209	2038	3013	534	1209	2038	3013
MI	1.91	2.66	3.44	1.91	2.66	3.44	3.90	1.91	2.66	3.44	3.90

high-speed camera to start the data acquisition. The AM waveforms were amplified by 55 dB with a RF-amplifier (A300, Electronics & Innovation, Rochester, NY, US) and applied to the transducer via an impedance matching box.

The experimental ultrasound parameters measured in distilled/degassed water using a calibrated needle hydrophone (HNA-400, Onda Corporation, Sunnyvale, CA, US) are presented in Table 4.2. The ultrasound propagation distance in the phantom was short (1 cm) which resulted in negligible reduction of ultrasound pressure (−1.86 dB). The frequency response of the hydrophone was taken into account when calculating the ultrasound parameters (Howard and Zanelli, 2007). Spatial peak temporal average intensity I_{SPTA} [W/m^2] values were calculated using the equation (Cobbold, 2006):

$$I_{\mathrm{SPTA}} = \frac{1}{t_{\mathrm{pc}}} \int_0^{t_{\mathrm{pc}}} \frac{P(t)^2}{\rho_0 c} dt \tag{4.3}$$

where t_{pc} [s] is the duration of the pressure cycle with the highest peak value and $P(t)$ [Pa] is the corresponding time dependent pressure waveform. Mechanical index (MI) values were calculated using the equation (Szabo, 2004):

$$\mathrm{MI} = \frac{P_{\mathrm{PN}}}{\sqrt{f_0}} \tag{4.4}$$

where P_{PN} [MPa] is the peak negative pressure of the ultrasound field.

4.1.3 Data acquisition

A total of 11 experiments were conducted for both square and sine AM waveforms using the same protocol. Parameters that were altered are shown in Table 4.2. Each excitation consisted of 10 periods based on the modulation frequency, i.e., 200 ms at 50 Hz. Simultaneously, at the beginning of the ultrasound excitation, a trigger signal was sent to the high-speed camera, which started capturing images through the objective and the mirror system. The frame rate of the camera was set to 10 kHz for all the square modulated excitations, and frame rates of 1, 2 and 10 kHz were used for 50, 160 and 1000 Hz sine modulated excitations, respectively. This

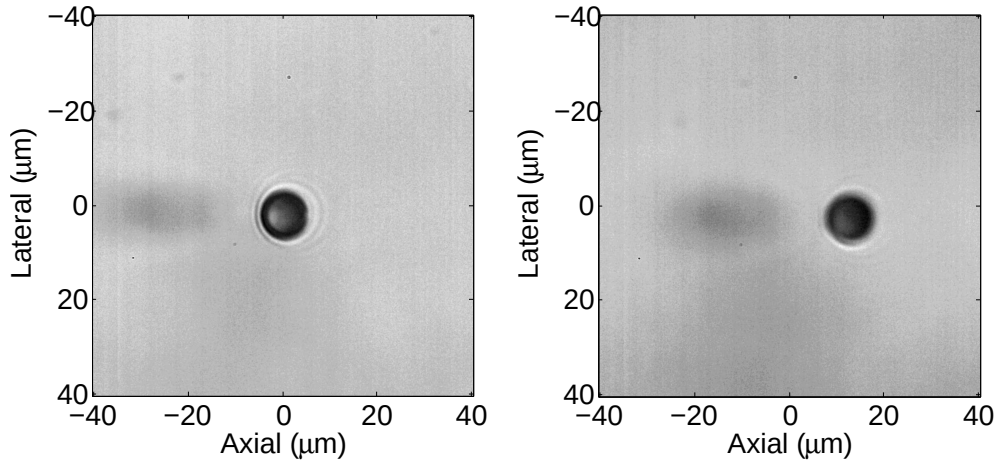

Figure 4.3: Representative high-speed camera images captured (a) before and (b) during ultrasound excitation. The focal point of the ultrasound field is in the middle of the image.

was done to reduce the file size of the acquired image data whilst keeping the frame rate at least 10 times higher than the modulation frequency. The shutter speed of the camera was set to be the inverse of the frame rate. The trigger signal in the camera software was adjusted so that it was in the middle of the image buffer, i.e., the same number of frames were captured before and after the ultrasound excitation. Representative image frames recorded before and during ultrasound excitation are shown in Figure 4.3. The field-of-view (FOV) of the objective was kept the same in all the experiments so that the initial position of the microshpere was in the middle of the image. All the measurements were conducted at room temperature 21 $\pm$ 1 °C and the light source was turned off for approximately one minute between the acquisitions to prevent unnecessary heat production in the water bath.

4.1.4 Data analysis

After each experiment, a sequence of images was captured in the camera buffer and a set of images from 5 frames before the beginning of the ultrasound excitation to 100 frames after the end of the excitation were selected. These image sets were then processed through an algorithm pipeline in Matlab R2013b (MathWorks Inc, Natick, MA, US) to calculate axial deformation in time, average peak-to-peak displacements, average phase shifts, frequency spectra and the magnitudes of harmonic frequencies. The image data from all the experiments were analysed using the same method.

The first image of each image set was selected as the reference image in which the microsphere was at rest state. The horizontal location of the microsphere central point in the image was manually selected and an intensity threshold value was used to determine the edges of the sphere. By knowing the diameter of the microspheres (10.23 μm), the corresponding pixel diameter in the image could be calculated. Each of the images were captured with 1280 (axial) $\times$ 720 (lateral) resolution resulting in a spatial resolution of 0.1 μm per pixel. After the resolution of the image set was determined, each of the images in the sequence was compared to the reference image using a 2-D cross-correlation algorithm. The maximum value of the cross-correlation output in each image pair determined the axial and lateral displacement of the microsphere, which was saved into a vector variable. Maximum correlation values were typically over 0.8 throughout the whole image set. After all the images in the sequence had been analysed, the displacement vectors were used to plot tissue deformation in the time domain. The data analysis was done based on the axial displacement curves, which are referred to as displacement curves from now on.

After obtaining the time domain displacement curves, the average peak-to-peak displacement of each harmonic modulation was calculated. The original waveforms exhibited a baseline drift, which was removed by high-pass filtering (see Figure 4.4). High-pass filters with cut-off frequencies of 20, 50 and 250 Hz were used for 50, 160 Hz and 1000 Hz modulation frequencies, respectively. After the displacement curves were filtered, the maximum and minimum displacement values of each cycle were determined, and the average peak-to-peak value was calculated based on 8 cycles by ignoring the first and the last cycle of the 10-cycle modulation curve.

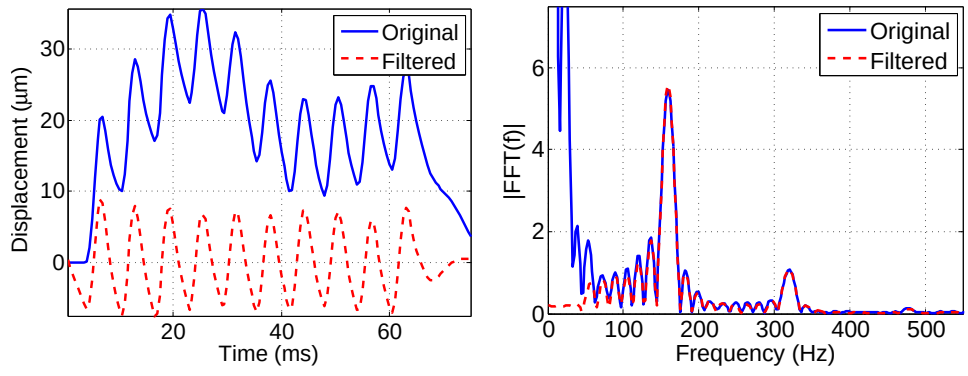

(a) (b)

Figure 4.4: The effect of high-pass filtering on (a) displacement curve and (b) amplitude spectrum when using 160 Hz sine modulation frequency. The data correspond to the experiment no. 7 in Table 4.2.

The average phase shifts between the displacement curves and the ARF were also determined. This was done by determining the corresponding ARF which was simulated using the mechanical properties of the tissue-mimicking phantom in Table 4.1 and the experimental ultrasound parameters in Table 4.2. The magnitude of the phase shift was obtained by comparing the temporal locations of the maximum peak values between the filtered displacement curves and ARF. In the case of square modulation, the middle point of the ARF duty cycle was used as the reference point. Similarly to peak-to-peak displacement, the phase shift in each case was calculated as the mean of eight cycles by ignoring the first and the last cycle of the 10-cycle modulation curve.

The frequency spectra of the displacement curves were calculated using fast Fourier transform (FFT) and the components of the individual spectra were identified. Furthermore, the magnitudes of first, second and third harmonic components were calculated by using discrete Fourier transform (DFT) at each harmonic frequency for displacement curves with different modulation frequencies. In this context the term 'first harmonic' is used to refer to the fundamental frequency, i.e., the ARF modulation frequency.

4.1.5 Simulations

The experimental data were compared with the results from a FEM model (Comsol Multiphysics 4.4, Comsol Inc, Burlington, MA, US). The FEM model was constructed using a 2-D axisymmetric phantom with dimensions 32 mm (lateral) $\times$ 20 mm (axial) with the symmetry axis along the axis of the transducer. A free triangular mesh consisting of 478 domain elements and 58 boundary elements was utilised so that the element size in the centre of the phantom, i.e., the focal point, was smaller (see Figure 4.5(a)). A mesh convergence study was performed to determine the element size. The outer surface of the cylinder phantom was constrained while the two surfaces in the axial direction were unconstrained. This mimicked the real situation in the experiments, where the phantom was attached to its holder from the both sides in lateral direction. The phantom material was modelled as a linear, isotropic and viscoelastic solid using the experimentally measured parameters in Table 4.1 and Poisson's ratio $\nu = 0.499$. The standard linear solid model (Zener) was used for viscoelasticity with the shear relaxation modulus $G = 4.8$ kPa and relaxation time $\tau = 0.35$ ms values listed in Table 4.1.

The simulations of the acoustic fields were conducted in Matlab R2013b (MathWorks Inc, Natick, MA, US) using an open source HIFU simulator (Soneson, 2009).

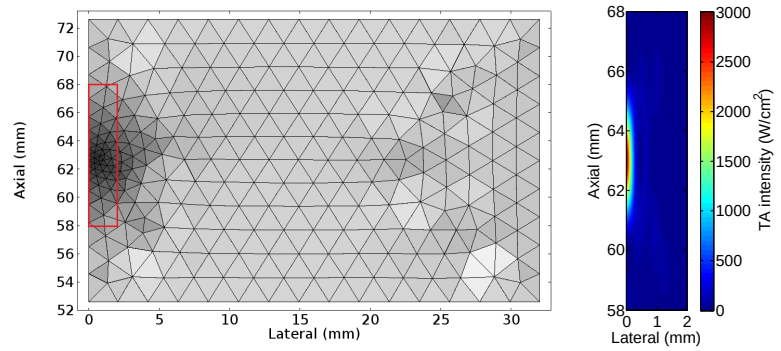

Figure 4.5: Presentation of (a) the computing mesh and (b) the focal area of simulated ultrasound field (red rectangle) used in the FEM model. Darker gray colours represent smaller elements in the mesh. The ultrasound field simulation corresponds to the experiments no. 7 and 11 in Table 4.2.

The ultrasound field was calculated as spatial pressure distribution of a spherical transducer by solving the axisymmetric KZK equation (Zabolotskaya and Khokhlov, 1969; Kuznetsov, 1971) in the frequency domain. The solution takes into account beam diffraction, nonlinear effects, wave reflections at interfaces and frequency dependence of absorption and phase speed dispersion in the medium. The pressure field of the transducer was solved in the axisymmetric spatial domain of the phantom (i.e., half surface) using 1361 mesh points in the axial and 1696 mesh points in the lateral directions (see Figure 4.5(b)). The frequency dependent attenuation of the phantom was taken into account by using the experimentally measured parameters in Table 4.1 and for water typical values at room temperature were employed (Pinkerton, 1949; Marczak, 1997). The pressure fields were solved with 128 harmonic frequency components so that the intensity levels matched with the experimentally measured values in Table 4.2. The corresponding ARF was then calculated using equation (1.1) from 1 for each mesh point taking into account the frequency dependent attenuation.

The simulated ARF mesh was modulated using normalised P^2_{square} or P^2_{sine} and applied as point body loads to the spatial domain of the axisymmetric FEM model. The dynamic response was monitored at the geometric focus of the transducer (62.6 mm). The position of the marker is slightly different from the actual focal point maximum in the phantom (63.2 mm) due to refraction effects. However, this was the case in the experiments as well, where the microsphere was placed in the geometric focus by finding the peak pressure of the focal point in water. The simulated ARF field was modulated using the same modulation frequencies and temporal resolutions as in the experiments.

4.2 Results

The analysis of the acquired displacement data has been divided into two sections: the time and frequency domains. The time domain section includes graphs of time domain displacement curves, average peak-to-peak displacements and phase shifts for different modulation frequencies and ultrasound intensities. The frequency domain section characterises the frequency spectra and the harmonic frequency components of both sine and square AM displacement curves. In addition to the experimental results, the simulated displacement data is presented and compared to the results in its own section. The possible sources of error are discussed in the last section.

4.2.1 Displacement analysis in time domain

The measured displacements were recorded so that all ten modulation cycles were captured. The first 10 ms of the obtained displacement curves with the same ultrasound intensity levels (i.e., the experiments no. 2, 5 and 9) are shown in Figure 4.6 for sine and square AM waveforms as well as the simulated ARF curves in the focal point. All the ARF values shown in the figures are spatial peak values in the phantom. The time axes are scaled so that the arrival of the ultrasound waveform to the phantom (i.e., the onset of ARF) is at 0 ms in all figures.

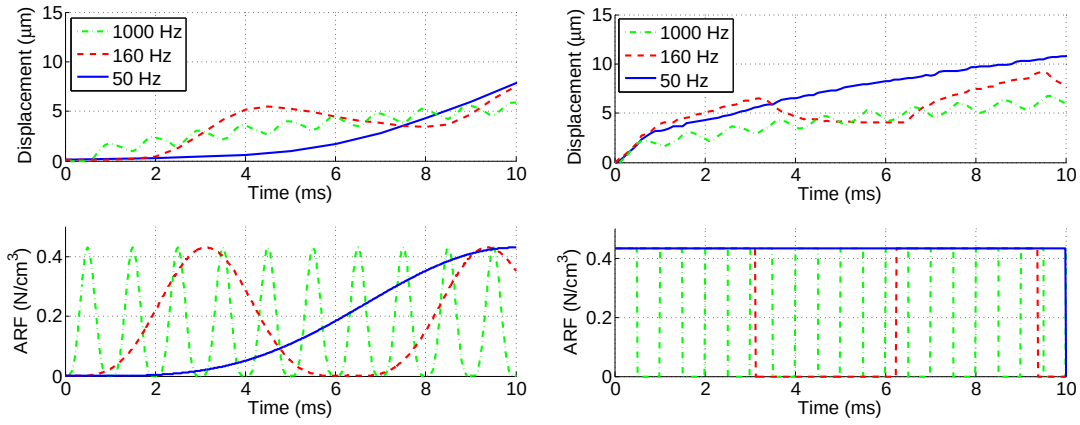

(a) (b)

Figure 4.6: Measured displacements for (a) sine and (b) square amplitude modulated waveforms (top) and the corresponding simulated ARF in the time domain (below). The level of ARF was kept the same and three modulation frequencies of 50, 160 and 100 Hz were used. The first 10 ms seconds are presented in all cases. The data correspond to the experiments no. 2, 5 and 9 in Table 4.2.

The finer details in the square AM displacement curves at 50 and 160 Hz are due to the usage of higher frame rates when capturing the image data. Whilst sine modulated data was captured with approximately 10 to 20-fold sampling frequencies compared to modulation frequencies, a constant frame rate of 10 kHz was used for all square AM data. This resulted in finer detail in square modulated displacements at low modulation frequencies, but does not affect the results of the data analysis.

The mean value of ARF is positive with both square and sine AM, which causes the overall upward trend of the displacement curves. This can be seen clearly in Figures 4.6(a) and (b), where in the case of 1000 Hz excitation, it has an almost linear slope within the 10 ms duration of the harmonic excitation. When lower modulation frequencies and longer time windows are used, the displacement curve eventually reaches its saturation point and starts to decrease again (recall Figure 4.4(a)).

The average peak-to-peak displacements as a function of ARF are presented in Figures 4.7(a) and (b) for sine and square AM waveforms, respectively. In each graph three curves are shown representing the three different modulation frequencies used in the experiments. The peak-to-peak displacement amplitudes were calculated as an average of eight cycles after filtering out the low frequency components in the displacement data. The standard deviation within these eight cycles are also shown in each case.

In Figure 4.7 it can be seen that the peak-to-peak displacement increases with applied ARF. The increase appears linear up to a displacement magnitude of about 10

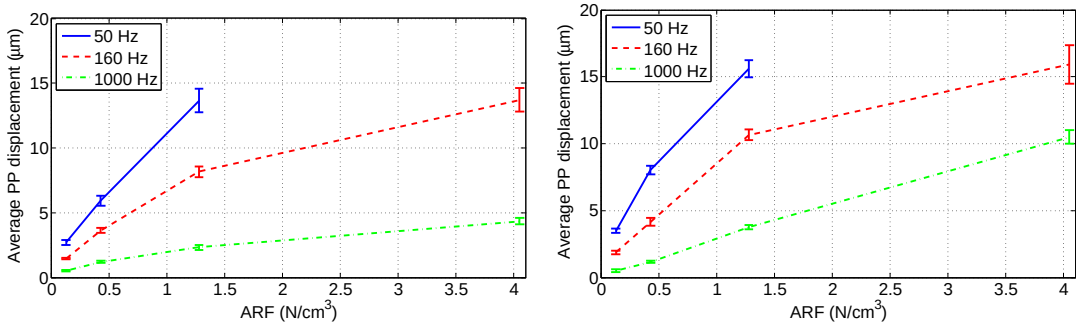

(a) (b)

Figure 4.7: Measured peak-to-peak displacements of (a) sine and (b) square amplitude modulated waveforms as a function of simulated ARF. Four different ultrasound intensity levels with 50, 160 and 1000 Hz modulation frequencies were used. The magnitude of the displacement is calculated as the mean of eight cycles by ignoring the first and the last cycle of the 10-cycle modulation waveform. The data are expressed as standard deviation of the eight cycles and corresponds to the experiments no. 1-11 in Table 4.2.

μm after which the slope decreases. The displacement is higher for lower modulation frequency, which suggests that the medium is stiffer at higher frequencies. This also means the nonlinear effects are more pronounced at low frequencies.

Another observation that can be made from Figure 4.7 is that sine modulated displacement curves have generally lower peak-to-peak amplitude values compared to those of square modulation. On average sine modulated displacement curves had 19.5% lower peak-to-peak amplitude values, while only in experiments no. 8 and 9 were the sine modulated values 6.7% and 2.1% higher compared to square modulation. The minimum average peak-to-peak displacement observed in the results was 0.5 μm, which was achieved using 1000 Hz modulation frequency and 0.13 N/cm^3 ARF using both sine and square modulation.

The viscoelastic behaviour of the phantom material can be seen in Figure 4.6(a), where the sine modulated displacement curve lags behind the applied ARF. A similar phase shift is also observable in the case of square modulation in Figure 4.6(b) when comparing the maximum peak values of the displacement curves to end point of the ARF excitation phase in each cycle.

Figure 4.8 shows the calculated phase shifts for sine and square modulated displacement curves with respect to the applied ARF. Four different levels of ARF are shown with three measurement points corresponding to the different modulation frequencies. The negative angle value indicates the lag in the displacement curve with respect to ARF. The phase shift values were calculated as an average of eight cycles

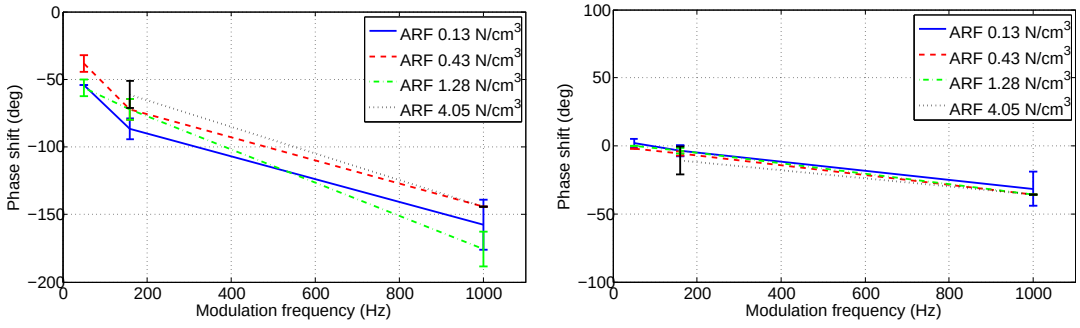

(a) (b)

Figure 4.8: Measured phase shifts relative to ARF for (a) sine and (b) square amplitude modulated waveforms as a function of modulation frequency. Negative values represent the lag in the displacement curve compared to the ARF. Four different ultrasound intensity levels with 50, 160 and 1000 Hz modulation frequencies were used. The phase shift was dependent on frequency but not intensity. The data are expressed as standard deviation of the eight cycles and corresponds to the experiments no. 1-11 in Table 4.2.

by ignoring the first and last excitation cycle, and standard deviations are shown within these cycles. It can be seen that the absolute phase shift becomes larger with increasing modulation frequency, but stays approximately the same with different levels of ARF. While the maximum phase shift for sine modulation is $-175.5°$ at 1000 Hz modulation frequency, the square modulation only reaches $-36.0°$.

4.2.2 Displacement analysis in frequency domain

A comparison of sine and square modulated displacement curves at 160 Hz modulation frequency together with the simulated ARF are presented in Figure 4.9(a). The first 30 ms are presented in the time domain so that the ultrasound excitation is at the beginning of the curves. Due to the shape of the sine modulated ARF waveform, the resulting displacement curve has an initial offset of about 1.5 ms. Both displacement curves reach their overall peak values at around 15 ms after which they start to decrease again. This behaviour causes lower frequency components in the frequency spectrum as seen in Figure 4.9(b). This low frequency vibration occurs at around 25 Hz and was observed in the all experiments. The large peak at low frequencies close to 0 Hz (partly cut out of the graph) is caused by the static component in the displacement curves, which causes the harmonic vibration to stay above the 0 μm rest state through the duration of 10-cycle ARF excitation.

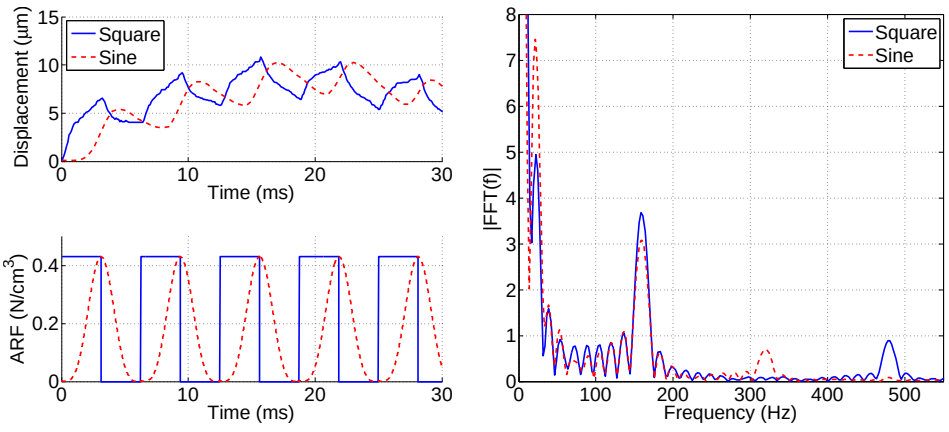

(a) (b)

Figure 4.9: A comparison of 160 Hz square and sine modulated displacement curves (a) in the time domain (above) together with the corresponding simulated ARF calculations (below) and (b) the frequency spectrum of the both displacement curves. The first 30 ms are presented in the time domain, but the frequency spectrum was calculated based on the full length of the displacement curves. The data correspond to the experiment no. 5 in Table 4.2.

The individual frequency components $1f_{\mathrm{AM}}$, $2f_{\mathrm{AM}}$ and $3f_{\mathrm{AM}}$ of displacement curves are presented in Figure 4.10 for 50, 160 and 1000 Hz modulation frequencies used in the experiments no. 3, 6 and 10, respectively. Harmonic component $1f_{\mathrm{AM}}$ corresponds to the fundamental modulation frequency. The magnitude of the fundamental component is larger for square modulated displacement curves in all three modulation frequencies. On average, the magnitude of the square modulated fundamental was 14.9% higher compared to sine modulation.

However, the situation changes when looking at the higher harmonic frequencies. In Figure 4.9(b) it can be seen that the second harmonic component at 320 Hz has almost completely vanished for square modulation, but is still visible in the case of sine modulation. This can also be observed in Figure 4.10(b), where the second harmonic component is at the noise level for square AM and significantly larger for sine AM. The same also applies to the 50 Hz modulation frequency in Figure 4.10(a), which shows no existence of a second harmonic frequency. Only in the case of 1000 Hz modulation in Figure 4.10(c) there seems to be a larger second harmonic component in the case of square modulation, but this is because the overall energy level at these high frequencies is already so low that the spectral noise contributes to the magnitude of these frequencies.

An opposite situation is observed in the case of $3f_{\mathrm{AM}}$, which is evident for square modulated displacement curves, but contains only a small amount of energy in the case of sine modulation. The effect is most pronounced at 50 and 160 Hz, but at 1000 Hz the energy contribution to third harmonic frequencies is due to the noise.

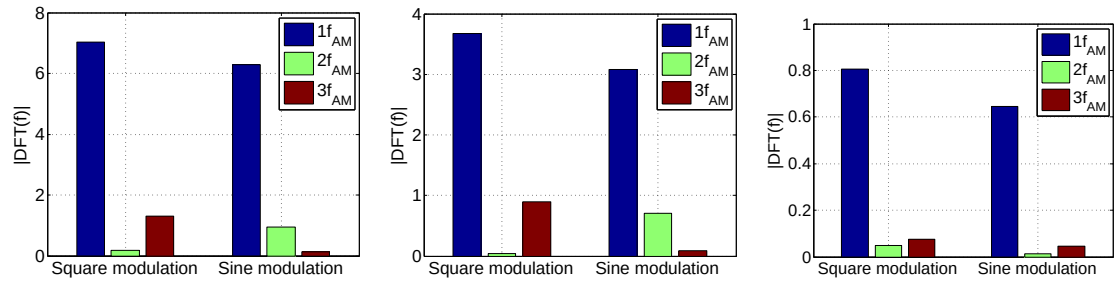

Figure 4.10: A comparison of the harmonic components of sine and square amplitude modulated waveforms when using (a) 50, (b) 160 and (c) 1000 Hz modulation frequency. The data correspond to the experiments no. 3, 6 and 10 in Table 4.2.

4.2.3 Simulations

The simulated displacement curves together with the experimental data for 50, 160 and 1000 Hz sine AM are shown in Figures 4.11(a)-(c), respectively. All ten ARF excitation cycles are shown for each modulation frequency, and the data are presented in absolute displacement values so that a quantitative comparison of the FEM model and the experiments can be carried out.

Figure 4.11(a) shows the simulated and measured displacement curves for 50 Hz sine AM. The simulation captures the dynamics that were observed experimentally. There is up to 5 μm discrepancy in the peak amplitude, but the simulation successfully reproduces the deeper relaxations of the measured curves at 40, 80, 120 and 160 ms which are associated with the low frequency baseline drift at around 25 Hz. Similarly,

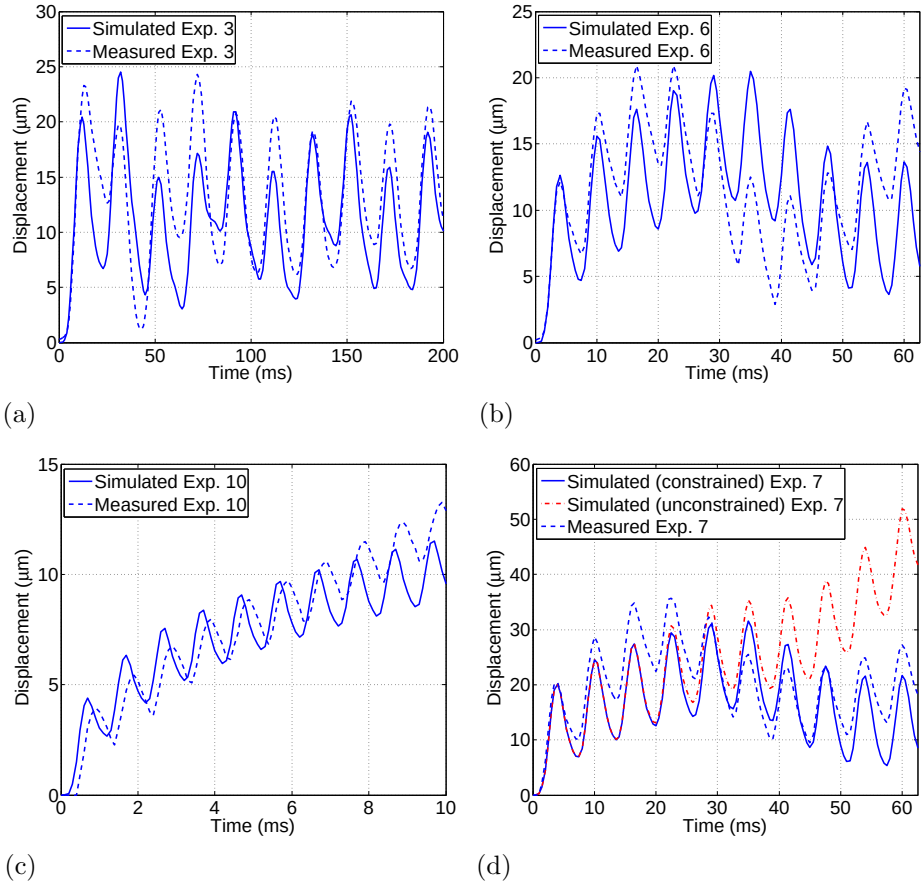

Figure 4.11: Simulated displacement curves compared with the experimental data for (a) 50 Hz, (b) 160 Hz and (c) 1000 Hz sine amplitude modulation. The effect of constrained vs. unconstrained boundary condition is shown in (d) together with the experimental data. The data correspond to the experiments no. 3, 6, 10 and 7 in Table 4.2, respectively.

the baseline drift is clearly visible in Figure 4.11(b) which shows the data for 160 Hz sine modulation. The experimental data shows higher peak values during the first four cycles, but the low frequency baseline drift relaxes faster, and thus, ends up to lower values at around 40 ms. In both cases, the peak-to-peak amplitudes of the simulation data are slightly higher compared to the measured values.

Figure 4.11(c) shows the data for 1000 Hz sine AM. The peak-to-peak displacement amplitudes of the simulation are similar to those of the experimental data, but the overall peak value after ten ARF cycles is slightly lower. Furthermore, a small phase shift of exists between the simulated and measured curves, whilst the peaks of the simulated data occur earlier. This is due to a delay in response of the phantom at the onset of ARF in the experiments, which causes 0.4 ms delay in the beginning of the displacement curve. A similar small delay was also observed in the case of 50 and 160 Hz sine modulation, but the phase shift is not clearly visible due to the longer period of the ARF cycles.

The effect of constrained boundary condition is demonstrated in Figure 4.11(d), which shows the simulated constrained and unconstrained displacement curves together with the corresponding experimental data with 160 Hz sine modulation. The unconstrained curve continues towards higher peak values whilst the constrained curve starts decreasing after four ARF cycles similarly to the experimental data, which causes the system to resonate at around 25 Hz.

Figure 4.12(a) shows the simulated displacement curves together with the corresponding experimental data with three different ultrasound intensity levels using sine AM at 1000 Hz. The simulated data achieves higher peak values at low intensity levels, but falls behind when the intensity of the ultrasound field is increased. Furthermore, the experimental data seems to grow slightly faster within ten ARF cycles, whilst the growth of the simulated data is slower causing it to achieve lower peak amplitude in the end. The delay at the onset of ARF is also visible in the experimental data and is smaller when using higher intensity levels. For the three different ultrasound intensities of 1209, 2038 and 3013 W/cm^2, respective delays of 0.5, 0.4 and 0.3 ms are induced in the beginning of the displacement curve.

Figure 4.12(b) is shows a 2-D deformation of the phantom mesh during the first ARF cycle using 1000 Hz sine modulation. The white arrows represent the direction of the displacement at 0.5 and 1.0 ms during the ARF excitation cycle and the colour map shows the normalised magnitude of the displacement. At 0.5 ms, the magnitude of the ARF is the highest and the material in front of the focal point is moved towards the ultrasound focal point both in axial and lateral directions. Simultaneously, due

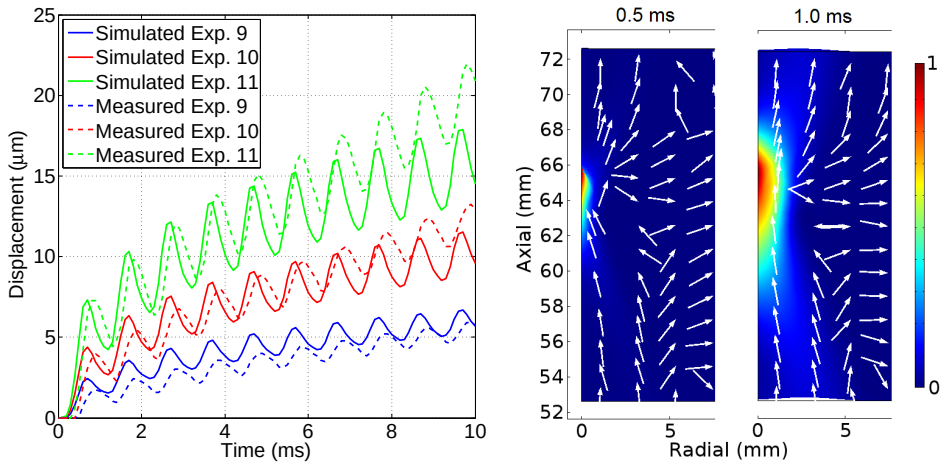

(a) (b)

Figure 4.12: Simulated displacement curves for (a) three different intensity levels with 1000 Hz sine amplitude modulation and (b) 2-D presentation of the phantom deformation field during the first cycle of the excitation. The white arrows represent the direction of deformation and the colour map shows the normalised magnitude of the displacement. The data correspond to the experiments no. 9-11 in Table 4.2 in (a) and the experiment no. 11 in (b).

to incompressibility, the material beyond the focal point is pushed away from the focal point towards the edge of the phantom causing it to deform. After a full ARF cycle at 1.0 ms, the material in the focal area has moved in the axial direction whilst the front and rear edge of the phantom have slightly deformed. This deformation causes the upward trend of the displacement curves and the static component in the frequency spectrum.

4.2.4 Error estimation

The main sources of experimental error were due to the registration of the optical and acoustic focal points and the alignment of the microsphere in the FOV of the objective. The determination of the acoustic focal point in lateral and elevation directions was possible within the diameter of the active element of the hydrophone ± 75 μm, which was accurate compared to the full width at half maximum (FWHM) of the transducer focal point. In the axial direction the accuracy was determined by the step size of the positioning system ± 1 μm.

The minimum distance between ultrasound focal point and the phantom edge was 3.3 mm which was due to the working distance of the objective. Bouchard et al. (2009a) reported the effect of shear wave reflection on the displacement curves from

the phantom edge using single excitation pulses. Similar phenomenon was observed in the experiments reported here, when a single excitation pulse was used resulting in a small peak of approximately 1 μm after the main excitation (less than 5% of the main peak). However, when harmonic excitation pulses were used, the shear wave reflection was not visible in the displacement curves. Furthermore, no differences in the displacement curves were observed when comparing the simulations with finite and infinite domains.

The first main source of error arose from the alignment of the transducer and objective focal points. First of all, the physical tip diameter of the hydrophone was 300 μm, which was approximately four times larger than the FOV of the objective (80 μm). This affected the alignment accuracy in the lateral direction, because the tip of the needle hydrophone could not completely fit in the lateral FOV of the objective. Secondly, the alignment in the elevation direction was determined by finding the visually sharpest point of the needle hydrophone tip. This could result in a maximum alignment offset of $\pm$110 μm, which is still within the FWHM of the acoustic focal point. The alignment accuracy in the axial direction was approximately $\pm$10 μm based on the accuracy of which the tip of the hydrophone could be positioned in the middle of the FOV.

The second source of error was a result of positioning the phantom in the optical focal point of the objective. Although the magnification of the objective was considerably higher than used in the earlier optical tracking studies (Bouchard et al., 2009a,b; Czernuszewicz et al., 2013), positioning the microsphere in the elevation direction could only be done by finding the visually sharpest point in the image. However, taking into account the small size of the microsphere (10.23 μm), this error is significantly smaller than what resulted from the registration of optical and acoustic focal points.

The shift of the maximum ARF in axial direction due to refraction effects in the phantom was estimated with nonlinear ultrasound simulations. The optical focal point of the objective was set at the maximum peak-positive pressure. The peak-positive pressure shift was found to be approximately 0.6 mm in axial direction away from the transducer focus. However, the location of the peak-positive pressure is slightly different from that of the peak intensity value and hence the maximum ARF. In simulations, the peak intensity was found to occur 0.2 mm before the peak-positive pressure, and therefore, combining these two effects result in 0.4 mm shift of the maximum ARF from the optical focal point in axial direction. The total focal shift is less than 9% of the FWHM pressure of the focal point along the same axis (4.5 mm).

The analysis of the image data could also result in errors at a sub-micrometre scale. The correlation coefficient value drops during the excitation phase, which affects the registration accuracy of the two subsequent image frames. The correlation coefficient values were typically high over 0.8, but in the case of high modulation frequencies, the accuracy might drop slightly due to the exposure time of the high-speed camera sensor. This error could be reduced using higher frame rates with a more powerful light source.

The accuracy of the simulation model to mimic the dynamics of the experiments is affected by several factors. The first source of simulation error comes from the location of the ultrasound focal point with respect to the marker. As stated earlier, the location of the microsphere in lateral and elevation directions is subject to a small misalignment in the experiment, whereas in the simulation the marker is placed exactly in the centre of the geometric focal point. The second source of error arises from determining the mechanical parameters of the phantom material. Whilst attenuation, density, speed of sound and Young's modulus values could be accurately measured, the choice of viscoelastic model and its parameters might not fully replicate the real dynamics of the medium. For example, the choice of Poisson's ratio has been shown to have an effect on the axial displacement amplitude (Palmeri et al., 2005). Adjusting material properties to improve agreement was not employed here.

The third source of error is related to the simulation of the nonlinear ultrasound field. Although the intensity of the ultrasound field could be accurately matched with the experimentally measured values, the size of the simulated focal point was observed to be slightly smaller. Smaller focal point, and consequently smaller displacement volume, has been shown to lead to shorter relaxation time of the material (Czernuszewicz et al., 2013). Finally, the phantom geometry in the FEM model was chosen to be axisymmetric cylinder due to the reduced computational time, which does not affect the displacement estimation accuracy in micrometre scale, but could have an effect if larger deformations are induced.

4.3 Discussion

Characterisation of harmonic displacements using different levels of ARF, AM waveforms and modulation frequencies was conducted in a tissue-mimicking phantom. The shapes of the harmonic displacement curves in the time domain correspond to the optically measured harmonic excitations by Bouchard et al. (2009b). Although they did not characterise the displacement amplitudes with respect to ARF, the magnitudes of the peak-to-peak displacements at the modulation frequency of 100 Hz are of the same order of magnitude at around 15 μm. Curiel et al. (2009) measured the average harmonic displacement amplitudes in *in vivo* rabbit muscle. Given the parameters of their experiments and assuming the mean sound speed in soft tissue (1540 m/s), the levels of ARF varied between 0.14 and 0.29 N/cm^3 resulting in average displacement amplitudes of 19-43 μm using 75 Hz modulation frequency. However, the harmonic amplitude measurements were performed during HIFU ablation, and hence, cannot be related to a specific stiffness value of the tissue (Sapin-de Brosses et al., 2010; Benech and Negreira, 2010). Furthermore, ARF is dependent on the attenuation of the tissue, which changes considerably during ablation (Jackson et al., 2014).

One of the observations in the measurement results was that larger peak-to-peak displacement amplitudes were achieved using square modulation: on average sine modulated displacements curves had 19.5% lower peak-to-peak amplitude values compared to square modulation. This is because the time average ARF of sine AM waveform within one cycle is 25% lower than that of square modulation, which results in smaller energy deposition with time. Furthermore, the instantaneous rise of ARF during the first half of the excitation cycle in square modulation causes greater displacement amplitude at the beginning. During the second half ARF is completely turned off, which results in a steeper slope of the displacement curve and consequently lower values.

The average peak-to-peak displacements were found to increase with simulated ARF. The dependence was approximately linear up to 10 μm after which the slope decreased slightly. This is consistent with Zaitsev et al. (2004) who studied how different acoustic output power affected the displacement amplitude in a silicone phantom using 10 ms ultrasound bursts and found the dependence to be approximately linear. However, this dependence is affected by the viscoelastic properties of the material and the nonlinearity of the ultrasound field.

The dependence of the displacement amplitude on modulation frequency was observed to be nonlinear. Similar results were also shown in experiments by Curiel et al.

(2009) and later in simulations by Heikkila et al. (2010), who examined how different modulation frequencies affect normalised harmonic displacement amplitudes. In both studies, the harmonic displacement amplitude was found to decrease with modulation frequency, whilst largest displacement amplitudes were achieved using low modulation frequencies. Although this relation has been a decreasing power fit in the previous cases, the shape of this nonlinear dependence is related to the frequency response of the material (Liu and Ebbini, 2007).

Another property which was observed to change with modulation frequency was the phase shift between the displacement curves and the applied ARF. For both sine and square modulation, the absolute phase shift was shown to increase with the modulation frequency. However, the magnitude of the phase shifts was not found to vary with different levels of ARF when the modulation frequency was kept constant. Similar phase shifts were also observed in experiments by Maleke et al. (2006), who generated harmonic sine AM displacements in gelatin phantoms. They found the magnitudes of the phase shifts to decrease with increasing phantom stiffness using a constant modulation frequency of 50 Hz. Bouchard et al. (2009b) used optical tracking method to measure the phase shifts in a gelatin phantom. They used sine AM waveforms with modulation frequencies from 50 to 300 Hz and found the absolute phase shifts to increase within this range.

The phase shifts occur due to the viscoelastic properties of the medium, and therefore, are dependent on the phase response of the material (Liu and Ebbini, 2007; Vappou et al., 2009). If the material was completely elastic, it would behave as a linear spring where all the deposited energy in the excitation phase would be deposited in storage modulus and released in phase with the ARF. However, because the tissue-mimicking phantom used in the experiments is viscoelastic material, part of the energy is lost to viscosity. Therefore, when a periodic force is applied to a material which is not perfectly elastic, the strain is not in phase with the force.

In all cases, a static offset of displacement was observed with time. The static component of the displacement curve was also observed in the phantom experiments conducted by Curiel and Hynynen (2011). They used 75 Hz modulation frequency to transmit five cycles of harmonic ultrasound pulses to three different locations in a phantom and rabbit thigh. The frequency spectrum analysis of the obtained displacement curves showed a strong static component at 0 Hz, but the time window used was not long enough to capture the baseline drift. The low frequency baseline drift was observed in simulations by Konofagou and Hynynen (2003) and Heikkila et al. (2010), who postulated them to be due to non-zero mean of the ARF. The non-zero

mean could explain the existence of the static component, but in addition to the static offset a low frequency oscillation at around 25 Hz was observed for long enough time windows. This is more likely related to the resonant frequency of the medium and its surroundings. This behaviour became evident in the simulation model, where the constrained outer surface of the phantom caused a low frequency baseline drift to the displacement curves. Therefore, the baseline drift in the experimental data is caused by fixing the phantom to its holder from the both ends in the lateral direction.

The characterisation of harmonic frequencies showed differences between sine and square modulated displacement curves. The magnitude of the fundamental component $1f_{\mathrm{AM}}$ was found to be consistently greater for square modulation, which was a direct result of larger average peak-to-peak displacement amplitudes. Another difference was found in the ratio between the components at $2f_{\mathrm{AM}}$ and $3f_{\mathrm{AM}}$. Where square modulated displacement curves had barely no energy at $2f_{\mathrm{AM}}$, sine modulation showed a detectable peak in the frequency spectrum. In contrast, the magnitude of $3f_{\mathrm{AM}}$ was noticeably larger for square modulation as opposed to sine modulation. The explanation for the absence of a second harmonic component in the case of square modulation is in the fundamental property of the Fourier expansion of a square wave, which contains only components of odd-integer harmonic frequencies. In a theoretical situation the magnitude of odd-integer harmonic frequencies would be zero, but in real world situation some energy still remains.

The simulation model successfully replicated the dynamics of the experimental data including some of the lower frequency oscillations. The small delays in the beginning of the displacement curves using sine AM were due to the behaviour of ARF according to equation (4.2) where ARF is modulated using normalised P^2_{sine}. This causes the ARF to increase slowly in the beginning causing smaller slope. The overall peak amplitudes of the simulations were up to 5 μm lower compared to the measured values, whereas the peak-to-peak amplitudes showed slightly larger values. This is most likely due to the chosen viscoelastic model and its parameters, which could not completely mimic the relaxation process of the medium with different modulation frequencies. For example, the peak-to-peak displacement amplitudes were higher in the simulations at 160 Hz compared to the experimental data, whilst at 1000 Hz the amplitudes were approximately the same, which suggest that the chosen parameters were better suited for high frequencies. Therefore, a more generalised viscoelastic model which takes into account multiple relaxation times, such as Maxwell-Wiechert model, could be more precise in predicting the relaxation process of the medium when

different modulation frequencies are used. However, this requires accurate determination of the parameters for the viscoelastic model, which was outside the scope of this study.

4.4 Conclusions

No previous work on characterisation of displacement amplitudes and phase shifts with respect to ARF has been reported. Although previous reports have shown single pulse displacement amplitudes with respect to ultrasound field intensity, the frequency dependent attenuation properties of tissue are significant when nonlinear ultrasound fields are used. Here it is shown that measured displacements are in quantitative agreement with simulated displacements when the tissue properties and ultrasound fields are known. This is useful in diagnostic applications such as ARFI imaging and HMI.

Comparison of square and sine amplitude modulation is useful in determining suitable modulation waveforms for diagnostic applications, such as HMI and EMA, at the frequency appropriate for the given modality. The characterisation of frequency components of different amplitude modulation waveforms is useful in diagnostic applications, such as EMA imaging, which rely on quantifying the frequency spectrum components. The comparison of square and sine modulation frequency components helps to define suitable waveforms to achieve maximum fundamental frequency component with minimum harmonic frequency components.

Optical tracking of harmonic displacements in a tissue-mimicking phantoms was successfully conducted. The square modulated ARF waveforms yielded higher average peak-to-peak amplitude values when compared to sine modulation. Furthermore, the displacement amplitudes showed increasing linear dependence on ARF up to about 10 μm after which the slope decreased with both sine and square modulation. Phase shifts between the ARF and AM displacement curves were also observed. The magnitude of the phase shift was approximately independent of ARF but increased with the modulation frequency in both cases.

In the frequency domain, energy was observed at the fundamental modulation frequency, its harmonics and close to 0 Hz. The magnitude of the fundamental modulation frequency was consistently higher in the case of square modulation, whereas the ratio between the second and third harmonic components differed as opposed to sine modulation. The second harmonic was almost non-existent in the case of square modulation, but energy was found in the third harmonic. An opposite situation was

observed in the case of sine modulation, where a stronger second harmonic and a very low energy third harmonic were detected. Lower frequency component occured due to a net force in waveform and resonance in the setup.

An advance over other studies is that a quantitative comparison of simulated and measured displacements was conducted. The simulation results were found to follow the dynamics of the experimental data, but small differences were seen in absolute peak and peak-to-peak displacement amplitudes. This was most likely due to the chosen viscoelastic model, which was unable to account for multiple modulation frequencies. A choice of more general viscoelastic model might be able to predict the dynamics more accurately when different modulation frequencies are used.

These results show that FEM models can quantitatively capture ARF induced displacements over a range of amplitudes and modulation frequencies. This provides a numerical tool to determine ultrasound intensity levels, AM waveforms and modulation frequencies in diagnostic applications, which are based on generating and tracking harmonic displacements in tissue.

Chapter 5

Temperature dependence of acoustic radiation force induced displacements

The work reported in this chapter[1] expands the study on ARF induced displacements of the previous chapter by incorporating the temperature dependence of tissue properties. The temperature dependence of the deformation is affected by the changes in the sound speed, attenuation and elasticity according to the equations (1.1) and (1.2) from Chapter 1:

$$F_V = \frac{2\alpha_{\text{abs}} I_{\text{TA}}}{c}$$
$$\rho \frac{\partial^2 u_i}{\partial t^2} = \frac{\partial \sigma_{ij}}{\partial x_j} + F_{Vi}$$

Therefore, extracting temperature from measured deformation is challenging. Ultrasound can be used to provide temperature information, but this has been found to be accurate only at hyperthermic temperatures below 50 °C (Lewis et al., 2015).

One tissue property that has been shown to change significantly and irreversibly after thermal ablation is tissue stiffness (Wu et al., 2001; Sapin-de Brosses et al., 2010). The increase in stiffness has been shown to be reversible at temperatures below 60 °C (Wu et al., 2001), and irreversible once temperatures exceed 60 °C due to collagen denaturation (Wu et al., 2001; Lepetit et al., 2000). A detailed review of temperature dependent tissue properties was given in Chapter 2. This suggests that measurements of stiffness can be used to distinguish thermally ablated tissue (Varghese et al., 2002, 2003).

[1]The contents of this chapter have been published in Suomi et al. (2016a). The experimental HMI measurements in this chapter were carried out at Ultrasound Elasticity Imaging Laboratory at Columbia University.

As alluded to in Chapter 2, although the elastic moduli have been reported to change with temperature, there is little data on the changes in the viscoelastic properties. In this chapter, the temperature dependence of viscoelastic properties in *ex vivo* liver is experimentally measured and both conventional and fractional Zener model parameters are fit to the data. Furthermore, HMI is used to monitor HIFU thermal ablation in *ex vivo* liver to acquire real-time displacement data during ablation. In the final part, ARFI displacements are modelled by viscoelastic FEM simulations using the previously quantified temperature dependent acoustic and viscoelastic parameters.

5.1 Materials and methods

5.1.1 Measurement of dynamic modulus

The temperature dependent dynamic modulus of liver was measured using DMA (Q800, TA Instruments, New Castle, DE, USA) in a frequency range from 0.1 to 200 Hz. An oscillation amplitude of 15 μm and a static force of 0.05 N were used in every measurement. A total of 5 samples were cut from freshly obtained (within 48 hours of slaughter) bovine liver. Each sample was cut to a rectangle shape with a size of approximately 20 mm $\times$ 20 mm $\times$ 10 mm and placed in a submersion sample holder which was filled with 0.96%-wt. phosphate buffered saline solution (Sigma-Aldrich, St Louis, MO, USA) so that the liquid level was flush with the sample. Neither the saline solution nor the liver samples were degassed in the DMA measurements. A thermocouple was placed in the saline solution so that the temperature of the liver could be monitored in real-time throughout the measurement in the enclosed measurement chamber of the DMA system. A compression clamp was used in all the dynamic modulus measurements.

The dynamic modulus measurement was conducted by first performing a frequency sweep from 0.1 to 200 Hz at room temperature 21 $\pm$ 1 °C. The temperature of the chamber was then heated using the built-in heating system of the DMA to 35 $\pm$ 1 °C and kept isothermal for 5 minutes to stabilise the temperature of the liver sample. Once the temperature of the liver sample had stabilized, the frequency sweep was performed again. This process was then repeated by increasing the temperature of the sample by 15 °C steps until the final temperature of 80 $\pm$ 1 °C was reached. The whole measurement process was repeated for 5 different liver samples from different locations of the same liver.

5.1.2 Fitting dynamic modulus to fractional Zener model

The conventional Zener model of viscoelasticity consists of an elastic (spring) and viscous (damper) elements in series both of which are also parallel with another elastic element (recall Figure 3.3 in Chapter 3). In the fractional Zener model, the integer-order time variables of stress and strain are replaced with fractional order variables, which allows for more complex responses to be modelled.

In the frequency domain, the dynamic modulus is defined by the equation:

$$M^*(\omega) = M_\mathrm{S}(\omega) + \mathrm{i}M_\mathrm{L}(\omega) \tag{5.1}$$

where M_S [Pa] is the storage modulus, M_L [Pa] is the loss modulus, ω [rad/s] is the angular frequency and i is the imaginary unit. In the Zener model, the storage and loss moduli are defined in terms of a relaxation time τ [s], the spring constant M_0 [Pa] and the high-frequency limit of the storage modulus M_∞ [Pa] by the equations (Kohandel et al., 2005):

$$M_\mathrm{S}(\omega) = M_0 \frac{1 + (d_M + 1)\cos(\alpha_\mathrm{Z}\pi/2)\omega_\mathrm{n}^{\alpha_\mathrm{Z}} + d_M\omega_\mathrm{n}^{2\alpha_\mathrm{Z}}}{1 + 2\cos(\alpha_\mathrm{Z}\pi/2)\omega_\mathrm{n}^{\alpha_\mathrm{Z}} + \omega_\mathrm{n}^{2\alpha_\mathrm{Z}}} \tag{5.2}$$

$$M_\mathrm{L}(\omega) = M_0 \frac{(d_M - 1)\sin(\alpha_\mathrm{Z}\pi/2)\omega_\mathrm{n}^{\alpha_\mathrm{Z}}}{1 + 2\cos(\alpha_\mathrm{Z}\pi/2)\omega_\mathrm{n}^{\alpha_\mathrm{Z}} + \omega_\mathrm{n}^{2\alpha_\mathrm{Z}}} \tag{5.3}$$

where $d_M = M_\infty/M_0$, $\omega_\mathrm{n} = \omega\tau$ [rad] is the normalised frequency, $\alpha_\mathrm{Z} = 1$ for the conventional Zener model and $0 \leq \alpha_\mathrm{Z} \leq 1$ for the fractional Zener model.

The Zener model's spring constants E_1 and E_2 can be defined in terms of M_0 and M_∞ by using the time domain presentation of elastic modulus (recall equation (3.38) from Chapter 3):

$$\begin{aligned} M_0 = E(t=\infty) = E_1 \quad &\Longleftrightarrow \quad E_1 = M_0 \\ M_\infty = E(t=0) = E_1 + E_2 \quad &\Longleftrightarrow \quad E_2 = M_\infty - M_0 \end{aligned}$$

Note that the high frequency limit of dynamic modulus M_∞ is $E(t=0)$ in the time domain presentation of elastic modulus due to the inverse relationship between time and frequency.

Both conventional and fractional Zener models were used to derive temperature dependent viscoelastic parameters from the experimentally measured dynamic modulus data. The magnitude of the modulus was then averaged over the five samples resulting in one frequency dependent magnitude curve at each measurement temperature. Both the conventional and fractional models were then fit to the measured modulus amplitude using a nonlinear least squares method.

5.1.3 Thermal ablation monitoring using harmonic motion imaging

The HMI system shown in Figure 5.1 was used to acquire real-time displacement data during thermal ablation in *ex vivo* canine liver. The HMI system was comprised of a 4.755 MHz HIFU transducer (Riverside Research Institute, New York, NY, USA) together with a 7.5 MHz circular single-element pulse-echo transducer (Olympus NDT Inc., Waltham, MA, USA) in the middle. The HIFU transducer was used for ablation as well as to generate ARF for tissue displacements, while the inner transducer was used to simultaneously acquire pulse-echo data for displacement tracking. The HIFU transducer had a focal length of 90 mm, an outer diameter of 80 mm and an inner diameter of 16.5 mm (i.e., the diameter of the single-element transducer) and the two transducer were axially aligned.

A function generator (33522A, Agilent Technologies Inc., Santa Clara, CA, USA) was used to generate a 4.755 MHz signal amplitude-modulated at 50 Hz, which was then amplified (3100L, E&I, Rochester, NY, USA) for the HIFU transducer. The single-element transducer was operated by a pulser-receiver (5072PR, Olympus, Waltham, MA, USA) with a pulse repetition frequency of 1000 Hz. The received echo signals were transmitted through an analog band-pass filter (Reactel Inc., Gaithersburg, MD, USA), with cut-off frequencies $f_{c1} = 5.84$ MHz and $f_{c2} = 8.66$ MHz in order to attenuate HIFU signals, and recorded for data analysis using a high-speed digitiser (Gage Applied, Lockport, IL, USA) with a sampling frequency of 100 MHz.

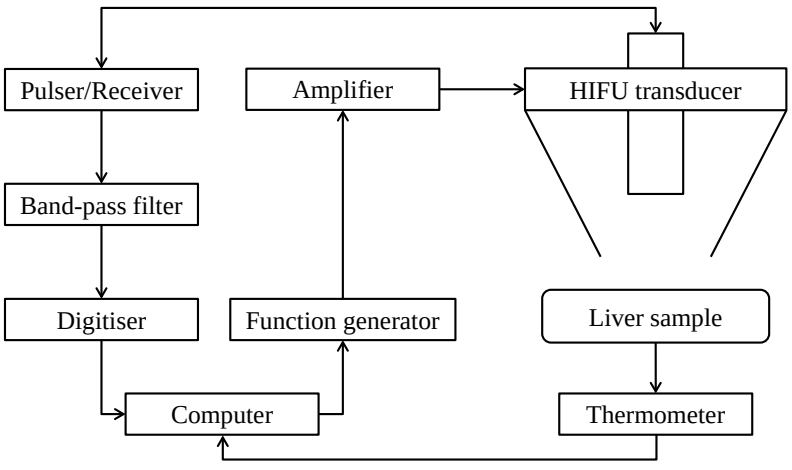

Figure 5.1: Experimental set-up used to acquire displacement data during thermal ablation using HMI. Thermocouple was placed in the liver sample to record temperature data during sonications.

During the experiments, the liver sample with a size of approximately 6 cm × 6 cm × 3 cm was placed in a degassed saline solution water bath in room temperature. The temperature acquisition during HIFU thermal ablation was conducted using a thermocouple placed in the middle of the liver sample. The focal point of the HIFU transducer was aligned with the thermocouple by performing raster scans in both axial and lateral planes. The HIFU transducer was moved using a step size of 0.2 mm and at each location of the raster grid a short duration sonication (less than 2 seconds) was performed. The temperature rise due to the short duration sonication was then recorded using a thermometer (HH506RA, Omega Engineering Inc., Stamford, CT, USA) and the raster scans were continued in both planes until the location of the maximum temperature rise was found.

The experimental protocol consisted of multiple sonications in different locations of the liver sample. After the location of the thermocouple was properly aligned with the ultrasound focal point by raster scanning, a 60-second sonication with 7.5 MPa peak-positive pressure was performed using 50 Hz amplitude-modulation. Simultaneously, the temperature in the focal point was recorded throughout the whole duration of the sonication and both the displacement and temperature data were saved for data analysis. Once the sonication had finished, the thermocouple was moved to another location so that the lesion created by the previous sonication would not interfere and the whole process was repeated. In post-processing, the acquired peak-to-peak displacement data was normalised to 37 °C and averaged over 25 samples to suppress the high-frequency noise in the data. A total of seven sonications were performed of which four sets exhibited cavitation. This lead to unreliable estimate of the displacement as the cross-correlation algorithm for the pulse-echo signals was not able to perform. Therefore data on three sonications that did not exhibit detectable cavitation is reported here.

5.1.4 Thermal ablation simulation model using acoustic radiation force impulse

The simulations for viscoelastic behaviour of liver during HIFU therapy were conducted using ARFI rather than HMI. This was done in order to get rid off the shear wave reflections from the lesion boundary, which would otherwise cause disturbances in the displacement amplitudes. The pulse lengths used in ARFI were short enough so that the shear wave reflections from the lesion boundary could be excluded from the measurement window.

The ARFI simulations were conducted in two parts for each temperature step. First, acoustic simulations were conducted to solve the nonlinear ultrasound fields in tissue, from which the temperature field was determined using the BHT equation (3.12), and subsequently the size of the lesion. The development of lesion length and diameter during HIFU therapy was estimated using 240 $\mathrm{CEM}_{43^\circ\mathrm{C}}$ thermal dose fields from the equation (3.17), which was updated to the FEM model at each temperature step. Once these values were obtained, the ultrasound intensity field was converted into ARF field according to the equation (1.1) and the force field was then applied to the viscoelastic domain in the FEM model and the tissue deformation was calculated. This iteration was repeated at every temperature step from 35 to 70 °C at 5 °C intervals by updating the attenuation, viscoelasticity and lesion size values at each step. This allowed for the evolution of acoustic and viscoelastic parameters and lesion size on tissue deformation to be determined.

The simulations of the acoustic fields were conducted in Matlab R2015b (MathWorks Inc, Natick, MA, USA) using a modified version of a HIFU simulator (Soneson, 2009), which solves the axisymmetric KZK equation (Zabolotskaya and Khokhlov, 1969; Kuznetsov, 1971) in the frequency domain using 128 harmonics. The original code was modified to handle multiple tissue layers so that the geometry of the simulations corresponded to a real therapeutic situation, where the pathway from

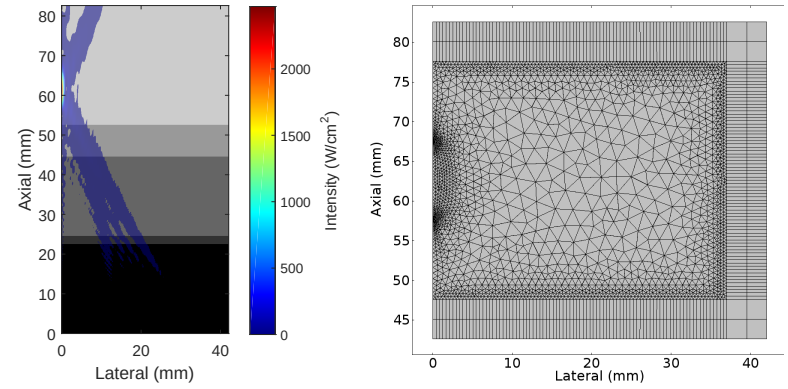

Figure 5.2: (a) 2-D axisymmetric acoustic simulation geometry together with the simulated ultrasound intensity field thresholded at −30 dB. The different levels of gray from black to light correspond to layers of water, skin, fat, muscle and liver respectively. (b) 2-D axisymmetric computation mesh used in the FEM model in liver: rectangular elements were used in the infinite element domains and free triangular elements elsewhere.

Table 5.1: Acoustic simulation parameters for different tissue types at 35 °C. (*) The attenuation of liver was updated at each temperature step according to the fourth order polynomial dependence.

	Density (kg/m^3)	Sound speed (m/s)	Attenuation ($dB/MHz^n/cm$)	n	B/A
Water	1000	1482	0.00217	2.00	5.0
Skin	1090	1615	0.35	1.55	7.9
Fat	950	1478	0.48	1.20	10.0
Muscle	1050	1547	1.09	1.10	7.4
Liver*	1060	1584	0.35	1.00	7.2

transducer to liver goes through the layers of water, skin, fat and muscle. The acoustic simulation geometry is presented in Figure 5.2(a). Typical values for density, sound speed, attenuation and B/A were used for each tissue type (see Table 5.1), while the polynomial fit to the temperature dependent attenuation of the liver (see Table 2.2 in Chapter 2) was updated at each temperature step. The ultrasound field was calculated as spatial pressure distribution of a HIFU transducer (outer diameter = 6.4 cm, inner diameter = 2.0 cm, focal length = 6.26 cm, frequency = 1.1 MHz). The pressure field of the transducer was solved in the axisymmetric geometry (i.e., half domain) using 2019 grid points in the axial and 672 grid points in the lateral directions. The corresponding ARF field was then calculated using the equation (1.1) for each mesh point taking into account the frequency dependent attenuation and applied as point body loads to the spatial domain of the axisymmetric FEM model. The acoustic field calculation was then repeated at each temperature step.

A FEM model (Comsol Multiphysics 4.4, Comsol Inc, Burlington, MA, USA) was used to simulate the ARF induced displacements. In the FEM model, a 2-D axisymmetric geometry for the liver was used so that the symmetry axis was set along the axis of the HIFU transducer (see Figures 5.2(b) and (c)). The liver had a size of 42 mm (lateral) × 40 mm (axial) corresponding to the size of the liver in the acoustic simulations (i.e., the calculated ARF field size). Furthermore, 5 mm infinite element layers on the outer edges were used in order to minimise reflections from the boundaries. The outer surface of the liver was constrained to reflect a situation where the liver is in a fixed position within the body. The mechanical properties of the liver were modelled as a linear, isotropic and viscoelastic solid using properties derived from measurements and are defined later in the results section. A free triangular mesh was utilised in the central area of the liver and a rectangular mesh in the infinite element layers. Using triangular elements for nearly incompressible materials

can lead to problems with ill-conditioning, which was overcome by utilizing mixed formulation in Comsol. A convergence study was run before the actual simulations to determine the proper element size for the computation mesh.

5.1.5 Simulation execution

The ARFI induced displacements were calculated for a 60-second sonication resulting in a temperature range 35-70 °C with 5 °C intervals. At each discrete temperature point during the sonication, both the viscoelastic Zener model parameters and the attenuation of the liver and the lesion were updated to correspond to the measured values. The attenuation power law coefficient of the liver was kept at a constant value of 1.0, because no significant changes had been observed in the literature. The liver tissue was then pushed using a rectangular 0.5 ms ARFI pulse and the dynamic response was tracked at the geometric focus of the transducer. The displacement value at 0.5 ms was recorded and the viscoelastic and attenuation parameters were set for the next temperature iteration. It should be noted that the lesion did not appear until 60 °C was achieved, and hence, only the attenuation changed up to this point. At temperatures of 60 °C and above the viscoelastic parameters and attenuation were adjusted within the lesion while the parameters of the surrounding liver tissue were kept constant. For the lesion area, the viscoelastic properties varied linearly from the peak temperature at the centre to the background values at the edge in order to reduce shear wave reflections.

In the second simulation study, a Monte-Carlo style approach was conducted to determine the effect of variation in tissue property changes. This was done by varying the spring constant $M_\infty - M_0$ (i.e., the elastic branch in the Zener model) of the liver between 5-155 kPa and the attenuation between 0.15-1.35 dB/cm which are the typical ranges before and after thermal ablation found in the literature (recall Figure 2.6(a) and Figure 2.21(a) in Chapter 2). Varying the values of M_0 and τ within the range of their variance in the experimental data did not result in changes in the displacement amplitude due to the overpowering effect of M_∞. Therefore, the Zener model viscoelastic branch parameters were kept constant at $M_0 = 8.0$ Pa and $\tau = 0.5$ s representing the average values of liver tissue in the experiments. In the simulation model, the values were changed for the whole area of the liver phantom (i.e., no lesion present), which is similar to the situation with one large or multiple lesions next to each other. At each elastic modulus/attenuation coefficient combination the tissue was pushed with a 0.5 ms long pulse and the displacement amplitude was recorded at the geometric focus of the transducer.

5.2 Results

5.2.1 Temperature dependence of viscoelastic properties in liver

The magnitude of dynamic modulus measured in five *ex vivo* liver samples at 35 °C is presented in Figure 5.3. For both conventional and fractional Zener models the average magnitude of dynamic modulus were fit by using a nonlinear least squares method. The frequency ranges for the fits were chosen to exclude the rapidly fluctuating or increasing magnitude values which the models cannot capture. At high frequencies (above 30-40 Hz), rapid fluctuations in the magnitude of dynamic modulus were observed at all temperatures. This behaviour was also noted by Kiss et al. (2004) who postulated them to be an electronic signal-to-noise ratio artefact in the force measurement. It is likely that at high frequencies the DMA system cannot distinguish between ambient system noise and the response due to the tissue.

The experimentally measured magnitude of the dynamic modulus averaged over the five of samples is presented in Figure 5.4 over the frequency range 0.1-200 Hz at temperatures from 21 to 80 °C. The corresponding phase values (i.e., $\tan\delta$) are presented in Figure 5.5. The viscoelastic fitting parameters are shown in Table 5.2 for both models.

At 21 °C and 35 °C temperatures in Figure 5.4(a), the conventional Zener model predicts the magnitude to increase from a initial value of 1.2-1.4 kPa up to approximately 2.0 kPa for both temperatures. The high stiffness below 0.3 Hz at 21 °C is most likely caused by low signal to noise ratio at these frequencies. The modulus is

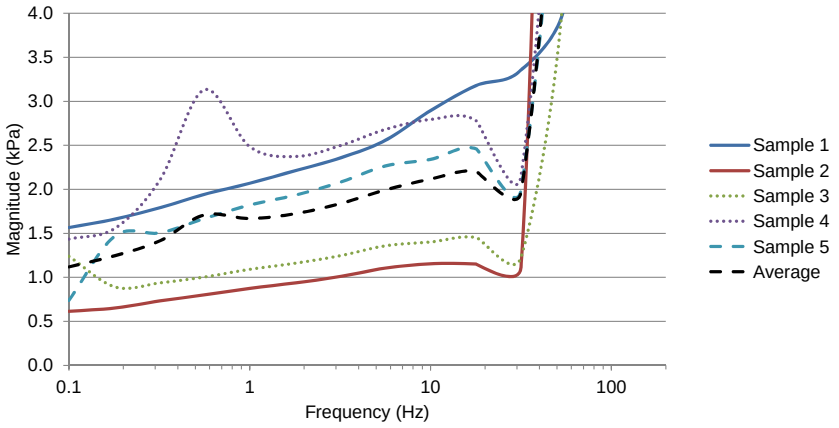

Figure 5.3: The magnitude of dynamic modulus measured in five *ex vivo* liver samples at 35 °C.

predicted to stabilise at frequencies above 10 Hz. The fractional model predicts the magnitude to increase from a initial value of around 1.2 kPa to approximately 2.4 kPa at 200 Hz for both temperatures.

At 50 °C temperature in Figure 5.4(b), the conventional Zener model predicts the magnitude to increase from a initial value of 5 kPa up to 15 kPa stabilising at frequencies above 1 Hz. The fractional model follows the experimental data better at higher frequencies reaching approximately 19 kPa at 200 Hz.

At 65 °C in Figure 5.4(c), the conventional Zener model starts from the initial value around 40 kPa stabilising to approximately 100 kPa at frequencies above 1 Hz. At 80 °C, the values increase from around 70 kPa up to 140 kPa. The fractional model again follows the experimental data better reaching values of approximately 140 kPa and 200 kPa for 65 °C and 80 °C temperatures, respectively.

In general, the sum of squared errors (SSE) (see Table 5.2) of the fractional model are two magnitudes lower compared to the conventional model for all temperatures. This is because the fractional model better captures the continuous increase in the magnitude and is not trying to stabilise the values at high frequencies.

Table 5.2: Conventional and fractional Zener model fitting parameters for thermally ablated liver at different temperatures. The SSE is also shown in each case.

	f (Hz)	M_∞ (kPa)	M_0 (Pa)	τ (s)	α_Z	SSE
Z 21 °C	0.6-31.6	2.1	1351.1	3.45E−02	1	0.008
Z 35 °C	0.1-17.8	2.0	1102.3	3.09E−01	1	0.044
Z 50 °C	0.1-31.6	15.0	8.0	4.62E−01	1	0.237
Z 65 °C	0.1-56.0	99.1	8.1	6.74E−01	1	0.349
Z 80 °C	0.1-100.0	138.0	8.1	9.32E−01	1	0.366
FZ 21 °C	0.6-31.6	3.0	855.2	1.23E−02	0.40	0.000
FZ 35 °C	0.1-17.8	2.5	8.0	7.52E−01	0.38	0.014
FZ 50 °C	0.1-31.6	20.2	8.1	2.24E−01	0.55	0.011
FZ 65 °C	0.1-56.0	171.2	8.1	9.99E−02	0.32	0.002
FZ 80 °C	0.1-100.0	335.5	8.1	5.20E−03	0.19	0.002

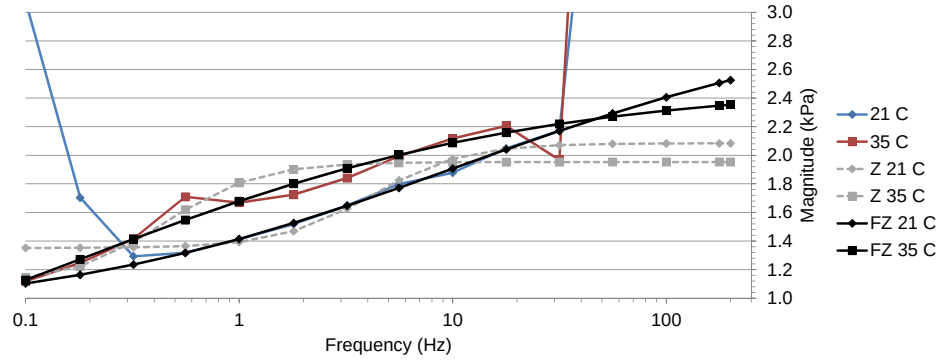

(a)

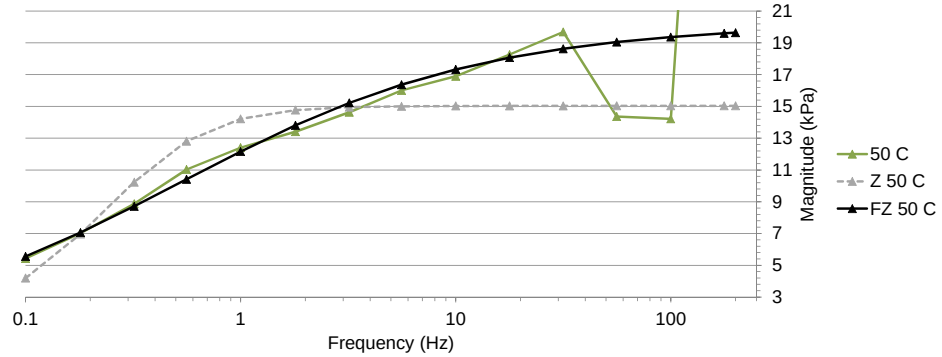

(b)

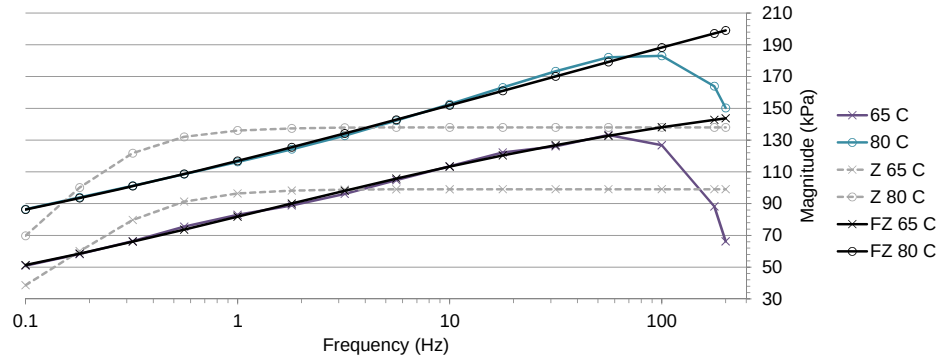

(c)

Figure 5.4: The average (5 samples) magnitude of the compressional dynamic modulus of *ex vivo* bovine liver samples during heating at temperatures of (a) 21 to 35 °C, (b) 50 °C and (c) 65 to 80 °C over the frequency range from 0.1 to 200 Hz. Conventional and fractional Zener models of viscoelasticity were fit to the data.

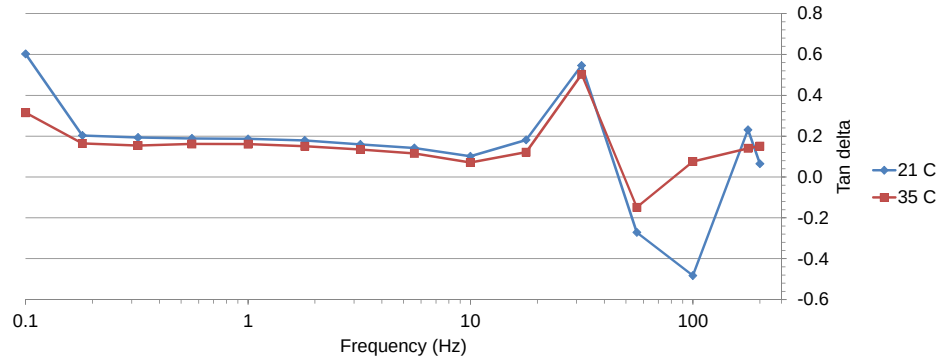

(a)

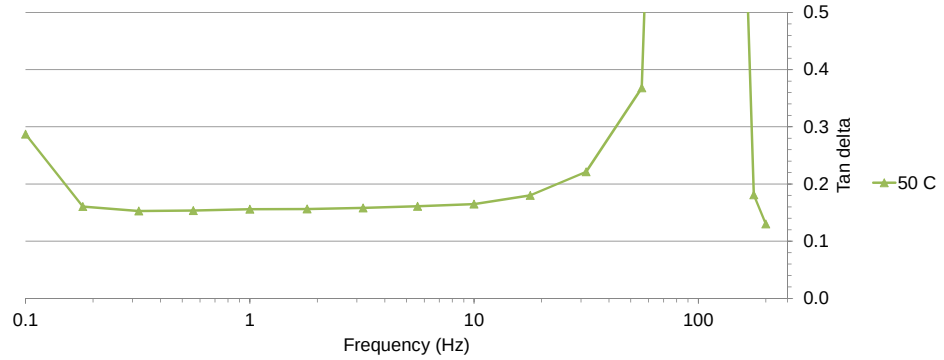

(b)

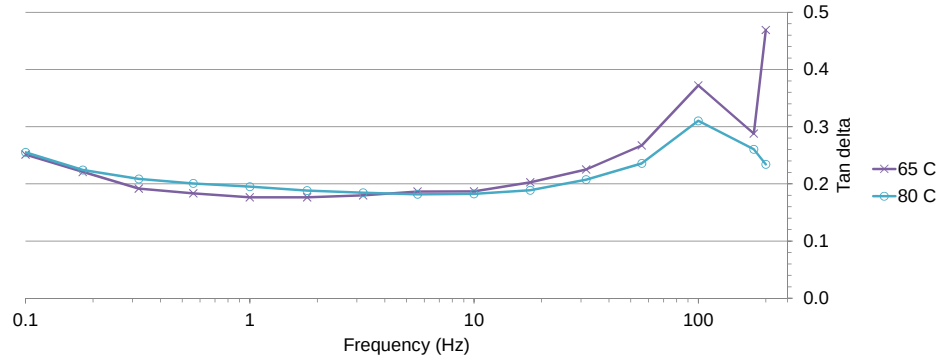

(c)

Figure 5.5: The average (5 samples) tan δ phase values of *ex vivo* bovine liver samples during heating at temperatures of (a) 21 to 35 °C, (b) 50 °C and (c) 65 to 80 °C over the frequency range from 0.1 to 200 Hz.

5.2.2 Experimental displacements during thermal ablation

The HMI system and thermocouple were used to monitor the evolution of the ARF induced displacements over 60-second sonications in *ex vivo* liver. Figure 5.6 shows an example dataset of (a) recorded peak-to-peak displacement amplitudes and the corresponding temperature values with time and (b) the two measurements combined.

The normalised (to 37 °C) and averaged peak-to-peak displacement data as a function of temperature for three different sonications are presented in Figure 5.7. The mean for the same data is also shown. For the first sonication, the peak-to-peak amplitude decreases to a minimum value of 99% at approximately 45-50 °C after which an increase to the peak value of 110% at around 70 °C is observed. After the peak value, there is a relative slow decrease to 96% at the temperature of 84 °C. Similar behaviour is observed in the case of the second sonication, where the peak-to-peak displacement decreases to 99% at around 45 °C and the increases reaching a peak value of 105% at approximately 60-65 °C. After the peak value, the curve decreases to 65% at 84 °C. In the third sonication, the amplitude first decreases to 96% around 45 °C after which a peak value of 100% at 59 °C is reached. After the peak, the minimum value of 65% at the temperature of 84 °C is measured.

It should be noted that the peak displacements occur at different temperatures in different sonications. For example at around 70 °C the amplitude has risen approximately to 110% in the first sonication whereas in the second and third sonications the amplitudes have decreased to 95% and 85% respectively. This suggests that the

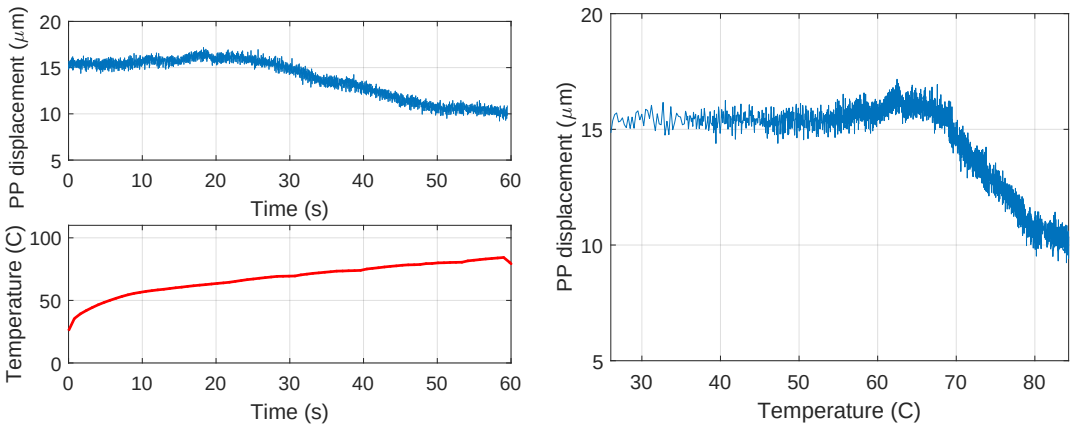

(a) (b)

Figure 5.6: (a) An example dataset of measured peak-to-peak displacement amplitudes and the corresponding temperature data with time. (b) The two measurements combined.

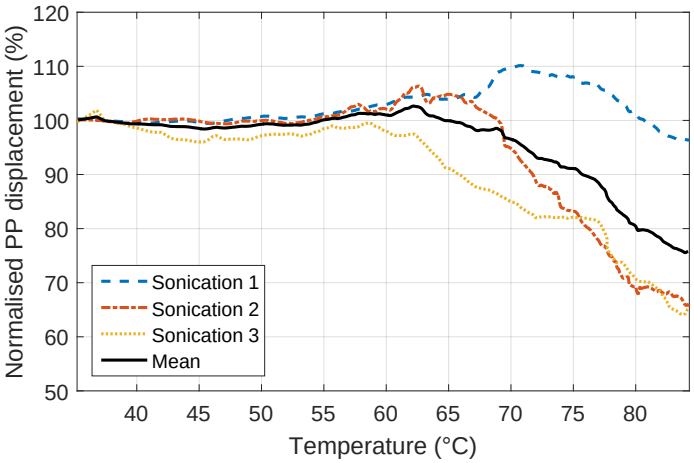

Figure 5.7: Experimental HMI data showing the change in normalised (to 37 °C) peak-to-peak displacement amplitude with temperature during three different 60-second sonications in *ex vivo* canine liver.

time history of the displacements during HIFU therapy is an important indicator of the state of the ablation as the decrease in amplitude does not occur at a constant temperature. This effect can also been seen in the large deviation of the displacement estimates after about 60 °C where the stiffness changes due to thermal ablation has been shown to occur (Wu et al., 2001; Sapin-de Brosses et al., 2010).

5.2.3 Simulations of thermal ablation

The simulations of ARFI induced displacements during HIFU employed the temperature dependent models described in the simulation model section with the polynomial constants for attenuation in Table 2.2 and the viscoelastic parameters in Table 5.3. The Poisson's ratio for both liver and lesion was set to 0.499.

The viscoelastic parameters for liver tissue were kept constant at all temperatures while the parameters for lesion were changed at 60 °C and above when the lesion

Table 5.3: Temperature dependent viscoelastic parameters for background liver tissue and lesion used in the FEM model.

	Liver	Lesion		
T (°C)	35-70	60	65	70
M_0 (Pa)	1.1	8.1	8.1	8.1
$M_\infty - M_0$ (kPa)	0.9	34.7	52.6	79.6
τ (s)	0.309	0.626	0.699	0.772
Lesion length (mm)	N/A	3.0	5.0	6.8
Lesion diameter (mm)	N/A	0.6	1.2	1.7

started to form. In addition to the average values presented in the tables, the attenuation and elastic modulus $M_\infty - M_0$ of the lesion were individually changed ±25% to examine their effect on the displacements. The effect of temperature dependent sound speed and attenuation power law coefficient were also studied by changing the corresponding values in the lesion parameters by ±0.5% and ±25%, respectively. However, no effect on the displacement was observed due to high stiffness of the lesion at various temperatures, and hence, their temperature dependence was excluded from the final simulations.

The simulated evolution of the normalised (to 35 °C) displacement amplitude with temperature during HIFU therapy is presented in Figure 5.8. The average displacement amplitude starts to decrease from the initial value of 100% at 35 °C down to 95% at approximately 40-45 °C due to the changes in the polynomial attenuation of liver. After the initial decrease, the amplitude starts to increase, due to the increase in attenuation, peaking at 105% at 55 °C. At 60 °C, the amplitude rapidly decreases down to 85% due to the lesion growth. Although the attenuation of the lesion is still growing at this point, the effect is overshadowed by the large changes in lesion stiffness. At higher temperatures, the lesion continues to grow in size and stiffness, which brings the displacement amplitude down to 49% at the final temperature of 70 °C in the end of the sonication.

In addition to the average response, the displacement amplitudes are shown by changing the attenuation and elastic modulus of the lesion by ±25%. Changing atten-

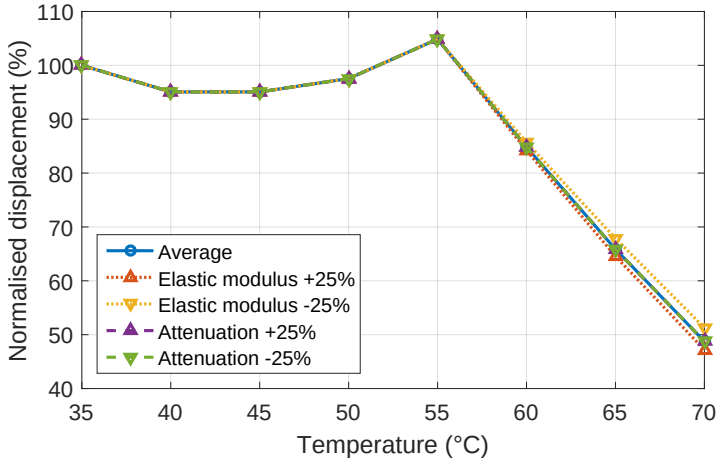

Figure 5.8: Simulated data showing the change in normalised (to 35 °C) ARF displacement amplitude with temperature during HIFU therapy in liver using the parameters from Table 5.3. The values for attenuation and elastic modulus of the lesion were changed ±25% to examine their effect with respect to the average response.

uation by ±25% resulted in a negligible change in displacement amplitude (less than 0.1%). Changing elastic modulus of the lesion by ±25% resulted in a small change in displacement for temperatures of 60 °C and above, but differences of approximately 2%-points were observed at 70 °C. This suggest that changes in attenuation and displacement have very little effect on the displacement amplitude, and that displacement is robust to these changes.

The growth of the lesion size with respect to the ARF field is shown in Figure 5.9. At 55 °C (see Figure 5.9(a)), a lesion has not formed yet but the magnitude of the ARF field has increased due to the increase in attenuation, which causes the displacement amplitude to increase to 105% in Figure 5.8. At 60 °C (see Figure 5.9(b)), the lesion has grown approximately the size of the ARF field, whose magnitude still keeps increasing, however, the displacement decreases in Figure 5.8 due to the stronger effect of stiffness growth compared to the attenuation. At 65 °C (see Figure 5.9(c)), the size of the lesion has become larger than the ARF field and the displacement in Figure 5.8 continues to decrease steeply as the increase in stiffness dominates the response.

In the second part of the simulation study, a Monte-Carlo type approach was undertaken to determine the effect of variations in changes in the attenuation and elastic modulus $M_\infty - M_0$ over the range of values found in the literature. The viscoelastic parameters were kept constant at $M_0 = 8.0$ Pa and $\tau = 0.5$ s. The values for attenuation and elastic modulus were changed for the whole liver mimicking a therapeutic situation where multiple lesions are created next to each other. The FEM model was then used to predict the resulting ARFI induced displacement with each combination of attenuation and elasticity.

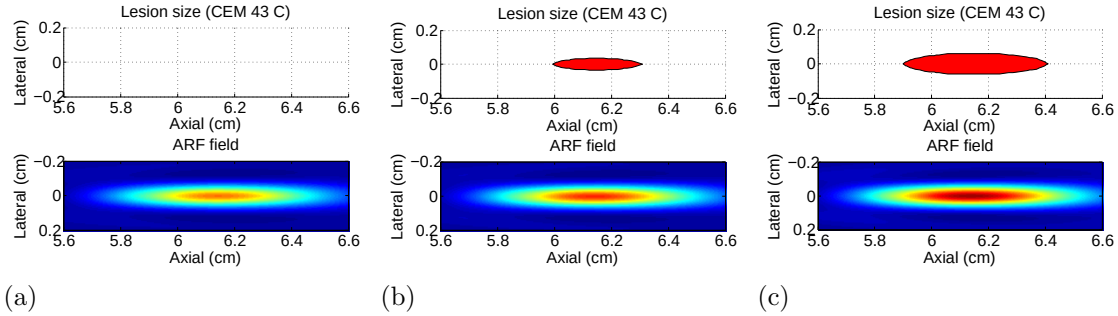

Figure 5.9: The evolution of the lesion size and the ARF field at (a) 55, (b) 60 and (c) 65 °C, which can be related to changes in displacement in Figure 5.8.

The isocontours at 5 μm intervals of the predicted displacement are shown in Figure 5.10 as a function of attenuation and elasticity. The data show that if the effective change in attenuation and elastic modulus is the same, the ablated and non-ablated regions cannot be distinguished based on the amplitude of ARFI excitation. For example, if tissue goes from the combination of 0.3 dB/cm/MHz and 20 kPa to 0.6 dB/cm/MHz and 60 kPa, the displacement remains approximately at 5 μm. Therefore, the typical regions before and after ablation based on the values found in the literature are shown with blue (solid) and red (dashed) rectangles, respectively, with average values are denoted by blue (cross) and red (circle) markers. The displacement for the average values of unablated tissue was 9 μm which decreased by 30% to 6 μm when employing the average values for ablated tissue.

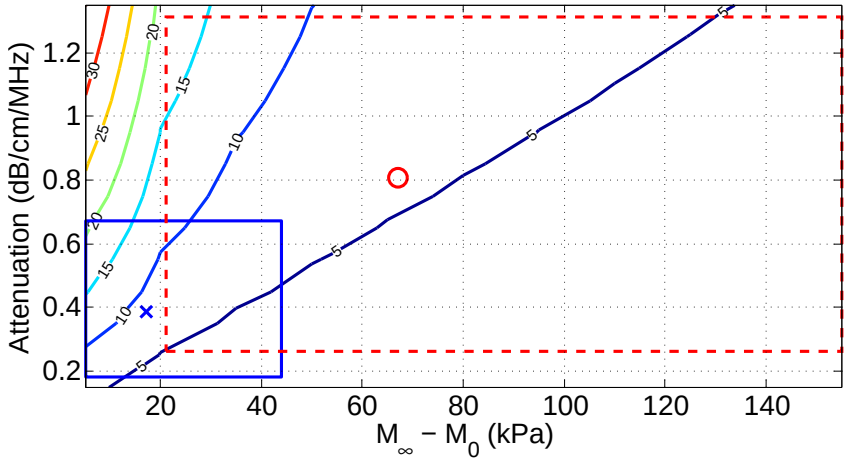

Figure 5.10: Simulated data showing isocontours of displacement amplitude (μm) when the attenuation and elastic modulus $M_\infty - M_0$ of the liver were varied. The viscoelastic parameters were kept constant at $M_0 = 8.0$ Pa and $\tau = 0.5$ s. Blue (solid) and red (dashed) rectangles are showing the range of literature values before and after thermal ablation respectively. The blue (cross) and red (circle) markers show the average literature values for both regions.

5.3 Discussion

This study addressed the utility of ARF induced displacements as a means of monitoring HIFU. Analysis of literature data indicated that changes in acoustic attenuation and elasticity with temperature will dominate changes in the displacement. The temperature dependence of the attenuation of liver reported in the literature was modelled using a polynomial fit which was able to capture the initial decrease in the attenuation and the subsequent rise (Damianou et al., 1997; Choi et al., 2011; Jackson et al., 2014).

The viscoelastic properties have been reported to increase almost exponentially at temperatures above about 50 °C (Sapin-de Brosses et al., 2010). DMA measurements of bovine liver were carried out in order to determine changes to the viscoelastic properties as a function of temperature. Both conventional and fractional Zener model fits to the experimental data showed changes in the viscoelastic parameters with temperature. The fractional model was found to fit the experimental data better with up to two orders of magnitude lower SSE when compared to the conventional model, which is consistent with Kiss et al. (2004) who found the fractional Kelvin-Voigt model to predict the frequency response better when compared to the conventional model. This is because the fractional model has a frequency dependence which better reflects the characteristics of dynamic modulus in liver.

The motivation of this study was to investigate how these changes in acoustic and viscoelastic tissue parameters affect the ARF induced displacements during HIFU therapy. For this purpose, HMI was used to monitor thermal ablation with real-time temperature data collected using an embedded thermocouple in *ex vivo* liver. The temperature acquisition using this method has been shown to suffer from so-called viscous heating artefact (Morris et al., 2008), which can potentially lead to an error in the measured temperature value. However, this error has been shown to be significant only during the initial few seconds of the sonication (Dasgupta et al., 2011), and with the 60-second sonications employed here, the effect should be less than a few degrees along the temperature axis.

During HIFU thermal ablation, the displacement amplitude was observed to decrease slightly with temperature up to 45-50 °C after which an increase to about 60-70 °C was seen followed by a steep decrease due to thermal necrosis (Wall et al., 1999; Wright and Humphrey, 2002). Similar observations were also reported by Heikkila et al. (2010); Konofagou et al. (2012), who found the displacement amplitudes to increase before thermal ablation. The initial slight decrease in the amplitude is not

always reported, but has been found to occur in some cases (Konofagou et al., 2012). The increase in displacement amplitude before necrosis could potentially be due to tissue softening at low temperatures as observed by Wu et al. (2001) in *ex vivo* bovine muscle, but this phenomenon has not been found in liver (Sapin-de Brosses et al., 2010). Furthermore, the viscoelastic measurements conducted in this and other studies (Kiss et al., 2009) do not support this hypothesis. The slight decrease and following increase in the displacement amplitude before thermal necrosis is therefore more likely to be caused by the change in attenuation with temperature which exhibits a similar trend (Damianou et al., 1997; Choi et al., 2011). The changes in viscoelasticity likely do not have a significant effect until the lesion starts to grow, which will only occur later in the sonication.

To better understand how these different tissue properties affect the ARF induced displacements in liver, a linear viscoelastic FEM model together with nonlinear acoustic simulations were used. The simulation model took into account the temperature dependent changes in attenuation, viscoelastic parameters and lesion growth. The effect of temperature dependent sound speed and attenuation power law coefficient on displacement amplitude were found to be minimal, and thus, they were left out from the simulation model. Furthermore, the effect of thermal lensing (Connor and Hynynen, 2002) was not taken into account which could potentially shift the focal point of the ultrasound field with temperature. The magnitude of focal shift due to thermal lensing is related to the ultrasound frequency and F-number of the transducer which, for the configuration used here, should result in a few millimetre axial shift of the ultrasound focal point towards the transducer during sonication. In practice, this would mean that the lesion would slightly spread in size towards the transducer. This could potentially lead to slightly lower displacement amplitudes than shown in the simulation results due to the error in the lesion size.

The simulated ARFI displacement amplitudes in liver were seen to decrease up to 40-45 °C together with the attenuation, which is where it reached its local minimum. The decrease in simulated displacement amplitude was observed to be approximately 5%, which is larger compared to experimentally observed ∼1% average decrease. This is probably because the viscoelastic properties of liver were kept constant while only the value of attenuation was changed. In reality, the heating of the liver in the ultrasound focal point would cause slight changes in the viscoelasticity before the ablation, which are likely to counteract the effect of attenuation changes.

After 45 °C, the attenuation started to increase which also caused the displacement amplitude to increase up to 55 °C. Similar increasing amplitude was also seen in the

experimental data, where the peak occurred approximately at 60-70 °C. The difference in the peak location on temperature axis is probably due to different transducer configuration and therapeutic geometry between the experiments and simulations, which cause differences in the lesion size. However, the magnitude of the increase was similar in both the experimental and simulation data with both showing approximately 3-5% increase. There is a large deviation in the experimental displacement values in the 60-70 °C temperature region, which indicates that the peak in displacement amplitude (and hence thermal ablation) does not occur at constant temperature. Therefore, it is important to record the whole time history of the displacement data to ascertain when the ablation occurs. Furthermore, there is a threshold in the lesion size (i.e., 240 $\mathrm{CEM}_{43^\circ\mathrm{C}}$ volume) which starts to cause the decrease in the displacement amplitude, but its determination requires further research.

After 55 °C, the attenuation further increased but simultaneously a lesion started to develop causing the displacement amplitude to rapidly decrease as the increasing stiffness of the lesion outweighs the effect of increasing attenuation. The decrease in amplitude was observed to be approximately 51% in the simulations, while experimental data showed larger variation of 6-42% decrease.

The final simulation study considered how the ARFI displacement amplitudes behave in the situation after HIFU therapy, where one large lesion or multiple small lesions are next to each other. For this purpose, the typical ranges in attenuation and elastic modulus in liver were used. The regions before and after thermal ablation were found to overlap slightly, although this was partly due to the relatively high elastic modulus values found in the literature for normal liver (Righetti et al., 1999). Furthermore, the large deviation in the attenuation coefficient also makes the two regions to overlap. When looking at the average values, the simulations predicted a 30% decrease in displacement after ablation. However, the 5, 10 and 15 μm contours traverse both regions of non-ablated and ablated tissue, i.e., the blue and the red rectangles. This suggests that looking only at the changes in ARF induced displacement before and after thermal ablation is not enough to determine whether the tissue has undergone ablation, but rather the whole time history of the displacement during the ablation should be considered.

5.4 Conclusions

The effect of temperature dependent acoustic and viscoelastic tissue parameters on ARF induced displacements in liver was studied. The temperature dependent tissue properties that will most strongly affect the magnitude of ARF induced displacements were found to be attenuation and viscoelasticity. The effect of a representative temperature dependent attenuation power law coefficient and sound speed were found to be negligible.

Experimental HMI data during HIFU ablation in *ex vivo* liver showed an initial variable increase in the displacement amplitude at temperatures below 60-70 °C followed by a robust decrease in amplitude due to thermal ablation. The viscoelastic simulation model, employing temperature dependent tissue parameters, exhibited similar behaviour with the increasing attenuation providing the initial increasing in the displacement amplitude at lower temperatures before thermal ablation. At higher temperatures, the lesion growth together with the exponentially increasing elastic modulus overpowered the changes in attenuation and a decrease in amplitude was predicted.

At temperatures above 60 °C, the experimental HMI data showed large deviation in the displacement amplitude between the three measurements. Both experimental data and numerical simulations indicate that monitoring displacement before and after HIFU ablation is not sufficient to determine the state of ablation. Therefore, it is concluded that monitoring ARF induced displacements continuously during thermal ablation is necessary in order to ascertain when ablation occurs. Once displacement amplitude reduces by 15% compared to its initial value at body temperature, then a lesion approximately the size of the focal region should exist.

Chapter 6

Simulations of therapeutic ultrasound field

The aim of this chapter[1] is to investigate how the combination of attenuation, refraction and reflection of different tissue layers in front of the kidney affect the intensity and geometry of the ultrasound field. This is done by performing nonlinear HIFU therapy simulations in segmented three-dimensional CT datasets of three different patients. After the acoustic simulations, the heating efficacy of HIFU therapy in the kidney is determined with thermal simulations. The acoustic and thermal parameters as well as the perfusion of the kidney are varied within their physiological limits in order to examine their effect on heating. In addition, an aberration study to examine the effect of tissue layers on phase shifts at the transducer face is conducted. These results provide a quantitative analysis of the factors affecting the overall efficacy of HIFU therapy of the kidney.

6.1 Kidney cancer and current therapies

The incidence of kidney (renal) cancer has been growing at an annual rate of 2% with the vast majority of the cases being renal cell carcinomas (RCC) (Luciani et al., 2000; Ljungberg et al., 2011; Ferlay et al., 2012a). In 2012 it was the 13$^{\text{th}}$ most common cancer in the world (Ferlay et al., 2012a) with approximately 338,000 new cases diagnosed (214,000 in men and 124,000 in women), representing 2.4% of all cancers. In the same year approximately 143,000 people died due to the disease. The five-year survival rate of kidney cancer has been around 74% in recent years, but

[1]The contents of this chapter have been published in Suomi et al. (2016b) and Suomi et al. (2017). The parallelised k-Wave ultrasound simulation code used in the simulations in this chapter was developed by Jaros et al. (2015).

patients with advanced RCC have five-year survival rates of only 11-12% (NCI, 2016). Early diagnosis as well as safe and effective therapy methods are therefore crucial for improving patient outcomes.

Improvements in diagnostic imaging modalities, such as ultrasound, MRI and CT, have benefited the early detection of kidney cancer, but effective treatment of the disease still remains a challenge. Typically kidney cancer is treated surgically, which is currently the only curative option available (Van Poppel et al., 2011), but it can lead to complications in as many as 19% of cases (Gill et al., 2003). Alternative, minimally invasive therapies such as cryotherapy (Gill et al., 2005) and radiofrequency ablation (Gervais et al., 2005) reduce the risk of complications and often result in shorter hospital stays. However, neither of these methods is completely non-invasive and therefore still present a risk of infection, seeding metastases and other complications.

HIFU therapy can be used clinically to treat cancerous tissue in kidney, but the oncological outcomes have been variable (Wu et al., 2003b; Illing et al., 2005; Marberger et al., 2005; Ritchie et al., 2010). Wu et al. (2003b) demonstrated the feasibility of HIFU ablation of renal malignancies, all but one being RCC. A total of 13 patients were treated, of which 10 had partial ablation and three had complete tumour ablation. Illing et al. (2005) also demonstrated the safety and feasibility of HIFU renal ablation in eight patients. Four of the treated patients had surgical resection of the kidney after the treatment, of which only one showed features of ablation. The remaining six had a MRI assessment of the response and ablation was demonstrated in four. Marberger et al. (2005) presented a clinical phase II trial results of extracorporeal ablation of renal tumours with 16 treated patients. They found acute tissue necrosis (Susani et al., 1992) in nine tumours exposed to the highest dose of ultrasound, but this only covered 15-35% of the targeted area. Other clinical studies have shown successful ablation to occur only in less than two-thirds of the treatments (Ritchie et al., 2010).

The variable degree of efficacy in HIFU ablation of the kidney could be due to two reasons: limitations in the therapeutic HIFU system and the physical factors related to the human body. With respect to the therapy system, the diameter of the HIFU transducer has to be relatively large, typically above 10 cm in diameter, which allows the pre-focal ultrasound beam energy to be spread over a wider area. This reduces the pre-focal heating and the possible effect of shielding, particularly from the rib cage. In addition, large diameter transducers allow for greater focal lengths which are in the range of 5-15 cm, thus allowing the treatment of deep-lying organs such as the kidney. Due to the location of the kidney, the ultrasound frequency also

needs to be low enough that the attenuation from intervening tissue layers does not remove much energy. Therefore, extracorporeal HIFU systems typically operate in the frequency range of 0.5-1.5 MHz to maximise the ultrasound penetration depth with high enough intensity (ter Haar and Coussios, 2007).

In addition to the requirements for the HIFU system, the structure and acoustic properties of tissues in front of the transducer affect the efficacy of HIFU therapy. Due to the deep location of the kidney, several tissue layers, including skin, fat, muscle and soft tissue, lie in front the kidney. These layers might significantly reduce the intensity of the ultrasound field due to attenuation. The effect of attenuation might be particularly significant in the nonlinear case in which higher harmonic frequencies generated during HIFU therapy are more strongly attenuated. In addition to attenuation, the defocusing of ultrasound due to refraction and reflections at tissue interfaces might result in significant loss of HIFU energy in the target location. Kidneys are also highly perfused organs, which causes fast heat dissipation, and thus, reduced heating efficacy. Therefore, all the factors discussed above should be considered in order to achieve successful thermal ablation in the kidney.

6.2 Computational model

6.2.1 Parallelised nonlinear ultrasound simulation model

The acoustic simulations were performed using the open-source k-Wave Toolbox (Treeby et al., 2012). This solves a set of coupled first-order partial difference equations, which are equivalent to a generalised version of the Westervelt equation (3.8) from Chapter 3:

$$\nabla^2 P - \frac{1}{c^2}\frac{\partial^2 P}{\partial t^2} + \frac{b}{c^4}\frac{\partial^3 P}{\partial t^3} + \frac{\beta}{\rho_0 c^4}\frac{\partial^2 P^2}{\partial t^2} = 0$$

The solution accounts for second-order acoustic nonlinearity, power law acoustic absorption and a heterogeneous distribution of material properties (sound speed, density, nonlinearity and absorption coefficient).

The governing equations were solved using a k-space pseudospectral method, where spatial gradients are calculated using the Fourier collocation spectral method, and time integration is performed using an explicit dispersion-corrected finite-difference scheme (Tabei et al., 2002). The advantage of this method is that it only requires two grid points per maximum supported frequency which allows smaller grid sizes and larger time steps when compared to FEM and other finite difference methods. The model was implemented in C++ and optimised for distributed computing

environments using the standard message passing interface (MPI) (Jaros et al., 2015). The 3-D domain was distributed across multiple cores using 1-D slab decomposition, and the MPI version of the FFTW library was used to perform the requisite Fourier transforms (Frigo and Johnson, 1998).

6.2.2 Thermal simulation model

The thermal simulation model was constructed using the BHT equation (3.12) from Chapter 3:

$$\rho_{\mathrm{k}} c_{P\mathrm{k}} \frac{\partial T_{\mathrm{k}}}{\partial t} = k_{\mathrm{k}} \nabla^2 T_{\mathrm{k}} - w_{\mathrm{k}} c_{P\mathrm{b}} (T_{\mathrm{k}} - T_{\mathrm{b}}) + H$$

where the subscripts 'k' and 'b' refer to kidney and blood, respectively, T_{k} [°C] is the three-dimensional (x, y, z) temperature field in the kidney and $T_{\mathrm{b}} = 37$ °C. Because the simulated ultrasound fields were nonlinear, the heating rate was calculated using the harmonic components of the acoustic field according to the equation (3.16) from Chapter 3:

$$H = \frac{1}{c_{\mathrm{k}} \rho_{\mathrm{k}}} \sum_h \alpha_{\mathrm{k}}(h f_0) |P_h|^2$$

where the number of harmonics $h = 4$. The pressure values of each harmonic component were obtained using the DFT of the time-domain ultrasound waveforms at each spatial location. The heat equation was solved using the ADI method (Ames, 1977) presented in Appendix A.

6.3 Simulations

6.3.1 Therapeutic high-intensity focused ultrasound simulations

The simulation geometries were derived using CT datasets of three different patients (see Figure 6.1 for patient 1). Thresholds were used to automatically segment the datasets into bone, fat and other soft tissue after which the kidneys were segmented manually. The medium outside the patients was segmented as water. Typical values reported by Mast (2000) for sound speed, attenuation, density and B/A were used for each tissue type (see Table 6.1). The HIFU transducer was modelled on a clinical system (Model JC200, Haifu, Chongqing, China) with an annular transmitting surface of outer diameter 20 cm, inner hole diameter 6 cm, operating frequency 0.95 MHz and focal length 14.5 cm (Ritchie et al., 2013). The transducer was positioned so that

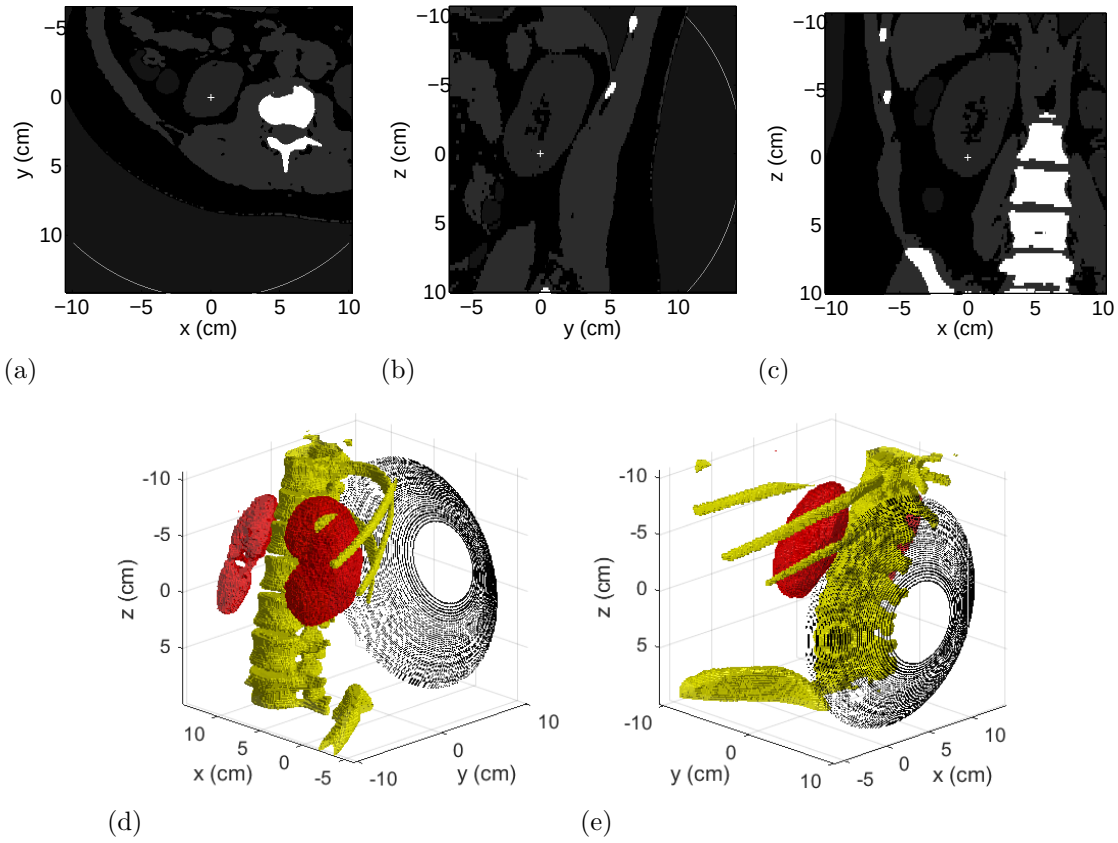

Figure 6.1: (a) Axial, (b) sagittal and (c) coronal slices of the CT scan in patient 1. The different gray levels in the CT data correspond to the density of each tissue type: white - bone, gray - kidney/soft tissue, black - water/fat. The ultrasound focal point target location is marked with a white cross. (d)-(e) 3-D visualisation of the CT geometry in patient 1 showing the simulation geometry (without soft tissue, fat and water). Similar geometries targeting the lower part of left kidney were used for patients 2 and 3.

Table 6.1: Acoustic simulation parameters for different tissue types. The simulations without refraction effects were performed using the sound speed of water in all tissues. In addition variability was considered by changing kidney sound speed ±10 m/s and attenuation ±0.24 dB/MHz$^{1.1}$/cm.

	Density (kg/m^3)	Sound speed (m/s)	Attenuation (dB/MHz$^{1.1}$/cm)	B/A
Water	1000	1520	0.00217	5.2
Bone	1908	4080	20.00	7.4
Soft tissue	1055	1575	0.60	7.0
Fat	950	1478	0.48	10.0
Kidney	1050	1560 ± 10	1.00 ± 0.24	7.4

the geometric focal point of the transducer (the white cross in Figures 6.1(a)-(c)) was located in the bottom part of the left kidney. This was done in order to avoid the ribs which would otherwise cause significant pressure losses due to strong reflection.

A reference simulation was carried out in water and two additional simulations for each patient: (i) with all tissue properties varying; and (ii) constant sound speed in all tissues to remove refraction, but all other properties varying. Four additional simulations for patient 1 were conducted by changing the attenuation and sound speed of the kidney by ±0.24 dB/cm and ±10 m/s, respectively, which correspond to ±2 standard deviations (SD) based on 30 kidney samples in humans (Turnbull et al., 1989).

Before performing the actual simulations, several convergence simulations were conducted in order to find the optimal grid size and temporal resolution. The computational grid consisted of 1200 × 1200 × 1200 grid points (i.e., 22.2 cm × 22.2 cm × 22.2 cm) giving a spatial resolution of 185 μm which supported nonlinear harmonic frequencies up to 4 MHz. Perfectly matched layers (PML) were used on the edges of the grid. The simulation time duration was set to 260 μs with a temporal resolution of 8.15 ns giving a total of 31876 time steps per simulation. The simulations were run using 400 computing cores for approximately 50 hours per simulation and requiring 200 GB of memory. The simulations were conducted using the computing facilities provided by advanced research computing (ARC) at the University of Oxford (Richards, 2016). For data analysis, the time-domain waveforms and the peak pressures were saved in a three-dimensional grid around the focal point in each case. In addition, axial, sagittal and coronal slices of the ultrasound field over the whole spatial domain were saved.

Table 6.2: Thermal simulation parameters for kidney and blood. In addition to the values given in the table, the thermal conductivity and perfusion rate of the kidney were changed ±0.04 W/m/K and ±8.3 kg/m^3/s, respectively, to study the effect of natural variability.

	Thermal conductivity (W/m/K)	Specific heat capacity (J/kg/K)	Perfusion rate (kg/m^3/s)
Kidney	0.53 ± 0.04	3763	9.2 ± 8.3
Blood	N/A	3617	N/A

6.3.2 Thermal simulations

Thermal simulations were conducted in Matlab (R2015b, MathWorks Inc, Natick, MA, USA) using the nonlinear ultrasound fields from the acoustic simulations. The simulations were run for each patient in the kidney with the parameters presented in Table 6.2. The thermal conductivity and perfusion rate of the kidney in patient 1 were also changed by ±0.04 W/m/K and ±8.3 kg/m^3/s, respectively, which correspond to a ±2 SD change (Hasgall et al., 2015; Roberts et al., 1995). This was done in addition to the acoustic simulations in patient 1 which already included changing the attenuation and sound speed of the kidney. The simulations were conducted in a 2 cm × 2 cm × 2 cm spatial domain around the target focal point (i.e., in the kidney) with a fixed temperature (Dirichlet) boundary condition of 37 °C on the edges. Each sonication was conducted for 120 seconds which was followed by a 10-second cooling period. The evolution of the maximum temperature was recorded throughout the whole duration of the simulation. Furthermore, the temperature and $CEM_{43°C}$ (i.e., a measure of thermal dose) over the whole domain at the end of the cooling period were saved.

6.4 Results

6.4.1 Ultrasound waveforms in time and frequency domain

Figure 6.2(a) shows the time domain waveforms at the location of the global peak pressure in water and kidney for the three different patients including refraction. The individual peak pressures and spatial peak-temporal average intensity I_{SPTA} values for each case are also listed in Table 6.3. In water the peak pressure was 14.49 MPa with a corresponding I_{SPTA} of 4116 W/cm^2. In all patients, the mean peak pressure was 3.50 MPa which corresponds to an approximately 76% drop in pressure amplitude. The range was from 3.33 to 3.66 MPa, which suggests that there is not much difference in the outcome between the three different patients. Similarly, the I_{SPTA} in patients dropped to an average value of 318 W/cm^2, which corresponds to a 92% or an 11.1 dB drop. The range varied from 283 to 346 W/cm^2, which shows an 11% variation around the mean, suggesting that heating should not vary dramatically across patients.

When no refraction effects were included in the simulations, the peak pressures and I_{SPTA} increased in all three patients, with an average value of 6.46 MPa (i.e., a 55% drop in amplitude), which is approximately twice higher than that with refraction. The range was from 6.25 to 6.67 MPa indicating 3% variation around the mean value. The average I_{SPTA} was 938 W/cm^2 which corresponds to a 77% or a 6.4 dB drop in intensity. In this case, patient 2 had the lowest I_{SPTA} of 887 W/cm^2 with patients 1 and 3 having 957 W/cm^2 and 971 W/cm^2, respectively. The small range suggests that heating should be very similar in these three patients.

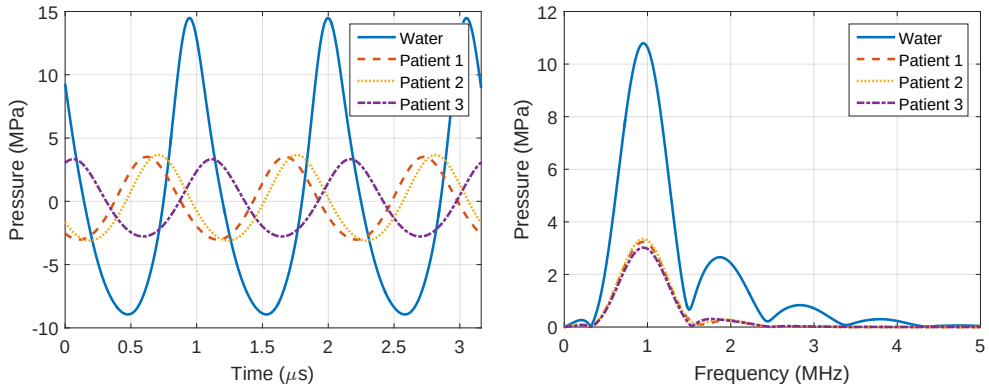

(a) (b)

Figure 6.2: (a) Time domain waveforms at the peak pressure location in water and kidney in patients 1-3 with refraction effects. (b) Windowed (Hann) frequency spectrum of the same waveforms.

Table 6.3: Acoustic simulation results in water and three different patients. Simulations marked with (*) are without refraction effects.

	Peak pressure (MPa)	I_{SPTA} (W/cm^2)	I_{SPTA} reduction (dB)	Focal shift Axial (mm)	Focal shift Radial (mm)	Parent focal size Length (mm)	Parent focal size Width (mm)
Water	14.49	4116	0.0	0.0	0.0	6.5	1.3
Patient 1	3.51	324	−11.0	2.6	1.8	11.4	1.8
Patient 2	3.66	346	−10.8	0.6	1.2	9.5	1.4
Patient 3	3.33	283	−11.6	3.1	1.1	7.3	1.2
Average	**3.50**	**318**	**−11.1**	**2.1**	**1.4**	**9.4**	**1.5**
SD	**0.13**	**26**	**0.4**	**1.1**	**0.3**	**1.7**	**0.2**
Patient 1*	6.46	957	−6.3	1.3	0.4	7.4	1.5
Patient 2*	6.25	887	−6.7	1.3	0.3	7.4	1.4
Patient 3*	6.67	971	−6.3	0.9	0.3	7.2	1.3
Average	**6.46**	**938**	**−6.4**	**1.2**	**0.3**	**7.3**	**1.4**
SD	**0.17**	**37**	**0.2**	**0.2**	**0.1**	**0.1**	**0.1**

Figure 6.2(b) shows the frequency spectra of the same focal waveforms in water and the three patients with refraction. A peak at the centre frequency of 0.95 MHz is clearly visible in each case as are the nonlinearly generated harmonics. However, in the case of tissue, the nonlinear effects are much less pronounced when compared to water. In water the second harmonic is 25% of the fundamental component compared to 7% in patients. All three patients show a low magnitude second harmonic while the third and fourth harmonics are barely visible. These data suggest that for this HIFU system nonlinearity does not play a major role in heating.

6.4.2 Ultrasound pressure fields

Figures 6.3(a), (c) and (e) show the axial, sagittal and coronal slices of the ultrasound pressure field generated by the HIFU transducer in patient 1. The pressure fields are displayed using a log-scale thresholded at −30 dB below the maximum pressure in each slice. The annular nature of the ultrasound source results in the shadow region in the centre of the beam. In the focal area, it can be seen that the region of high pressure does not form the archetypical ellipse shape, but is more diffuse instead. Furthermore, the areas of high pressure are offset from the focal point target location (white cross marker) in all slices.

Figures 6.3(b), (d) and (f) show close-ups of the axial, sagittal and coronal slices of the pressure field in the ultrasound focal area. It can be seen that the peak pressure does not occur at the target location (the white cross). This effect was observed in

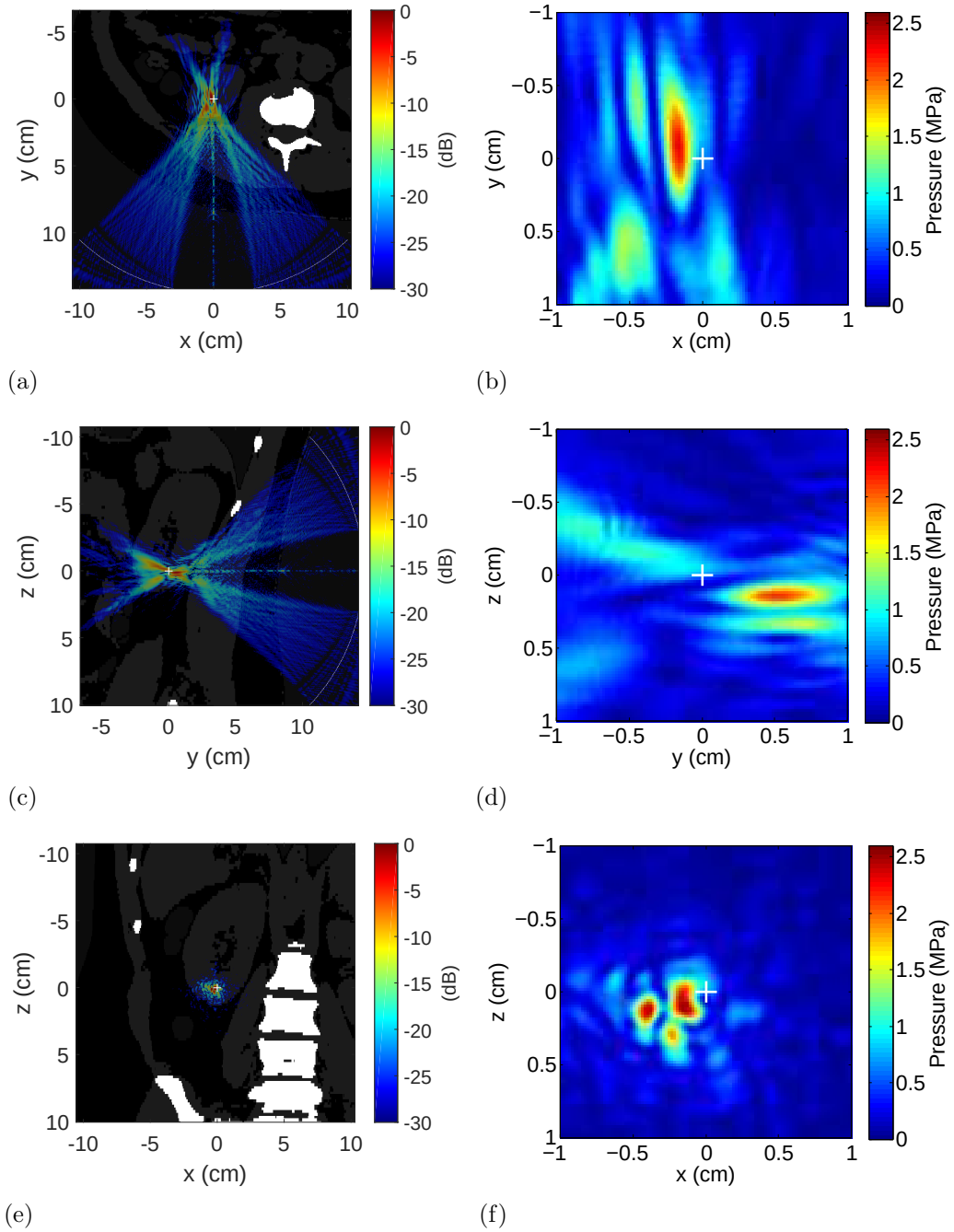

Figure 6.3: (a) Axial, (c) sagittal and (e) coronal slices of the CT scan showing the ultrasound pressure field in patient 1. The pressure field is displayed on a log-scale with a dynamic range of 30 dB. The ultrasound focal point target location is marked with a white cross. (b) Axial, (d) sagittal and (f) coronal slices of the same ultrasound field in the focal area in the kidney.

all three patients and the offsets are given in Table 6.3. On average the shifts were observed to be 2.1 mm in the axial and 1.4 mm in the radial directions. By examining the focal area in more detail in the coronal slice in Figure 6.3(f), it can be seen that in addition to the focal shifting, a region of high pressure has split into a number of less well-defined subvolumes.

The splitting of the focal point is more clearly visualised in Figures 6.4(a)-(c), which show the isosurfaces of the focal pressure regions thresholded at -6 dB in the three patients. The simulations with refraction are shown with blue isosurfaces while the simulations without refraction are green and transparent. The target focal point is marked with a black cross. For simulations with refraction, the largest -6 dB focal volume was identified as the parent focal volume and the others as child volumes. The parent focal volume lengths and widths are presented in Table 6.3 for all three patients. In the case of patient 1 in Figure 6.4(a), it can be seen that the focal region consists of five focal volumes with the largest (i.e., the parent) being approximately 11.4 mm in length and 1.8 mm in width. The corresponding values were observed to be 9.5 and 1.4 mm in patient 2 and 7.3 and 1.2 mm in patient 3. On average the parent focal size was 9.4 mm in length and 1.5 mm in width. Without refraction there was no splitting of the focal volume and the focus coincided with the target. The average values for length and width of the focal point without refraction were 7.3 mm and 1.4 mm which are 22% and 7% smaller, respectively. For comparison, the size of the -6 dB focal point in water was approximately 6.5 mm in length and 1.3 mm in width. This indicates that it is refraction that dominates the shifts and splitting of the focus.

The splitting of the focal region was quantified by comparing the size and pressure distribution above -6 dB in the child volumes to those of the parent volume in each patient. This was done in order to estimate the heating efficacy of the child volumes. For a given pressure bin (defined between 50% and 100% of the global maximum pressure with 10% bin width) the cumulative volume of the child voxels in the bin was compared to the volume of all voxels in the parent focal point. Figure 6.5 shows a histogram of the analysis for three different patients.

In the 50-60% pressure region, the cumulative size of child voxels was approximately 28% of the parent focal point in patient 1. In patient 2 the same value was 23% while in patient 3 a considerably higher value of 81% was observed. This is also apparent from Figure 6.4(c), where the sizes of the child volumes are large compared to the parent focal volume. In the 60-70% pressure bin, the cumulative size of the child voxels was 13% in patient 1 and 9% in patient 3. However, patient 2 had no

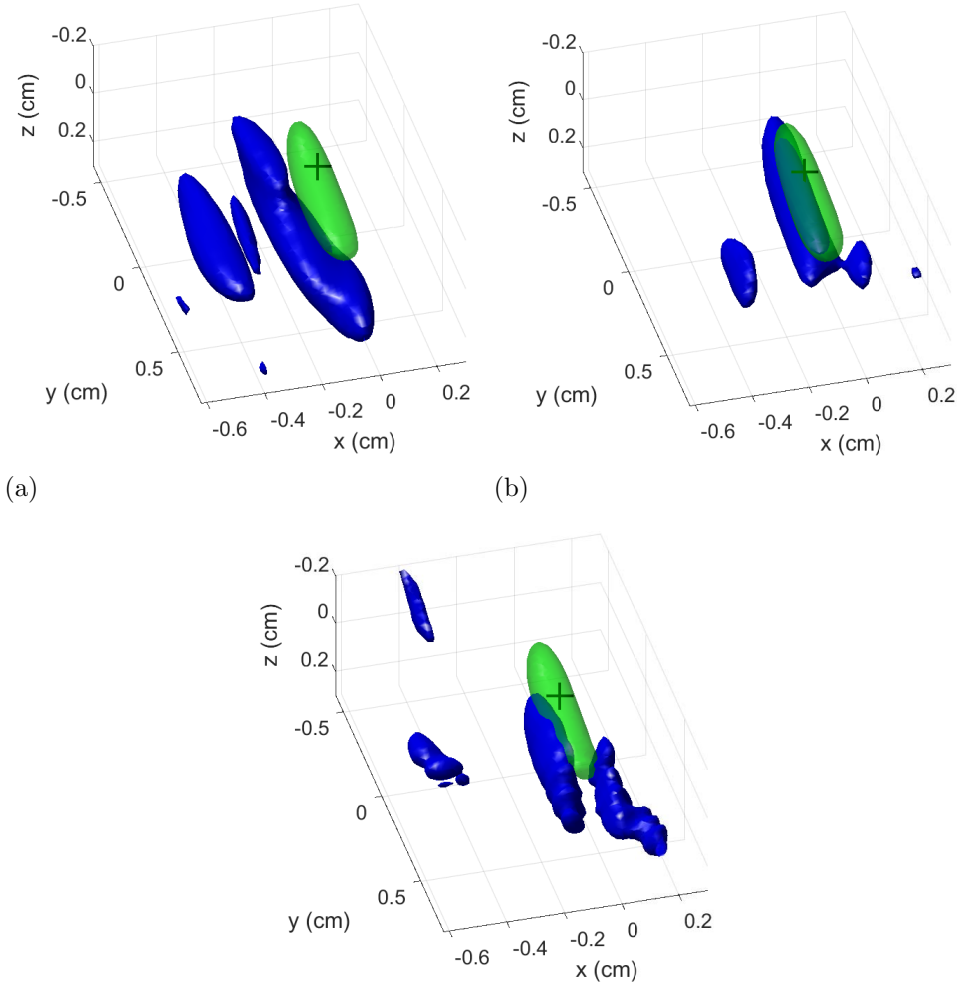

Figure 6.4: (a)-(c) The −6 dB focal point volumes in the kidney for patients 1-3, respectively. The simulations with refraction are shown with blue isosurfaces while the simulations without refraction are shown with transparent green isosurfaces. The target focal point is marked with a black cross. The shifting and splitting of the focal point into one parent and several child focal volumes due to refraction can be seen in different patients.

voxels in the child volumes above 60% of the global peak pressure, which can also be seen as a lower degree of splitting in Figure 6.4(b). At even higher pressures at 70-80% of the global peak pressure, only patient 1 had voxels in the child volumes, with a cumulative size of approximately 5% of the parent focal point. Above 80% of the global peak pressure none of the patients had voxels in child regions. The total volumes of the child regions with respect to the parent regions were 46%, 23% and 90% for patients 1-3, respectively. In other words, patient 3 had the highest degree of focal splitting. These data suggest that undesired heating effects might occur at child focal points due to focal point splitting.

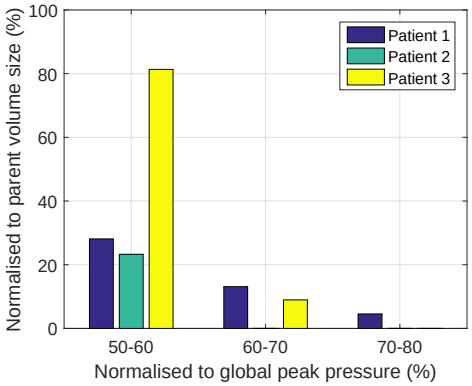

Figure 6.5: Histogram showing the pressure distribution in the child volumes with respect to the parent focal volume (i.e., the largest blue volumes) with bins varying from 50% to 80% of the global peak pressure in each case.

6.4.3 Temperature evolution and thermal dose

The evolution of the maximum temperature during a 120-second sonication in the three patients with and without refraction are shown in Figures 6.6(a) and (b), respectively. For the simulations with refraction (see Figure 6.6(a)), the temperature evolution in patients 1 and 2 follow similar trends with respective peak temperatures of 46.0 and 45.9 °C at the end of the sonication. In patient 3, however, the peak temperature is 43.5 °C, a 28% decrease in temperature elevation compared to the other two patients. This is most likely due to the higher degree of focal splitting as observed earlier. On average the peak temperature at the end of the sonication was 45.1 °C when refraction effects were incorporated (see Table 6.4 for summary).

The simulations without refraction (see Figure 6.6(b)) show similar peak temperatures (54.8, 54.0 and 55.2 °C) in all three patients. Here the peak temperatures at the end of the sonication are significantly higher when compared to the sonications with

Table 6.4: Thermal simulation results in three different patients after 120-second sonications. Simulations marked with (*) are without refraction effects.

	Peak temperature (°C)	Peak temp. shift Axial (mm)	Radial (mm)	240 $CEM_{43°C}$ size Length (mm)	Width (mm)	Volume (mm^3)
Patient 1	46.0	2.0	2.4	4.5	1.6	5.2
Patient 2	45.9	1.7	1.8	4.2	1.3	3.8
Patient 3	43.5	2.0	2.2	0.0	0.0	0.0
Average	**45.1**	**1.9**	**2.1**	**2.9**	**1.0**	**3.0**
SD	**1.2**	**0.1**	**0.2**	**2.1**	**0.7**	**2.2**
Patient 1*	54.8	1.7	0.6	9.8	4.2	95.8
Patient 2*	54.0	1.7	0.3	9.6	4.0	83.2
Patient 3*	55.2	0.9	0.3	9.7	4.3	94.5
Average	**54.7**	**1.4**	**0.4**	**9.7**	**4.2**	**91.2**
SD	**0.5**	**0.4**	**0.2**	**0.1**	**0.1**	**5.7**

refraction and the variation is small. This is consistent with the lack of focal splitting and small fluctuations in I_{SPTA} when refraction was neglected. On average the peak temperature at the end of the sonication was 54.7 °C, which is approximately 10 °C higher than with refraction, i.e., a doubling in the temperature rise.

The change in peak temperature, however, is not the complete story when it comes to thermal ablation. The treatment is desired over a volume and the location and the extent of the volume is important. Figures 6.7(a)-(c) show the 240 $CEM_{43°C}$ isosurfaces for each sonication both with (red) and without (yellow) refraction. It can be seen that adding refraction decreased the treated volume significantly (to zero

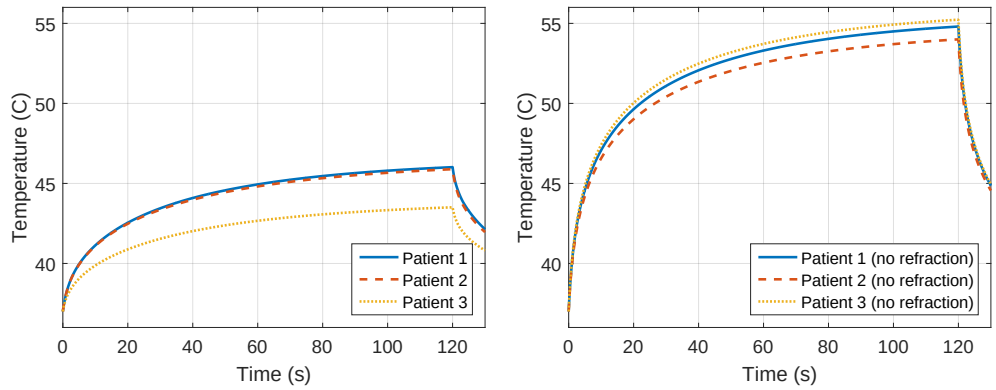

(a) (b)

Figure 6.6: Evolution of maximum temperature with time during a 120-second sonication in the kidney of all three patients (a) with refraction; and (b) without refraction (i.e., constant sound speed in all tissues).

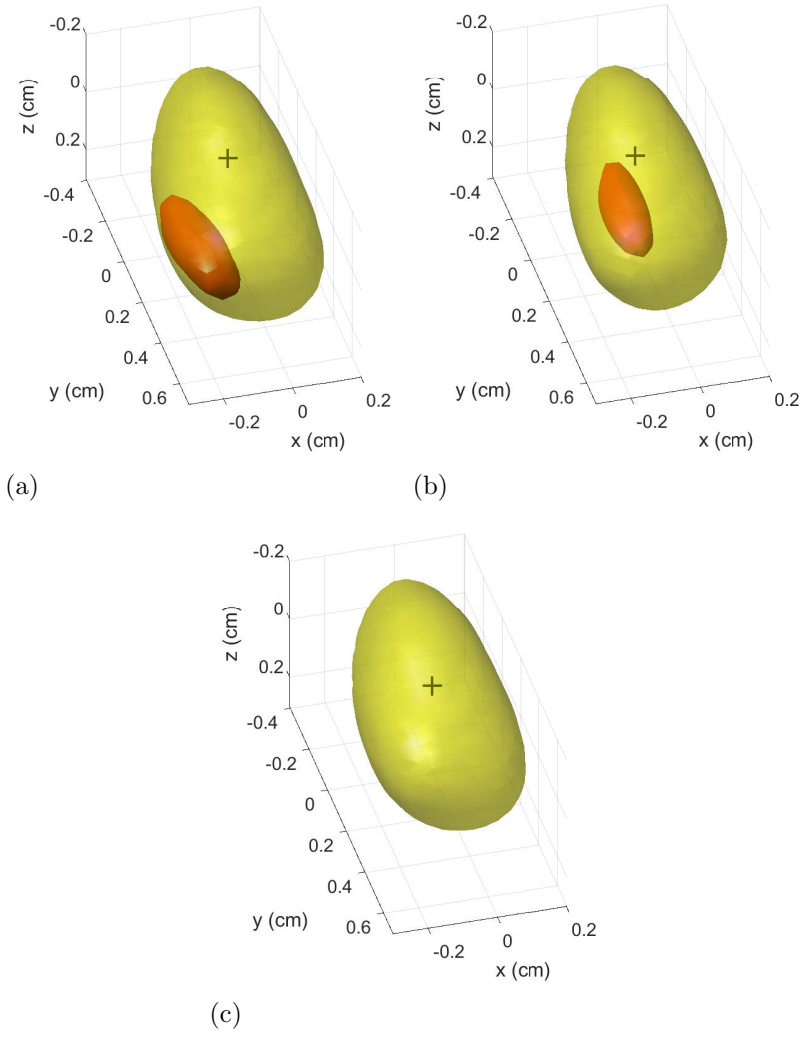

Figure 6.7: (a)-(c) Thermal dose volumes in the kidney after 120-second sonications for patients 1-3, respectively. The 240 $CEM_{43°C}$ thermal dose volumes with refraction are shown with red isosurfaces and the volumes without refraction with transparent yellow isosurfaces. The target focal point is marked with a black cross. No thermal dose above 240 $CEM_{43°C}$ was created in patient 3 when refraction effects were incorporated.

for patient 3) and resulted in shifts of the volume away from the target. Not only are the volumes significantly larger when refraction is absent, they are also evenly located around the target focal point. The size differences are also apparent when comparing the values in Table 6.4. On average the thermal dose volume with refraction was 3.0 mm^3. Without refraction the average volume was 91.2 mm^3 which is 30 times larger. Therefore, it is evident that focal point splitting is significantly affecting the creation of thermal dose in the kidney.

Table 6.4 gives numerical data for the changes in temperature and location of the thermal simulations. The average shifts in the peak temperature were 1.9 mm in the axial and 2.1 mm in the radial directions with refraction. These are comparable to the corresponding shifts in the peak pressure of 2.1 mm and 1.4 mm. Without refraction the shifts were reduced to 1.4 mm and 0.4 mm again comparable to the 1.2 mm and 0.3 mm shifts in the peak pressure locations.

6.4.4 Tissue property variability study

The evolution of the maximum temperature, when changing the attenuation, sound speed, perfusion and thermal conductivity of the kidney by ±2 SD in patient 1, are shown in Figures 6.8(a)-(d), respectively. Increasing attenuation from 1.00 to 1.24 $dB/MHz^{1.1}/cm$ (see Figure 6.8(a)) results in a slightly lower heating with the peak temperature of 45.5 °C at the end of the sonication when compared to the value of 46.0 °C with 'normal' attenuation. The decrease in attenuation results in slightly higher peak temperature of 46.6 °C. When the sound speed is changed by ±10 m/s (see Figure 6.8(b)), no significant differences in the peak temperature are seen. This suggests that the changes in sound speed of the kidney do not result in significant differences in focal splitting. The primary source of splitting is thus caused by the compounded effects of refraction from all the tissue layers in front of the transducer.

Decreasing perfusion (see Figure 6.8(c)) resulted in a peak temperature of 48.0 °C, which is 2.0 °C higher than with the normal perfusion value. Increasing perfusion resulted in 1.3 °C lower peak temperature of 44.7 °C. This suggests that perfusion is a significant tissue parameter affecting heating efficacy in the kidney. It has to be noted that the perfusion values used in the thermal simulations were those of renal medulla. The perfusion rate of renal cortex is approximately five-fold higher, which would result in even lower temperature values (Roberts et al., 1995). The decrease in thermal conductivity (see Figure 6.8(d)) resulted in a slightly higher peak temperature of 46.5 °C when compared to the normal value of 46.0 °C and 45.6 °C with increased thermal conductivity.

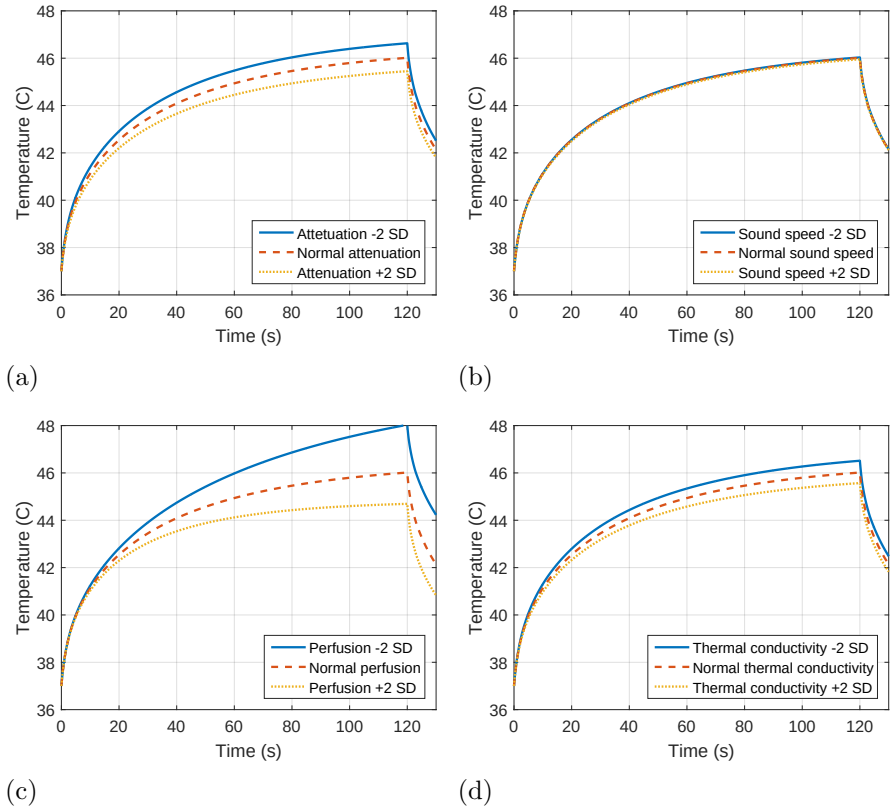

Figure 6.8: Evolution of maximum temperature with time during a 120-second sonication in the kidney of patient 1 with (a) attenuation, (b) sound speed, (c) perfusion and (d) thermal conductivity of the kidney changing by ±2 standard deviations (SD).

6.4.5 Aberration study

The simulations suggest that refraction has a dramatic effect on the desired heating in the kidney. The effects of refraction can be mitigated by adjusting the phase of the source using the principle of time-reversal (Fink, 1992). Using this technique, the aberration simulations were conducted with the same transducer positions, acoustic parameters and tissue parameters as in the ultrasound pressure simulations, but in a reverse manner. In this case, the therapeutic transducer was used as a receiver and an acoustic point pressure source was placed at the geometric focus of the transducer (i.e., inside the kidney of the patient). The acoustic point source was set to transmit a continuous wave at 0.95 MHz. The simulations were run using a computational grid of 640 × 640 × 640 grid points which supported harmonic frequencies up to 2 MHz. PMLs were used on the edges of the grid. The temporal resolution of the simulations was set to 15.99 ns which gave 17329 time steps per simulation with 277 μs simulation duration. The simulations were run using 320 computing cores with an

average simulation duration of 5.5 hours per simulation.

For data analysis, three cycles of the ultrasound pressure waveforms at the surface of the therapeutic transducer were saved for each grid point. The phase shifts of these ultrasound pressure waveforms were then calculated using the DFT at the fundamental frequency (0.95 MHz) and projected on the transducer plane for visualisation. The phase shifts were then unwrapped using a two-dimensional phase unwrapping algorithm (Goldstein et al., 1988; Ghiglia and Pritt, 1998) and the unwrapped values were similarly projected on the transducer face.

The phase shifts obtained directly from the DFT are presented in Figures 6.9(a)-(c) for patients 1-3, respectively. The phase shifts are presented using a cyclic colour map (i.e., phase shifts of $-\pi$ and π are the same colour) which allows visualisation of the areas with similar magnitude phase shifts. Areas of similar magnitude phase shifts are seen crossing the width of the transducer in the radial direction. Furthermore, a 'wave-like' behaviour is seen where the phase shifts increase and decrease subsequently when moving towards the upper right corner of the transducer.

The unwrapped phase shifts are presented in Figures 6.9(d)-(f) for patients 1-3, respectively. The phase shifts follow a trend which starts from the lower left part of the transducer and increases towards the upper right corner in all three patients. The areas with negative phase shifts are on the lower left section while the positive phase shifts are located on the upper right section. Some artefacts appear as horizontal lines in the areas where the algorithm was unable to resolve the underlying phase shift, however, the behaviour suggest that a function representation of the spatial phase shifts is possible due to the relatively smooth transition.

In order to quantify the phase shifts on the transducer face, a second order polynomial function was fit to the unwrapped phase data in the form:

$$\varphi(x, z)\ \text{(radians)} = p_{00} + p_{10}x + p_{01}z + p_{20}x^2 + p_{11}xz + p_{02}z^2 \tag{6.1}$$

where φ is the phase shift at the spatial location (x, z); and p_{00}-p_{02} are the fitting parameters with the corresponding subscripts. The second order polynomial fits to the unwrapped phase data according to are shown in Figures 6.9(g)-(i) for patients 1-3, respectively. The polynomial fitting parameters together with the corresponding coefficients of determination R^2 are shown in Table 6.5. In all three patients, the second order polynomial function represents the underlying spatial phase shifts with $R^2 \geq 0.83$.

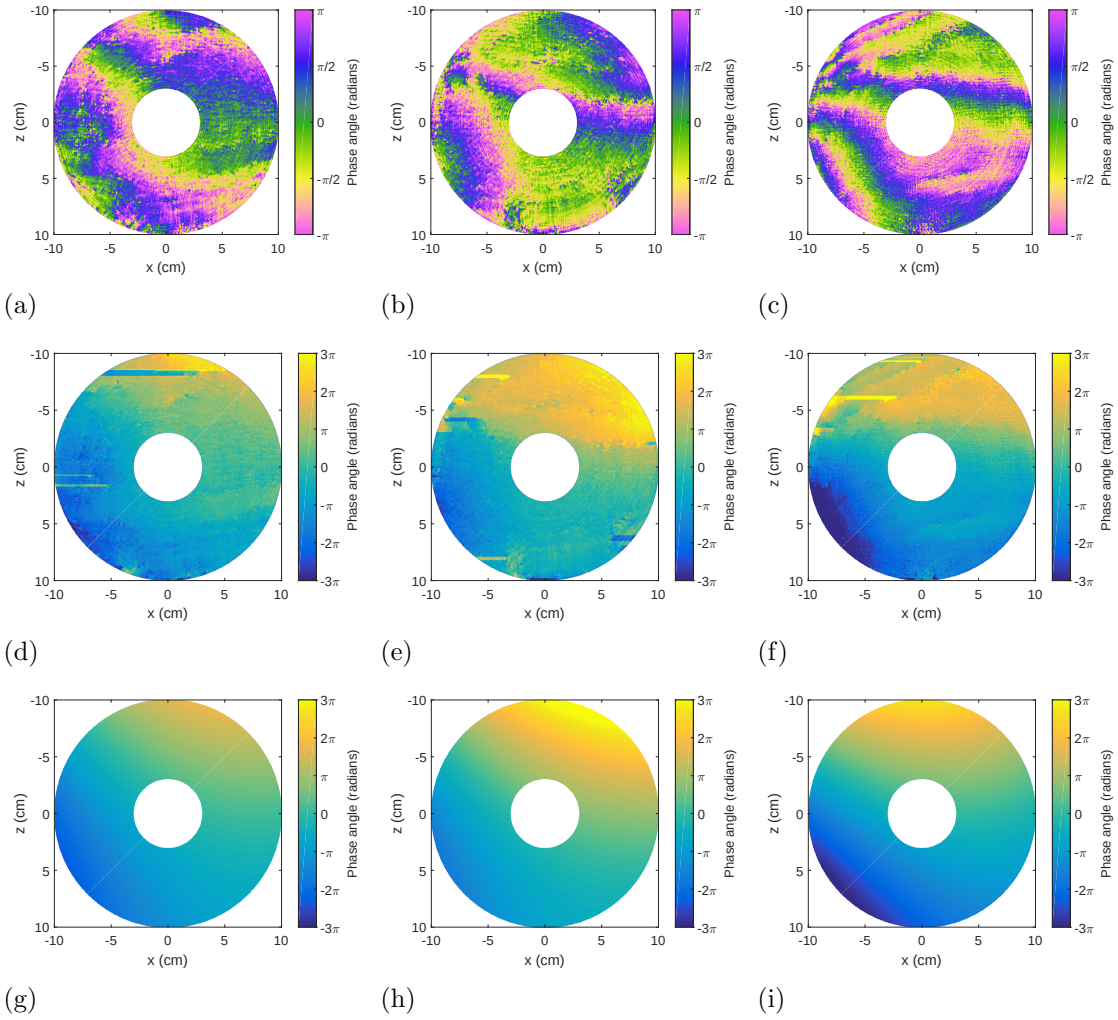

Figure 6.9: (a)-(c) Wrapped, (d)-(f) unwrapped and (g)-(i) fitted second order polynomial phase shifts for patients 1-3, respectively. The therapeutic transducer was used as a receiver for an acoustic point source located at the geometric focus.

Table 6.5: The second order polynomial surface fitting parameters on unwrapped phase aberration data.

	p_{00}	p_{10}	p_{01}	p_{20}	p_{11}	p_{02}	R^2
Patient 1	−0.9749	0.3462	−0.4437	−0.0215	−0.0002	0.0147	0.831
Patient 2	1.0920	0.3599	−0.5993	−0.0198	−0.0140	0.0253	0.840
Patient 3	−0.5279	0.2506	−0.7787	−0.0291	0.0260	0.0131	0.872

6.5 Discussion

In this study acoustic and thermal simulations in kidney have been carried out in realistic patient models. In the acoustic simulations in the body, the I_{SPTA} in the kidney dropped by 11.1 dB compared to simulations in water, which corresponds to a 92% drop in intensity. This effect was due to a combination of attenuation and refraction. By turning off refraction in the simulations the I_{SPTA} drop was reduced to 6.4 dB (77%). This suggests that attenuation and refraction have a similar impact on the intensity loss at the focus, contributing about 5 to 6 dB each. In practice, however, the energy loss could be even higher due to the attenuation properties of kidney-surrounding peri-nephric fat. Ritchie et al. (2013) studied the attenuation of peri-nephric fat tissue samples and found it to be significantly higher (1.36 dB/cm) compared to typical fat tissue attenuation (0.48 dB/cm) (Mast, 2000). In the simulations reported here, the segmentation was not able to distinguish different fat types and the typical value of 0.48 dB/cm was applied everywhere. For the patient datasets the thickness of peri-nephric fat was estimated to range between 0.4-1.6 cm, which would contribute an extra 0.35-1.41 dB of loss. This would give the total loss of 12.5 dB, i.e., a 2%-point increase to 94%. The most significant attenuation losses were caused by subcutaneous fat and soft tissue in front of the kidney whose thickness were approximately 1.8-2.6 and 3.0-5.0 cm, respectively.

In the simulations with refraction, focal splitting was found to reduce the ultrasound intensity considerably. At interfaces, changes in sound speed result in refraction, and in addition, the phase accumulation will change in different tissues affecting the constructive and destructive interference of the ultrasound waves. When focal point splitting was present, the cumulative size of the child focal volumes were found to be between 23-90% of the parent focal point. The pressure distribution analysis in the child volumes also showed peak pressures reaching up to 80% of the global peak pressure, which suggest that considerable heating might occur in the child regions.

The presence of refraction was also shown to result in focal shifts with average axial and radial shifts of 2.1 and 1.4 mm, respectively. The axial shifts are relatively

small compared to the average axial parent −6 dB focal length (9.4 mm). In the radial direction the shifts are large in terms of the average −6 dB focal width (1.5 mm), and thus, they might result in an offset in the lesion creation. Focal shifting due to subcutaneous and peri-nephric fat was studied by Ritchie et al. (2013) who found the shift to be approximately 1 mm in both transverse directions. In reality, the shifts are not only affected by the thickness of the tissue layers but also their geometries. However, these shifts are still small compared typical renal tumour sizes of several centimetres (Remzi et al., 2007).

In addition to attenuation and refraction, energy losses also occur due to reflections and scattering at interfaces, such as, the rib cage, tissue interfaces and air pockets. In the simulations the transducer was positioned so that reflections due to rib bones and air pockets were not present. For the parameters used here, the normalised intensity transmission coefficients for water-fat, fat-soft tissue, soft tissue-fat and fat-kidney interfaces were 99.84%, 99.29%, 99.29% and 99.41%, respectively. For all the interfaces the total transmission is 97.85% which corresponds to a loss of less than 0.1 dB. This is consistent with the findings by Damianou (2004), who studied the penetration of HIFU in rabbit kidney *in vivo*. They found the ultrasound penetration through muscle-kidney and fat-kidney interfaces to be excellent in a situation where no air bubbles were present. However, in some cases air spaces existed in between these interfaces which caused strong reflections and acted as possible sites for cavitation during the HIFU therapy.

Thermal simulations were conducted with 120-second sonications in each patient. The sonication times were long due to the relatively low I_{SPTA} of the ultrasound fields (on average 318 W/cm^2 with refraction). Thermal simulations with refraction showed the impact of patient variability. Patients 1 and 2 achieved similar heating over the course of sonication, however, patient 3 showed significantly degraded heating efficiency with a 28% drop in temperature rise. However, when the same simulations were done without refraction, all three patients showed similar temperature increases with patient 3 showing even slightly higher temperatures at the end of the sonication. The pressure distribution analysis showed that patient 3 had the highest degree of focal splitting with the cumulative size of child volumes being 90% of the parent focal volume. The same values for patient 1 and 2 were 46% and 23%, respectively. This suggest that focal splitting is a significant factor affecting the heating efficacy of the ultrasound field and that the effect is patient-specific. This is consistent with the variability observed in the clinical studies.

Although focal splitting potentially provides larger total heating volume, the efficiency is reduced, because the acoustic energy is distributed over a larger volume, which leads to longer therapy times, and more importantly, may result in undesired heating in regions away from the target region. In the simulations, the lower degree of focal splitting consequently lead to larger lesions, i.e., volumes of 240 $\mathrm{CEM}_{43^\circ\mathrm{C}}$ thermal dose. When refraction effects were present, no lesion was created in patient 3, while small, off-target lesions were created in patients 1 and 2. All the lesions with refraction were up to 2 mm offset from the target location. The thermal simulations without refraction created lesions on average 30 times larger over the course of 120-second sonication. Not only were the lesions larger, but they were also centred at the target focal point.

The effect of variation in tissue parameters on the heating efficiency of HIFU therapy was also studied by individually changing the values for attenuation, sound speed, perfusion and thermal conductivity of the kidney within their physiological variance (Roberts et al., 1995; Turnbull et al., 1989; Hasgall et al., 2015). Attenuation was found to have a small effect on heating efficiency with lower attenuation achieving slightly higher temperatures. Similar small changes were seen when thermal conductivity was varied within its physiological variance. No visible changes in the temperature were seen when the sound speed was varied, which indicates that the changes in refraction in the kidney alone do not affect the degree of focal splitting, but it is rather determined by the compound effect of all the tissue layers before the focal point. Perfusion was found to have the biggest effect on temperature. Lower perfusion lead to approximately a 2 °C higher peak temperatures at the end of the sonication when compared to the average value. This is consistent with observations made by Chang et al. (2004), who found the obstruction of the blood flow to increase the size of the created thermal lesions in kidneys. The perfusion values used in the thermal simulations were for renal medulla (i.e, the inner part of the kidney), which are lower than those of renal cortex (Roberts et al., 1995). Therefore, sonication of the renal cortex would result in even lower temperatures. The effect of perfusion, and thermal diffusion thereof, can potentially be eliminated by using high intensities with sonication durations less than few seconds (Billard et al., 1990; Chen et al., 1993). However, due to high losses in the propagation to the kidney, this could lead to significant pre-focal heating and possible skin damage (Watkin et al., 1996).

The effective source of focal splitting associated with refraction was evaluated by back propagating a spherical wave from the target location to the transducer face. The resulting phase was not uniform, but exhibited a relatively smooth transition

with negative and positive phase shifts occurring on the lower left and upper right corners of the transducer face, respectively. This behaviour is consistent with the thickness of tissue, particularly subcutaneous fat, and supports the hypothesis that it is the outer tissue layers that contribute to the splitting. What these simulations further suggest is that by correcting the phase at the surface a specific patient, the splitting effects could be minimal.

Another phenomenon that has been shown to reduce the efficacy of renal HIFU therapy is respiratory movement (Schwartz et al., 1994; Marberger et al., 2005). The respiration-induced movement of kidneys has been shown to be approximately 16-17 mm in the craniocaudal direction (i.e., from head to feet) (Bussels et al., 2003), which is large compared to the radial size of the simulated focal points ($\sim$1.5 mm). This effect was not incorporated in the simulation model, but could potentially result in significant reduction in heating efficiency and generation of unintended lesions caused by overheating of adjacent healthy tissue. In practice, this effect can be controlled using respiratory gating (Muller et al., 2013), but in this case the sonication durations have to be significantly shorter than used here.

6.6 Conclusions

The efficacy of HIFU therapy of the kidney was investigated with fully three-dimensional acoustic and thermal simulations in three different patients. The acoustic simulations showed that the intensity of the ultrasound field dropped on average by 11.1 dB when all effects were present. It was found that the intensity loss could be roughly divided equally between attenuation and refraction. Reflections due to the rib cage could possibly cause significant losses, but in these simulations were avoided by optimal positioning of the transducer. The reflections due to tissue interfaces were found to be minimal with a total loss of less than 0.1 dB. Refraction also lead to splitting of the focal zone and shifting of the position of the focus.

Thermal simulations showed the refraction effects to almost halve the heating efficacy (i.e., the temperature rise) of the ultrasound field. Without refraction the temperature increase at the end of the sonication was approximately two-fold when compared to the simulations with refraction. This indicates the degree of focal splitting to be a significant factor affecting the efficacy of the treatment. The splitting was patient-specific and may be responsible for variability in patient outcomes.

The effect of variation in kidney attenuation, sound speed, perfusion and thermal conductivity on HIFU heating was also studied. Variations in perfusion were found to be the biggest factor affecting the heating. Small changes in the temperature were seen when the attenuation and thermal conductivity were changed, but no visible changes were observed with sound speed.

Back-propagation simulations revealed an underlying trend in the phase shifts with negative and positive values occurring at the lower left and upper right areas of the transducer. Second order polynomial functions representing the spatial shifts were determined, which could be used for aberration correction during the HIFU therapy in the kidney by defining the spatial space shifts on the transducer face.

These results suggest that the delivery of HIFU therapy to the kidney results in significant energy loss and is patient-specific. Two approaches to overcome this are: (i) to increase the intensity of the ultrasound field and (ii) to reduce the degree of focal splitting. The former method contains a risk of unpredictable pre-focal heating, cavitation and skin burns. The latter can be achieved with aberration correction at the source, but this requires a HIFU system with multiple transmitting elements in the transducer. In either scenario patient-specific treatment planning would need to be carried out in order to determine the appropriate source conditions.

Chapter 7

Summary and conclusions

The goal of this thesis was to reduce barriers to the use of HIFU for ablation of soft tissue, and more specifically, to identify methods to improve the monitoring of HIFU therapy with ultrasound elastography and the delivery of HIFU energy to the kidney. As stated in the first chapter, the three objectives for the thesis were:

(i) *to quantify the temperature dependent tissue parameters affecting the ARF*

(ii) *to evaluate their effect on ARF induced displacements*

(iii) *to characterise therapeutic HIFU fields in the human body*

All of these points were addressed in this thesis using a combination of experimental methods and simulations.

7.1 Summary

The first chapter introduced the principles of HIFU therapy and gave a brief overview of the history of HIFU. The history of HIFU started in the 1920s (Wood and Loomis, 1927) and has since evolved into a significant therapy method which has a wide number of clinical applications with over 116,000 patients treated to date (Foley, 2016). The number of companies in the field of HIFU has also grown steadily in the past 20 years is now standing at 32 (Foley, 2016). All the signs indicate that HIFU therapy is a rapidly growing field with new clinical applications and hundreds of research papers published every year. The new therapeutic applications also introduce challenges for therapy monitoring, and therefore, alternative imaging modalities, such as ultrasound elastography, are needed to achieve the desired clinical outcome.

In the second chapter, the relevant acoustic, thermal and mechanical tissue parameters were extensively reviewed using the published literature (Suomi and Cleveland,

2017). The temperature dependence of each tissue property was quantified and polynomial models were fit to the data. Quantification of the temperature dependence of tissue parameters is important in HIFU monitoring, in which rapid temperature rises cause tissue properties to change. The changes in tissue properties consequently affect the displacements induced by ARF, and thus, the therapy monitoring capabilities of ultrasound elastography applications. *A priori* knowledge of these tissue property changes enables them to be taken into account in therapy monitoring and increase its reliability. Furthermore, the derived numerical expressions for temperature dependence can also be used in computational simulations of ARF excitation.

In the third chapter, the fundamental equations for acoustic, thermal and viscoelastic models used in the thesis were introduced. All the acoustic models were nonlinear incorporating the generation of harmonic frequencies. This is an important factor especially in HIFU, because the nonlinearly generated harmonics can potentially cause higher heating rates and larger displacements during ARF excitation. The thermal model was based on the BHT equation which took into account tissue perfusion and heating rate due to nonlinear ultrasound pressure fields. The viscoelastic models were used to accurately predict the displacements induced by ARF. All the viscoelastic models were linear, which is a justifiable assumption in the case of ARF, as only small magnitude deformations are induced.

The fourth chapter presented the published work (Suomi et al., 2015) on quantifying ARF induced displacements in a tissue-mimicking phantom. An optical system was employed to experimentally measure the characteristics of the harmonic ARF deformations using both sine and square amplitude modulation. It was shown that using square modulation results in higher peak-to-peak amplitudes and smaller phase shifts. Furthermore, in the frequency domain, square modulated displacements had lower second harmonic components when compared to sine modulated displacements. The FEM simulation model using the measured acoustic and viscoelastic parameters was able to quantitatively capture ARF induced displacements over a range of intensities and modulation frequencies. The results show that numerical models can be used to accurately predict displacements induced by ARF.

The fifth chapter expanded the study on quantifying ARF induced displacements and took into account the effect of temperature - an important aspect in HIFU monitoring. The study (Suomi et al., 2016a) utilised the temperature dependence of acoustic and viscoelastic parameters determined in the second chapter, and applied them to a FEM simulation model to examine their effect on ARF deformations. The attenuation was shown to have a slight effect on displacement values before thermal

ablation. The change in viscoelastic properties after thermal ablation was the dominating effect rapidly reducing the displacement amplitude. This behaviour was also observed in the HMI experiments in *ex vivo* liver. It was further shown that in some cases the effects of increasing attenuation and stiffness might cancel each other out resulting in similar measured displacement values before and after ablation. Therefore, it is necessary to monitor ARF displacements continuously during thermal ablation to ascertain when ablation occurs.

In the sixth chapter, the effect of different tissue layers of the human body on HIFU therapy of the kidney was studied (Suomi et al., 2016b). The work was motivated by clinical data from various studies showing that the outcomes of the treatment are very variable. Therefore, nonlinear acoustic and thermal simulations were carried out for three different clinical patients based on the CT data. The ultrasound intensity reduction due to reflections at tissue interfaces was found to be negligible. The loss of focal energy was shown to be due to the combined effect of attenuation and refraction. Refraction caused the ultrasound focal point to split into several smaller subvolumes reducing the overall heating efficacy of HIFU therapy. To overcome the refraction effects, an aberration study was also conducted in order to determine the phase shifts at the transducer face. These data could potentially be used to account for refraction in order to achieve a more uniform single focal point. Furthermore, the acquired data are useful for defining the transducer design for future studies in terms of the number of elements and their sizes.

7.2 Research contributions

The work presented in this thesis has been published in two journal papers (Suomi et al., 2015, 2016a), one conference paper (Suomi et al., 2016b) and one book chapter (Suomi and Cleveland, 2017). In particular, new data was provided with the following contributions:

- Harmonic ARF induced displacements were quantified with 50, 160 and 1000 Hz frequencies using both sine and square AM. These data showed that higher displacement amplitudes, smaller phase shifts and lower second harmonic components are achieved using square modulation.

- A viscoelastic FEM model was successfully employed to reproduce ARF induced displacements in absolute values in contrast to most other studies which show

normalised data. This shows that similar models can accurately be used to predict μm-scale displacements induced by ARF.

- Quantitative data were provided on the temperature dependence of acoustic, thermal and mechanical properties in several tissue types. Although the data were collected from the published literature, they were extensively summarised and provide a useful reference for future studies.

- Viscoelastic data for the temperature dependence of *ex vivo* liver tissue were measured. This is also a contribution to the tissue characterisation literature. Furthermore, a fractional Zener model was fit to the data to provide parameters for viscoelastic simulation models.

- The effect of temperature dependent acoustic and viscoelastic changes on ARF induced displacements was studied in liver. The data showed that attenuation should be considered at temperatures below 60 °C, but after ablation the changes in viscoelasticity are the dominant effect reducing the amplitude.

- Attenuation and refraction were shown to be the main effects reducing the efficacy of HIFU therapy in the kidney. Both effects contributed to an approximately 5-6 dB intensity loss.

- Patient-specific phase shifts at the transducer face were determined and second order polynomial functions were fit to the data. These data can be used to evaluate the aberration correction values to compensate the refraction effects.

7.3 Future work

Although the work presented in this thesis addressed several problems, it also identified gaps in the literature and aspects that should be considered in therapy monitoring and treatment planning. Looking at the published literature on temperature dependence of different tissues, there exist several areas in which there is currently insufficient data to draw reliable conclusions. The sound speed is well covered for most relevant tissues, except brain and fat. This is especially evident at higher temperatures above 60 °C. The same applies to attenuation data for brain, prostate and fat tissue, which are lacking data in the temperature regime above 60 °C. Furthermore, the attenuation data measured before and after thermal ablation has been well characterised for liver, but not for any other tissue. Liver and muscle are also the only

organs for which there are measured data for the nonlinearity parameter B/A. However, in this case more data for all tissues are required to make conclusions. In terms of mechanical properties, more elastic (Young's and shear moduli) and viscoelastic (dynamic modulus) measurements are needed for kidney and brain tissues.

The study on temperature dependence of ARF displacements could be expanded to cover other organs as well. For example, kidney, prostate and brain tissue all exhibit similar behaviour of increasing attenuation below ablative temperatures. Since these tissues have different mechanical properties, the effect on ARF induced displacements should be studied. With respect to therapy monitoring, ARF has not widely been studied in brain tissue due to the strongly reflecting skull bone and aberration effects. MR-ARFI has been used to measure the stiffness of brain tissue but only without thermal ablation. Therefore, studying the possibility of using ultrasound elastography (without MRI) to monitor HIFU treatment in brain is one future possibility. Since therapeutic intensities have been produced inside the brain, the same ultrasound fields could also be used to induce ARF. The problem to solve, however, is how to compensate for the refraction and reflection effects of the pulses which are tracking the ARF displacements through the skull. This seems like a tempting opportunity especially now that new brain applications are emerging such as the treatment of essential tremor and ultrasonic neuromodulation. Liver is well established as a target for HIFU with excellent acoustic access and minimal aberration effects. However, the movement of liver during the breathing cycle has to be compensated for before effective ablation and monitoring of the therapy becomes feasible.

The simulations of HIFU therapy in the kidney showed the importance of aberration correction in increasing heating efficacy. Since the patient-specific values for aberration correction were determined, the next step would be to apply these values to a number of elements on the transducer face. A simulation study should be run in order to determine the optimal number, location and size of these elements to compensate for refraction in different patients. After this, experimental studies using the obtained transducer geometries could be performed to validate the design. Another possibility would be to utilise the phase shift data to create a patient-specific acoustic lens, which could similarly be used to cancel out refraction. The effectiveness of the design should also be validated with experimental studies. From the therapy monitoring perspective, ultrasound elastography in the kidney is another largely unexplored area. The feasibility of using ARF in the kidney could be studied using the presented viscoelastic simulation models and experiments. In this case, patient specific aberration correction should also be used.

Appendix A

Numerical solution to heat equation

The heat equation is a PDE which describes the change in temperature in a given spatial domain over time. In general form the heat equation is defined as (Widder, 1976):

$$\boxed{\frac{\partial T}{\partial t} = D\nabla^2 T} \tag{A.1}$$

which in three spatial dimensions can be written as:

$$\frac{\partial T}{\partial t} = D\left(\frac{\partial^2 T}{\partial x^2} + \frac{\partial^2 T}{\partial y^2} + \frac{\partial^2 T}{\partial z^2}\right) \tag{A.2}$$

where x, y and z [m] are the spatial coordinates. The three-dimensional heat equation can be discretised as (Ames, 1977):

$$\begin{aligned}\frac{T^{\text{new}} - T}{\Delta t} = D\Bigg[&\left(\frac{T_{-x} - 2T + T_{+x}}{2\Delta x^2}\right) + \left(\frac{T_{-x}^{\text{new}} - 2T^{\text{new}} + T_{+x}^{\text{new}}}{2\Delta x^2}\right) \\ &+ \left(\frac{T_{-y} - 2T + T_{+y}}{2\Delta y^2}\right) + \left(\frac{T_{-y}^{\text{new}} - 2T^{\text{new}} + T_{+y}^{\text{new}}}{2\Delta y^2}\right) \\ &+ \left(\frac{T_{-z} - 2T + T_{+z}}{2\Delta z^2}\right) + \left(\frac{T_{-z}^{\text{new}} - 2T^{\text{new}} + T_{+z}^{\text{new}}}{2\Delta z^2}\right)\Bigg]\end{aligned} \tag{A.3}$$

where T and T^{new} [K/°C] are the current and new temperatures respectively; Δt [s] is the temporal resolution; Δx, Δy and Δz [m] are the spatial resolutions; and the subscripts $-x$, $-y$, $-z$, $+x$, $+y$, $+z$ refer to one positive or negative step in each spatial direction with respect to the location of T and T^{new}.

In this form, the three-dimensional heat equation has a total of seven unknown new temperature values for every location of T (two in each spatial direction plus

the central point). The equation could potentially be solved in this form using the Crank-Nicolson (CN) method (Crank and Nicolson, 1947), which combines explicit and implicit form of the right-hand side and is unconditionally stable. CN method works well with one-dimensional heat equations which can be solved in the tridiagonal matrix form. However, in three dimensions, this would result in a sparse matrix with seven diagonal matrix bands, which is computationally heavy to solve. This problem can be overcome by using so-called alternating direction implicit (ADI) method (Ames, 1977) which applies the CN method one direction at a time using two intermediate temperature fields T^* and T^{**} before obtaining the new temperature field T^{new}.

By applying the ADI method first in x-direction the equation (A.3) becomes:

$$\begin{aligned} T^* - T = {} & \overbrace{\frac{D\Delta t}{\Delta x^2}}^{\text{r}_1}\left[\left(\frac{T_{-x} - 2T + T_{+x}}{2}\right) + \left(\frac{T^*_{-x} - 2T^* + T^*_{+x}}{2}\right)\right] \\ & + \underbrace{\frac{D\Delta t}{\Delta y^2}}_{\text{r}_2}(T_{-y} - 2T + T_{+y}) + \underbrace{\frac{D\Delta t}{\Delta z^2}}_{\text{r}_3}(T_{-z} - 2T + T_{+z}) \end{aligned} \tag{A.4}$$

By sorting the new and current temperatures on the left and right sides, respectively, the equation can then be written as:

$$\begin{aligned} -\frac{r_1}{2}T^*_{-x} + (1 + r_1)T^* - \frac{r_1}{2}T^*_{+x} = {} & \frac{r_1}{2}T_{-x} + \frac{r_1}{2}T_{+x} + r_2T_{-y} + r_2T_{+y} \\ & + r_3T_{-z} + r_3T_{+z} + (1 - r_1 - 2r_2 - 2r_3)T \end{aligned} \tag{A.5}$$

Now, on the left hand side, there are three unknown temperature values T^*_{-x}, T^* and T^*_{+x} while the right hand side is known. Solving the equation over the whole spatial domain results in a tridiagonal matrix. This can be efficiently done by using a tridiagonal matrix algorithm, such as the Thomas algorithm (Ames, 1977), to obtain the unknown intermediate temperature values T^*_{-x}, T^* and T^*_{+x} for every x, y and z. Next, by applying ADI method in y-direction, the equation (A.3) becomes:

$$\begin{aligned} T^{**} - T = {} & r_1\left[\left(\frac{T_{-x} - 2T + T_{+x}}{2}\right) + \left(\frac{T^*_{-x} - 2T^* + T^*_{+x}}{2}\right)\right] \\ & + r_2\left[\left(\frac{T_{-y} - 2T + T_{+y}}{2}\right) + \left(\frac{T^{**}_{-y} - 2T^{**} + T^{**}_{+y}}{2}\right)\right] \\ & + r_3(T_{-z} - 2T + T_{+z}) \end{aligned} \tag{A.6}$$

which again can be sorted by placing the unknown temperature values on the left and the known values on the right:

$$-\frac{r_2}{2}T^{**}_{-y} + (1+r_2)T^{**} - \frac{r_2}{2}T^{**}_{+y} = \frac{r_1}{2}T_{-x} + \frac{r_1}{2}T_{+x} + \frac{r_1}{2}T^{*}_{-x} + \frac{r_1}{2}T^{*}_{+x} + \frac{r_2}{2}T_{-y} + \frac{r_2}{2}T_{+y} + r_3T_{-z} + r_3T_{+z} + (1-r_1-r_2-2r_3)T - r_1T^{*} \tag{A.7}$$

This can again be solved using the tridiagonal matrix algorithm to obtain T^{**}_{-y}, T^{**} and T^{**}_{+y} for every x, y and z. Finally, the z-direction values can be solved to obtain the new temperature field as:

$$T^{\text{new}} - T = r_1\left[\left(\frac{T_{-x} - 2T + T_{+x}}{2}\right) + \left(\frac{T^{*}_{-x} - 2T^{*} + T^{*}_{+x}}{2}\right)\right] + r_2\left[\left(\frac{T_{-y} - 2T + T_{+y}}{2}\right) + \left(\frac{T^{**}_{-y} - 2T^{**} + T^{**}_{+y}}{2}\right)\right] + r_3\left[\left(\frac{T_{-z} - 2T + T_{+z}}{2}\right) + \left(\frac{T^{\text{new}}_{-z} - 2T^{\text{new}} + T^{\text{new}}_{+z}}{2}\right)\right] \tag{A.8}$$

which can be expressed as:

$$-\frac{r_3}{2}T^{\text{new}}_{-z} + (1+r_3)T^{\text{new}} - \frac{r_3}{2}T^{\text{new}}_{+z} = \frac{r_1}{2}T_{-x} + \frac{r_1}{2}T_{+x} + \frac{r_1}{2}T^{*}_{-x} + \frac{r_1}{2}T^{*}_{+x} + \frac{r_2}{2}T_{-y} + \frac{r_2}{2}T_{+y} + \frac{r_2}{2}T^{**}_{-y} + \frac{r_2}{2}T^{**}_{+y} + \frac{r_3}{2}T_{-z} + \frac{r_3}{2}T_{+z} + (1-r_1-r_2-r_3)T - r_1T^{*} - r_2T^{**} \tag{A.9}$$

Solving this equation for every x, y and z gives the new temperature values $T^{\text{new}}_{-z}, T^{\text{new}}$ and T^{new}_{+z} over the whole spatial domain. All three iterations for x-, y- and z-directions above have to done for each time step. However, because the solution is unconditionally stable, the time step can be much larger than it would be in the explicit case. The errors of ADI solution are in the order of $\mathcal{O}\big((\Delta t)^2\big)$ and $\mathcal{O}\big((\max[\Delta x, \Delta y, \Delta z])^2\big)$, which gives it an advantage over the explicit methods, whose errors are typically $\mathcal{O}(\Delta t)$ and $\mathcal{O}\big((\max[\Delta x, \Delta y, \Delta z])^2\big)$. A Matlab-code for the numerical solution of the three-dimensional heat equation can be found from (Suomi, 2016).

References

Ames, W. F. *Numerical methods for partial differential equations*. Academic press, 1977.

Anema, S. G. and McKenna, A. B. Reaction kinetics of thermal denaturation of whey proteins in heated reconstituted whole milk. *Journal of Agricultural and Food Chemistry*, 44(2):422–428, 1996.

Arnal, B., Pernot, M., and Tanter, M. Monitoring of thermal therapy based on shear modulus changes: Ii. shear wave imaging of thermal lesions. *Ultrasonics, Ferroelectrics, and Frequency Control, IEEE Transactions on*, 58(8):1603–1611, 2011.

Bamber, J. and Hill, C. Ultrasonic attenuation and propagation speed in mammalian tissues as a function of temperature. *Ultrasound in medicine & biology*, 5(2):149–157, 1979.

Beissner, K. Exact integral expression for the diffraction loss of a circular piston source. *Acta Acustica united with Acustica*, 49(3):212–217, 1981.

Benech, N. and Negreira, C. A. Monitoring heat-induced changes in soft tissues with 1d transient elastography. *Physics in medicine and biology*, 55(6):1753, 2010.

Bercoff, J., Pernot, M., Tanter, M., and Fink, M. Monitoring thermally-induced lesions with supersonic shear imaging. *Ultrasonic imaging*, 26(2):71–84, 2004a.

Bercoff, J., Tanter, M., and Fink, M. Supersonic shear imaging: a new technique for soft tissue elasticity mapping. *Ultrasonics, Ferroelectrics, and Frequency Control, IEEE Transactions on*, 51(4):396–409, 2004b.

Bharat, S., Techavipoo, U., Kiss, M. Z., Liu, W., and Varghese, T. Monitoring stiffness changes in lesions after radiofrequency ablation at different temperatures and durations of ablation. *Ultrasound in medicine & biology*, 31(3):415–422, 2005.

Bhattacharya, A. and Mahajan, R. Temperature dependence of thermal conductivity of biological tissues. *Physiological measurement*, 24(3):769, 2003.

Billard, B., Hynynen, K., and Roemer, R. Effects of physical parameters on high temperature ultrasound hyperthermia. *Ultrasound in medicine & biology*, 16(4): 409–420, 1990.

Bing, K. F., Rotemberg, V. M., Palmeri, M. L., and Nightingale, K. R. Concurrent arfi imaging and hifu ablation using a diagnostic transducer array and ultrasound system with custom beam sequences. In *Ultrasonics Symposium (IUS), 2009 IEEE International*, pages 65–68. IEEE, 2009.

Bing, K. F., Rouze, N. C., Palmeri, M. L., Rotemberg, V. M., and Nightingale, K. R. Combined ultrasonic thermal ablation with interleaved arfi image monitoring using a single diagnostic curvilinear array: a feasibility study. *Ultrasonic imaging*, 33(4): 217–232, 2011.

Blana, A., Murat, F. J., Walter, B., Thuroff, S., Wieland, W. F., Chaussy, C., and Gelet, A. First analysis of the long-term results with transrectal hifu in patients with localised prostate cancer. *european urology*, 53(6):1194–1203, 2008.

Bouchard, R. R., Palmeri, M. L., Pinton, G. F., Trahey, G. E., Streeter, J. E., and Dayton, P. A. Optical tracking of acoustic radiation force impulse-induced dynamics in a tissue-mimicking phantom. *The Journal of the Acoustical Society of America*, 126(5):2733–2745, 2009a.

Bouchard, R. R., Van Soest, G., Trahey, G. E., and Van Der Steen, A. F. Optical tracking of superficial dynamics from an acoustic radiation force-induced excitation. *Ultrasonic imaging*, 31(1):17–30, 2009b.

Boyle, P. and Levin, B. *World cancer report 2008.* IARC Press, International Agency for Research on Cancer, 2008.

Bronez, M., Shung, K., Heidary, H., and Hurwitz, D. Measurement of ultrasound velocity in tissues utilizing a microcomputer-based system. *Biomedical Engineering, IEEE Transactions on*, (9):723–726, 1985.

Burov, A. and Andreevskaya, G. The effect of ultra-acoustic oscillation of high intensity on malignant tumors in animals and man. In *Dokl Akad Nauk SSSR*, volume 106, pages 445–8, 1956.

Bush, N., Rivens, I., Ter Haar, G., and Bamber, J. Acoustic properties of lesions generated with an ultrasound therapy system. *Ultrasound in medicine & biology*, 19(9):789–801, 1993.

Bussels, B., Goethals, L., Feron, M., Bielen, D., Dymarkowski, S., Suetens, P., and Haustermans, K. Respiration-induced movement of the upper abdominal organs: a pitfall for the three-dimensional conformal radiation treatment of pancreatic cancer. *Radiotherapy and Oncology*, 68(1):69–74, 2003.

Callé, S., Remenieras, J.-P., Matar, O. B., Hachemi, M. E., and Patat, F. Temporal analysis of tissue displacement induced by a transient ultrasound radiation force. *The Journal of the Acoustical Society of America*, 118(5):2829–2840, 2005.

Catheline, S., Gennisson, J.-L., Delon, G., Fink, M., Sinkus, R., Abouelkaram, S., and Culioli, J. Measurement of viscoelastic properties of homogeneous soft solid using transient elastography: an inverse problem approach. *The Journal of the Acoustical Society of America*, 116(6):3734–3741, 2004.

Cetas, T. and Connor, W. Thermometry considerations in localized hyperthermia. *Medical Physics*, 5(2):79–91, 1978.

Chang, I., Mikityansky, I., Wray-Cahen, D., Pritchard, W. F., Karanian, J. W., and Wood, B. J. Effects of perfusion on radiofrequency ablation in swine kidneys 1. *Radiology*, 231(2):500–505, 2004.

Chen, L., ter Haar, G., Hill, C., Dworkin, M., Carnochan, P., Young, H., and Bensted, J. Effect of blood perfusion on the ablation of liver parenchyma with high-intensity focused ultrasound. *Physics in medicine and biology*, 38(11):1661, 1993.

Chivers, R. and Parry, R. Ultrasonic velocity and attenuation in mammalian tissues. *The Journal of the Acoustical Society of America*, 63(3):940–953, 1978.

Choi, M. J., Guntur, S. R., Lee, J. M., Paeng, D. G., Lee, K. I., and Coleman, A. Changes in ultrasonic properties of liver tissue in vitro during heating-cooling cycle concomitant with thermal coagulation. *Ultrasound in medicine & biology*, 37(12): 2000–2012, 2011.

Clarke, R., Bush, N., and Ter Haar, G. The changes in acoustic attenuation due to in vitro heating. *Ultrasound in medicine & biology*, 29(1):127–135, 2003.

Cobbold, R. *Foundations of Biomedical Ultrasound*. Biomedical engineering series. Oxford University Press, 2006. ISBN 9780199775125.

Connor, C. W. and Hynynen, K. Bio-acoustic thermal lensing and nonlinear propagation in focused ultrasound surgery using large focal spots: a parametric study. *Physics in medicine and biology*, 47(11):1911, 2002.

Cosgrove, D., Piscaglia, F., Bamber, J., Bojunga, J., Correas, J., Gilja, O., Klauser, A., Sporea, I., Calliada, F., Cantisani, V., et al. Efsumb guidelines and recommendations on the clinical use of ultrasound elastography. part 2: Clinical applications. *Ultraschall Med*, 34(3):238–253, 2013.

Crank, J. and Nicolson, P. A practical method for numerical evaluation of solutions of partial differential equations of the heat-conduction type. In *Mathematical Proceedings of the Cambridge Philosophical Society*, volume 43, pages 50–67. Cambridge Univ Press, 1947.

Crouzet, S., Chapelon, J. Y., Rouviere, O., Mege-Lechevallier, F., Colombel, M., Tonoli-Catez, H., Martin, X., and Gelet, A. Whole-gland ablation of localized prostate cancer with high-intensity focused ultrasound: oncologic outcomes and morbidity in 1002 patients. *European urology*, 65(5):907–914, 2014.

Curiel, L. and Hynynen, K. Localized harmonic motion imaging for focused ultrasound surgery targeting. *Ultrasound in medicine & biology*, 37(8):1230–1239, 2011.

Curiel, L., Chopra, R., and Hynynen, K. In vivo monitoring of focused ultrasound surgery using local harmonic motion. *Ultrasound in medicine & biology*, 35(1): 65–78, 2009.

Curra, F. P., Mourad, P. D., Khokhlova, V. A., Cleveland, R. O., and Crum, L. A. Numerical simulations of heating patterns and tissue temperature response due to high-intensity focused ultrasound. *IEEE transactions on ultrasonics, ferroelectrics, and frequency control*, 47(4):1077–1089, 2000.

Czernuszewicz, T. J., Streeter, J. E., Dayton, P. A., and Gallippi, C. M. Experimental validation of displacement underestimation in arfi ultrasound. *Ultrasonic imaging*, 35(3):196–213, 2013.

Damianou, C. Mri monitoring of the effect of tissue interfaces in the penetration of high intensity focused ultrasound in kidney in vivo. *Ultrasound in medicine & biology*, 30(9):1209–1215, 2004.

Damianou, C. A., Sanghvi, N. T., Fry, F. J., and Maass-Moreno, R. Dependence of ultrasonic attenuation and absorption in dog soft tissues on temperature and thermal dose. *The Journal of the Acoustical Society of America*, 102(1):628–634, 1997.

Dasgupta, S., Banerjee, R. K., Hariharan, P., and Myers, M. R. Beam localization in hifu temperature measurements using thermocouples, with application to cooling by large blood vessels. *Ultrasonics*, 51(2):171–180, 2011.

Dickinson, R. and Hill, C. Measurement of soft tissue motion using correlation between a-scans. *Ultrasound in medicine & biology*, 8(3):263–271, 1982.

Diederich, C. J. and Burdette, E. C. Transurethral ultrasound array for prostate thermal therapy: initial studies. *Ultrasonics, Ferroelectrics, and Frequency Control, IEEE Transactions on*, 43(6):1011–1022, 1996.

Doherty, J. R., Trahey, G. E., Nightingale, K. R., and Palmeri, M. L. Acoustic radiation force elasticity imaging in diagnostic ultrasound. *IEEE transactions on ultrasonics, ferroelectrics, and frequency control*, 60(4):685–701, 2013.

Dong, F., Madsen, E. L., MacDonald, M. C., and Zagzebski, J. A. Nonlinearity parameter for tissue-mimicking materials. *Ultrasound in medicine & biology*, 25(5): 831–838, 1999.

Dubinsky, T. J., Cuevas, C., Dighe, M. K., Kolokythas, O., and Hwang, J. H. High-intensity focused ultrasound: current potential and oncologic applications. *American journal of roentgenology*, 190(1):191–199, 2008.

Duck, F. A. *Physical properties of tissues: a comprehensive reference book*. Academic press, 1990.

Dunn, F. and Fry, W. J. Ultrasonic absorption and reflection by lung tissue. *Physics in medicine and biology*, 5(4):401, 1961.

Elias, W. J., Lipsman, N., Ondo, W. G., Ghanouni, P., Kim, Y. G., Lee, W., Schwartz, M., Hynynen, K., Lozano, A. M., Shah, B. B., et al. A randomized trial of focused ultrasound thalamotomy for essential tremor. *New England Journal of Medicine*, 375(8):730–739, 2016.

Fatemi, M. and Greenleaf, J. F. Ultrasound-stimulated vibro-acoustic spectrography. *Science*, 280(5360):82–85, 1998.

Fei, D. and Shung, K. Ultrasonic backscatter from mammalian tissues. *The Journal of the Acoustical Society of America*, 78(3):871–876, 1985.

Ferlay, J., Soerjomataram, I., Ervik, M., Dikshit, R., Eser, S., Mathers, C., Rebelo, M., Parkin, D., Forman, D., and Bray, F. Globocan 2012 v1.0, cancer incidence and mortality worldwide: Iarc cancerbase no. 11 [internet]. Available from: `http://globocan.iarc.fr`, 2012a. Accessed: 2016-06-24.

Ferlay, J. S., Bray, H., Forman, F., and Mathers, D. C. and parkin, dm. globocan 2012 v1. 2, cancer incidence and mortality worldwide: Iarc cancerbase no. 10 [internet]. lyon, france: International agency for research on cancer; 2012, 2012b.

Fink, M. Time reversal of ultrasonic fields. i. basic principles. *IEEE transactions on ultrasonics, ferroelectrics, and frequency control*, 39(5):555–566, 1992.

Fisher, B., Anderson, S., Bryant, J., Margolese, R. G., Deutsch, M., Fisher, E. R., Jeong, J.-H., and Wolmark, N. Twenty-year follow-up of a randomized trial comparing total mastectomy, lumpectomy, and lumpectomy plus irradiation for the treatment of invasive breast cancer. *New England Journal of Medicine*, 347(16): 1233–1241, 2002.

Foley, J. *Focused Ultrasound: State of Field 2016*. Focused Ultrasound Foundation, 2016.

Frigo, M. and Johnson, S. G. Fftw: An adaptive software architecture for the fft. In *Acoustics, Speech and Signal Processing, 1998. Proceedings of the 1998 IEEE International Conference on*, volume 3, pages 1381–1384. IEEE, 1998.

Fry, F. and Johnson, L. Tumor irradiation with intense ultrasound. *Ultrasound in medicine & biology*, 4(4):337–341, 1978.

Fry, W. J., Mosberg Jr, W., Barnard, J., and Fry, F. Production of focal destructive lesions in the central nervous system with ultrasound*. *Journal of neurosurgery*, 11(5):471–478, 1954.

Fry, W. J., Fry, F., Barnard, J., Krumins, R., and Brennan, J. Ultrasonic lesions in mammalian central nervous system. *Science*, 122(3179):1091–1091, 1955.

Fung, Y. *Biomechanics: Mechanical Properties of Living Tissues*. Biomechanics. Springer New York, 1993. ISBN 9780387979472.

Gammell, P., Le Croissette, D., and Heyser, R. Temperature and frequency dependence of ultrasonic attenuation in selected tissues. *Ultrasound in medicine & biology*, 5(3):269–277, 1979.

Gennisson, J.-L., Deffieux, T., Fink, M., and Tanter, M. Ultrasound elastography: principles and techniques. *Diagnostic and interventional imaging*, 94(5):487–495, 2013.

Gertner, M., Wilson, B., and Sherar, M. Ultrasound properties of liver tissue during heating. *Ultrasound in medicine & biology*, 23(9):1395–1403, 1997.

Gervais, D. A., McGovern, F. J., Arellano, R. S., McDougal, W. S., and Mueller, P. R. Radiofrequency ablation of renal cell carcinoma: part 1, indications, results, and role in patient management over a 6-year period and ablation of 100 tumors. *American Journal of Roentgenology*, 185(1):64–71, 2005.

Ghiglia, D. C. and Pritt, M. D. *Two-dimensional phase unwrapping: theory, algorithms, and software*, volume 4. Wiley New York, 1998.

Ghoshal, G., Luchies, A. C., Blue, J. P., and Oelze, M. L. Temperature dependent ultrasonic characterization of biological media. *The Journal of the Acoustical Society of America*, 130(4):2203–2211, 2011.

Giering, K., Lamprecht, I., Minet, O., and Handke, A. Determination of the specific heat capacity of healthy and tumorous human tissue. *Thermochimica acta*, 251: 199–205, 1995.

Gill, I. S., Matin, S. F., Desai, M. M., Kaouk, J. H., Steinberg, A., Mascha, E., Thornton, J., Sherief, M. H., Strzempkowski, B., and Novick, A. C. Comparative analysis of laparoscopic versus open partial nephrectomy for renal tumors in 200 patients. *The Journal of urology*, 170(1):64–68, 2003.

Gill, I. S., Remer, E. M., Hasan, W. A., Strzempkowski, B., Spaliviero, M., Steinberg, A. P., Kaouk, J. H., Desai, M. M., and Novick, A. C. Renal cryoablation: outcome at 3 years. *The Journal of urology*, 173(6):1903–1907, 2005.

Goldstein, R. M., Zebker, H. A., and Werner, C. L. Satellite radar interferometry: Two-dimensional phase unwrapping. *Radio science*, 23(4):713–720, 1988.

Goss, S., Frizzell, L., and Dunn, F. Ultrasonic absorption and attenuation in mammalian tissues. *Ultrasound in medicine & biology*, 5(2):181–186, 1979.

Guntur, S. R., Lee, K. I., Paeng, D.-G., Coleman, A. J., and Choi, M. J. Temperature-dependent thermal properties of ex vivo liver undergoing thermal ablation. *Ultrasound in medicine & biology*, 39(10):1771–1784, 2013.

Haemmerich, D., dos Santos, I., Schutt, D. J., Webster, J. G., and Mahvi, D. M. In vitro measurements of temperature-dependent specific heat of liver tissue. *Medical engineering & physics*, 28(2):194–197, 2006.

Hamilton, M. F., Blackstock, D. T., et al. *Nonlinear acoustics*, volume 427. Academic press San Diego, 1998.

Haney, M. and OBrien, W. Temperature dependency of ultrasonic propagation properties in biological materials. *Tissue Characterization with Ultrasound. CRC Press, Boca Raton, Fla*, 1986.

Hasgall, P., Di Gennaro, F., Baumgartner, C., Neufeld, E., Gosselin, M., Payne, D., Klingenböck, A., and Kuster, N. Itis database for thermal and electromagnetic parameters of biological tissues. version 3.0, september 1st, 2015.

Heikkila, J., Curiel, L., and Hynynen, K. Local harmonic motion monitoring of focused ultrasound surgery - a simulation model. *Biomedical Engineering, IEEE Transactions on*, 57(1):185–193, 2010.

Heilman, W. and Morrison, D. Transparent gel candles, June 12 2002. URL `http://worldwide.espacenet.com/publicationDetails/biblio?CC=EP&NR=0871692B1&KC=B1&FT=D`. EP Patent 0,871,692.

Hou, G. Y., Marquet, F., Wang, S., and Konofagou, E. Optimization of real-time acoustical and mechanical monitoring of high intensity focused ultrasound (hifu) treatment using harmonic motion imaging for high focused ultrasound (hmifu). In *Engineering in Medicine and Biology Society (EMBC), 2013 35th Annual International Conference of the IEEE*, pages 6281–6284. IEEE, 2013.

Hou, G. Y., Marquet, F., Wang, S., and Konofagou, E. E. Multi-parametric monitoring and assessment of high-intensity focused ultrasound (hifu) boiling by harmonic motion imaging for focused ultrasound (hmifu): an ex vivo feasibility study. *Physics in medicine and biology*, 59(5):1121, 2014.

Howard, S. M. and Zanelli, C. I. Hifu transducer characterization using a robust needle hydrophone. In *6 th International Symposium on Therapeutic Ultrasound(AIP Conference Proceedings Volume 911)*, volume 911, pages 8–14, 2007.

Hoyt, K., Castaneda, B., Zhang, M., Nigwekar, P., di Sant'Agnese, P. A., Joseph, J. V., Strang, J., Rubens, D. J., and Parker, K. J. Tissue elasticity properties as biomarkers for prostate cancer. *Cancer Biomarkers*, 4(4, 5):213–225, 2008.

Huang, J. *Heating in vascular tissue and flow-through tissue phantoms induced by focused ultrasound*. PhD thesis, Boston University, 2002.

Illing, R., Kennedy, J., Wu, F., Ter Haar, G., Protheroe, A., Friend, P., Gleeson, F., Cranston, D., Phillips, R., and Middleton, M. The safety and feasibility of extracorporeal high-intensity focused ultrasound (hifu) for the treatment of liver and kidney tumours in a western population. *British journal of cancer*, 93(8): 890–895, 2005.

Jackson, E., Coussios, C., and Cleveland, R. Nonlinear acoustic properties of ex vivo bovine liver and the effects of temperature and denaturation. *Physics in medicine and biology*, 59(12):3223, 2014.

Jaros, J., Rendell, A. P., and Treeby, B. E. Full-wave nonlinear ultrasound simulation on distributed clusters with applications in high-intensity focused ultrasound. *International Journal of High Performance Computing Applications*, page 1094342015581024, 2015.

Kemmerer, J. P. and Oelze, M. L. Ultrasonic assessment of thermal therapy in rat liver. *Ultrasound in medicine & biology*, 38(12):2130–2137, 2012.

Kennedy, J. E. High-intensity focused ultrasound in the treatment of solid tumours. *Nature reviews cancer*, 5(4):321–327, 2005.

Keshavarzi, A., Vaezy, S., Kaczkowski, P. J., Keilman, G., Martin, R., Chi, E. Y., Garcia, R., and Fujimoto, V. Y. Attenuation coefficient and sound speed in human myometrium and uterine fibroid tumors. *Journal of ultrasound in medicine*, 20(5): 473–480, 2001.

Khokhlova, T. D., Canney, M. S., Lee, D., Marro, K. I., Crum, L. A., Khokhlova, V. A., and Bailey, M. R. Magnetic resonance imaging of boiling induced by high intensity focused ultrasound. *The Journal of the Acoustical Society of America*, 125(4):2420–2431, 2009.

Kim, H. and Varghese, T. Attenuation estimation using spectral cross-correlation. *Ieee Transactions on Ultrasonics Ferroelectrics and Frequency Control*, 54(3):510, 2007.

Kiss, M. Z., Varghese, T., and Hall, T. J. Viscoelastic characterization of in vitro canine tissue. *Physics in medicine and biology*, 49(18):4207, 2004.

Kiss, M. Z., Daniels, M. J., and Varghese, T. Investigation of temperature-dependent viscoelastic properties of thermal lesions in ex vivo animal liver tissue. *Journal of biomechanics*, 42(8):959–966, 2009.

Klatt, D., Hamhaber, U., Asbach, P., Braun, J., and Sack, I. Noninvasive assessment of the rheological behavior of human organs using multifrequency mr elastography: a study of brain and liver viscoelasticity. *Physics in medicine and biology*, 52(24): 7281, 2007.

Kohandel, M., Sivaloganathan, S., Tenti, G., and Darvish, K. Frequency dependence of complex moduli of brain tissue using a fractional zener model. *Physics in medicine and biology*, 50(12):2799, 2005.

Köhler, M. O., Mougenot, C., Quesson, B., Enholm, J., Le Bail, B., Laurent, C., Moonen, C. T., and Ehnholm, G. J. Volumetric hifu ablation under 3d guidance of rapid mri thermometry. *Medical physics*, 36(8):3521–3535, 2009.

Konofagou, E., Ottensmeyer, M., Dawson, S., and Hynynen, K. Harmonic motion imaging-applications in the detection of stiffer masses. In *Ultrasonics, 2003 IEEE Symposium on*, volume 1, pages 558–561. IEEE, 2003.

Konofagou, E., Ottensmeyer, M., Agabian, S., Dawson, S., and Hynynen, K. Estimating localized oscillatory tissue motion for assessment of the underlying mechanical modulus. *Ultrasonics*, 42(1):951–956, 2004.

Konofagou, E. E. and Hynynen, K. Localized harmonic motion imaging: theory, simulations and experiments. *Ultrasound in medicine & biology*, 29(10):1405–1413, 2003.

Konofagou, E. E., Maleke, C., and Vappou, J. Harmonic motion imaging for tumor imaging and treatment monitoring. In *Soft Tissue Biomechanical Modeling for Computer Assisted Surgery*, pages 257–280. Springer, 2012.

Kremkau, F. W., Barnes, R. W., and McGraw, C. P. Ultrasonic attenuation and propagation speed in normal human brain. *The Journal of the Acoustical Society of America*, 70(1):29–38, 1981.

Kruse, S., Smith, J., Lawrence, A., Dresner, M., Manduca, A., Greenleaf, J., and Ehman, R. Tissue characterization using magnetic resonance elastography: preliminary results. *Physics in medicine and biology*, 45(6):1579, 2000.

Kuznetsov, V. Equations of nonlinear acoustics. *Soviet Physics Acoustics - USSR*, 16(4):467, 1971.

Larrat, B., Pernot, M., Montaldo, G., Fink, M., and Tanter, M. Mr-guided adaptive focusing of ultrasound. *Ultrasonics, Ferroelectrics, and Frequency Control, IEEE Transactions on*, 57(8):1734–1747, 2010.

Lele, P. Hyperthermia by ultrasound. In *Proceedings of the International Symposium on Cancer Therapy by Hyperthermia and Radiation (JE Robinson and MJ Wizenberg, Eds.)*, pages 168–178, 1975.

Lepetit, J., Grajales, A., and Favier, R. Modelling the effect of sarcomere length on collagen thermal shortening in cooked meat: consequence on meat toughness. *Meat Science*, 54(3):239–250, 2000.

Lewis, M. A., Staruch, R. M., and Chopra, R. Thermometry and ablation monitoring with ultrasound. *International Journal of Hyperthermia*, 31(2):163–181, 2015.

Liu, D. and Ebbini, E. S. Viscoelastic tissue property measurement using high frequency ultrasound. In *Biomedical Imaging: From Nano to Macro, 2007. ISBI 2007. 4th IEEE International Symposium on*, pages 892–895. IEEE, 2007.

Lizzi, F. L., Muratore, R., Deng, C. X., Ketterling, J. A., Alam, S. K., Mikaelian, S., and Kalisz, A. Radiation-force technique to monitor lesions during ultrasonic therapy. *Ultrasound in medicine & biology*, 29(11):1593–1605, 2003.

Ljungberg, B., Campbell, S. C., Cho, H. Y., Jacqmin, D., Lee, J. E., Weikert, S., and Kiemeney, L. A. The epidemiology of renal cell carcinoma. *European urology*, 60 (4):615–621, 2011.

Lu, J., Ying, H., Sun, Z., Motamedi, M., Bell, B., and Sheppard, L. C. In vitro measurement of speed of sound during coagulate tissue heating. In *Ultrasonics Symposium, 1996. Proceedings., 1996 IEEE*, volume 2, pages 1299–1302. IEEE, 1996.

Lu, Y., Liu, X., Gong, X., and Zhang, D. Relationship between the temperature and the acoustic nonlinearity parameter in biological tissues. *Chinese Science Bulletin*, 49(22):2360–2363, 2004.

Lubinski, M. A., Emelianov, S. Y., Raghavan, K., Yagle, A. E., Skovoroda, A. R., and O'Donnell, M. Lateral displacement estimation using tissue incompressibility. *IEEE Transactions on Ultrasonics Ferroelectrics and Frequency Control*, 43(2):247–256, 1996.

Luciani, L. G., Cestari, R., and Tallarigo, C. Incidental renal cell carcinomaage and stage characterization and clinical implications: study of 1092 patients (1982–1997). *Urology*, 56(1):58–62, 2000.

Lynn, J. G. and Putnam, T. J. Histology of cerebral lesions produced by focused ultrasound. *The American journal of pathology*, 20(3):637, 1944.

Lynn, J. G., Zwemer, R. L., Chick, A. J., and Miller, A. E. A new method for the generation and use of focused ultrasound in experimental biology. *The Journal of general physiology*, 26(2):179, 1942.

Lyons, M. E. and Parker, K. J. Absorption and attenuation in soft tissues. ii. experimental results. *Ultrasonics, Ferroelectrics and Frequency Control, IEEE Transactions on*, 35(4):511–521, 1988.

Madsen, E. L., Dong, F., Frank, G. R., Garra, B. S., Wear, K. A., Wilson, T., Zagzebski, J. A., Miller, H. L., Shung, K. K., Wang, S., et al. Interlaboratory comparison of ultrasonic backscatter, attenuation, and speed measurements. *Journal of ultrasound in medicine*, 18(9):615–631, 1999.

Maleke, C. and Konofagou, E. E. Harmonic motion imaging for focused ultrasound (hmifu): a fully integrated technique for sonication and monitoring of thermal ablation in tissues. *Physics in medicine and biology*, 53(6):1773, 2008.

Maleke, C. and Konofagou, E. E. In vivo feasibility of real-time monitoring of focused ultrasound surgery (fus) using harmonic motion imaging (hmi). *Biomedical Engineering, IEEE Transactions on*, 57(1):7–11, 2010.

Maleke, C., Pernot, M., and Konofagou, E. E. A single-element focused transducer method for harmonic motion imaging. In *IEEE Ultrasonics Symposium*, pages 17–20, 2005.

Maleke, C., Pernot, M., and Konofagou, E. E. Single-element focused ultrasound transducer method for harmonic motion imaging. *Ultrasonic imaging*, 28(3):144–158, 2006.

Manduca, A., Muthupillai, R., Rossman, P., Greenleaf, J. F., and Ehman, R. L. Local wavelength estimation for magnetic resonance elastography. In *Image Processing, 1996. Proceedings., International Conference on*, volume 3, pages 527–530. IEEE, 1996.

Marberger, M., Schatzl, G., Cranston, D., and Kennedy, J. Extracorporeal ablation of renal tumours with high-intensity focused ultrasound. *BJU international*, 95 (s2):52–55, 2005.

Marczak, W. Water as a standard in the measurements of speed of sound in liquids. *the Journal of the Acoustical Society of America*, 102(5):2776–2779, 1997.

Marmor, J., POSTIC, T., and HAHN, G. Treatment of spontaneous tumors in dogs and cats by hyperthermia induced by ultrasound. In *Radiation research*, volume 74, pages 526–527. Radiation research soc 2021 Spring Rd, STE 600, Oak Brook, IL 60521, 1978.

Marmor, J. B., Pounds, D., Postic, T. B., and Hahn, G. M. Treatment of superficial human neoplasms by local hyperthermia induced by ultrasound. *Cancer*, 43(1): 188–197, 1979.

Mast, T. D. Empirical relationships between acoustic parameters in human soft tissues. *Acoustics Research Letters Online*, 1(2):37–42, 2000.

McAleavey, S. A., Nightingale, K. R., and Trahey, G. E. Estimates of echo correlation and measurement bias in acoustic radiation force impulse imaging. *Ultrasonics, Ferroelectrics and Frequency Control, IEEE Transactions on*, 50(6):631–641, 2003.

McDannold, N. and Maier, S. E. Magnetic resonance acoustic radiation force imaging. *Medical physics*, 35(8):3748–3758, 2008.

Morris, H., Rivens, I., Shaw, A., and ter Haar, G. Investigation of the viscous heating artefact arising from the use of thermocouples in a focused ultrasound field. *Physics in medicine and biology*, 53(17):4759, 2008.

Muller, A., Petrusca, L., Auboiroux, V., Valette, P., Salomir, R., and Cotton, F. Management of respiratory motion in extracorporeal high-intensity focused ultrasound treatment in upper abdominal organs: current status and perspectives. *Cardiovascular and interventional radiology*, 36(6):1464–1476, 2013.

Muthupillai, R., Lomas, D., Rossman, P., Greenleaf, J. F., et al. Magnetic resonance elastography by direct visualization of propagating acoustic strain waves. *Science*, 269(5232):1854, 1995.

Nasoni, R., Bowen, T., Connor, W., and Sholes, R. In vivo temperature dependence of ultrasound speed in tissue and its application to noninvasive temperature monitoring. *Ultrasonic Imaging*, 1(1):34–43, 1979.

NCI. Seer stat fact sheets: Kidney and renal pelvis cancer [internet]. Available from: `http://seer.cancer.gov/statfacts/html/kidrp.html`, 2016. Accessed: 2016-06-24.

Nightingale, K., McAleavey, S., and Trahey, G. Shear-wave generation using acoustic radiation force: in vivo and ex vivo results. *Ultrasound in medicine & biology*, 29 (12):1715–1723, 2003.

Nightingale, K., Soo, M. S., Palmeri, M., Congdon, A., Frinkley, K., and Trahey, G. Imaging tissue mechanical properties using impulsive acoustic radiation force. In *Biomedical Imaging: Nano to Macro, 2004. IEEE International Symposium on*, pages 41–44. IEEE, 2004.

Nightingale, K., Fahey, B., Hsu, S., Frinkley, K., Dahl, J., Palmeri, M., Zhai, L., Pinton, G., and Trahey, G. On the potential for guidance of ablation therapy using acoustic radiation force impulse imaging. In *Biomedical Imaging: From Nano to Macro, 2007. ISBI 2007. 4th IEEE International Symposium on*, pages 1116–1119. IEEE, 2007.

Nyborg, W. Acoustic streaming. *Physical acoustics*, 2(Pt B):265, 1965.

Olympus. *Ultrasonic transducers technical notes*, 2011.

Ophir, J., Cespedes, I., Ponnekanti, H., Yazdi, Y., and Li, X. Elastography: a quantitative method for imaging the elasticity of biological tissues. *Ultrasonic imaging*, 13(2):111–134, 1991.

Palmeri, M. L. and Nightingale, K. R. Acoustic radiation force-based elasticity imaging methods. *Interface Focus*, page rsfs20110023, 2011.

Palmeri, M. L., Sharma, A. C., Bouchard, R. R., Nightingale, R. W., and Nightingale, K. R. A finite-element method model of soft tissue response to impulsive acoustic radiation force. *Ultrasonics, Ferroelectrics and Frequency Control, IEEE Transactions on*, 52(10):1699–1712, 2005.

Palmeri, M. L., McAleavey, S. A., Trahey, G. E., and Nightingale, K. R. Ultrasonic tracking of acoustic radiation force-induced displacements in homogeneous media. *Ultrasonics, Ferroelectrics and Frequency Control, IEEE Transactions on*, 53(7): 1300–1313, 2006.

Parker, K. J. Ultrasonic attenuation and absorption in liver tissue. *Ultrasound in medicine & biology*, 9(4):363–369, 1983.

Pauly, H. and Schwan, H. Mechanism of absorption of ultrasound in liver tissue. *The Journal of the Acoustical Society of America*, 50(2B):692–699, 1971.

Pennes, H. H. Analysis of tissue and arterial blood temperatures in the resting human forearm. *Journal of applied physiology*, 1(2):93–122, 1948.

Pinkerton, J. The absorption of ultrasonic waves in liquids and its relation to molecular constitution. *Proceedings of the Physical Society. Section B*, 62(2):129, 1949.

Pinton, G. F., Dahl, J. J., and Trahey, G. E. Rapid tracking of small displacements with ultrasound. *Ultrasonics, Ferroelectrics and Frequency Control, IEEE Transactions on*, 53(6):1103–1117, 2006.

Rabkin, B. A., Zderic, V., and Vaezy, S. Hyperecho in ultrasound images of hifu therapy: involvement of cavitation. *Ultrasound in medicine & biology*, 31(7):947–956, 2005.

Rajagopalan, B., JF, G., PJ, T., Johnson, S., and Bahn, R. Variation of acoustic speed with temperature in various excised human tissues studied by ultrasound computerized tomography. In *Ultrasonic Tissue Characterization II: A Collection of Reviewed Papers Based on Talks Presented at the Second International Symposium on Ultrasonic Tissue Characterization Held at the National Bureau of Standards, Gaithersburg, Maryland, June 13-15, 1977*, volume 525, page 227. US Department of Commerce, National Bureau of Standards, 1979.

Remzi, M., Katzenbeisser, D., Waldert, M., Klingler, H.-C., Susani, M., Memarsadeghi, M., Heinz-Peer, G., Haitel, A., Herwig, R., and Marberger, M. Renal tumour size measured radiologically before surgery is an unreliable variable for predicting histopathological features: benign tumours are not necessarily small. *BJU international*, 99(5):1002–1006, 2007.

Richards, A. University of oxford advanced research computing. `Zenodo.10.5281/zenodo.22558`, 2016.

Righetti, R., Kallel, F., Stafford, R. J., Price, R. E., Krouskop, T. A., Hazle, J. D., and Ophir, J. Elastographic characterization of hifu-induced lesions in canine livers. *Ultrasound in medicine & biology*, 25(7):1099–1113, 1999.

Ritchie, R., Collin, J., Coussios, C., and Leslie, T. Attenuation and de-focusing during high-intensity focused ultrasound therapy through peri-nephric fat. *Ultrasound in medicine & biology*, 39(10):1785–1793, 2013.

Ritchie, R. W., Leslie, T., Phillips, R., Wu, F., Illing, R., Ter Haar, G., Protheroe, A., and Cranston, D. Extracorporeal high intensity focused ultrasound for renal tumours: a 3-year follow-up. *BJU international*, 106(7):1004–1009, 2010.

Roberts, D. A., Detre, J. A., Bolinger, L., Insko, E. K., Lenkinski, R. E., Pentecost, M. J., and Leigh Jr, J. S. Renal perfusion in humans: Mr imaging with spin tagging of arterial water. *Radiology*, 196(1):281–286, 1995.

Robinson, T. and Lele, P. An analysis of lesion development in the brain and in plastics by high-intensity focused ultrasound at low-megahertz frequencies. *The Journal of the Acoustical Society of America*, 51(4B):1333–1351, 1972.

Rossmann, C. and Haemmerich, D. Review of temperature dependence of thermal properties, dielectric properties, and perfusion of biological tissues at hyperthermic and ablation temperatures. *Critical Reviews in Biomedical Engineering*, 42(6), 2014.

Roylance, D. Engineering viscoelasticity. *Department of Materials Science and Engineering–Massachusetts Institute of Technology, Cambridge MA*, 2139:1–37, 2001.

Sandrin, L., Tanter, M., Catheline, S., and Fink, M. Shear modulus imaging with 2-d transient elastography. *Ultrasonics, Ferroelectrics, and Frequency Control, IEEE Transactions on*, 49(4):426–435, 2002.

Sapareto, S. A. and Dewey, W. C. Thermal dose determination in cancer therapy. *International Journal of Radiation Oncology* Biology* Physics*, 10(6):787–800, 1984.

Sapin-de Brosses, E., Gennisson, J., Pernot, M., Fink, M., and Tanter, M. Temperature dependence of the shear modulus of soft tissues assessed by ultrasound. *Physics in medicine and biology*, 55(6):1701, 2010.

Sapin-de Brosses, E., Pernot, M., and Tanter, M. The link between tissue elasticity and thermal dose in vivo. *Physics in medicine and biology*, 56(24):7755, 2011.

Sarvazyan, A. A new approach to remote ultrasonic evaluation of viscoelastic properties of tissues for diagnostics and healing monitoring. In *Abstract of ARPA/ONR Medical Ultrasonic Imaging Technology Workshop, Landsdowne, Virginia*, pages 24–26, 1995.

Sarvazyan, A. P., Rudenko, O. V., Swanson, S. D., Fowlkes, J. B., and Emelianov, S. Y. Shear wave elasticity imaging: a new ultrasonic technology of medical diagnostics. *Ultrasound in medicine & biology*, 24(9):1419–1435, 1998.

Sarvazyan, A. P., Rudenko, O. V., and Nyborg, W. L. Biomedical applications of radiation force of ultrasound: historical roots and physical basis. *Ultrasound in medicine & biology*, 36(9):1379–1394, 2010.

Schwartz, L. H., Richaud, J., Buffat, L., Touboul, E., and Schlienger, M. Kidney mobility during respiration. *Radiotherapy and Oncology*, 32(1):84–86, 1994.

Sehgal, C., Brown, G., Bahn, R., and Greenleaf, J. Measurement and use of acoustic nonlinearity and sound speed to estimate composition of excised livers. *Ultrasound in medicine & biology*, 12(11):865–874, 1986.

Sekins, K., Leeper, D., Hoffman, J., Wolfson, M. R., and Shaffer, T. Feasibility of lung cancer hyperthermia using breathable perfluorochemical (pfc) liquids. part i: Convective hyperthermia. *International journal of hyperthermia*, 20(3):252–277, 2004.

Shahmirzadi, D., Hou, G. Y., Chen, J., and Konofagou, E. E. Ex vivo characterization of canine liver tissue viscoelasticity after high-intensity focused ultrasound ablation. *Ultrasound in medicine & biology*, 40(2):341–350, 2014.

Shi, X., Martin, R. W., Rouseff, D., Vaezy, S., and Crum, L. A. Detection of high-intensity focused ultrasound liver lesions using dynamic elastometry. *Ultrasonic imaging*, 21(2):107–126, 1999.

Shore, D., Woods, M., and Miles, C. Attenuation of ultrasound in post rigor bovine skeletal muscle. *Ultrasonics*, 24(2):81–87, 1986.

Soneson, J. E. A user-friendly software package for hifu simulation. In *8th International Symposium on Therapeutic Ultrasound*, volume 1113, pages 165–169. AIP Publishing, 2009.

Stafford, R. J., Kallel, F., Price, R. E., Cromeens, D. M., Krouskop, T. A., Hazle, J. D., and Ophir, J. Elastographic imaging of thermal lesions in soft tissue: a preliminary study in vitro. *Ultrasound in medicine & biology*, 24(9):1449–1458, 1998.

Starritt, H., Duck, F., and Humphrey, V. Forces acting in the direction of propagation in pulsed ultrasound fields. *Physics in medicine and biology*, 36(11):1465, 1991.

Sugimoto, T., Ueha, S., and Itoh, K. Tissue hardness measurement using the radiation force of focused ultrasound. In *Ultrasonics Symposium, 1990. Proceedings., IEEE 1990*, pages 1377–1380. IEEE, 1990.

Suomi, V. Matlab file exchange: 3-D heat equation numerical solution, 2016. URL `https://uk.mathworks.com/matlabcentral/fileexchange/59336-3-d-heat-equation-numerical-solution`.

Suomi, V. and Cleveland, R. Acoustic, thermal and mechanical properties of tissue. In Khokhlova, V., Crum, L., Aubry, J.-F., and ter Haar, G., editors, *Introduction to high-intensity focused ultrasound therapy*. Springer, 2017. (in press).

Suomi, V., Edwards, D., and Cleveland, R. Optical quantification of harmonic acoustic radiation force excitation in a tissue-mimicking phantom. *Ultrasound in medicine & biology*, 41(12):3216–3232, 2015.

Suomi, V., Han, Y., Konofagou, E., and Cleveland, R. O. The effect of temperature dependent tissue parameters on acoustic radiation force induced displacements. *Physics in Medicine and Biology*, 61(20):7427–7447, 2016a.

Suomi, V., Jaros, J., Treeby, B., and Cleveland, R. Nonlinear 3-d simulation of high-intensity focused ultrasound therapy in the kidney. In *Engineering in Medicine and Biology Society (EMBC), 2016 IEEE 38th Annual International Conference of the*, pages 5648–5651. IEEE, 2016b.

Suomi, V., Jaros, J., Treeby, B., and Cleveland, R. Full modelling of high-intensity focused ultrasound and thermal heating in the kidney of realistic patient models. 2017. (submitted).

Susani, M., Madersbacher, S., Kratzik, C., Vingers, L., and Marberger, M. Morphology of tissue destruction induced by focused ultrasound. *European urology*, 23: 34–38, 1992.

Szabo, T. *Diagnostic Ultrasound Imaging: Inside Out*. Academic Press series in biomedical engineering. Elsevier Academic Press, 2004. ISBN 9780126801453.

Tabei, M., Mast, T. D., and Waag, R. C. A k-space method for coupled first-order acoustic propagation equations. *Journal of the Acoustical Society of America*, 111 (1):53–63, 2002.

Techavipoo, U., Varghese, T., Zagzebski, J., Stiles, T., and Frank, G. Temperature dependence of ultrasonic propagation speed and attenuation in canine tissue. *Ultrasonic imaging*, 24(4):246–260, 2002.

Techavipoo, U., Varghese, T., Chen, Q., Stiles, T., Zagzebski, J., and Frank, G. Temperature dependence of ultrasonic propagation speed and attenuation in excised canine liver tissue measured using transmitted and reflected pulses. *The Journal of the Acoustical Society of America*, 115(6):2859–2865, 2004.

ter Haar, . G. and Coussios, C. High intensity focused ultrasound: physical principles and devices. *International Journal of Hyperthermia*, 23(2):89–104, 2007.

Ter Haar, G., Sinnett, D., and Rivens, I. High intensity focused ultrasound-a surgical technique for the treatment of discrete liver tumours. *Physics in medicine and biology*, 34(11):1743, 1989.

Ter Haar, G., Clarke, R., Vaughan, M., and Hill, C. Trackless surgery using focused ultrasound: Technique and case report. *Minimally Invasive Therapy*, 1(1):13–19, 1991a.

Ter Haar, G., Rivens, I., Chen, L., and Riddler, S. High intensity focused ultrasound for the treatment of rat tumours. *Physics in medicine and biology*, 36(11):1495, 1991b.

Torr, G. The acoustic radiation force. *American Journal of Physics*, 52(5):402–408, 1984.

Treeby, B. E. and Cox, B. Modeling power law absorption and dispersion for acoustic propagation using the fractional laplacian. *The Journal of the Acoustical Society of America*, 127(5):2741–2748, 2010a.

Treeby, B. E. and Cox, B. T. k-wave: Matlab toolbox for the simulation and reconstruction of photoacoustic wave fields. *Journal of biomedical optics*, 15(2):021314–021314, 2010b.

Treeby, B. E., Jaros, J., Rendell, A. P., and Cox, B. Modeling nonlinear ultrasound propagation in heterogeneous media with power law absorption using a k-space pseudospectral method. *The Journal of the Acoustical Society of America*, 131(6): 4324–4336, 2012.

Turnbull, D., Wilson, S., Hine, A., and Foster, F. Ultrasonic characterization of selected renal tissues. *Ultrasound in medicine & biology*, 15(3):241–253, 1989.

Vaezy, S., Shi, X., Martin, R. W., Chi, E., Nelson, P. I., Bailey, M. R., and Crum, L. A. Real-time visualization of high-intensity focused ultrasound treatment using ultrasound imaging. *Ultrasound in medicine & biology*, 27(1):33–42, 2001.

Valvano, J., Cochran, J., and Diller, K. Thermal conductivity and diffusivity of biomaterials measured with self-heated thermistors. *International Journal of Thermophysics*, 6(3):301–311, 1985.

Van Poppel, H., Da Pozzo, L., Albrecht, W., Matveev, V., Bono, A., Borkowski, A., Colombel, M., Klotz, L., Skinner, E., Keane, T., et al. A prospective, randomised eortc intergroup phase 3 study comparing the oncologic outcome of elective nephron-sparing surgery and radical nephrectomy for low-stage renal cell carcinoma. *European urology*, 59(4):543–552, 2011.

Vappou, J., Maleke, C., and Konofagou, E. E. Quantitative viscoelastic parameters measured by harmonic motion imaging. *Physics in medicine and biology*, 54(11): 3579, 2009.

Varghese, T., Zagzebski, J., and Lee, F. Elastographic imaging of thermal lesions in the liver in vivo following radiofrequency ablation: preliminary results. *Ultrasound in medicine & biology*, 28(11):1467–1473, 2002.

Varghese, T., Techavipoo, U., Liu, W., Zagzebski, J. A., Chen, Q., Frank, G., and Lee Jr, F. T. Elastographic measurement of the area and volume of thermal lesions resulting from radiofrequency ablation: pathologic correlation. *American journal of roentgenology*, 181(3):701–707, 2003.

Vieira, S. L., Pavan, T. Z., Junior, J. E., and Carneiro, A. A. Paraffin-gel tissue-mimicking material for ultrasound-guided needle biopsy phantom. *Ultrasound in medicine & biology*, 39(12):2477–2484, 2013.

Wall, M. S., Deng, X.-H., Torzilli, P. A., Doty, S. B., O'Brien, S. J., and Warren, R. F. Thermal modification of collagen. *Journal of Shoulder and Elbow Surgery*, 8 (4):339–344, 1999.

Wang, T.-Y., Hall, T., Xu, Z., Fowlkes, J., and Cain, C. Imaging feedback for histotripsy by characterizing dynamics of acoustic radiation force impulse (arfi)-induced shear waves excited in a treated volume. *Ultrasonics, Ferroelectrics and Frequency Control, IEEE Transactions on*, 61(7):1137–1151, 2014.

Watkin, N., Ter Haar, G., and Rivens, I. The intensity dependence of the site of maximal energy deposition in focused ultrasound surgery. *Ultrasound in medicine & biology*, 22(4):483–491, 1996.

Westervelt, P. J. Parametric acoustic array. *The Journal of the Acoustical Society of America*, 35(4):535–537, 1963.

Widder, D. V. *The heat equation*, volume 67. Academic Press, 1976.

Wikimedia Commons. Media repository, 2016. URL `https://commons.wikimedia.org/wiki/Main_Page`. Accessed: 07-July-2016.

Wladimiroff, J., Craft, I., and Talbert, D. In vitro measurements of sound velocity in human fetal brain tissue. *Ultrasound in medicine & biology*, 1(4):377–382, 1975.

Wood, R. W. and Loomis, A. L. Xxxviii. the physical and biological effects of high-frequency sound-waves of great intensity. *The London, Edinburgh, and Dublin philosophical magazine and journal of science*, 4(22):417–436, 1927.

Worthington, A. and Sherar, M. Changes in ultrasound properties of porcine kidney tissue during heating. *Ultrasound in medicine & biology*, 27(5):673–682, 2001.

Worthington, A., Trachtenberg, J., and Sherar, M. Ultrasound properties of human prostate tissue during heating. *Ultrasound in medicine & biology*, 28(10):1311–1318, 2002.

Wright, N. and Humphrey, J. Denaturation of collagen via heating: an irreversible rate process. *Annual review of biomedical engineering*, 4(1):109–128, 2002.

Wu, F., Wang, Z.-B., Cao, Y.-D., Chen, W., Bai, J., Zou, J., and Zhu, H. A randomised clinical trial of high-intensity focused ultrasound ablation for the treatment of patients with localised breast cancer. *British journal of cancer*, 89(12): 2227–2233, 2003a.

Wu, F., Wang, Z.-B., Chen, W.-Z., Bai, J., Zhu, H., and Qiao, T.-Y. Preliminary experience using high intensity focused ultrasound for the treatment of patients with advanced stage renal malignancy. *The Journal of urology*, 170(6):2237–2240, 2003b.

Wu, F., Wang, Z.-B., Chen, W.-Z., Zhu, H., Bai, J., Zou, J.-Z., Li, K.-Q., Jin, C.-B., Xie, F.-L., and Su, H.-B. Extracorporeal high intensity focused ultrasound ablation in the treatment of patients with large hepatocellular carcinoma. *Annals of surgical oncology*, 11(12):1061–1069, 2004.

Wu, T., Felmlee, J. P., Greenleaf, J. F., Riederer, S. J., and Ehman, R. L. Assessment of thermal tissue ablation with mr elastography. *Magnetic Resonance in Medicine*, 45(1):80–87, 2001.

Yang, D., Converse, M. C., Mahvi, D. M., and Webster, J. G. Measurement and analysis of tissue temperature during microwave liver ablation. *IEEE transactions on biomedical engineering*, 54(1):150–155, 2007.

Yao, L. X., Zagzebski, J. A., and Madsen, E. L. Backscatter coefficient measurements using a reference phantom to extract depth-dependent instrumentation factors. *Ultrasonic Imaging*, 12(1):58–70, 1990.

Yarmolenko, P. S., Moon, E. J., Landon, C., Manzoor, A., Hochman, D. W., Viglianti, B. L., and Dewhirst, M. W. Thresholds for thermal damage to normal tissues: an update. *International Journal of Hyperthermia*, 27(4):320–343, 2011.

Zabolotskaya, E. and Khokhlov, R. Quasi-plane waves in the nonlinear acoustics of confined beams. *Sov. Phys. Acoust*, 15(1):35–40, 1969.

Zaitsev, A., Raymond, S., Thierman, J., Juste, J., and Hynynen, K. Focused ultrasound thermal surgery, imaging, and elastometry using the same phased array: Feasibility study. In *Ultrasonics Symposium, 2004 IEEE*, volume 3, pages 2231–2234. IEEE, 2004.

Zderic, V., Keshavarzi, A., Andrew, M. A., Vaezy, S., and Martin, R. W. Attenuation of porcine tissues in vivo after high-intensity ultrasound treatment. *Ultrasound in medicine & biology*, 30(1):61–66, 2004.

Zhai, L., Palmeri, M. L., Bouchard, R. R., Nightingale, R. W., and Nightingale, K. R. An integrated indenter-arfi imaging system for tissue stiffness quantification. *Ultrasonic imaging*, 30(2):95–111, 2008.

Zhang, N., Cleveland, R., and Edwards, D. J. Electromagnetic-acoustic imaging of stiffness and dielectric properties in gels. *The Journal of the Acoustical Society of America*, 133(5):3358–3358, 2013.